Particle Dynamics near Fluid Interfaces in Low-Reynolds Number Flows

Thesis by
James Arthur Stoos

in Partial Fulfillment of the Requirements
for the Degree of
Doctor of Philosophy

California Institute of Technology
Pasadena, California
1988
(Submitted September 24, 1987)

To my best friend, Ruthie,

and to my family

Acknowledgments

I would like to thank my advisors, Professor Gary Leal and Dr. Eric Herbolzheimer, both for suggesting this research topic and for their help during the course of this research. In addition I wish to thank Dr. Leal for proofreading the manuscript; his comments have greatly improved the presentation of this material. The help of both my advisors has not only aided me directly in formulating the research for this thesis, but their questions have shaped the way I approach new research problems in general.

Much of my research was improved greatly by the use of the excellent facilities and support provided by the faculty, staff and students of Caltech; for this I am grateful. In particular, George Griffith and Seichi Nakatawase were invaluable in the design and construction of the experimental apparatus. Also, I would like to thank Professor Flagen and Professor Morgan and their students Brian Wong and Liuann Liang for their assistance and for the use of their equipment in these experiments. My research has benefited greatly from the interactions with both the Leal and Herbolzheimer research groups, in particular, I am very grateful to Howard Stone, Ed Ascoli, Enrique Geffroy-Aguilar, David Dandy and Chris Chow for their assistance and for all that I have learned in working with them. It would be impossible to list all of the other people who have helped me through their comments and their camaraderie and friendship, but to name a few, I would like to thank Seung-Man Yang, In-Seok Kang, Sonia Kreidenweis-Dandy, Hong-Man Chan, Tony Geller, Francisco Avila-Segura, Lou Durlofsky, Roger Bonnecaze, Dave Loren and John Bauer.

Also, I would like to thank Dr. Collins and Dr. Hoffman for providing me with copies of their results. Gordon Kent at Questar provided much help with the microscope, for which I am grateful.

I would also like to thank Weyerhauser Corporation and Chevron Corporation for providing me with fellowships during part of my stay at Caltech.

Most of all, I would like to thank my father, for his support and encouragement; all that I am, I owe to him. I would like to dedicate this thesis to my departed Mother, one of the nicest people I have ever known, and to my best friend and wife, Ruthie, with love.

Abstract

Numerical solutions for the creeping motion of a spherical particle in a linear axisymmetric straining flow normal to a deformable interface are presented for a range of viscosity ratios, capillary numbers and Bond numbers. The parameter ranges investigated have applications in areas of flotation (small interface deformation) and material processing (large interface deformation). The accuracy of previous solutions for flotation problems, which neglect interface deformation is considered, along with the magnitude and form of interface deformation "defects" that may appear in material processing applications involving fluids containing bubbles or small particles.

Numerical solutions for the equilibrium particle-interface configuration for a neutrally buoyant spherical particle contacting a deformable fluid/gas interface in a linear axisymmetric straining flow at low Reynolds number are presented for a range of contact angles and capillary numbers. These solutions may have applications both in flotation separation processes and in contact angle and surface tension measurement. In addition, the accuracy of simply combining previous results for particle detachment due to particle buoyancy with the results for particle detachment due to viscous forces is considered. The equilibrium configuration is especially sensitive to the inclusion of a small amount of flow for small contact angles and for capillary numbers near the critical capillary number.

Trajectories of small spherical particles around a spherical drop (bubble and solid) are calculated from an approximate solution employing a matched asymptotic expansion. Viscous interaction is seen to have a large effect on the trajectory around a solid collector and a small effect on the trajectory around a bubble. Previous solutions are found to be in error in their prediction of an increase in the capture efficiency because of viscous interactions; the capture efficiency decreases significantly in this case.

Finally, the trajectories of particles around bubbles and the capture of particles by bubbles is investigated experimentally.

Table of Contents

1. Introduction†

Many industrial processes produce liquid waste products containing very small particles. Because of the small size of these particles, often less than 50 microns in diameter, separation by sedimentation is very slow and separation by filtration is not economically feasible. Increasing concern over water pollution has prompted the application of flotation technology to this problem. Flotation consists of adsorption of these particles onto significantly larger, although still small, bubbles which transport the particles to the solution surface where they can be mechanically removed.

Mineral or froth flotation has been used for many years as a method of concentrating and separating valuable minerals. From the first true flotation process, used in 1877 to concentrate graphite ore, flotation has evolved into a substantial industry which in 1962 accounted for over 1 million tons of minerals processed per day in the United States, Sutherland and Wark (1955), Fuerstenau and Healy (1972). Froth flotation, named for the bubbles or froth produced on the liquid surface, is characterized by: fairly high concentration of particles, up to 25 % by weight; bubbles generally between 0.5 and 2 millimeters in diameter and particles generally larger than 100 microns in diameter. Also, froth flotation is a selective separation which utilizes the selective adsorption of additives, termed collectors, to render the desired mineral hydrophobic and thus attracted to the bubble-liquid interface. Other additives, termed activators and depressants, are used to further improve the selectivity of this adsorption. In fact, it has been observed that very clean mineral surfaces will not stick to the bubble surface, although trace contaminants always present in real processes reduce the practicality of this observation, Sutherland and Wark (1955). Suspensions treated by froth flotation are generally stirred to prevent the sedimentation of larger mineral particles, which would reduce the efficiency of the process. Fi-

† The references for this section may be found with the references for Chapter 4, starting on page 237.

nally, in froth flotation a frother or surfactant, if not already present, is added to solution to prevent the bubbles from rupturing upon reaching the liquid surface and consequently losing captured minerals back into solution.

On the other hand, waste treatment or effluent flotation is generally concerned with removal of all the suspended particles and is not a selective separation. Some other differentiating characteristics of effluent flotation are: much lower particle concentrations, as low as 20 parts per million; significantly smaller bubbles, less than 0.1 millimeters in diameter; and smaller particles, generally less than 20 microns in diameter. Because these small particles are often very close to neutrally buoyant, effluent flotation solutions are generally not stirred and often no frother is required.

There are three principal techniques for producing flotation bubbles. In the first and simplest method, a "dispersed air" process, bubbles are formed by forcing gas through spargers. The second method, a "dissolved air" process, utilizes a pressure drop to nucleate bubbles directly on the particles from a solution saturated with a gas. The final method, which consists of electrolytically generating the bubbles, has the advantage of producing much smaller bubbles with a more uniform size distribution. Fukui and Yuu (1980) report that initial problems with electrode scumming have been solved and Elwood (1968) indicates that "electro-flotation" has been used effectively.

The utility of many of the previous studies on flotation has been limited by the empirical nature of these studies. In this thesis, a fundamental study of effluent flotation is undertaken to determine the relative contributions of the many process variables to the process efficiency. As most of the earlier work has concentrated on the effects of the "chemical" variables, i.e. on the relative effects of the various additives, we will concentrate on the hydrodynamic effects in the process, however nonhydrodynamic effects will be considered briefly in Chapters 4 and 5. Generally the effects of the mechanical variables, e.g., particle and bubble size, charge and concentration have been studied by assuming the rate

of removal of particles follows a first order chemical reaction type of behavior,

$$-\frac{\partial c}{\partial t} = kc, \tag{1}$$

where c is the number density of particles of a given diameter and k is the rate constant incorporating the effects of all the other mechanical and chemical variables. However results from initial experiments on the effects of the particle radius, a, on k have produced a variety of results including: k independent of a, $k \propto lna$, $k \propto a$ and, $k \propto a^2$, Morris (1952), Bushell (1962), Tominson and Fleming (1963), Gaudin et al. (1942). More recent studies by Reay and Ratcliff (1973, 1975) and Collins and Jameson (1976, 1977) have found agreement with $k \propto a^{\frac{3}{2}}$ for glass beads. However, their results for polystyrene particles are in disagreement, giving $k \propto a^{\frac{1}{2}}$ and $k \propto a^{\frac{3}{2}}$, respectively. These discepancies are not surprising, considering the large number of variables which must be controlled in a flotation experiment. Clearly, a fundamental theoretical analysis of flotation is needed, both to predict the effects of the multiple operating variables on the process efficiency and as a guide to the key variables which must be controlled in flotation experiments. The need for this study also becomes evident when examining the relatively well developed literature for the similar problem of particulate capture by solid collectors, the filtration problem Spielman (1977).

Because of the complexity of the flotation process, initial theoretical treatments of the process hydrodynamics have necessarily been very simplified. Generally, the solution is assumed so dilute that only one particle and bubble need be considered. The first studies treated the particles as fluid points and considered gravity and inertia as the only forces causing the particles to deviate from the fluid streamlines, Reay and Ratcliff (1973) and Flint and Howarth (1971). Effects that were neglected include: hydrodynamic interactions between the particle and bubble, electroviscous forces due to particle and bubble charges and resulting double-layers, bubble deformation, bubble-bubble hydrodynamic interactions, Brownian motion of the particles, and the effects of viscous drag of the fluid on the stability of captured particles attached to the rear of the

bubble. Rulev, Deryagin and Dukhin have attempted to consider some of these effects in a series of papers published in the Soviet Union, by Deryagin, Dukhin and Rulev (1971, 1976, 1977). Also, hydrodynamic interactions between two solid spheres and between two drops have been investigated by a number of researchers, see Chapter 3., however these investigations have failed to take advantage of the limiting solutions suggested by the characteristics of the flotation problem. Furthermore, although small bubbles tend to rise with terminal velocities of equivalent solid spheres, Garner and Hammerton (1954), the observed mobility of captured particles on the surfaces of bubbles and the deformation of bubble surfaces accompanying the interaction of a bubble with a nearby particle (or other bubble) demonstrates that caution is required in describing the bubbles as "solid". Although these previous investigations represent a significant contribution, they rely on a number of ad-hoc approximations which are difficult, (if not impossible in some cases), to justify.

In the following chapters we investigate some of the above problems, specifically as they apply to flotation applications, but in all cases trying to maintain generality so that these investigations can also be applied to relevent problems in other areas. The investigations which have the most general applications to other areas are considered first and those more specific to flotation are considered last. Thus, in Chapter 1, the effects of interface deformation will be investigated both for applications to flotation operations and for applications to ploymer processing operations by studying the approach of a solid spherical particle towards a deformable fluid interface in an extensional flow. In Chapter 2, the effects of viscous drag of the fluid on the stability of captured particles attached to the rear of a bubble is investigated. This applies both to the flotation problem and to the effects of drainage flow on surface tension measurements in tensiometers. In Chapter 3, trajectories of spherical particles near spherical droplets are calculated using methods which are specifically applicable to the flotation problem, although these methods also can be applied to liquid-solid

extraction processes. Apologies are made for the amount of detail included in Chapter 3, however in order to obtain these solutions, an extreme amount of manipulation was necessary. Thus, although we have attempted to simplify the discusion of this analysis as much as possible, we did not want to simply give the solution without demonstrating how it was obtained, and thus that it is a valid solution. Finally in Chapter 4, an experimental study measuring both the trajectories of model spherical particles near bubbles and the capture of these particles by bubbles is discussed.

Chapter I

The creeping motion of a spherical particle in a linear axisymmetric straining flow normal to a deformable interface.

Abstract

Numerical solutions for the creeping motion of a spherical particle in a linear axisymmetric straining flow normal to a deformable interface are presented for a range of viscosity ratios, capillary numbers and Bond numbers. The parameter ranges investigated have applications in areas of flotation (small interface deformation) and material processing (large interface deformation). The accuracy of previous solutions for flotation problems that neglect interface deformation is considered, along with the magnitude and form of interface deformation "defects" that may appear in material processing applications involving fluids containing bubbles or small particles.

1. Introduction

Many processes of great practical interest involve small particles in flowing fluids near interfaces. In a polymer processing operation these particles may be dust contaminants or an intentionally added composite reinforcing material or even very small bubbles (which behave essentially as solid particles), which are formed in the processing itself. An important problem in this general area is that the processing operation, which may involve a polymer melt or blend in pipe flow, extrusion, mold filling or coating operations, can lead to surface defects in the finished product as the particles interact with the flow and the interface to produce bumps on the surface (Fritch 1979, Hoffman 1985). In separation processes, the particles may be mineral fines, effluent waste or biological products that one wishes to remove either by flotation, or by capturing the particles on a condensed film of a fibrous mat collector. The final step of removing a particle in these separation processes involves capturing the particle on the fluid/fluid interface. Hydrodynamic interactions between the particle and interface, as well as the resulting interface deformation, may greatly affect the separation between the surface of the particle and the interface, and thus ultimately the efficiency of capture.

In spite of the large number of applications where it is important to understand the flow-driven motion of a particle near a deformable interface, the problem has received little attention in the literature, as already observed by Hoffman. This is most likely because the full nonlinear problem of a particle moving in a complicated flow near a deforming interface is difficult or impossible to solve analytically and is, in fact, of little general interest since the nonlinearity prohibits superposition of solutions. Thus, the solution is restricted to the particular flow and geometry being investigated. However, when the particle size is small compared to the radius of curvature of the interface, a first

approximation of the basic flow that forces the particle towards the interface, for both flotation (Stoos 1987) and mold-filling operations (Hoffman 1985), is a linear axisymmetric straining flow. Also, in coating flows it is easy to visualize from the geometries of typical coating devices (Ruschak 1985) how extensional flow components might arise. Thus, to understand the complicated interactions between the particle, the flow field, and the interface deformation, we investigate the basic problem of a spherical particle moving towards a deforming fluid interface under the action of a linear axisymmetric straining flow. Specifically, for separation processes, we would like to know how the interface deformation affects the rate of change of the minimum gap between the particle and interface, and thus how the deformation affects the capture process. For polymer processing applications, we are primarily interested in the degree and character of the interface deformation, which gives an indication of the magnitude of possible surface defects.

The related problems of a sphere approaching a deforming fluid interface under the action of an external force (gravity) or at a constant velocity have been extensively studied, and comprehensive reviews are given by Jeffreys and Davies (1971) and Geller, Lee and Leal (1986). To summarize, the majority of these investigations have studied the film drainage configuration as the limiting step in a breakthrough or coalescence process; see for example, Princen (1963); Hartland (1969a & b); Jones and Wilson (1978); Smith and Van de Ven (1984); and Shah, Wasan and Kintner (1971). However, Geller, Lee and Leal (1986), Leal and Lee (1981), Lee and Leal (1982) and Maru, Wasan and Kintner (1971) have shown, that in certain cases the final breakthrough process may *not* occur by a film-thinning mechanism, and it is generally necessary to consider the complete process of particle motion toward the interface rather than a single isolated step.

In comparison, the problem of sphere motion driven by a flow field has received little attention. For instance, applications in flotation have relied on the assumption that interface deformation is negligible because of the small capillary numbers associated with the small bubble sizes (Jameson, Nam and Young 1977). However, allowing even slight deformation would relax the physically unrealistic singular resistance to approach experienced by spheres in the no-deformation case (which is usually compensated for by the faster singular growth of molecular attractive forces). Also, interface deformation may not be small on the scale of these small particles and certainly should not be small on the length scale of molecular attractive forces. This interface deformation may lead to larger separation distances when the particle approach velocity is at a minimum and therefore to much larger approach and film thinning times. For the cases where interface deformation is neglected, bipolar coordinate solutions have been used for spheres near gas/fluid interfaces (Dukhin and Rulev 1977) and asymptotic solutions for large separations have been developed for spheres and slender bodies near interfaces of arbitrary viscosity ratios (Yang and Leal 1984, Stoos 1987). In the one case where interface deformation was included, Hoffman (1985) studied the flow-driven approach of a sphere toward a deformable free interface ($\lambda = 0$) both theoretically and experimentally. However, his theoretical analysis involves a number of ad hoc assumptions and is based upon the presumed existance of a rate-limiting step, or quasi-equilibrium configuration so that the full evolutionary problem of interface shape and sphere position is not solved. It is, of course, well-known that the interface shape and other features of the flow at any instant depend upon the configuration and flow at earlier times. Thus, in general, we must investigate the entire process of sphere motion normal to the interface, starting from an initial state in which the sphere is far from the interface, which exists in its undisturbed state. Indeed,

this may be especially important in the present problem because the driving force for particle motion varies with particle position and will be sensitive to any assumed configuration.

2. Problem Statement

We consider a spherical particle of radius a approaching normal to a deformable interface along the axis of symmetry of a linear biaxial extensional flow, starting with the sphere far from the undeformed interface. In terms of cylindrical coordinates (r,z) centered at the intersection of the axis of symmmetry and the plane of the undeformed interface, the sphere center is located at (0,l) and the undisturbed extensional flow has the form $\mathbf{u}_\infty = G(r\mathbf{i}_r - 2z\mathbf{i}_z)$ in both fluids, where G is the strain rate. The nomenclature and particle/interface configuration is shown in Figure 1. The spherical particle is entirely immersed in the lower fluid (fluid 2), which has viscosity μ_2 and density ρ_2. The upper fluid is characterized by viscosity μ_1 and density ρ_1. The interface is characterized by a constant surface tension σ. The particle is assumed to be neutrally buoyant with density ρ_2, although nonneutrally buoyant particles could easily be considered.

The small velocities resulting from the small size of "collection" bubbles in effluent flotation and the high viscosities characteristic of polymer processing operations often allow the fluid and particle inertia to be neglected. Thus, we assume

$$Re = \frac{Ga^2\rho_2}{\mu_2} \ll 1. \tag{1}$$

Furthermore, the particle-interface separation is restricted to moderate values, i.e., less than 5 particle radii. In part, this is because the approximations of a planar interface and an axisymmetric extensional undisturbed flow break down at large separations in the "applications" that motivate our work. However, the particle-interface interaction also becomes increasingly unimportant for large

separations. Since the particle is force-free, the slowest decaying singularity that characterizes the disturbance flow is a "stresslet" (Chwang and Wu 1975; Yang and Leal 1984), for which the velocity decays like $(\frac{1}{l^2})$. Even though the particle velocity increases like (l), the resulting disturbance velocity is thus $O(\frac{1}{l})$ or smaller at the interface and is unimportant for large separations. The relative insignificance of the disturbance flow at large separations is seen in both the asymptotic and bipolar analytic solutions for a flat interface. Later we will discuss the effects of the initial position of the sphere in more detail.

Although the governing flow equations are linear, the problem is nonlinear in the boundary conditions because of the unknown interface shape and the influence of this shape on the flow. An excellent method of solution for this type of free boundary problem is the boundary integral method used by Youngren and Acrivos (1975, 1976); Geller, Lee and Leal (1986); Lee and Leal (1982); and Chi and Leal (1987), among others. We refer the reader to these papers for many of the details.

Nondimensionalizing with characteristic velocity Ga, length a and stress $\mu_i G$, the governing flow and continuity equations for the two fluids become

$$\left.\begin{aligned} 0 &= -\nabla p_1 + \lambda \nabla^2 \mathbf{u}_1 \\ 0 &= \nabla \cdot \mathbf{u}_1 \end{aligned}\right\} \quad \text{in fluid 1} \tag{2}$$

$$\left.\begin{aligned} 0 &= -\nabla p_2 + \nabla^2 \mathbf{u}_2 \\ 0 &= \nabla \cdot \mathbf{u}_2 \end{aligned}\right\} \quad \text{in fluid 2} \tag{3}$$

$$\mathbf{u}_1, \mathbf{u}_2 \to \mathbf{u}_\infty \quad \text{as} \quad |\mathbf{x}| \to \infty \tag{4}$$

and the boundary conditions at the interface are

$$\mathbf{u}_1 = \mathbf{u}_2 \tag{5}$$

$$\lambda \mathbf{n} \cdot \mathbf{T}_1 - \mathbf{n} \cdot \mathbf{T}_2 = -\frac{1}{Ca}(\nabla \cdot \mathbf{n})\mathbf{n} + \frac{1}{Cg} f \mathbf{n} \tag{6}$$

$$(\mathbf{n}\cdot\mathbf{u}_1)\mathbf{n} = (\mathbf{n}\cdot\mathbf{u}_2)\mathbf{n} = (\frac{\partial f}{\partial t})\mathbf{i}_z + (\frac{\partial r}{\partial t})\mathbf{i}_r. \tag{7}$$

Boundary conditions (5), (6) and (7) are continuity of velocity, the stress balance and the kinematic condition for the interface motion, respectively. Here, as in Lee and Leal (1982), the interface shape is represented by z = f(r,t) and the outward pointing normal at the interface is $\mathbf{n} \equiv \frac{\nabla H}{|\nabla H|}$, where H = z - f(r,t). Since the driving force for sphere motion diminishes and may even change sign as the sphere approaches and crosses the plane of the undeformed interface, the interface deformation is expected to be moderate and the multiple coordinate representation of Geller, Lee and Leal (1986) should not be required.

The relevant independent dimensionless parameters are the viscosity ratio $\lambda = \frac{\mu_1}{\mu_2}$, the capillary number $Ca = \frac{\mu_2 Ga}{\sigma}$, and $Cg = \frac{\mu_2 Ga}{a^2 g(\rho_2 - \rho_1)}$, which is the ratio of capillary to bond numbers. Ca is the ratio of characteristic viscous disturbance forces in the lower fluid to capillary forces that resist deformation. The parameter, Cg is the ratio of characteristic viscous forces in the lower fluid to forces arising from the density difference between the fluids, which also tend to resist interface deformation.

The final conditions are the no-slip boundary condition on the sphere and the force balance on the sphere. The no-slip condition on the sphere surface can be expressed in the form

$$\mathbf{u}_2 = u_p \mathbf{i}_z \quad \text{at} \quad x \in S_p, \tag{8}$$

where u_p is the unknown particle velocity. The force balance on the sphere after performing an azimuthal integration yields

$$\int_0^\pi \mathbf{T}^p_{nz} \sin\theta d\theta \;=\; 0, \tag{9}$$

where T^p_{nz} is the stress component on the particle surface in the z direction; i.e., $\mathbf{i}_z \cdot (\mathbf{n}\cdot\mathbf{T}^p)$.

The boundary integral method for an unbounded domain requires that the flow variables decay to zero at infinity. Therefore, the velocity and stress are written in terms of disturbance variables as in Rallison and Acrivos (1978), where $\mathbf{u}' \equiv \mathbf{u} - \mathbf{u}^{\infty}$ is the disturbance velocity and $\mathbf{T}' \equiv \mathbf{T} - \mathbf{T}^{\infty}$ is the disturbance stress. Ladyzhenskaya's general solution for the disturbance velocity and disturbance pressure at any point $\mathbf{x}$ is

$$\mathbf{u}'(\mathbf{x}) = \frac{1}{8\pi}\int_S \left(\frac{\mathbf{I}}{R} + \frac{(\mathbf{x}-\eta)(\mathbf{x}-\eta)}{R^3}\right)\cdot\mathbf{T}'(\eta)\cdot\mathbf{n}dS_\eta$$
$$-\frac{3}{4\pi}\int_S \frac{(\mathbf{x}-\eta)(\mathbf{x}-\eta)(\mathbf{x}-\eta)}{R^5}\cdot\mathbf{u}'(\eta)\cdot\mathbf{n}dS_\eta \qquad (10)$$

$$p'(\mathbf{x}) = \frac{1}{2\pi}\int_S \left(\frac{\mathbf{I}}{R} - \frac{3(\mathbf{x}-\eta)(\mathbf{x}-\eta)}{R^5}\right)\cdot\mathbf{u}'(\eta)\cdot\mathbf{n}dS_\eta$$
$$+\frac{1}{4\pi}\int_S \frac{(\mathbf{x}-\eta)}{R^3}\cdot\mathbf{T}'(\eta)\cdot\mathbf{n}dS_\eta. \qquad (11)$$

For a finite closed boundary the above equations can be conveniently represented in terms of the actual velocity and stress, $\mathbf{u}$, $\mathbf{T}$, by analytically integrating out the contribution from the flow at infinity, as in Rallison and Acrivos (1978). However, for the unbounded problem considered here this is not possible because the interface extends to infinity, where the flow strength becomes singular. Nevertheless, it is convenient to express the contributions over the particle surface in terms of the actual velocity and stress and the velocity and stress arising from the undisturbed flow field, rather than in terms of the disturbance variables.

The details of applying the boundary conditions to (10) to derive a system of integral equations for the unknown velocity and stress components at the interface and the particle surface is similar to the constant velocity case of Lee and Leal (1982), with additional terms in the equations from the flow at infinity. After applying the double-layer jump condition, the velocity on the interface in the limit as $\mathbf{x} \rightarrow S_I$ from fluid 2 is given by

$$\frac{1}{2}\mathbf{u}^{I'}(\mathbf{x}) = -\frac{3}{4\pi}\int_{S_I}\left[(\frac{\mathbf{rrr}}{R^5})\cdot\mathbf{u}^{I'}\right]\cdot\mathbf{n}dS + \frac{1}{8\pi}\int_{S_I}\left[(\frac{\mathbf{I}}{R}+\frac{\mathbf{rr}}{R^3})\cdot\mathbf{T}_2^{I'}\right]\cdot\mathbf{n}dS$$
$$+\frac{1}{8\pi}\int_{S_P}\left[(\frac{\mathbf{I}}{R}+\frac{\mathbf{rr}}{R^3})\cdot\mathbf{T}^{P}\right]\cdot\mathbf{n}dS + \frac{3}{4\pi}\int_{S_P}\left[(\frac{\mathbf{rrr}}{R^5})\cdot\mathbf{u}_\infty\right]\cdot\mathbf{n}dS$$
$$-\frac{1}{8\pi}\int_{S_P}\left[(\frac{\mathbf{I}}{R}+\frac{\mathbf{rr}}{R^3})\cdot\mathbf{T}_\infty^{P}\right]\cdot\mathbf{n}dS. \qquad (12)$$

The velocity on the sphere surface including the double-layer jump condition is given by

$$\mathbf{u}^{P}(\mathbf{x}) = -\frac{3}{4\pi}\int_{S_I}\left[(\frac{\mathbf{rrr}}{R^5})\cdot\mathbf{u}^{I'}\right]\cdot\mathbf{n}dS + \frac{1}{8\pi}\int_{S_I}\left[(\frac{\mathbf{I}}{R}+\frac{\mathbf{rr}}{R^3})\cdot\mathbf{T}_2^{I'}\right]\cdot\mathbf{n}dS$$
$$+\frac{1}{8\pi}\int_{S_P}\left[(\frac{\mathbf{I}}{R}+\frac{\mathbf{rr}}{R^3})\cdot\mathbf{T}^{P}\right]\cdot\mathbf{n}dS \quad + \quad \frac{1}{2}\mathbf{u}_\infty$$
$$+\frac{3}{4\pi}\int_{S_P}\left[(\frac{\mathbf{rrr}}{R^5})\cdot\mathbf{u}_\infty\right]\cdot\mathbf{n}dS - \frac{1}{8\pi}\int_{S_P}\left[(\frac{\mathbf{I}}{R}+\frac{\mathbf{rr}}{R^3})\cdot\mathbf{T}_\infty^{P}\right]\cdot\mathbf{n}dS. \qquad (13)$$

Following the example of Lee and Leal, the stress jump (6) is incorporated by combining (12) with the similar expression for the velocity on the interface as $\mathbf{x} \to S_I$ from fluid 1 multiplied by λ, and applying boundary conditions (5) and (6) to obtain

$$\frac{1}{2}(\lambda+1)\mathbf{u}^{I'}(\mathbf{x}) = -\frac{3}{4\pi}(1-\lambda)\int_{S_I}\left[(\frac{\mathbf{rrr}}{R^5})\cdot\mathbf{u}^{I'}\right]\cdot\mathbf{n}dS$$
$$+\frac{1}{8\pi}\int_{S_P}\left[(\frac{\mathbf{I}}{R}+\frac{\mathbf{rr}}{R^3})\cdot\mathbf{T}^{P}\right]\cdot\mathbf{n}dS$$
$$-\frac{1}{8\pi}\int_{S_I}\left[(\frac{\mathbf{I}}{R}+\frac{\mathbf{rr}}{R^3})\cdot\mathbf{F}'(f)\right]\cdot\mathbf{n}dS$$
$$+\frac{3}{4\pi}\int_{S_P}\left[(\frac{\mathbf{rrr}}{R^5})\cdot\mathbf{u}_\infty\right]\cdot\mathbf{n}dS$$

$$-\frac{1}{8\pi}\int_{S_P}\left[\left(\frac{\mathbf{I}}{R}+\frac{\mathbf{rr}}{R^3}\right)\cdot\mathbf{T}^P_\infty\right]\cdot\mathbf{n}dS. \tag{14}$$

The disturbance stress difference $\mathbf{F}'$ is given by

$$\mathbf{F}' \equiv (\lambda\mathbf{n}\cdot\mathbf{T}^I_1-\mathbf{n}\cdot\mathbf{T}^I_2)-(\lambda\mathbf{n}\cdot\mathbf{T}^I_{1\infty}-\mathbf{n}\cdot\mathbf{T}^I_{2\infty}), \tag{15}$$

where in cylindrical coordinates (r,θ,z), the stress associated with the undisturbed flow and the flat interface is

$$\mathbf{T}^I_{2\infty}=-p_{2\infty}\mathbf{I}+\begin{pmatrix}2&0&0\\0&0&0\\0&0&-4\end{pmatrix},$$

$$\mathbf{T}^I_{1\infty}=-p_{1\infty}\mathbf{I}+\begin{pmatrix}2&0&0\\0&0&0\\0&0&-4\end{pmatrix}, \tag{16}$$

and $p_{2\infty}$ $p_{1\infty}$ are constants that must satisfy the normal stress balance on a flat interface with the velocity field $\mathbf{u}_\infty$; i.e.,

$$\mathbf{n}\cdot(\lambda\mathbf{n}\cdot\mathbf{T}^I_{1\infty}-\mathbf{n}\cdot\mathbf{T}^I_{2\infty})=p_{2\infty}-\lambda p_{1\infty}+4(1-\lambda)=0. \tag{17}$$

A solution of (17) is $p_{2\infty}=p_{1\infty}=-4$. The dynamic pressure from the undisturbed flow is negative (the hydrostatic pressure jump across a flat interface is identically zero) and balances the viscous stress, which would tend to move the interface from a nonequilibrium position in a situation with unequal fluid viscosities. Thus, the known weighting functions in the integral equations are

$$\mathbf{F}'(f)=-\frac{1}{\mathrm{Ca}}\left(\frac{\kappa}{r}\frac{\partial \mathrm{f}}{\partial \mathrm{r}}+\kappa^3\frac{\partial^2 \mathrm{f}}{\partial \mathrm{r}^2}\right)\mathbf{n}+\frac{1}{\mathrm{Cg}}\mathrm{f}\mathbf{n}+6(\lambda-1)(\mathbf{n}\cdot\mathbf{i}_r)\mathbf{i}_r, \tag{18}$$

$$\mathbf{T}_\infty=6(\mathbf{n}\cdot\mathbf{i}_r)\mathbf{i}_r, \tag{19}$$

$$\mathbf{u}_\infty=(\mathrm{r}\mathbf{i}_r-2\mathrm{z}\mathbf{i}_z). \tag{20}$$

The last term in Equation (18), which depends on λ, is the stress difference arising from the undisturbed flow at infinity and is zero for a flat interface or for

two fluids of equal viscosity. The surface integrals in Equations (12), (13) and (14) are reduced to line integrals by integrating out the azimuthal dependence for this axisymmetric problem. Then Equations (9), (12), (13) and (14) are solved simultaneously to determine the unknown velocity and stress components on the interface and particle surface $\mathbf{u}^I$, $\mathbf{T}_2^I$, $\mathbf{T}^P$, and the particle velocity u_p.

3. Numerical Algorithm

The method of solution is a numerical collocation scheme, similar to that used by Geller, Lee and Leal (1986). The infinite interface boundary is truncated at some large but finite radius, R_o, and is subdivided, along with the particle surface, into N_I and N_P small segments, respectively. The number of segments used varied between 25 - 35 unequal sized segments for N_I, with the highest concentration of segments near the particle where the interface deformation is largest and 15 - 25 evenly spaced segments for N_P. The unknown basis functions for the velocity and stress are assumed to vary linearly over these small segments. Alternatively, high accuracy could be maintained by increasing the number of boundary elements and assuming that the basis functions are constant over the elements. However, the use of linear basis functions is numerically faster than increasing the number of boundary elements. First of all, the integrands (in terms of elliptic integrals after the axisymmetric integration) for the additional integrals that arise with linear basis functions must be evaluated anyway for the terms with constant weighting functions; i.e., the integrand for the b term in the representation $u_r = m\,r + b$, once evaluated, can also be used with the corresponding mr term. Second, the size of the matrix that must be inverted is not increased by assuming a linear variation in the unknown velocity and stress, as it would be for an increase in the number of boundary elements. Vector Equations (12) and (14) are evaluated at the N_I interface interval centers, and vector Equation (13) is evaluated at the N_P particle interval centers

thus generating a system of $4N_I + 2N_P$ linear algebraic equations (Kantorovich and Krylov 1958). Including the force balance on the particle, Equation (9), we have $4N_I + 2N_P + 1$ equations to solve for the $4N_I + 2N_P + 1$ unknowns: $u'_r(N_I)$, $u'_z(N_I)$, ${T_2^I}_{nr}'(N_I)$, ${T_2^I}_{nz}'(N_I)$, $T^P_{nr}(N_P)$, $T^P_{nz}(N_P)$ and u_p.

The normal vector to the interface and the local interface curvature, which appear in the integrands of (12) - (14), are evaluated using a cubic spline to represent the interface shape in terms of a function f(r). For cases with large interface deformation, the f(r) representation is replaced by a parameterization in terms of arc length s, and cubic splines are fit to both f(s) and r(s); however, this method is somewhat slower and thus is not used if the deformation is not large; i.e. $\frac{df}{dr} < 10$. The azimuthal integration reduces the surface integrals to line integrals with integrands in terms of elliptic integrals (Lee and Leal (1982)). These final line integrals are evaluated numerically using a 7 point Gaussian quadrature and the accuracy is checked by occasionally comparing to an 11 point Gaussian quadrature. In performing this integration, a small line element is cut out around the singular point and evaluated analytically. In addition, the accuracy is improved by further subdividing the main element into smaller elements near the singular points. Once the interface and sphere velocities have been evaluated, the interface shape is allowed to evolve by explicitly stepping the position of each of the node points on the interface with the normal velocity at that node point. Since the actual node point position is important only as it relates to the description of the interface shape, convection of the node points tangent to the interface is not of interest. Furthermore, restriction of nodes to normal motion reduces the depletion of node points near the particle. Nevertheless, some spreading of node points does still occur and thus, periodically, the points are redistributed using the cubic spline to maintain the initial spacing. Similarly, the sphere position is changed by $u_p \cdot \Delta t$.

A sufficiently small time step is used so that relative changes in velocity at each time step are small. If the change in velocity is relatively large (greater than 5%) either at a node point on the interface, or for the particle, the evolution is stopped and restarted from a previous point in time, using a smaller time step. The initial nondimensional time step used was 0.01, (nondimensionalized with characteristic time G^{-1}), which is somewhat smaller than in Geller,Lee and Leal (1986), since the initial sphere velocity is larger, thus producing larger relative changes in the particle-interface configuration. Adjusting the time step to maintain small changes in velocities results in smaller time steps for smaller particle/interface separations, since at this point small changes in position produce large relative changes in particle/interface separation and thus large relative changes in particle velocity. The smallest time step used was 0.0001. If smooth changes in velocity were not achieved with this time step, the calculation was stopped.

The effects of the interface truncation are shown in Figure 2. Because the flow disturbance due to the particle is convected radially by the undisturbed flow, the interface truncation distance must be substantially larger than in the constant force case of Geller, Lee and Leal (1986). Similarly to the latter case, however, the truncation distance must be increased as the particle/interface separation becomes larger. However, for separation distances of 3.0 (from the particle center), the sphere velocity in the present case is insensitive to truncation distances for R_o of 30.0 or more. In addition, the disturbance velocity and stress on the interface at $R_o = 30$ are both less than $5 \cdot 10^{-4}$.

The effect of the initial starting position is shown in Figure 3, where interface shapes are plotted for Ca = Cg = λ = 1, with starting positions of 3 and 5 and an initially flat interface. Initially the starting position can affect the interface shape and the sphere velocity, but since the interaction is small

at large separations, the interface remains nearly flat in either case. As we will show later, the sphere velocity for large separations, is very close to the results for a flat (but deforming) interface, so the effect of this small change in interface shape on the sphere velocity is small. As the separation decreases, the interface shapes and sphere velocities agree more closely for the two cases. Thus, the major characteristics of the solutions for identical Ca, Cg and λ are insensitive to the initial starting position as long as it is not too small. An initial separation of 3 is found to be sufficiently large and this is used in all the subsequent calculations.

4. Results

In this section, we present results from our calculations for various combinations of the dimensionless parameters. The results divide nicely into two quite distinct groupings. In the first set, we briefly consider cases involving a large viscosity ratio, or very small values of Ca or Cg, in which the interface deformation is small. The solutions in this case are presented, in part, as an indication of the accuracy and reliability of the numerical technique. However, the results are also of some direct interest in the context of particle capture in flotation processes, where Ca and Cg are typically very small, and the interface deformation is also small. Following this, we consider a second set of results for $0.1 \leq Ca, Cg \leq 10.0$, and $0.0 \leq \lambda \leq 10.0$, where interface deformation is large. These results are of more direct interest in materials processing applications, as discussed earlier, where an understanding of the deformation process and the factors that control it is important in controlling the magnitude of surface bumps or defects in products produced using particle- or bubble-filled molten materials. In the latter case, we compare the results from our computations with experimental observations from the study of Hoffman (1985).

A. Limiting Cases of Small Deformation

We begin by considering cases involving a large viscosity ratio ($\lambda \gg 1$) or weak viscous forces (i.e., $Ca, Cg \ll 1$), where interface deformation is small. The *limiting* cases of small capillary number or large viscosity ratios are of special interest in the context of particle capture in the flotation process, where the corresponding approximation of a *flat* nondeforming interface, ($\mathbf{u} \cdot \mathbf{n} = 0$), has formed the basis of existing theoretical models and predictions of capture efficiency. However, it seems evident that the occurrence of even a small amount of interface deformation accompanying the approach of a small particle toward the bubble surface may be an important factor in the capture process, which relies on nonhydrodynamic, but extremely short-range attractive forces, in its final stages. It is particularly interesting, in this regard, to compare results from the present numerical scheme, with the limiting, flat-interface analytical results. The two most important points for comparison are the minimum gap width between the particle and the interface as a function of time, and the position of the particle relative to the plane of the undeformed interface (the latter controls the magnitude of the *tangential* velocity of a particle as it passes around the bubble, and thus also controls the time (sliding time) available for thinning of the minimum gap between the particle and the interface to a point where capture is possible, c.f., Dobby and Finch (1985), where sliding times for the intermediate Reynolds number case are considered).

The related problem of small deformation accompanying the approach of a sphere towards an interface at constant velocity was investigated by Berdan and Leal (1982), using a domain perturbation technique. However, this type of analytic approach has limited value for analysis of the effect of interface deformation on particle capture, because tractable analytic forms for the velocity and pressure fields are possible only in the limit of a *large* separation between the sphere and the interface, where the method of reflections can be employed along

with "simple" solutions based upon a superposition of fundamental singularities at the sphere center. Theories for the opposite limit of "lubrication-like" film drainage rely upon either input of an initial "shape" for the film from experimental (or other) evidence, or "ad hoc" approximations.

In the present section, we consider numerical results for two cases: first, $\lambda = 0$ and small $Ca = Cg = 0.01$, which is "representative" of conditions for flotation processes, and second, $Ca = Cg = 1$ with $\lambda = 100$, which provides a comparison in which interface deformation is very small because of dominant viscous effects.

Results showing the interface shape for these two cases are presented in Figures 4 and 5, where for clarity of presentation, we adopt a frame of reference in which the particle appears to be fixed, with the interface approaching it, starting from an initial configuration in which the interface is flat and located three radii away from the center of the sphere. The interface in these figures is pictured at equal time intervals, (0.25 nondimensional time units), so that the contours become closer together as the sphere slows down because of the combined effects of hydrodynamic interaction with the interface, and a decrease in the undisturbed fluid velocity for positions that are closer to the interface.

The most striking feature of the results shown in Figures 4 and 5 is that the degree of interface deformation is almost imperceptible with the scale of resolution that is inherent in these figures, until the sphere is extremely close to the plane of the undeformed interface. Indeed, in order to provide a useful view of the actual shape of the thin fluid region for the last few time-steps in Figures 4 and 5, we reproduce an expanded local view of both of these thin films in Figure 6 at times 1.25 and 1.0, respectively.

The very small deformation in the present case for $Ca=Cg=0.01$ and $\lambda = 0.0$ may be contrasted with the earlier predictions of Geller et al. (1986) for a

sphere approaching an interface through a quiescent fluid under the action of a constant force. In the latter case, considerable deformation occurred for Ca, Cg = $O(10^{-2})$. Indeed, to restrict the interface to a nearly flat shape, comparable qualitatively with that shown in Figures 4 and 5, it was necessary to reduce Ca and/or Cg by another order of magnitude. We shall see that the degree of deformation in the present case is always considerably smaller for equal values of the dimensionless parameters, λ, Ca, and Cg than that predicted by Geller et al. (1986) for motion under the action of a constant force.

There are at least three reasons for this fact. First, the magnitude of the undisturbed velocity, in the present case, decreases linearly with distance from the plane of the undeformed interface. Hence, the velocity of the particle will decrease as the interface is approached (and would do so in the complete absence of any hydrodynamic interactions with the interface - e.g., in an *unbounded* fluid that undergoes uniaxial extensional flow as the particle approaches the stagnation point of the flow), and the magnitude of viscous deforming forces will likewise decrease. It is noteworthy in this regard, that the characteristic velocity inherent in Ca and Cg is the velocity of the undisturbed flow at a distance of one sphere radius from the interface, whereas the characteristic velocity used by Geller et al. was the Stokes velocity for a sphere moving at very large distances from the interface under the action of the applied force. The second factor in the present case is that the disturbance flow produced by the sphere is much "weaker." In particular, since the particle is force- and torque-free, the disturbance velocity produced by the particle decays like a force-dipole (in particular, a "stresslet") proportional to $\frac{1}{l^2}$, rather than a point force (or "stokeslet") proportional to $\frac{1}{l}$ as in the earlier studies. This results in smaller disturbance effects and less deviation of the particle velocity from the undisturbed fluid velocity for large particle/interface separations. Third, and finally, the undisturbed flow field

tends to maintain the interface in a flat configuration. This effect is inherent in both the form of the undisturbed flow field (which is added to the disturbance velocity in calculating the net velocity of the interface) and in the last term of the normal stress difference given by Equation (18), which act together as a "restoring" force that will cause an initially deformed interface to return to a flat configuration even in the absence of interfacial tension or a density jump across the interface (i.e., for Ca=Cg=∞). An explicit computational demonstration of this latter fact will be given in the next section, where we consider large amplitude deformations.

As indicated in the introduction to this section, the most important characteristic for the small deformation problems considered here are not the overall interface shape, but rather the time-dependent thickness of the thin film that eventually appears between the sphere and the interface, and the position of the sphere relative to the plane of the undeformed interface. These factors are explored in Figure 7 for the "flotation" parameters (i.e., Ca = Cg = 0.01, $\lambda = 0$). For the present "exact" numerical solution, we plot both the minimum distance of the surface of the sphere from the plane z=0, and the minimum thickness of the thin liquid film. Also shown, for comparison, are predictions of the minimum film thickness for a flat interface via the asymptotic (far-field) solution of Yang and Leal (1984), and the bipolar coordinate solution of Dukhin and Rulev (1977). Superficially, the various curves in Figure 7 look very similar, and, indeed, the importance of the differences depends on the critical film thickness for capture (i.e., the gap width at which nonhydrodynamic forces of attraction become sufficiently strong to cause the thin film to rupture, Deryagin and Dukhin (1979)). For example, the time for the sphere/interface gap to decrease below 0.01 of the particle radius is almost twice that predicted by the far-field result of Yang and Leal (1984). The bipolar solution of Dukhin and Rulev is much

closer to the exact solution for these particular values of Ca and Cg, but still slightly underestimates the minimum film thickness at any instant in time. The bipolar solution also overestimates slightly the position of the sphere relative to the plane z=0. Although both errors are relatively small in absolute terms, they may cause significant errors in the full flotation capture calculations. The error in the position of the particle relative to the plane z=0 will significantly affect the tangential velocity of the particle, Stoos (1987), and this in turn may affect whether or not the particle has sufficient time in the extensional flow near the interface to reach a critical film thickness for capture.

Another, more sensitive comparison between the present numerical results and previous analytic theories for a flat interface is shown in Figure 8. Here, we plot the *ratio* of the particle velocity to the velocity of the undisturbed flow field at the particle center - we shall refer to this as the "relative" velocity. The results from our present solution for Ca=Cg=0.01 and $\lambda = 0$ are plotted both as a function of particle position relative to the plane z=0 and as a function of particle position relative to the interface. Results are also shown for the far-field asymptotic and bipolar coordinate solutions for a flat, nondeforming interface and for a flat but *deforming* interface via a supplemental boundary integral calculation. The particle velocity as a function of particle position relative to the plane z=0 is significantly larger for the deformed interface than the particle velocity given for a flat, nondeforming interface by the bipolar coordinate solution, since the allowance of even a small amount of interface deformation reduces the resistance to the particle approach. However the particle velocity as a function of particle position relative to the interface agrees quite well with the bipolar coordinate solution for *no* deformation. From this, we conclude that interface deformation affects the particle velocity principally by changing the minimum separation between the particle and the interface, rather than as a consequence

of changes in the interface shape directly. The velocity for a sphere approaching a deformable interface with $\lambda = 100$, Ca = Cg =1 is also shown as a function of the particle position relative to the plane z=0, and is seen to be quite close to the result for $\lambda = 0.0$ and Ca = Cg = 0.01. At first, this agreement between results for low and high viscosity ratios appears to be quite surprising. However, it can be understood by extrapolating the far-field analytical results of Yang and Leal (1984) to the case of a sphere *near* a *flat* interface. In particular, Yang and Leal show that the ratio of the drag on a stationary sphere near a flat interface to Stokes' drag for an unbounded fluid is

$$\text{Drag Ratio} = 1 + \sum_{n=1}^{3} \left[\frac{3}{8l} \frac{(2+3\lambda)}{(1+\lambda)} \right]^n - \frac{(1+4\lambda)}{8(1+\lambda)} \left(\frac{1}{l}\right)^3 - \frac{10}{12} \left(\frac{1}{l}\right)^3 \left[\frac{3(2+3\lambda)}{8(1+\lambda)} \right] + O\left(l^{-4}\right), \tag{21}$$

(with a small algebraic error corrected). This drag ratio is plotted in Figure 9 for $\lambda = 0$ and $\lambda = 100$, and it can be seen that the result is *very* sensitive to λ, especially for $l \to -1$. On the other hand, the component of the resistance tensor K_{zz} for motion normal towards a flat, fluid interface is given by Lee, Chadwick and Leal (1979) and Yang and Leal (1984) as

$$\mathrm{K}_{zz} = 6\pi \left[1 + \sum_{n=1}^{3} \left[\frac{3}{8l} \frac{(2+3\lambda)}{(1+\lambda)} \right]^n - \frac{(1+4\lambda)}{8(1+\lambda)} \left(\frac{1}{l}\right)^3 \right] + O\left(l^{-4}\right), \tag{22}$$

and the *relative* velocity for a flat interface is given by the ratio of these two values, multiplied by the appropriate scales used in this study. Because the two expressions (21) and (22) exhibit very similar dependence on λ, the *ratio* becomes relatively insensitive to λ. In particular, we can see from Figure 9 that the asymptotic solution shows essentially the same sphere velocities for large and small λ. The boundary integral calculations for Figures 4 and 5 exhibit a similar *insensitivity* of sphere velocity to λ. Although the far-field asymptotic solution of

Yang and Leal agrees well with the bipolar coordinate solution for the drag near a flat interface (c.f. Yang and Leal (1984)) it does *not* give good agreement for the particle velocities, as we can see from Figure 8. The point is that an accurate representation of the drag force is captured by the asymptotic solutions since the drag does not become singular at small separations. However, the resistance tensor, both with and without interface deformation, grows much more rapidly than the asymptotic representation as the particle/interface separation becomes small. It may also be noted from Figure 8 that particle velocities based on a flat but deforming interface are much larger than the actual particle velocities for a deformed interface.

B. Large Deformation Problems

Let us now turn to a more general range of values for λ, Ca and Cg, where interface deformation does not necessarily remain small. As we have already noted, such problems find important application in evaluating surface roughness/defects in products manufactured from multi-phase fluids.

The only published experimental results, so far as we know, are contained in the work of Hoffman (1985), who studied the approach of a sphere toward the free surface between two immiscible fluids that were being pumped through a circular tube. At the end of this section, we will compare the solutions obtained here with Hoffman's experimental observations. First, however, we attempt to understand the interface deformation problem from a more fundamental point of view, based upon comparisons of solutions obtained with a systematic variation of the three dimensionless parameters, λ, Ca and Cg.

a. The Effect of Viscosity Ratio

We begin by considering the effects of variations in the viscosity ratio, λ, for fixed values of Ca=Cg=1. Results for the interface shapes and relative sphere/interface position are plotted in Figures 10, 11 and 12, at equal time

intervals of 0.25 for $\lambda = 0$, 1 and 10. The most obvious distinction from the preceding section is that the deformation is no longer small.

Perhaps the most surprising feature of the solutions for the interface shape is that they are qualitatively insensitive to λ over the whole range $0 \leq \lambda \leq 10$. To be sure, there is a quantitative difference in the degree of deformation, with the largest deformation for the free surface $\lambda = 0$, and smaller amounts for the larger viscosity ratios. However, it is not until $\lambda = 100$, considered in the preceding section, that an increase of the viscosity ratio produces a large reduction in the maximum degree of interface deformation. In contrast, the solutions obtained earlier by Geller et al. (1986), for motion of a sphere toward an interface under the action of a constant applied force, showed a very strong dependence of deformation on λ. What is more, the degree of deformation for equivalent values of λ, Ca and Cg was, in every case, much larger than what is found here, both in the magnitude of the maximum displacement from z=0 and in the breadth of the region of the interface over which the displacement occurred.

We have already noted three fundamental reasons for these differences in the preceding section: (1) the undisturbed velocity, and thus the driving force for particle motion, goes to zero as $l \rightarrow 0$; (2) the net force and torque on the sphere are zero and thus the disturbance flow produced is of shorter range ("weaker"); and (3) the undisturbed flow field tends to maintain the interface in a flat configuration. It is worthwhile to pursue the manifestation of these differences between the present problem, and the constant force problem of Geller et al. (1986) in some detail, based upon the solutions that we have obtained.

First, we may examine the strength of the disturbance produced by the sphere on the interface, and vice versa. For this purpose, we can examine the

particle velocity and the maximum normal interface velocity (u_z on the axis of symmetry), for the initial configuration where the interface is flat and l = -3. These are 6.19 and (0.99), respectively, for $\lambda = 0$; 6.00 (0.52) for $\lambda = 1$, and 5.84 (0.098) for $\lambda = 10$. The corresponding values for the constant force problem (with the force scaled so that the particle velocity is 6.0 for $\lambda = 1$ and l = -3) are 8.13 (5.60) for $\lambda = 0$, 6.00 (2.90) for $\lambda = 1$, and 4.23 (0.54) for $\lambda = 10$. Thus, the disturbance velocity at the interface is much larger in the constant force problem, suggesting that interface deformation will be smaller for the particle motion driven by an extensional flow. Furthermore, the influence of the interface on the sphere velocity is much weaker in the present case: to a first approximation, for l = -3, the sphere translates with the undisturbed fluid velocity for all values of λ, whereas a strong hydrodynamic interaction is evident in the constant force results.

We may also examine in more detail the tendency, claimed above, for the undisturbed flow to maintain the interface in its undeformed state. The interface shape evolves with a net velocity, which is the sum of the disturbance velocity and the undisturbed velocity. The undisturbed velocity, $\mathbf{u}_\infty$, always acts to restore the interface to flat. This tendency is also reflected in the term $[6(\lambda - 1)(\mathbf{n} \cdot \mathbf{i}_r)\mathbf{i}_r]$ which appears in the expression (18) for the stress difference at the interface, and plays the role of a third "restoring" mechanism, along with the usual mechanisms associated with interfacial tension and the density difference across the interface. The main distinction is that this contribution to the disturbance stress difference on the interface is proportional to the slope, $\frac{\partial f}{\partial r}$, as it appears in the determination of the normal to the interface, rather than the curvature, $\frac{\partial^2 f}{\partial r^2}$, for the capillary force, or the relative displacement, f, for the body force effect.

Useful insight into the restoring effect associated with the undisturbed flow

can be obtained by considering the hypothetical problem of a deformed interface with zero surface tension and equal fluid densities relaxing back toward a flat configuration under the action of an extensional flow. The *initial* deformed interface shape for this calculation is chosen as the *final* interface shape in Figure 11. An interface with this initial shape is allowed to relax back to flat with no particle present (remove the integral over the particle surface from Equations (12)-(14) and neglect Equation (9)), and with Ca=Cg=∞ (no interfacial tension and equal densities). Since the contribution to the stress difference from the flow at infinity is geometry-dependent, deformations both above and below the plane of the undeformed interface are considered. For $\lambda = 1$ Equation (14) reduces to $u^{I'} = 0$, and the disturbance velocity is zero. The interface simply "convects" back to flat with the local flow as shown in Figure 13 for deformations both above and below the plane z=0. The deformations above and below the plane z=0 relax back at the same rate, and this relaxation slows as the interface becomes less deformed (longer time steps are used at the end for clarity).

The cases $\lambda = 0$ and 10 (Ca=Cg=∞) are shown in Figures 14 and 15, respectively. The last term in Equation (18) changes sign for deformations above and below the interface and also for small and large λ. From a qualitative physical point of view, it is obvious that the case $\lambda = c$ with deformation above the plane, z=0, say, should be precisely equivalent to $\lambda = \frac{1}{c}$ with the same deformation below z=0. Thus, Figure 15 for $\lambda = 10$ is very similar to Figure 14 inverted. This is because $\lambda = 10$ is not too different from $\lambda = \infty$, insofar as this effect is concerned. For positive values of $6(\lambda - 1)(\mathbf{n} \cdot \mathbf{i}_r)$, this term in the stress balance tends to reduce the slope of the interface deformation by forcing the deformed part of the interface towards r=0, as in the bottom part of Figure 14 and the top part of Figure 15. For negative values of $6(\lambda - 1)(\mathbf{n} \cdot \mathbf{i}_r)$, this term in the stress balance tends to reduce the slope of the interface deformation

by pushing the deformed part of the interface out towards r=∞, as in the top part of Figure 14 and the bottom part of Figure 15. The z component of the relaxation velocities is initially larger for deformations above z=0 for small λ and for deformations below z=0 for large λ, although as the deformation flattens out and the contribution of the flow to the stress balance diminishes, this trend is reversed (as can be seen from the figures).

It appears that for the particle approach problems (Figures 10-12), a principal effect of the $6(\lambda-1)(\mathbf{n}\cdot\mathbf{i}_r)$ term in the stress balance will be to concentrate the deformation near r=0 for large λ, which may account in part for the pinching of the interface on the shoulder of the particle as seen in Figure 12. Because of the additional restoring forces, the decrease of the particle driving force as the particle approaches the interface, and the weaker disturbance produced by the particle, there is no large-scale deformation even in the $\lambda = 0$ case as found earlier in the constant velocity and constant force problems.

In the preceding several paragraphs we have concentrated almost entirely upon the magnitude of the interface deformation and its qualitative shape. Equally important, however, is the *rate* of deformation and its dependence upon λ. To examine this point, it is convenient to begin by investigating the particle velocities as a function of position and λ.

The calculated particle velocities relative to the velocity of the undisturbed flow field at the particle center ($\frac{u_p}{-2l}$) are shown in Figure 16 as a function of particle position (Figure 17 shows actual particle velocities for Ca=1, Cg and λ between 0.1 and 10.0). Also shown in Figure 16 are the relative particle velocities that would occur for the same fluid if the interface were flat but deforming (i.e., $\mathbf{u}\cdot\mathbf{n} \neq 0$) and the bipolar coordinate predictions of Dukhin and Rulev for a flat *nondeforming* interface (i.e., $\mathbf{u}\cdot\mathbf{n} = 0$) with $\lambda = 0$. The most surprising result from Figure 16 is that the relative particle velocities for the deformed interface

solutions are matched almost perfectly by the predictions for a flat but deforming interface all the way up to $l \approx -1$, in spite of the fact that the interface becomes quite deformed before that point. So far as we can tell, there is no simple explanation for this observation. In all three cases, the interface deforms prior to $l = -1$, and one would expect interfacial tension and the density difference to begin to play a role, which could not be duplicated by the results for a flat interface. The fact that the particle velocity does not deviate significantly from the results for a flat but deforming interface, as it does for Ca=Cg=0.01, $\lambda = 0$ in Figure 8, must reflect the presence of other compensating factors. Among these is the fact that the deformed interface lies farther from the sphere, thus reducing the importance of direct hydrodynamic interactions ("wall effects"). Another is the fact that the driving force for motion of the sphere is increased for $\lambda = 0$ and decreased for $\lambda = 10$ via the modification in the flow field that is necessary to accommodate interface deformation. Another puzzling feature of the results in Figure 16 is that the predictions from the bipolar coordinate solution for a flat interface that is *not* deforming (i.e., $\mathbf{u} \cdot \mathbf{n} = 0$) with $\lambda = 0$, give particle velocities that actually agree most closely with the numerical predictions for $\lambda = 10$! This latter behavior is most likely related to the agreement we saw earlier between particle velocities for $\lambda = 0$ and 10 for the small deformation case, since in the "large" deformation case, the deformation is not really large for $\lambda = 10$ until $l \geq -1$. This is a result of the effect of the flow field itself restoring the interface to flat for large λ.

Finally, it is interesting to note that the particle velocity, for $\lambda = 0$, is *larger* than if the particle simply convected along with the undisturbed flow. This is further evidence (along with the increase in drag) of the modification of the flow field resulting from the interface deformation; i.e., both the particle and fluid velocities are increased in the presence of the deformed interface from the

values they would have in an unbounded fluid. The velocity of a sphere near a *flat* but deforming interface, for $\lambda = 0$, is also increased over the value the *undisturbed* velocity would have at the particle center. This behavior is similar, in some respects, to that found by Lee and Leal (1982), where in the presence of a particle moving at a constant velocity, the velocity on a *flat* but deforming interface with $\lambda = 0$ exceeds the velocity which would be found at the same point in an unbounded fluid. This increase in interface velocity in Lee and Leal would no doubt lead to an increase in sphere velocity if the sphere were moving under the action of a constant force. Thus, as in Lee and Leal (1982), the velocity field can be modified by the interface deformation and this in turn modifies the sphere velocity.

It is important to note that it is only the *relative* velocity of the sphere that may *increase* as the distance from the interface gets smaller for $\lambda \ll 1$. Looking ahead to Figure 26, it can be seen that the actual particle velocity decreases monotonically as the sphere approaches the interface for all values of λ! We shall return to discuss the results of these two figures in more detail.

Two quantitative measures of the degree and rate of deformation are the minimum gap width between the sphere and the interface, and the maximum displacement (or penetration) of the interface from the plane z=0. These two quantities are plotted in Figure 17 as a function of the position of the sphere, and in Figure 18 as a function of time. It can be seen from Figure 17 that the minimum gap width is always smallest at a given sphere position for the largest value of λ. More noticeable, in Figure 18, is the fact that the interface for $\lambda = 10$ is displaced very little until the sphere is very close to the plane of the undeformed interface - essentially, this lack of significant deformation is the reason why the minimum gap width is smaller for $\lambda = 10$. In a practical context, either in terms of the potential to produce a significant bump on the

interface, or in terms of capture efficiencies in separation processes, it is more interesting to examine the minimum gap and the penetration depth as a function of time (recall that the motion toward the interface due to the axisymmetric stagnation component of a bulk flow is usually only one component of the particle trajectory, which also carries the particle parallel to the plane of the undeformed interface, and thus allows only a finite *time* for interface deformation, Stoos (1987)). Examining Figure 18, we see that neither the rate of thinning of the gap nor the rate of increase in the displacement of the interface is a very strong function of λ, at least in the range $0 \leq \lambda \leq 10$ that is considered in this section. This is especially true at large times where the dynamics of "film-drainage" takes over and the rate of thinning of the film becomes surprisingly invariant to changes in λ.

Finally, there is one additional comparison with earlier work, which is of some interest, and this is the fact that the shape of the thin film appears to be qualitatively different from the predictions of Lee et al. for motion of a solid sphere toward the interface, and of Chi and Leal (1987), who considered the closely related problem of the motion of a drop of fluid A toward an interface separating the suspending fluid B from a large additional "body" of fluid A. In the latter case, Chi and Leal found that the shape of the thin film depended strongly on the viscosity ratio, λ, i.e., $\frac{\mu_A}{\mu_B}$. In particular, in the present problem, the smallest particle-interface separation occurs on the axis of symmetry for both $\lambda = 0$ and 1, suggesting that if breakthrough ultimately occurs in these cases, it would occur initially at this point. In contrast, all of the previous studies had shown that the minimum film thickness occurred away from the axis (as in the present problem for $\lambda = 10$) if either the particle was solid, or the viscosity ratio was large, and the previous authors had tentatively concluded that the film on a solid sphere would always have a minimum thickness at an off-axis position.

Clearly, however, the present results show that this is not the case, and the film geometry is a more subtle function of the undisturbed flow and the material parameters.

b. The Effect of Surface Tension and Gravity Forces

Let us now turn to the effects of surface tension forces, i.e., Ca, and/or the density difference, as measured by Cg, in determining the nature and magnitude of interface deformation. For this purpose, we have considered Ca=0.1, 1 and 10 with Cg=1 for $\lambda = 0$, 1 and 10, as well as Cg=0.1, 1 and 10 with Ca=1 and $\lambda = 0$, 1 and 10. The majority of the particle/interface configurations for these solutions are similar to those already presented in Figures 10-12, and are not reproduced here. The reader interested in detailed interface shapes for cases that are not given here may refer to Stoos (1987). Specifically, we find that interface shapes for $Ca = 10$, $Cg = \lambda = 1$ and $Cg = 10$, $Ca = \lambda = 1$ are virtually identical with the case $Ca = Cg = \lambda = 1$ that was presented earlier. This is not surprising insofar as the magnitude of deformation is concerned - when $Ca \gg Cg$ and λ deformation is dominated by the latter factors, and vice versa for $Cg \gg Ca, \lambda$. Since the two dominant parameters are not changed in comparison with the case $Ca = Cg = \lambda = 1$, it is not surprising that the degree of deformation is essentially fixed. What is surprising, however, is that the interface shape does not change significantly, since Ca and Cg represent mechanisms that act in a qualitatively different way - one limiting deformation by restricting interface curvature, and the other acting directly to limit displacement above the plane z=0. The only viable explanation is that, for $Ca = Cg = \lambda = 1$, the dominant limitation on interface deformation must be due to viscous effects. When compared with the previous results of Geller et al. for motion due to a constant force, this conclusion is surprising, since interfacial tension and body force effects were found to be dominant in the latter case for Ca, Cg, $\lambda \approx O(1)$.

Not surprisingly, in view of the above results for $\lambda = 1$, the deformation for $\lambda = 10$ is even less sensitive to Ca and Cg than for $\lambda = 1$. Here, the interface configuration was found to be very similar to the case Ca = Cg = 1, $\lambda = 10$ that was shown in Figure 12, for all values of Ca and Cg down to and including 0.1. Again, in view of the similarity to Figure 12, the detailed results are not given here.

Only for Ca or Cg = 0.1 is a significant change in the interface shape observed for $\lambda = 1$. Results corresponding to the two cases Ca = 0.1, Cg = λ = 1 and Cg = 0.1, Ca = λ = 1 are shown in Figures 19 and 20, respectively. In these cases, it is evident that the degree of deformation is significantly reduced relative to Ca = Cg = λ = 1 (Figure 11). Furthermore, the active roles of interfacial tension and the density difference across the interface in determining the interface shape is reflected in the *differences* in the details of the interface shapes between Figures 19 and 20. The interface shape in the latter case is similar to the shapes seen earlier, with the minimum film thickness occurring at the symmetry axis, and the interface contour following the particle shape quite closely until a relatively sharp break occurs in the transition to the undeformed flat interface. On the other hand, the deformation is more restricted in magnitude in Figure 19 and there is a smoother, broader shape with no regions of high interface curvature in the transition to the undeformed shape. One consequence of the restriction on curvature is that the minimum film thickness no longer occurs at the symmetry axis. Indeed, the interface shapes in Figure 19 more closely resemble the interface shapes in Figure 12, which correspond to $\lambda = 10$, Ca = Cg = 1, pointing up again the complicated form of the dependence of the film geometry on the flow and material parameters.

Results for $\lambda = 0$, with various values of Ca and Cg, are shown in Figures 21 - 24. Several of the interface/sphere configurations for $0.1 \leq Ca \leq 10$ and

$0.1 \leq Cg \leq 10$ are extremely similar and thus only the interface shapes which vary significantly with changes in Ca or Cg are shown (the interested reader can again find the interface shapes that have been omitted in Stoos (1987)).

In Figure 21 we have plotted the interface shapes for Ca = Cg = 0.1, λ = 0, which represent an intermediate case between "small" and "large" interface deformations. For this intermediate case, the interface deformation is less than for O(1) values of Ca and Cg; however, the deformation is larger than what occurs for very small values of Ca and Cg. Thus, for $\lambda = 0$, it appears the transition between moderate and very small interface deformation occurs for Ca, Cg between 0.1 and 0.01. Therefore, in a polymer processing operation, comparison of Figures 4 and 21 may give an indication of the relative decrease in the defect size that may be expected for a change in the operating conditions (slower processing speed), which results in a decrease of Ca and Cg from 0.1 to 0.01. Also, in comparing Figures 4, 10 and 21 it is clear that the effectiveness of the flow field at maintaining the interface flat does *not* dominate the effects of changes in Ca and Cg for $\lambda = 0$ as it does for $\lambda = 1$ and 10; i.e., the interface shapes are significantly different for different values of Ca and Cg for $\lambda = 0$.

In order to isolate the effects of high surface tension and large density differences, the results in Figures 22 and 23 show solutions where either Ca or Cg is small while the other is large (while still maintaining $\lambda = 0$). Thus, Figure 22 shows results for Ca = 0.1, Cg = 10 and $\lambda = 0$, and Figure 23 shows results for Ca = 10, Cg = 0.1 and $\lambda = 0$. The interface shapes with capillary forces dominating (Ca=0.1, Cg=10 and λ =0) are considerably different from the interface shapes with gravity effects dominating (Ca=10, Cg=0.1 and λ=0) as shown in Figures 22 and 23, respectively, and both show more deformation than for Ca = Cg = 0.1 (Figure 21). With surface tension dominant, there is again a smooth interface shape with no region of high interface curvature in

the transition region. The interface deformation for $\lambda = 0$ is somewhat larger than what we find for $\lambda = 1$ in Figure 19, and the occurrence of the minimum separation point off the axis is accentuated for $\lambda = 0$. Indeed, the separation between the sphere and the interface on the axis is still quite large for $\lambda = 0$, at the point where the minimum separation becomes so small that the calculation must be stopped. On the other hand, for a dominant restoring force of gravity, i.e., for Ca = 10, Cg = 0.1 and $\lambda = 0$, as shown in Figure 23, the interface has large localized curvature in the transition region to a flat interface. At the point of this large curvature, the interface height actually dips slightly below the plane z=0. Thus, although the amplitude of the "bump" produced relative to the undeformed interface is the same magnitude as in the case Ca = 0.1, Cg = 10, the appearance is of a larger distortion of the interface shape. This slight interface depression seems to result from the larger downward tangential velocity that occurs when the heavy lower fluid, which has been forced above the plane z=0, drains from the top of the sphere. This interface depression occurs only after the sphere velocity has decreased to near zero, ($\leq$ 0.05 from an initial velocity of 6.2), and thus the velocity field in this region is dominated by the drainage flow rather than by the flow resulting from the motion of the sphere. It should also be noted that this interface depression does not occur for λ = 1, or 10. Most likely, a depression does not occur in these cases because the viscous effects of the flow field force this small depression back to flat. Finally, the minimum separation distance between the interface and the sphere occurs on the axis of symmetry in Figure 23, although the separation is quite small over the entire top of the sphere as the heavy fluid trapped there drains away.

Although the interface shapes are relatively insensitive to variations in the *nondominant* parameter (i.e., we found virtually identical shapes for Ca=10, Cg=λ=1 and Cg=10, Ca=λ=1 and Ca=Cg=λ=1), the particle velocity is sen-

sitive to changes in this parameter, as is seen in Figures 24 and 25 where the relative particle velocities for Ca=1 and $0.1 \leq Cg \leq 10$ and the absolute particle velocities for Cg=1 and $0.1 \leq Ca \leq 10$ are plotted, respectively. The corresponding plots for relative particle velocities with Cg=1 and absolute particle velocities with Ca=1 show qualitatively similar behavior (with Cg and Ca switched) and thus are not shown. From Figure 24, it is clear the relative particle velocity is sensitive to changes in Ca and Cg except when λ=10, in which case viscous effects dominate and the particle velocity is insensitive to variations in Ca and Cg. Small values of Ca and Cg are less dominant in controlling the particle velocity; e.g., there is still considerable variation in particle velocity with λ for Cg=0.1 (and also Ca=0.1). One noticeable feature of Figure 24 is the rapid increase in the particle relative velocity for λ=0, Cg=10 as the particle center approaches the plane z=0. This behavior is merely a consequence of the particle's having a finite velocity as it passes this plane and $\frac{1}{1}$ blows up. The actual particle velocity decreases monotonically as the particle approaches the interface, as can be seen in Figure 25.

c. The Magnitude of Surface Bumps

One of the primary motivations for interest in the motion of particles carried by a mean flow toward a fluid interface is the problem of surface bumps or imperfections that may be a consequence of the deformation produced by small particles during a manufacturing process that involves a flow (mold-filling, for example). This aspect was studied earlier by Hoffman (1985), as indicated in the introduction, and we use this final section of "results" for a brief comparison with his work, as well as for a summation of our predictions of the magnitude of interface deformation versus the dimensionless parameters λ, Ca and Cg. The problem considered experimentally by Hoffman corresponds to the final remaining case of interest, Ca and Cg both large with $\lambda = 0$. To compare with the

experimental results from Figure 12(c) in Hoffman (1985), calculations are performed for a particle approaching a deformable interface in an extensional flow with Ca=22.07, Cg=24.34 and $\lambda = 0$. This figure from Hoffman is chosen because the particle appears to be near the axis of the tube, and thus the variation of the extensional flow strength with the position in the tube can be neglected; i.e., if the position in the tube is specified by the angle θ_E, defined by Hoffman, it is assumed $\theta_E = 0$. The shape of the interface calculated numerically, which is shown in Figure 26, is quite similar to that obtained experimentally by Hoffman, although the numerics predict a somewhat larger maximum interface deformation. It should be kept in mind, however, that Figure 12 is just a representative sample of the bumps produced and is not claimed by Hoffman to be at a maximum deformation magnitude. The maximum heights of the deformed interface above the plane z=0 are given for all the systems considered by Hoffman in his Figure 11. The maximum deformation in the numerical solution in Figure 24 is approximately 0.75 (based on particle diameter) compared to 0.67 (based on particle diameter) from Figure 11 of Hoffman. The fact that there is some disagreement between the maximum deformation given by the numerics and by the experiments may be due to the finite curvature present in the experimental fluid front, which will affect both the flow field and the tendency of the interface to deform. Also, the asymmetry inherent in the experiments for particles that are off the tube axis may account for some of the scatter in the results in Hoffman's Figure 11. Other detailed comparisons are not possible because experimental difficulties make it impossible to determine the particle position in Hoffman's experiments. However, in a general sense, the agreement with Hoffman's experimental results appears to be good.

The final flow characteristic investigated is the maximum interface deformation for viscosity ratios of 0.0, 1.0, and 10.0, Capillary numbers of 0.1, 1.0 and

10.0, and Cg of 0.1, 1.0 and 10.0. Also, for completeness, the maximum interface deformation for the limiting cases of small deformation, i.e., Ca=Cg=0.01, λ=0 and Ca=Cg=1, λ=100, are considered also. In the interest of conserving space the interface shapes have not been presented for several of these parameter values, but the interested reader may find figures for these cases in Stoos (1987). However, the general trends of interface deformation are shown in Figure 27, where the maximum interface deformation (maximum distance of the interface from the plane z=0) is plotted for the above parameters. The most noticeable feature of this plot is the drastically decreased sensitivity of the deformation magnitude on Ca and Cg for increasing viscosity ratios. Viscous effects, from the undisturbed flow, control the deformation magnitude for large λ, and the effects of variations in Ca and Cg on the deformation are small. Thus, to maintain a bump size of 0.6 particle radii or less for small viscosity ratios, the operating conditions (processing speed) must correspond to Ca and Cg = 0.1 or less. On the other hand, for viscosity ratios $\lambda \geq O(10)$, Ca and Cg can be much larger without leading to larger deformations. In order to limit the deformation to a small percentage of the sphere size ($\leq$ 10%), however, Ca and Cg must be O(0.01) or smaller, or λ must be O(100) or larger. In attempting to partially control the degree of deformation, it would be useful to note that the variation in the deformation magnitude is much larger when decreasing Ca or Cg from 1.0 to 0.1 than when decreasing Ca or Cg from 10.0 to 1.0. Indeed, for many cases it appears that values of Ca or Cg of O(1) behave like Ca and Cg $\gg$ 1. Also, it appears that surface tension is somewhat more effective in decreasing the maximum deformation than are density differences. Specifically, the smallest deformations are found for the smallest values of *Ca* (Ca=0.1, Cg=1.0 always has smaller deformation than Cg=0.1, Ca=1.0).

Conclusions

Many characteristics of the interface deformation and particle velocity profiles for a sphere driven towards a deformable interface by a biaxial extensional flow are qualitatively similar to what has been observed for spheres and drops approaching a deformable interface at a constant velocity or under the action of a constant external force, e.g., gravity. For example, this is true of the qualitative changes associated with variations in λ, Ca and Cg. However, interfacial tension and/or the density difference across the interface play a dominant role only in determining the degree and nature of interface deformations for Ca, Cg $\leq O(0.01)$, and thus the viscosity ratio remains as the dominant factor even for Ca, Cg $= O(1)$. This may be contrasted with the results of earlier studies where the interfacial tension and density difference play a dominant role for Ca, Cg $= O(1)$. It may also be noted, in the present case, that the size and shape of the interface deformations agree reasonably well with the experimental results of Hoffman for large values of Ca and Cg, and the sphere velocities are in good agreement with bipolar coordinate solutions for very small deformations.

In addition, many detailed characteristics of the interface deformation are different from the previous cases and yield surprising results for some particular applications. In general, interface shapes in the presence of the flow field are flatter, with the deformation more localized near the sphere when compared to the constant velocity or constant force cases. This because the undisturbed flow field itself tends to maintain the interface flat. Hence, through the interaction of the viscosity ratio with the flow field, the "viscous" effects play a role in addition to controlling the rate of thinning of the fluid in the gap as in the constant force problem. Consequently, variations in λ have a larger effect on interface deformation and sphere velocity. Since the flow itself tends to keep the interface flat, broad, small-scale deformations are not seen for small Ca (the flow damps these out quickly) as was characteristic of the small Ca behavior for particle motion

at a constant velocity or because of a constant force. Rather, Ca influences the total amount of deformation primarily by controlling the curvature in the transition region between the sphere and the undeformed interface. Also, since the disturbance caused by the sphere is more rapidly decaying than the point force disturbances associated with the constant velocity and constant force cases, the variation of the sphere velocity resulting from hydrodynamic interaction with the interface is weaker.

Finally, the effect of interface deformation may be important in polymer processing operations. To aid in estimating the size of possible interface deformations, Figure 27 summarizes the dependence of the maximum interface deformation on the operating parameters Ca, Cg and λ.

References

Berdan, C. and Leal, L.G., 1982 Motion of a Sphere in the Presence of a Deformable Interface. Part I, Perturbation of the interface from flat: the effects on drag and torque. *J. Colloid Interface Sci.* **87**, 62 (1982).

Chi, B. and Leal, L.G., 1987 A Theoretical Study of the Motion of a Viscous Drop Toward a Fluid Interface at Low Reynolds Number. *J. Colloid Interface Sci.* Accepted.

Chwang, A.T. and Wu, T.Y-T. 1975 Hydrodynamics of low-Reynolds number flow. Part 2. Singularity method for Stokes Flows. *J. Fluid Mech.* **67**, 787.

Derjaguin, B.V. and Dukhin, S.S. 1979 Kinetic Theory of the Flotation of Fine Particles. *Proceedings of 13th International Mineral Processing Congress, Warsaw* (Elsevier, Amsterdam, 1981).

Dobby, G.S. and Finch, J.A. 1986 A Model of Particle Sliding Time for Flotation Size Bubbles *J. Colloid Int. Sci.* **109**, 493.

Dukhin, S.S. and Rulev, N.N. 1977 Hydrodynamic Interaction between a Solid Spherical Particle and a Bubble in the Elementary Act of Flotation. *Colloid J. USSR* **39**, 270.

Fritch, L. 1979 Injection-Molding ABS? Mold in Quality with the Machine. *Plastics Engineering* **35** (5), 68.

Geller, A.S., Lee, S.H. and Leal, L.G. 1986 The Creeping Motion of a Spherical Particle Normal to a Deformable Interface. *J. Fluid Mech.* **169**, 27-69.

Hartland, S. 1968 The Approach of a Rigid Sphere to a Deformable Liquid / Liquid Interface. *J. Colloid Interface Sci.* **26**, 383.

Hartland, S. 1969 The Profile of a Draining Film between a Rigid Sphere and a Deformable Fluid-Liquid Interface. *Chem. Eng. Sci.* **24**, 987.

Hoffman, R.L. 1985 Response of a Rigid Sphere to an Extensional Flow Field Near a Liquid-Gas Interface. *J. of Rheology* **29** (5), 579.

Jameson, G.J., Nam S. and Young, M.M. 1977 Physical Factors Affecting Recovery Rates in Flotation. *Minerals Sci. Engrng.* **9**, 103.

Jeffrey, D.J. and Onishi, Y. 1984 Calculation of the Resistance and Mobility Functions for Two Unequal Rigid Spheres in Low-Reynolds-number Flow. *J. Fluid Mech.* **139**, 261.

Jeffreys, G.V. and Davies, G.A. 1971 In *Recent Advances in Liquid/Liquid Extraction* (ed. C. Hanson). Pergamon Press, New York, p. 495.

Jones, A.F. and Wilson, S.D.R. 1978 The Film Drainage Problem in Droplet Coalescence. *J. Fluid Mech.* **87**, 263.

Kantorovich, L.V. and Krylov, V.I. 1958 *Approximate Methods of Higher Analysis.*, Interscience, New York.

Leal, L.G. and Lee, L.S. 1981 *Proceedings of IUTAM-IUTPAC Symposium on Interactions of Particles in Colloid Dispersions, March 16-21.*, Canberra.

Lee, S.H., Chadwick, R.S. and Leal, L.G. 1979 Motion of a Sphere in the Presence of a Plane Interface. Part 1: An Approximate Solution by Generalization of the Method of Lorentz. *J. Fluid Mech.* **93**, 705.

Lee, S.H. and Leal, L.G. 1982 Motion of a Sphere in the Presence of a Deformable Interface. Part 2: Numerical Study of the Translation of a Sphere Normal to an Interface. *J. Colloid Int. Sci.* **87**, 81.

Maru, H.C., Wasan, D.T. and Kintner, R.C. 1971 Behavior of a Rigid Sphere at a Liquid-Liquid Interface. *Chem. Eng. Sci.* **26**, 1615.

Princen, H.M. 1963 Shape of a Fluid Drop at a Liquid-Liquid Interface. *J. Colloid Sci.* **18**, 178.

Rallison, J.M. and Acrivos, A. 1978 A Numerical Study of the Deformation and Burst of a Viscous Drop in an Extensional Flow. *J. Fluid Mech.* **89**, 191.

Ruschak, K.J. 1985 Coating Flows. *Ann. Rev. Fluid Mech.* **17**, 65.

Shah, S.T., Wasan, D.T. and Kintner, R.C. 1972 Passage of a Liquid Drop Through a Liquid-Liquid Interface. *Chem. Eng. Sci.* **27**, 881.

Smith, P.G. and Van de Ven, T.G.M. 1984 The Effect of Gravity on the Drainage of a Thin Liquid Film between a Solid Sphere interface and a Liquid/Fluid Interface. *J. Colloid Interface Sci.* **100**, 456.

Stoos, J.A., 1987 Ph.D. dissertation. California Institute of Technology.

Yang, S.-M. and Leal, L.G. 1984 Particle Motion in Stokes Flow near a Plane Fluid-Fluid Interface. Part 2. Linear Shear and Axisymmetric Straining Flows. *J. Fluid Mech.* **149**, 275.

Youngren G.K. and Acrivos, A.A. 1975 Stokes Flow Past a Particle of Arbitrary Shape: a Numerical Method of Solution *J. Fluid Mech.* **69**, 377.

Youngren G.K. and Acrivos, A.A. 1976 On the Shape of a Gas Bubble in a Viscous Extensional Flow *J. Fluid Mech.* **76**, 433.

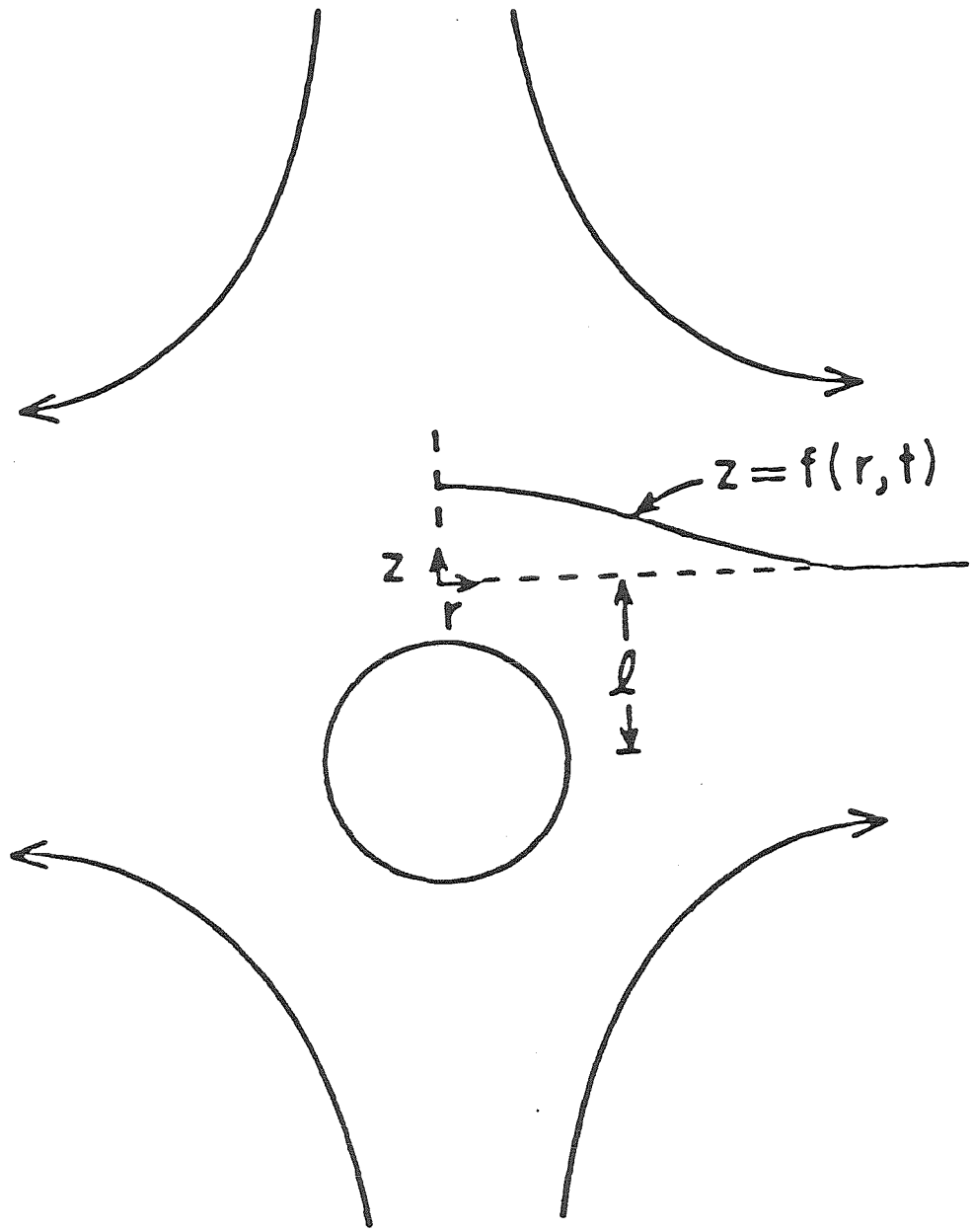

Figure 1. Schematic of problem.

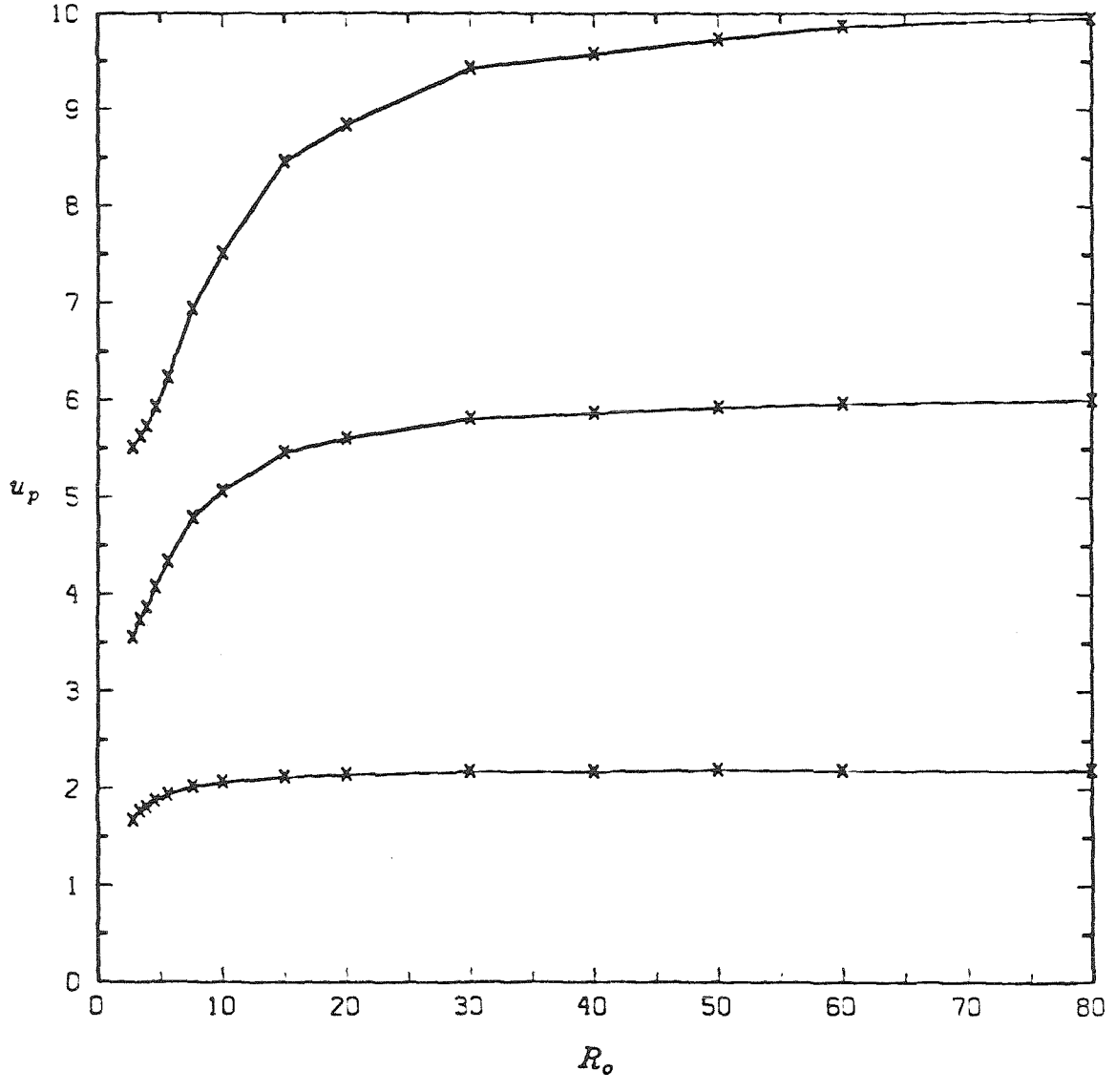

Figure 2. Effect of interface truncation on sphere velocity, with λ = Ca = Cg = 1, and fixed sphere positions l = -1.1, -3 and -5.

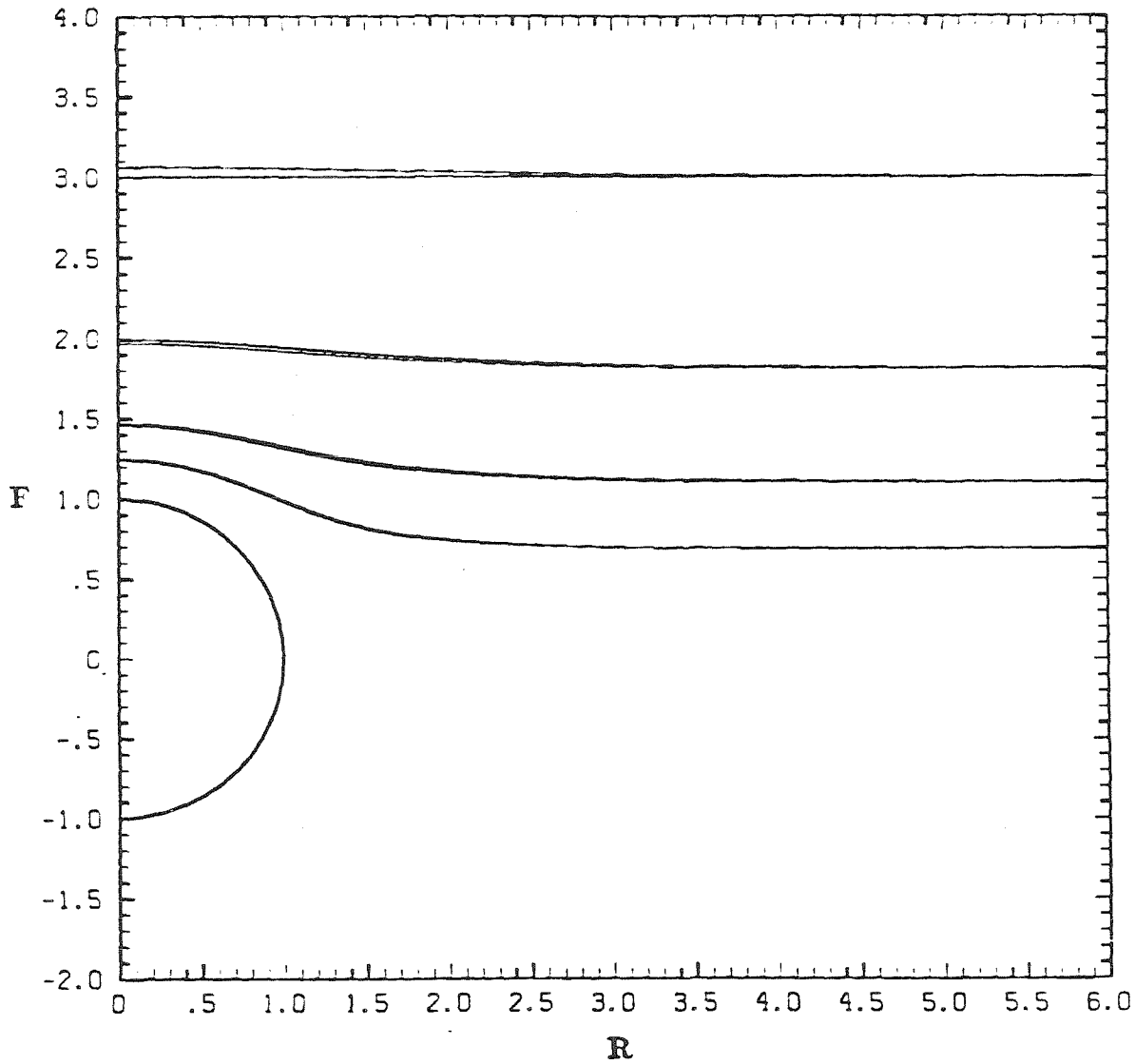

Figure 3. Effect of sphere starting position on interface shape. Initial starting positions l_o = -3 and -5, λ = Ca = Cg = 1, dimensionless time between contours Δt_c = 0.25.

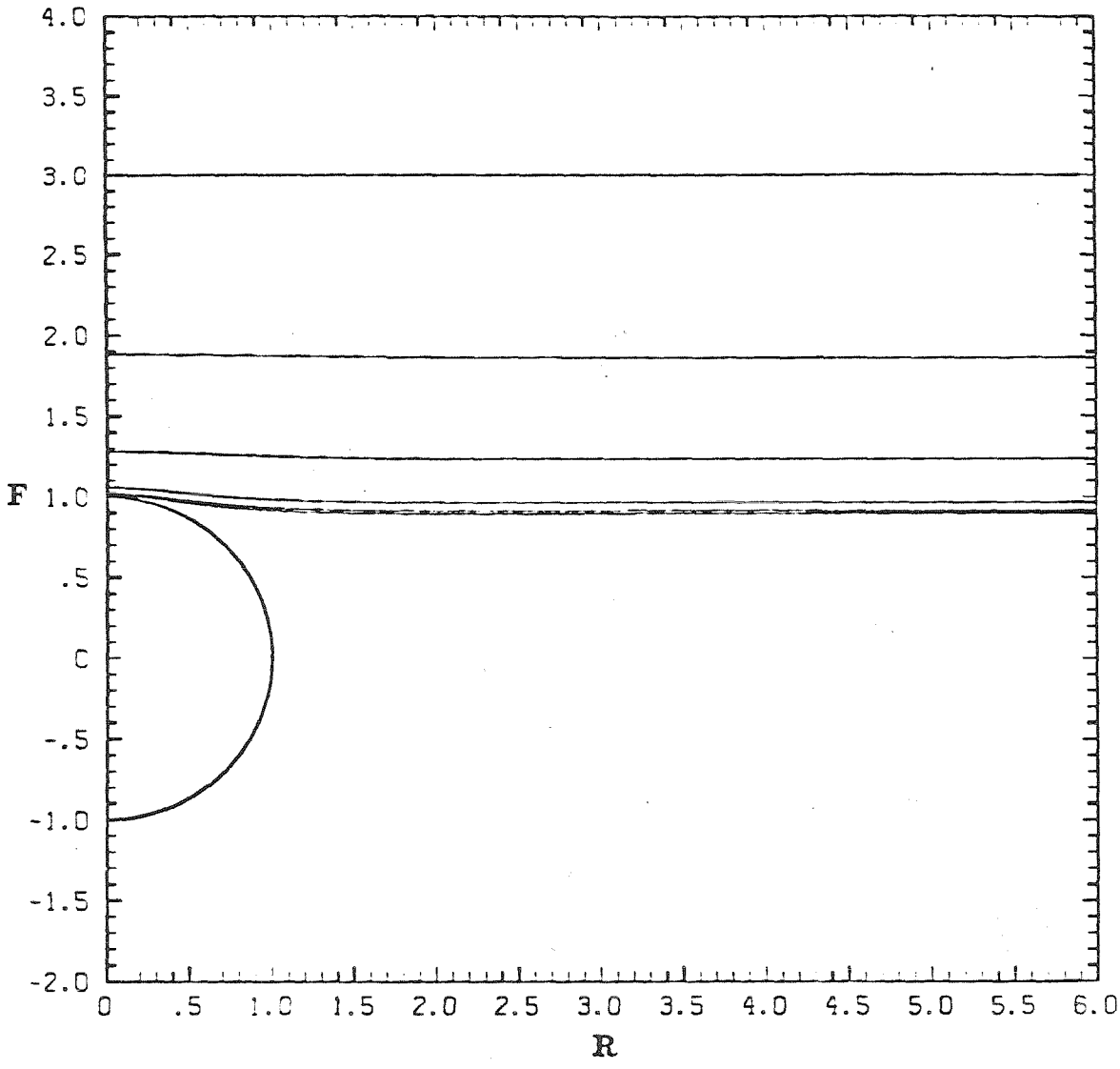

Figure 4. Interface shape as a function of sphere position with $\lambda = 0$, $Ca = Cg = 0.01$, $l_o = -3$, $\Delta t_c = 0.25$.

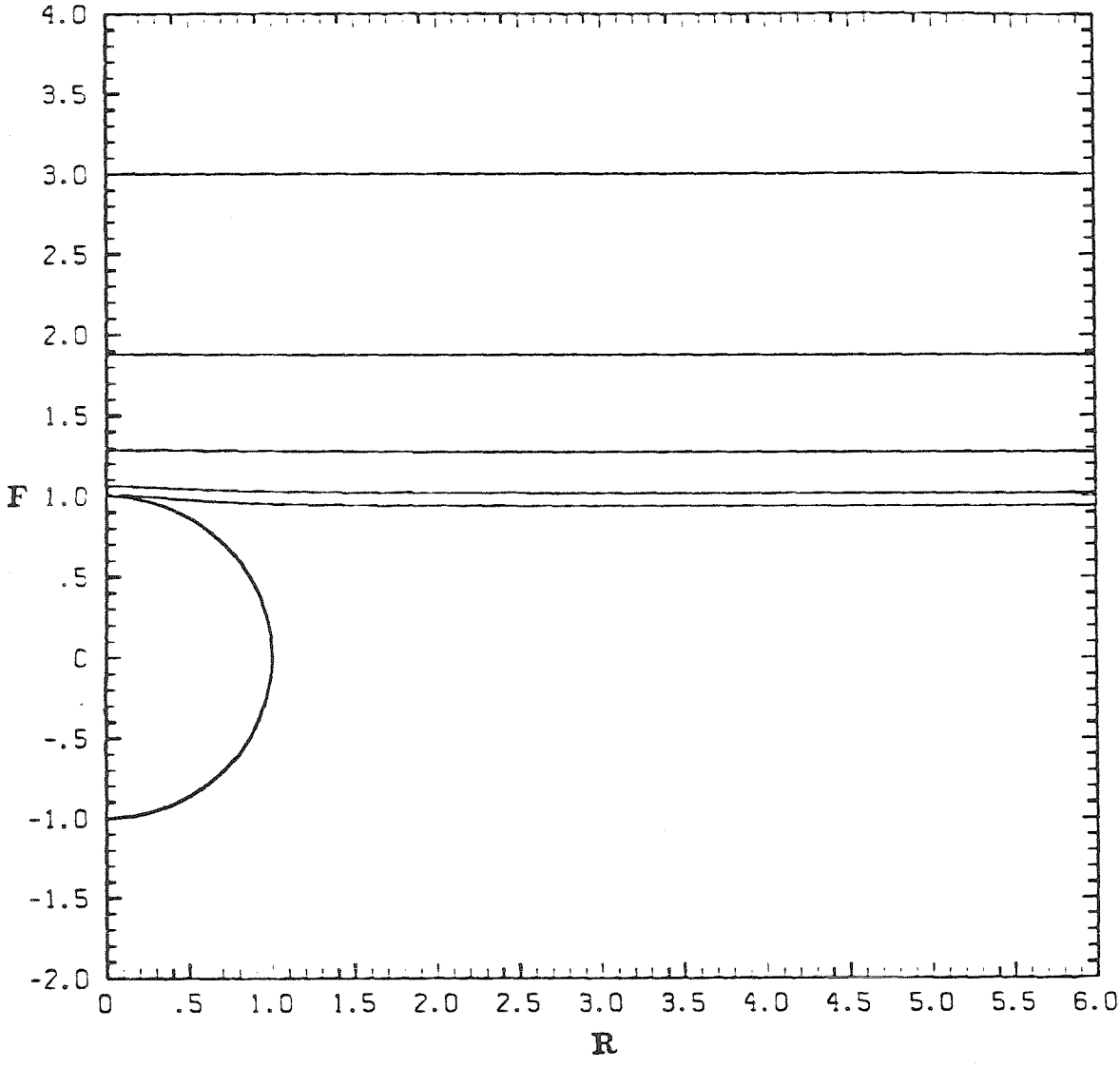

Figure 5. Interface shape as a function of sphere position with $\lambda = 100$, $Ca = Cg = 1$, $l_o = -3$, $\Delta t_c = 0.25$.

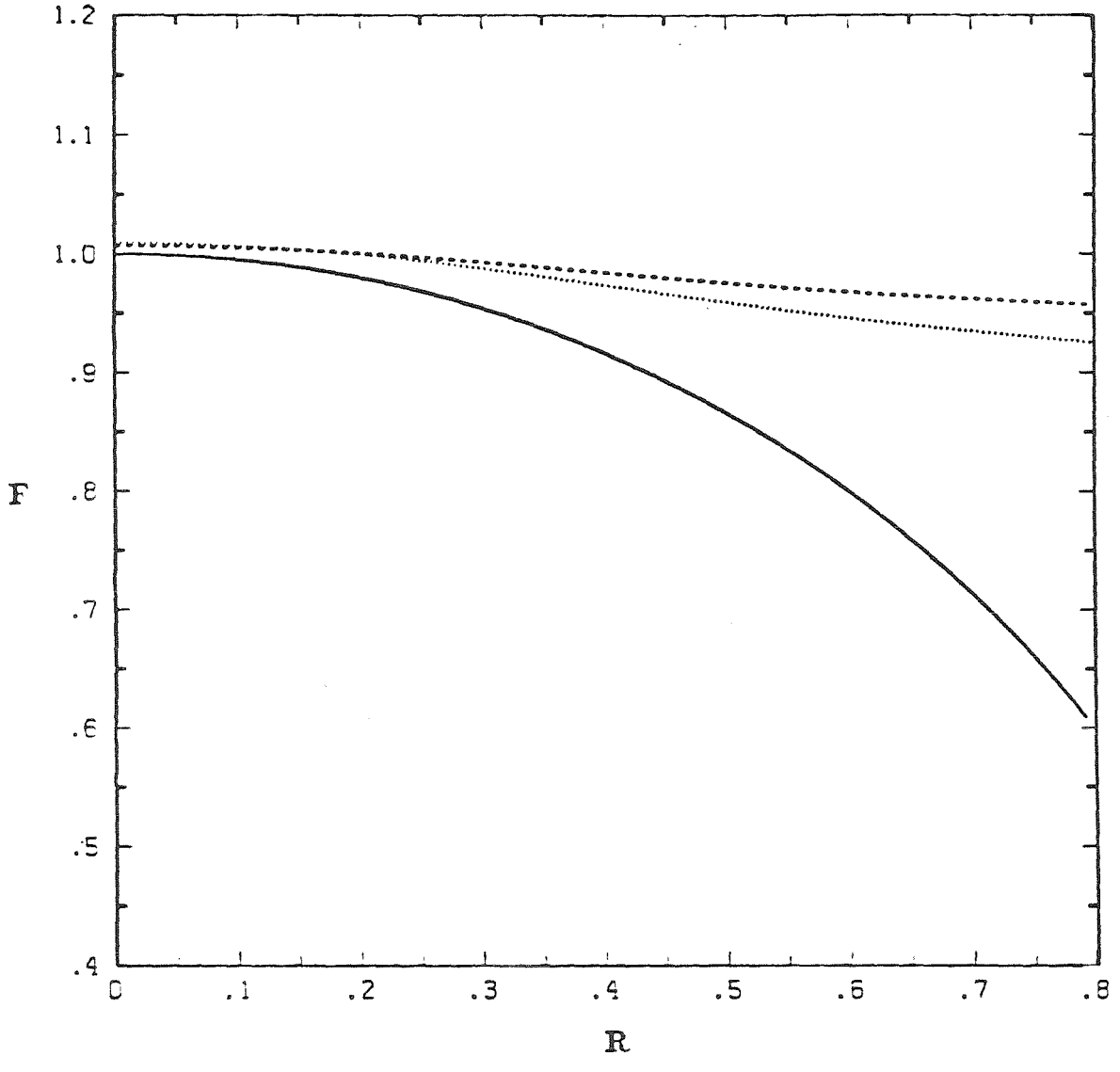

Figure 6. Expanded view of thin film regions in Figures 4 and 5: ——, Sphere surface; - - - - - $\lambda = 0$, $Ca = Cg = 0.01$; ·····, $\lambda = 100$, $Ca = Cg = 1$.

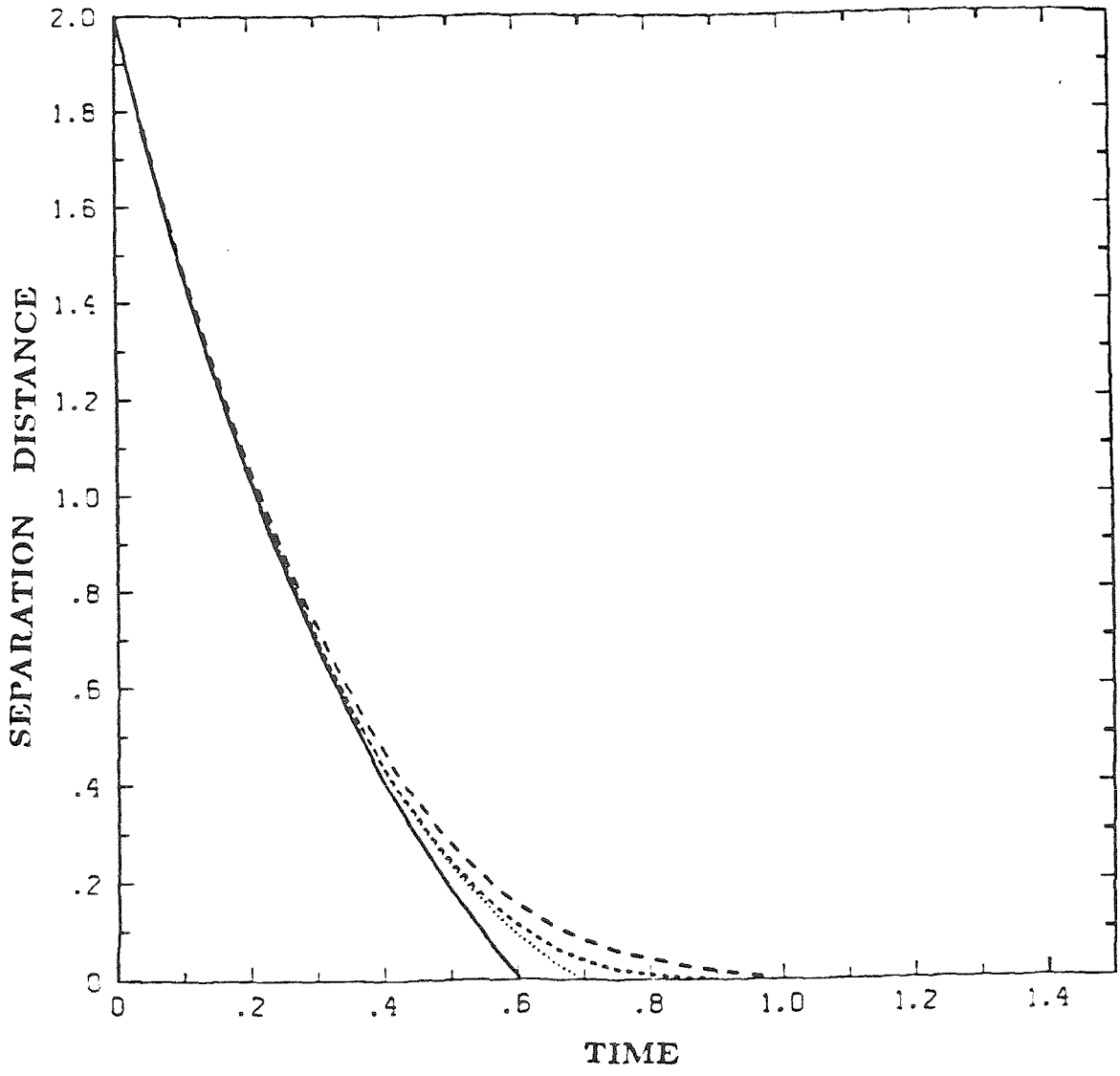

Figure 7. Particle position and minimum "film" thickness as a function of time for Ca = Cg = 0.01, $\lambda = 0$: ——, far-field asymptotic result for a flat interface; - - - - -, bipolar coordinate result for a flat interface; · · · · · · ·, boundary integral result for particle position relative to z = 0;— —, boundary integral result for the minimum thickness of the thin liquid film.

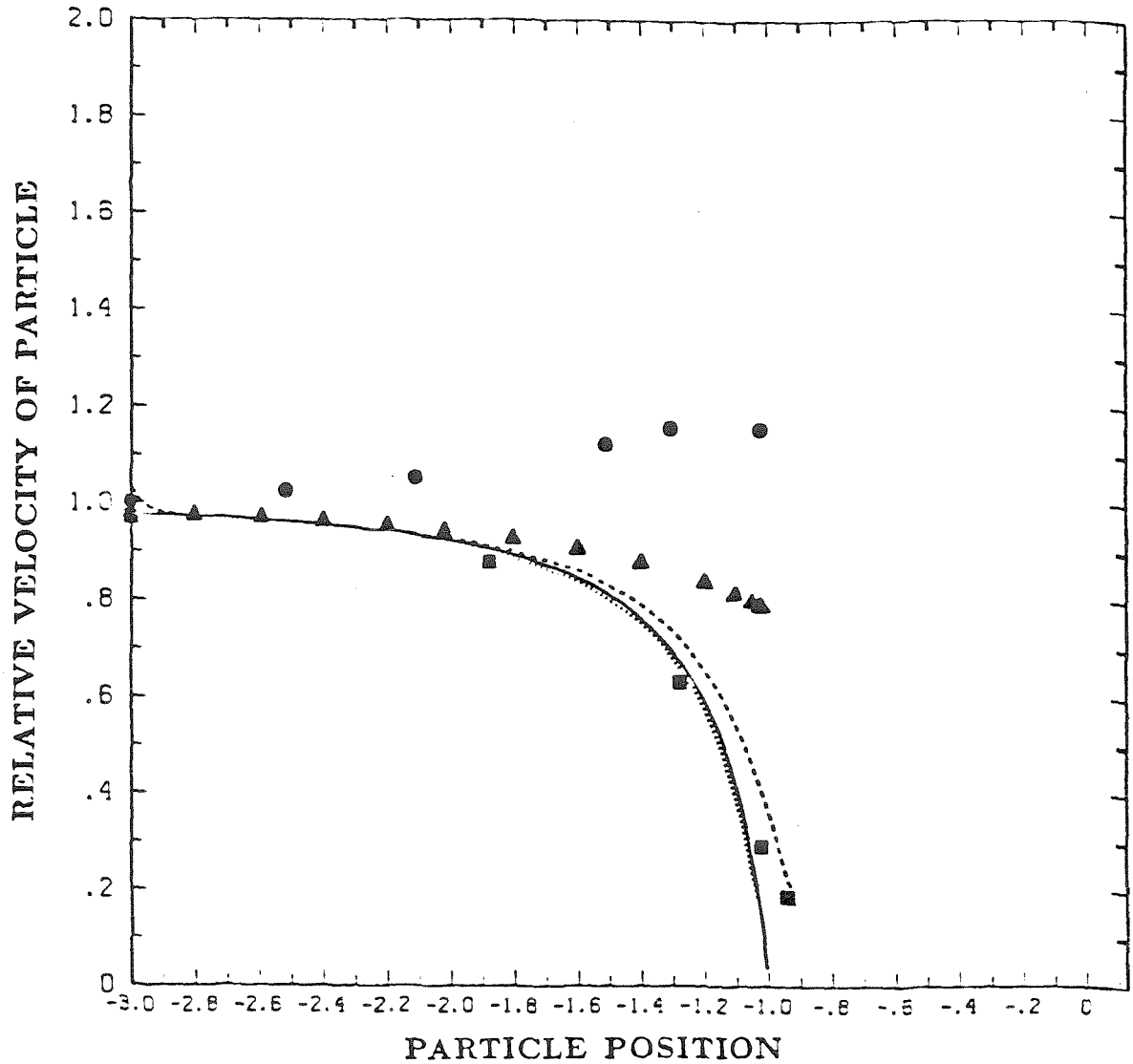

Figure 8. Relative velocity of the particle as a function of particle position for Ca = Cg = 0.01, $\lambda = 0$: ——, bipolar coordinate solution for a flat, nondeforming interface; - - - - -, boundary integral solution as a function of particle position relative to z = 0; · · · · · · ·, boundary integral solution as a function of particle position relative to the deformed interface; ▲, far-field asymptotic solution for a flat non-deforming interface; ●, boundary integral solution as a function of particle position relative to z = 0 for a flat but deforming interface. Also shown, for comparison, are boundary integral results for λ = 100, Ca = Cg = 1, ■.

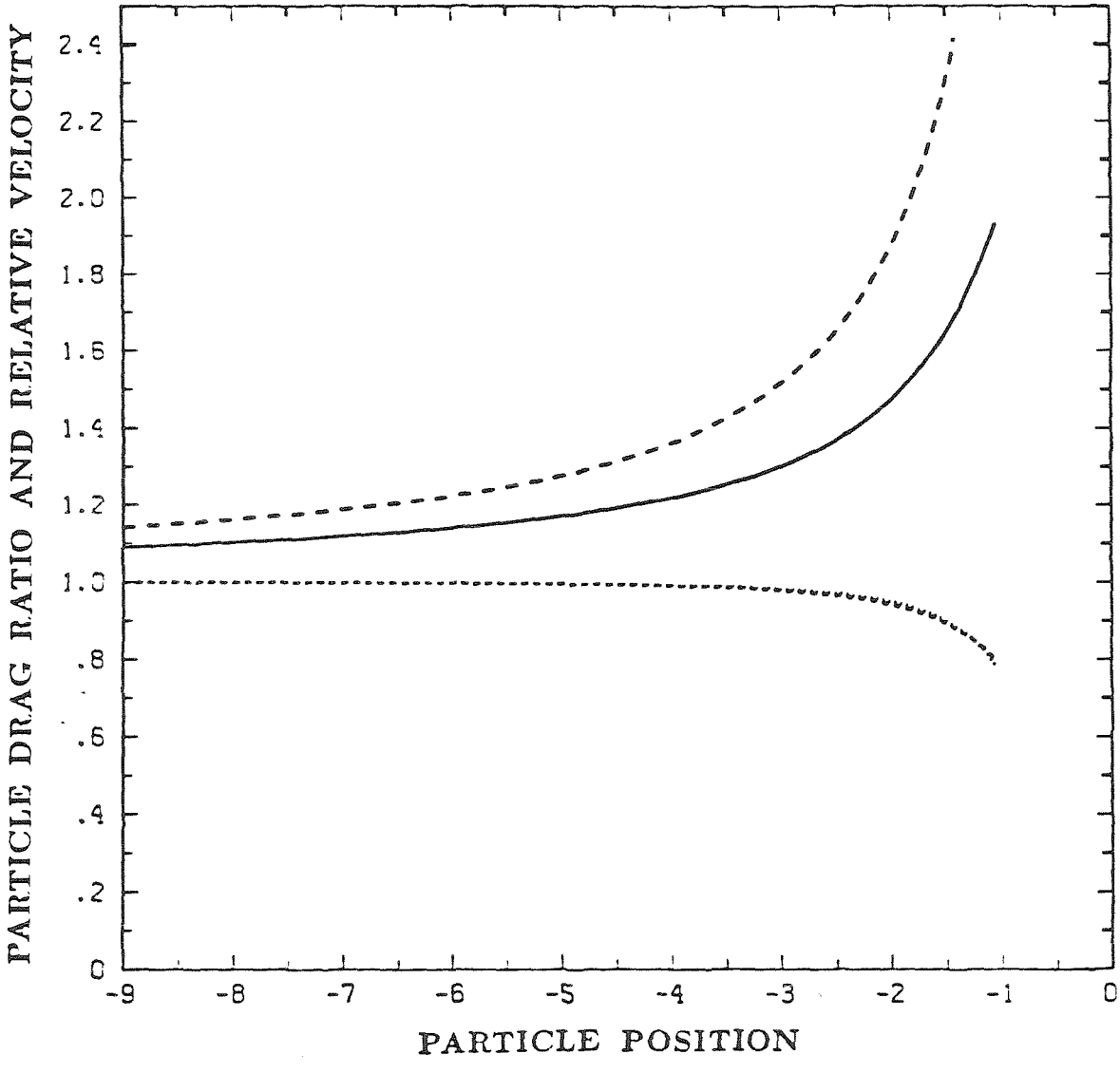

Figure 9. Particle drag ratio and relative velocity from far-field asymptotic solution: ——, drag for $\lambda = 0$; — — —, drag for $\lambda = \infty$; ·····, velocity for $\lambda = 0$; - - - - -, velocity for $\lambda = \infty$.

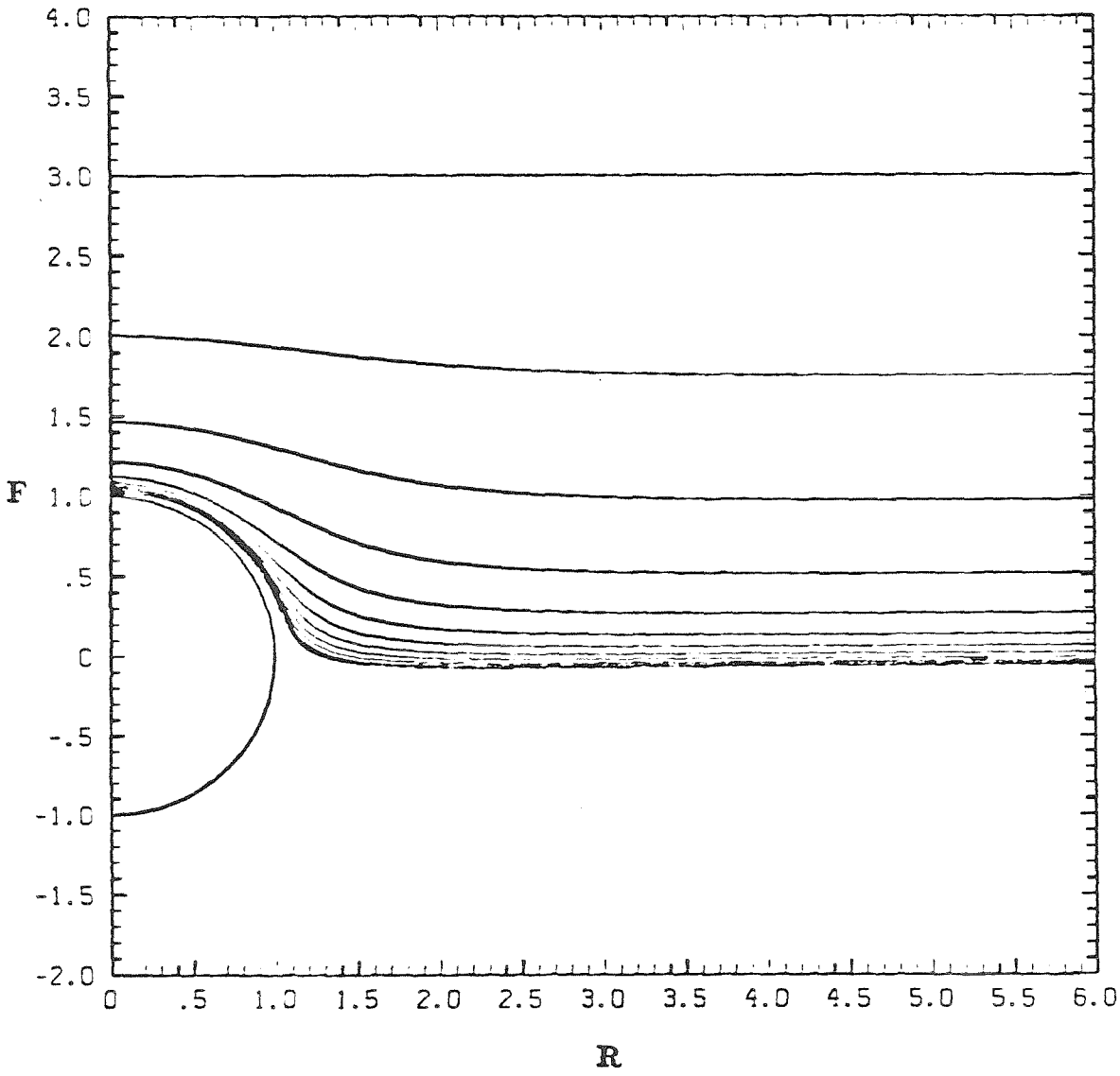

Figure 10. Interface shape as a function of sphere position with $\lambda = 0$, $Ca = Cg = 1$, $l_o = -3$, $\Delta t_c = 0.25$.

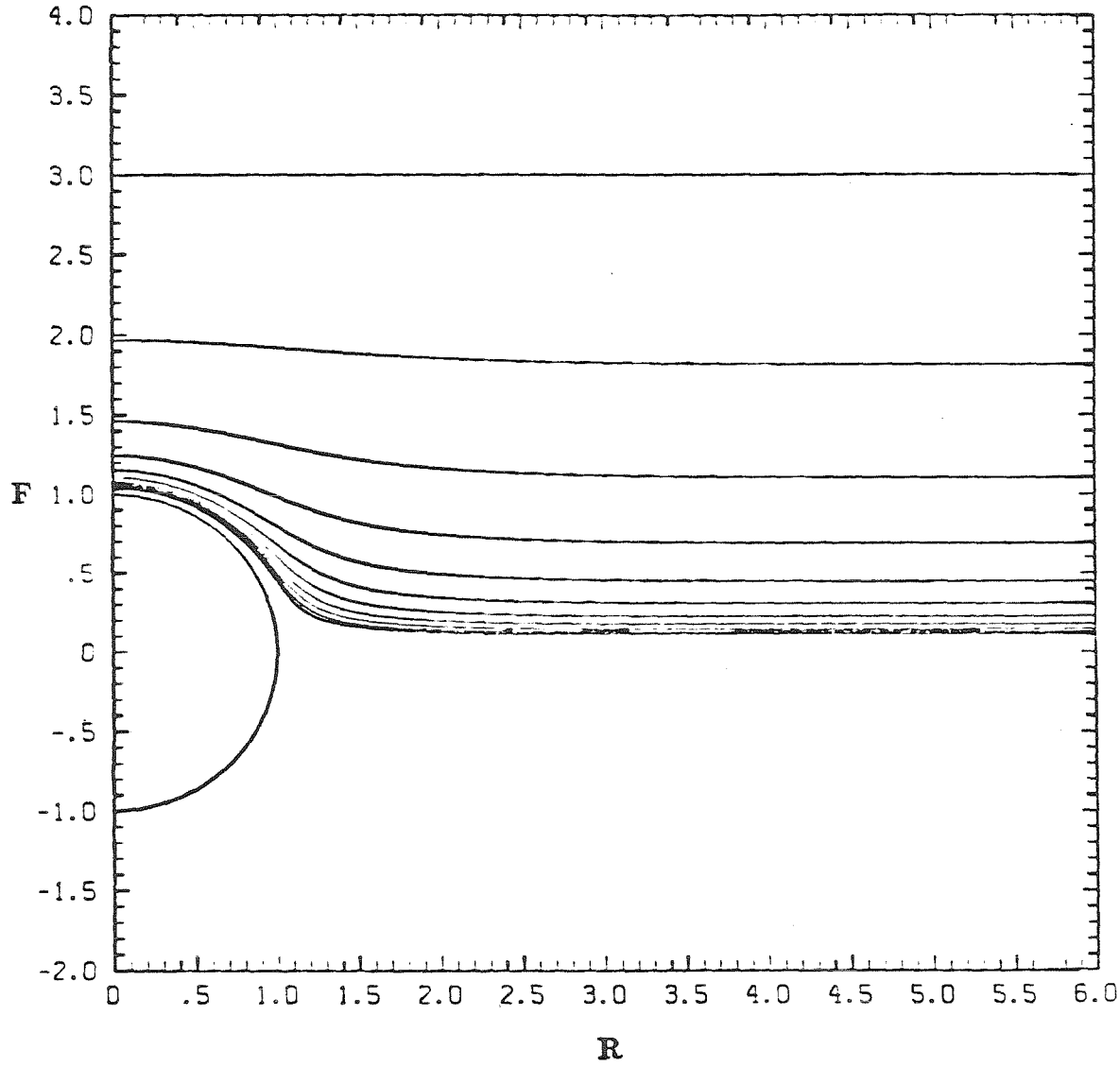

Figure 11. Interface shape as a function of sphere position with λ = Ca = Cg = 1, l_o = -3, Δt_c = 0.25.

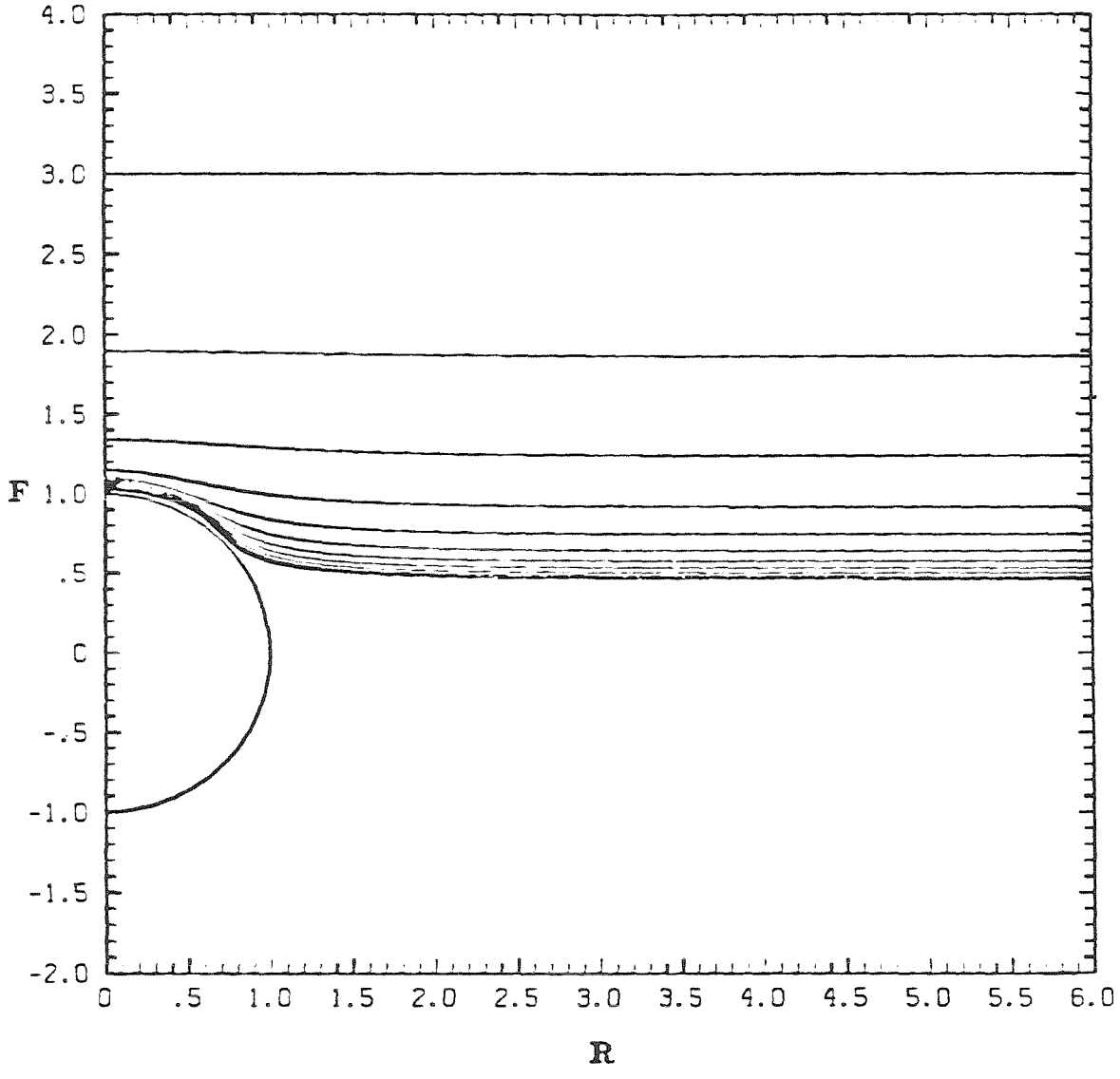

Figure 12. Interface shape as a function of sphere position with $\lambda = 10$, $Ca = Cg = 1$, $l_o = -3$, $\Delta t_c = 0.25$.

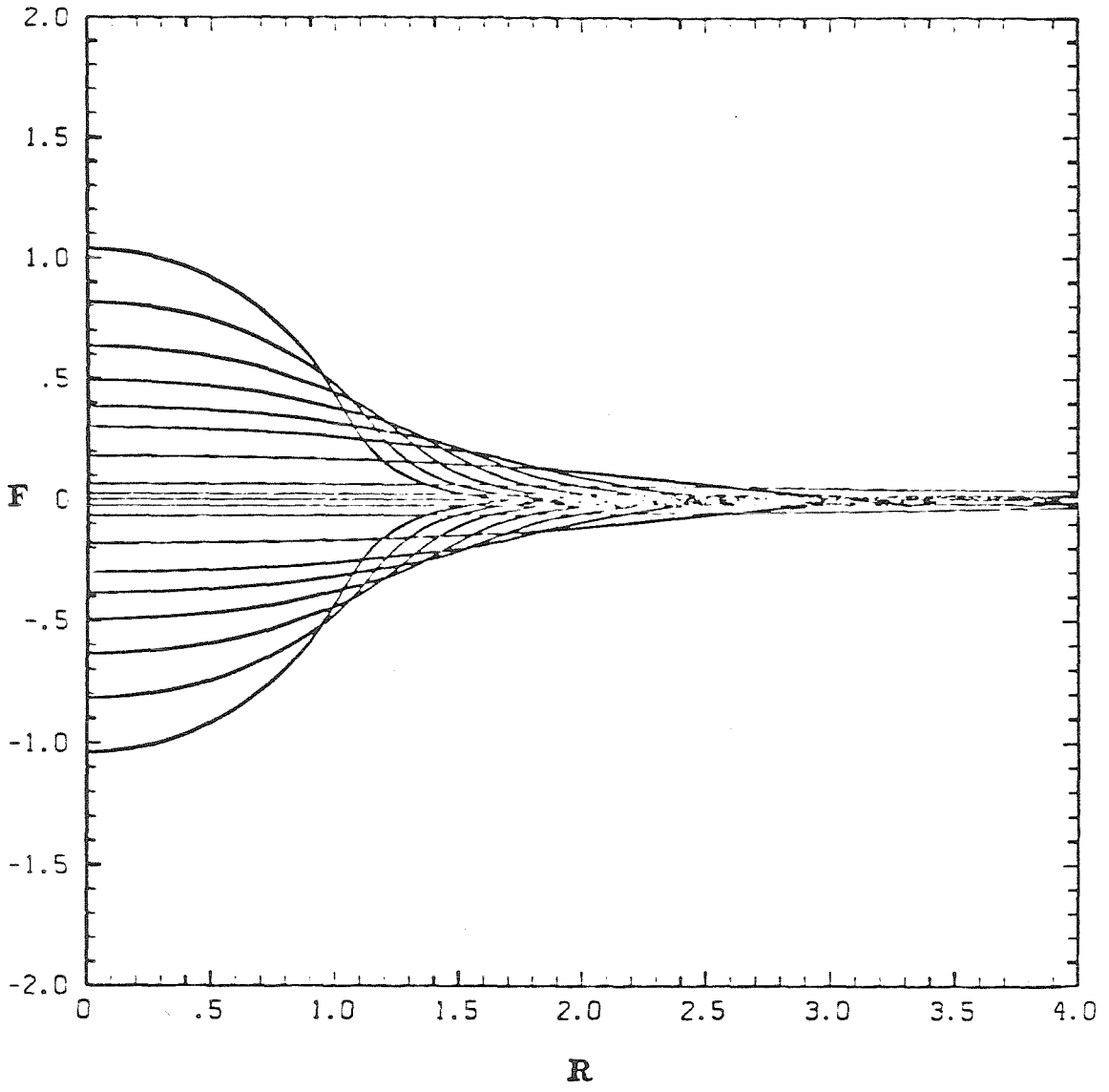

Figure 13. Shape of an initially deformed interface relaxing back to flat in the presence of an extensional flow with $\lambda = 1$, $Ca = Cg = \infty$, at times = 0.0, 0.125, 0.25, 0.375, 0.50, 0.675, 0.875, 1.375, 1.875.

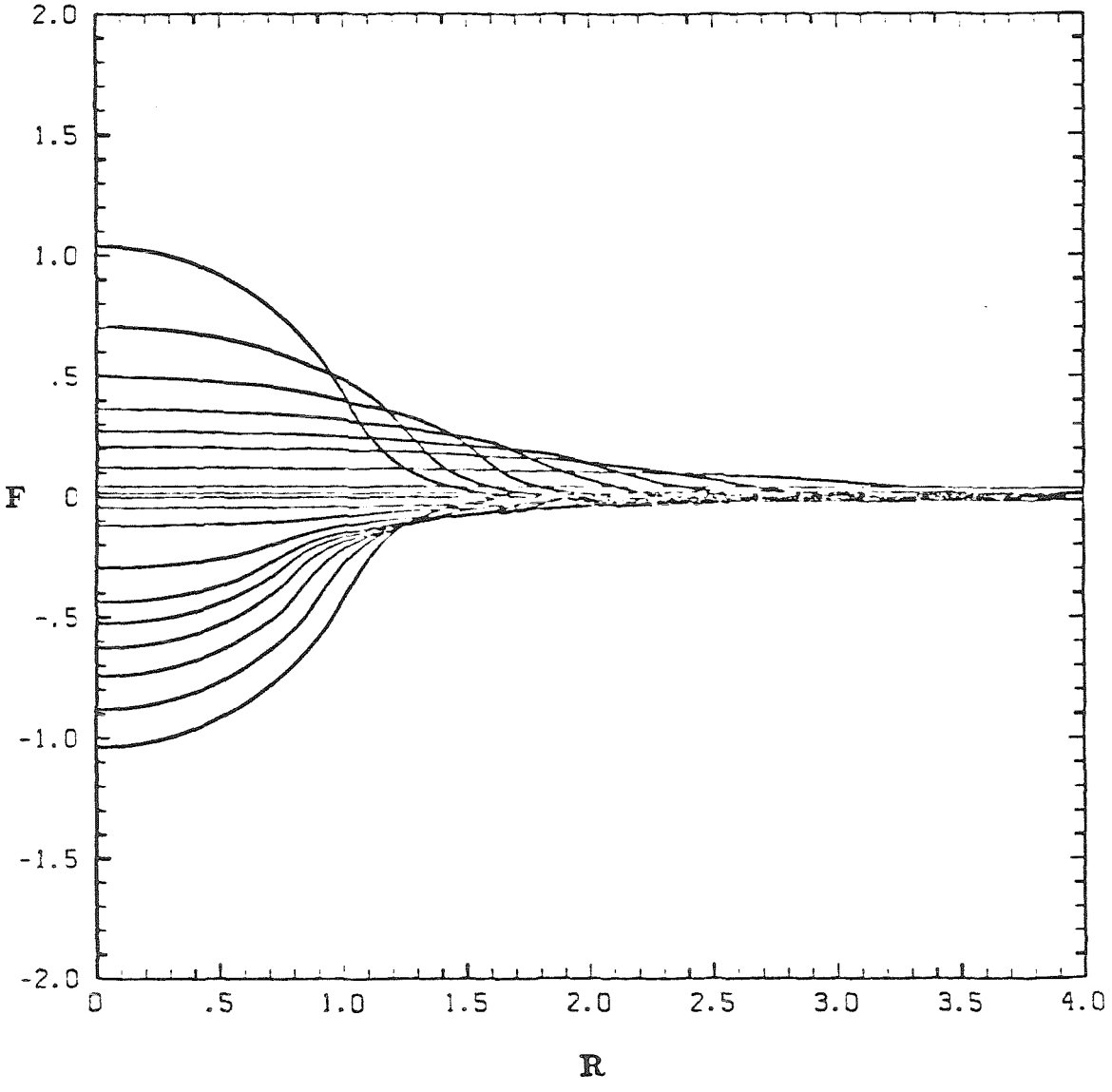

Figure 14. Shape of an initially deformed interface relaxing back to flat in the presence of an extensional flow with $\lambda = 0$, $Ca = Cg = \infty$, at times = 0.0, 0.125, 0.25, 0.375, 0.50, 0.675, 0.875, 1.375, 1.875.

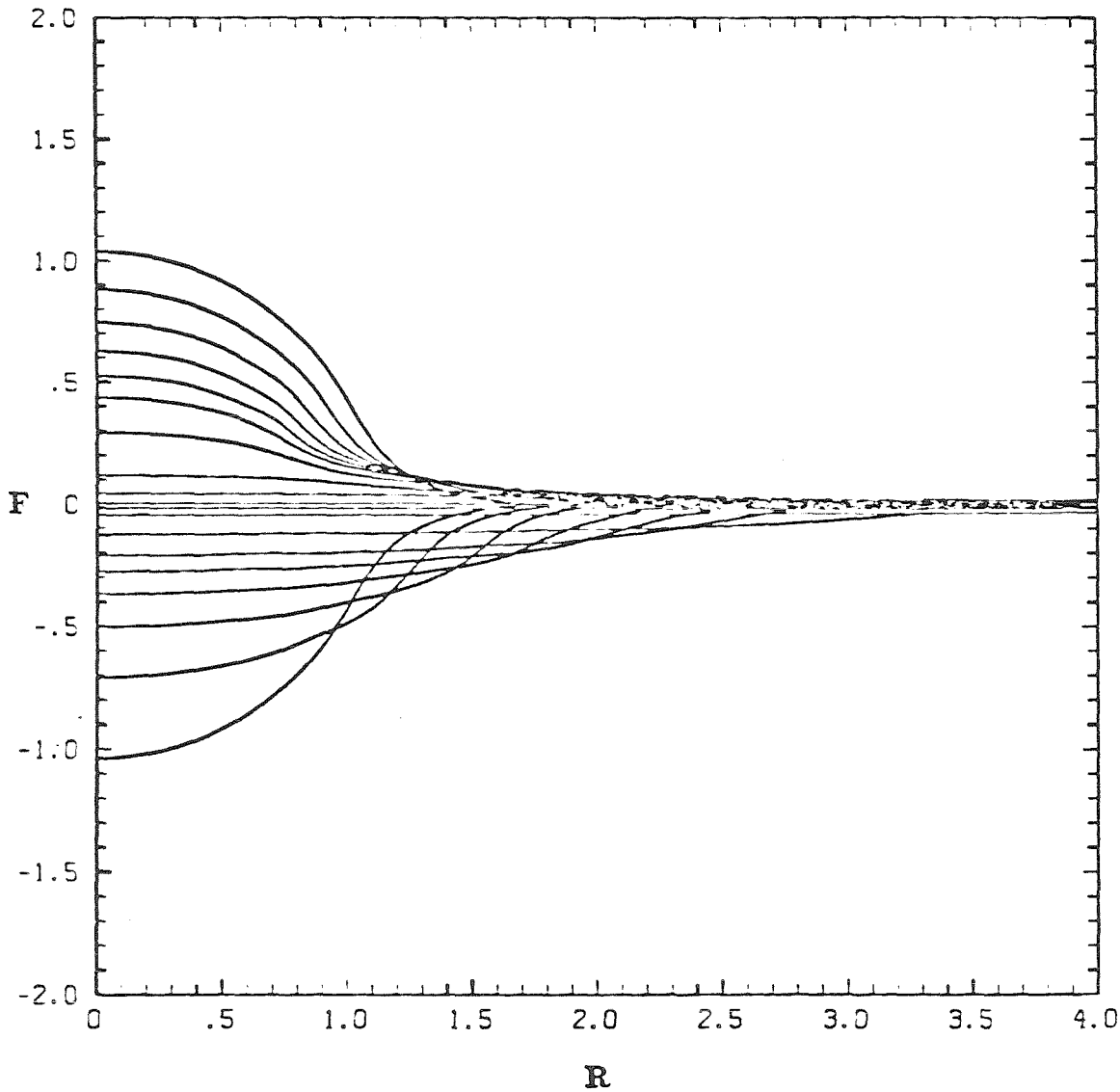

Figure 15. Shape of an initially deformed interface relaxing back to flat in the presence of an extensional flow with $\lambda = 10$, $Ca = Cg = \infty$, at times = 0.0, 0.125, 0.25, 0.375, 0.50, 0.675, 0.875, 1.375, 1.875.

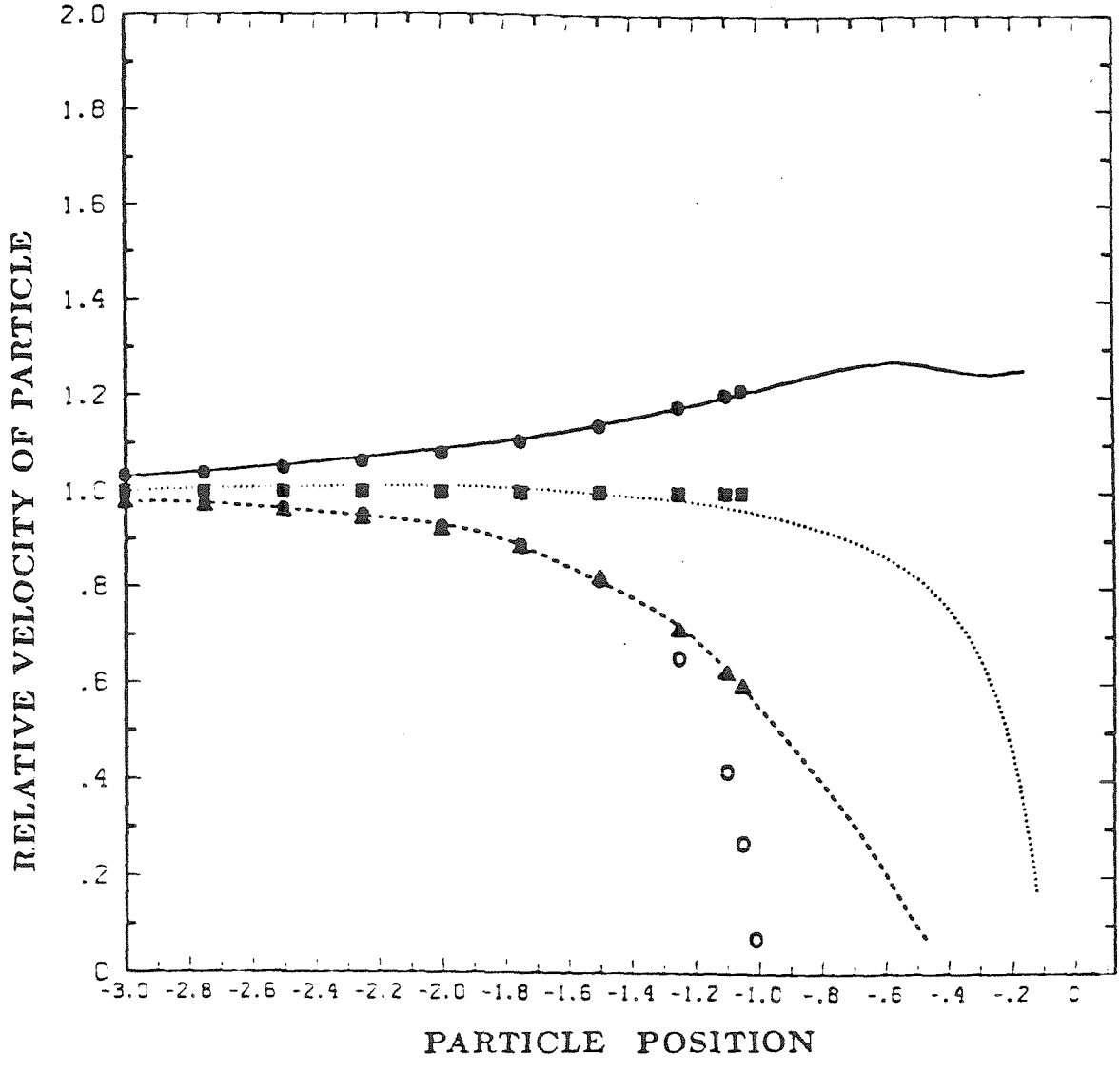

Figure 16. Relative velocity of the particle as a function of particle position: ——, $\lambda = 0$, $Ca = Cg = 1$; - - - - -, $\lambda = 10$, $Ca = Cg = 1$; ·····, $\lambda = 1$, $Ca = Cg = 1$; ■, boundary integral solution for a flat but deforming interface with $\lambda = 1$, $Ca = Cg = 1$; ▲, boundary integral solution for a flat but deforming interface with $\lambda = 10$, $Ca = Cg = 1$; ●, boundary integral solution for a flat but deforming interface with $\lambda = 0$, $Ca = Cg = 1$; ○, bipolar coordinate solution for a flat interface with $\lambda = 0$.

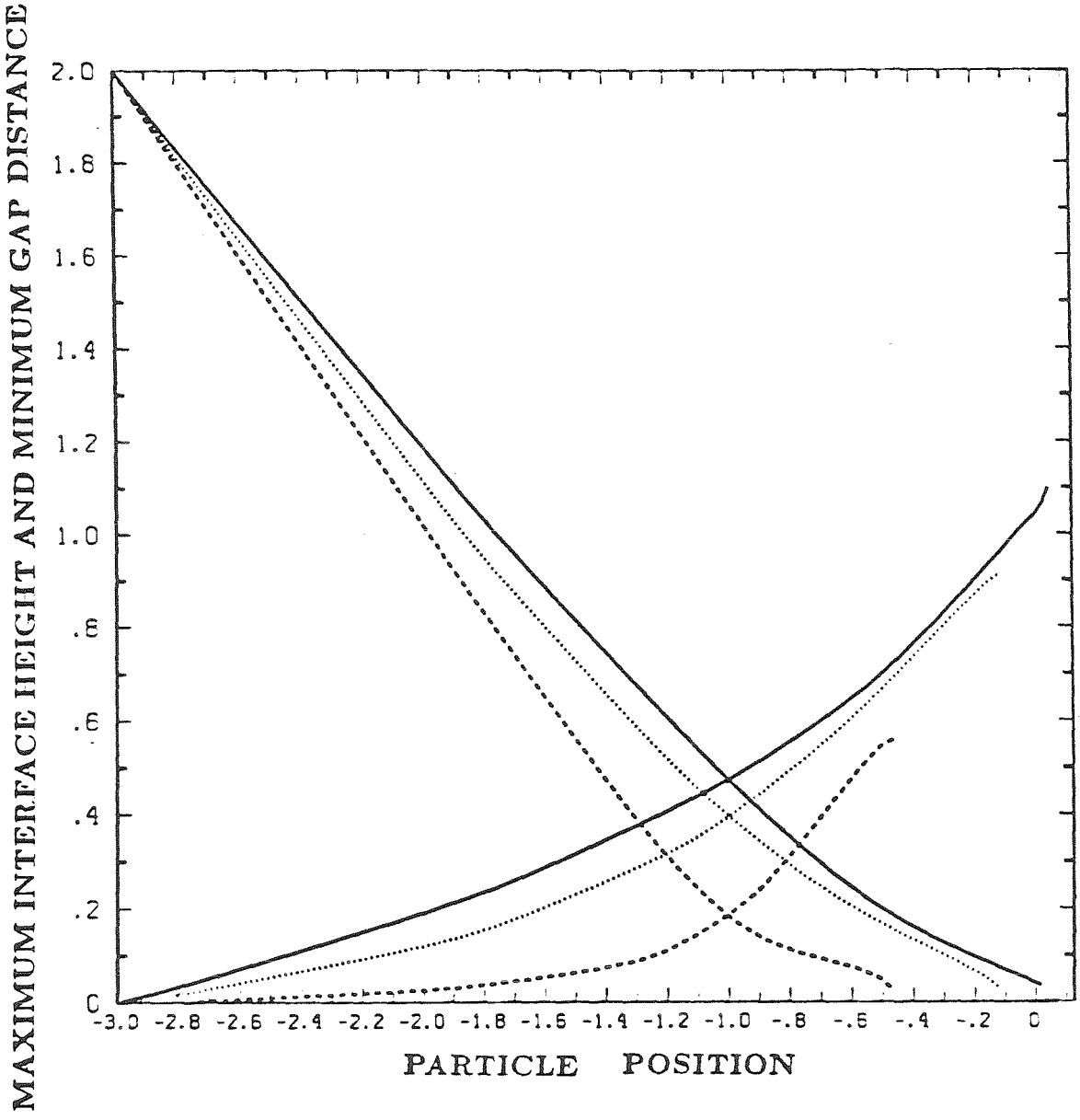

Figure 17. Maximum interface height above the plane $z = 0$ and minimum particle-interface separation distance as a function of particle position for $Ca = Cg = 1$: ———, $\lambda = 0$; · · · · ·, $\lambda = 1$; - - - - - -, $\lambda = 10$.

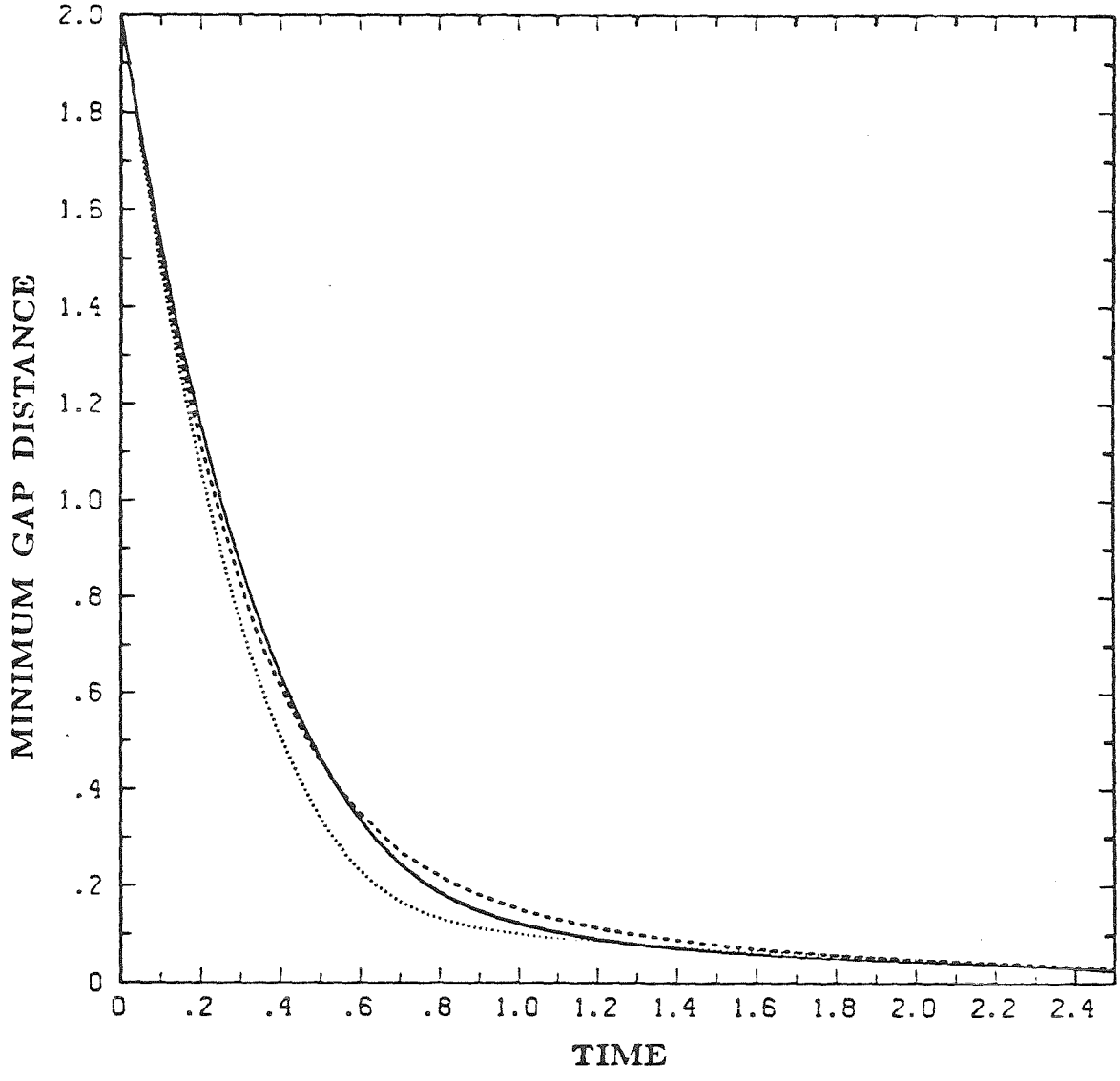

Figure 18. Minimum particle-interface separation distance as a function of time for Ca = Cg = 1: ——, $\lambda = 0$; ·····, $\lambda = 1$; - - - - - -, $\lambda = 10$.

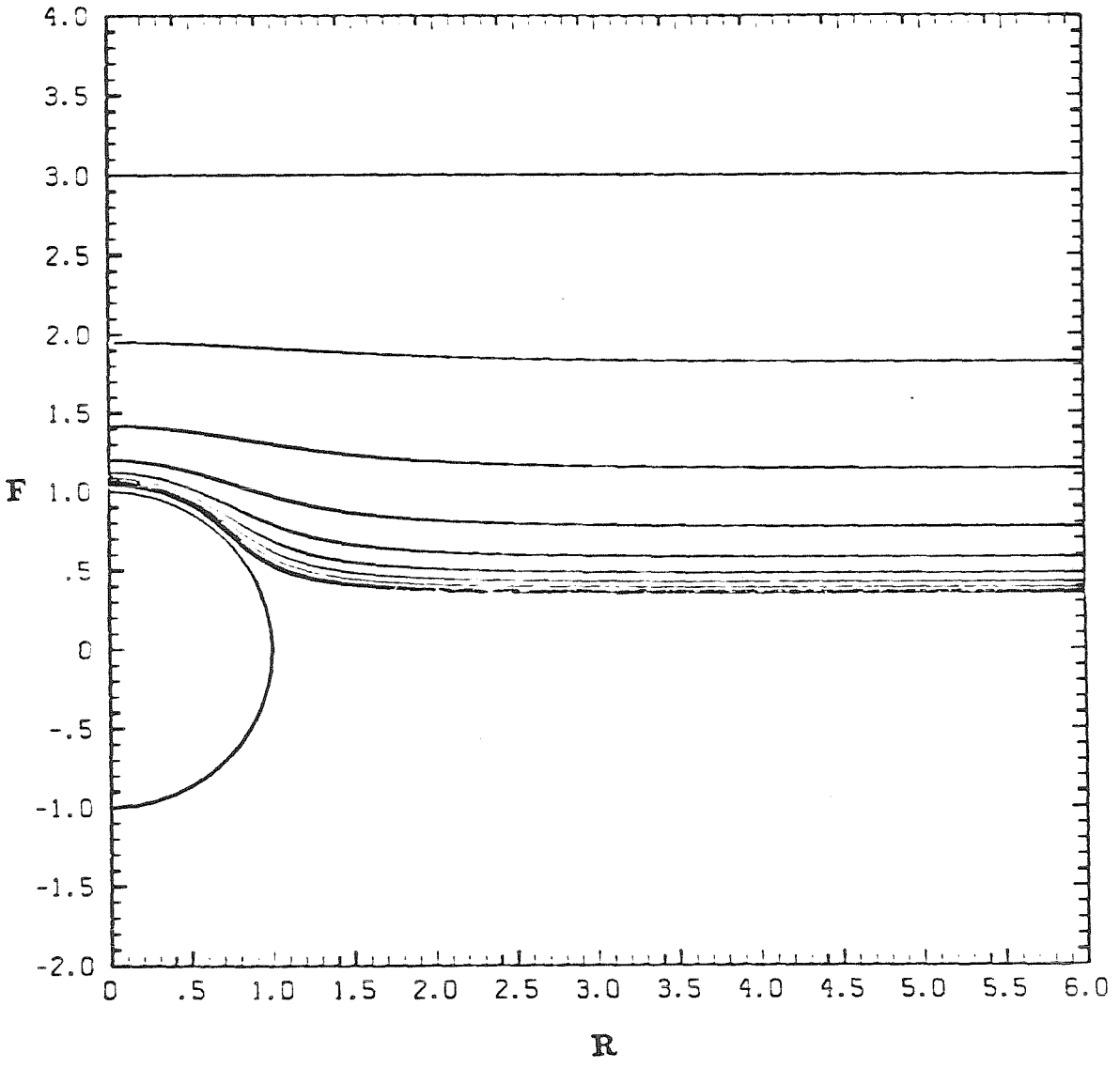

Figure 19. Interface shape as a function of sphere position with $\lambda = 1$, $Ca = 0.1$, $Cg = 1$, $l_o = -3$, $\Delta t_c = 0.25$.

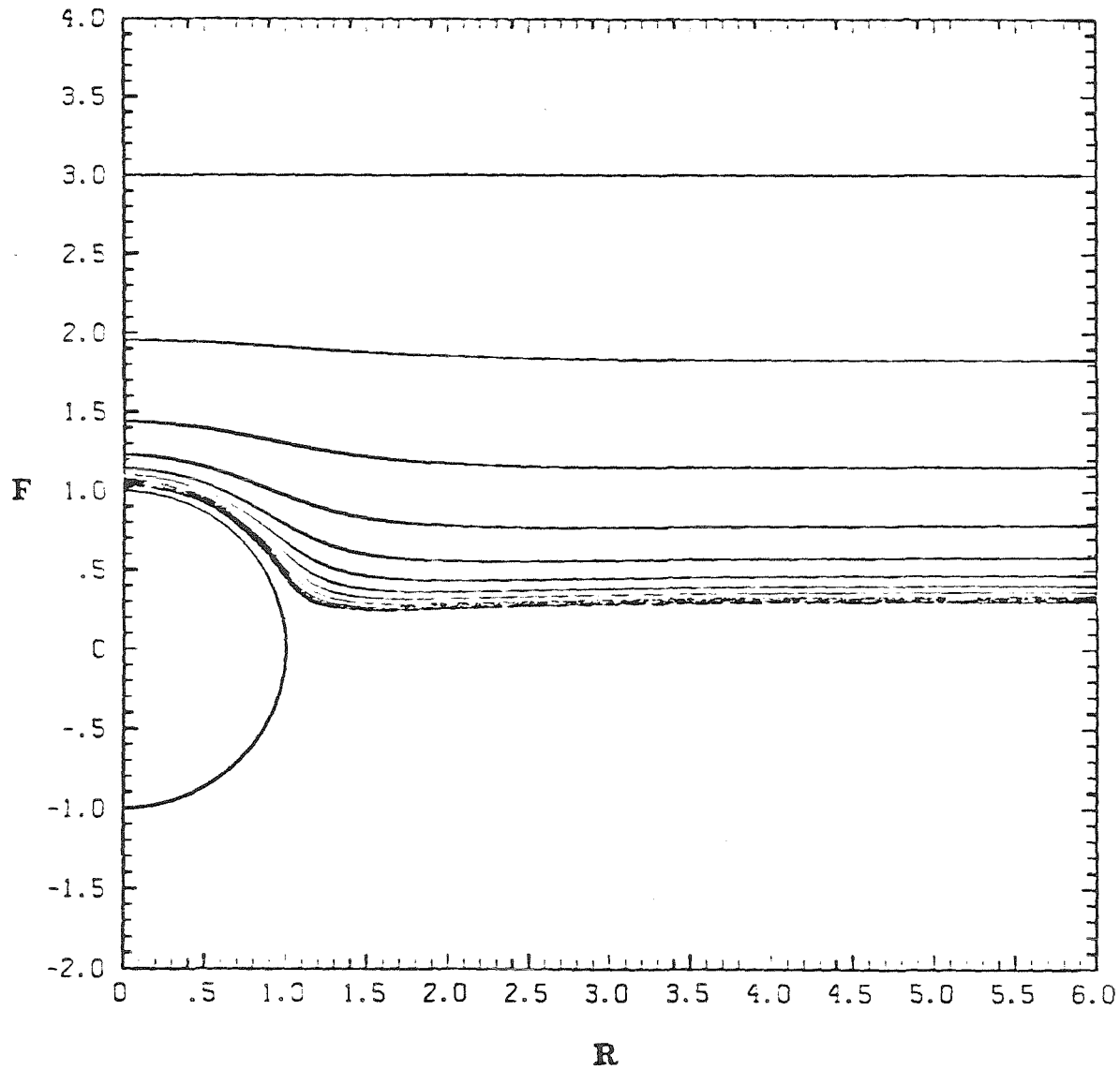

Figure 20. Interface shape as a function of sphere position with $\lambda = 1$, $Ca = 1$, $Cg = 0.1$, $l_o = -3$, $\Delta t_c = 0.25$.

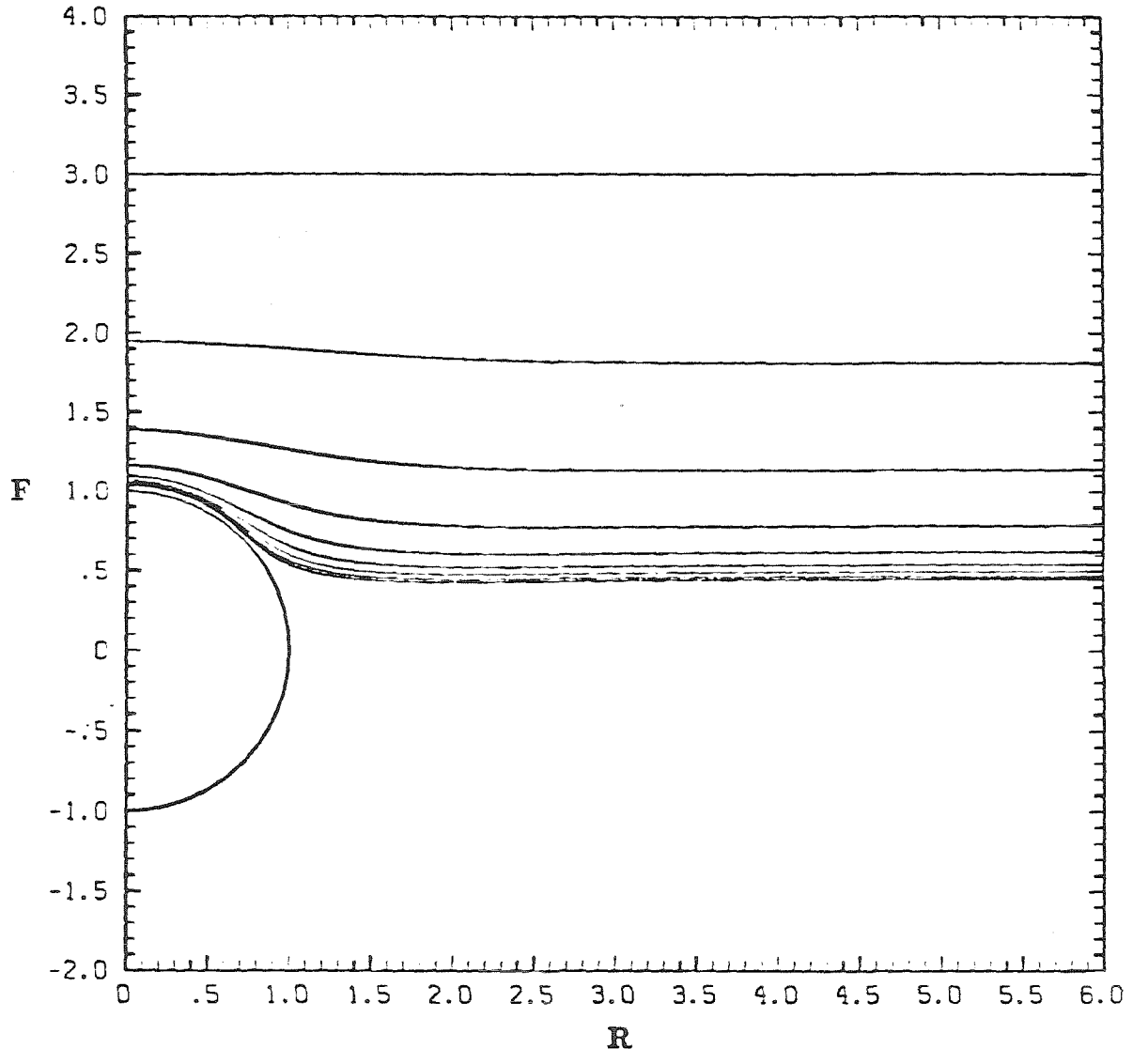

Figure 21. Interface shape as a function of sphere position with $\lambda = 0$, $Ca = Cg = 0.1$, $l_o = -3$, $\Delta t_c = 0.25$.

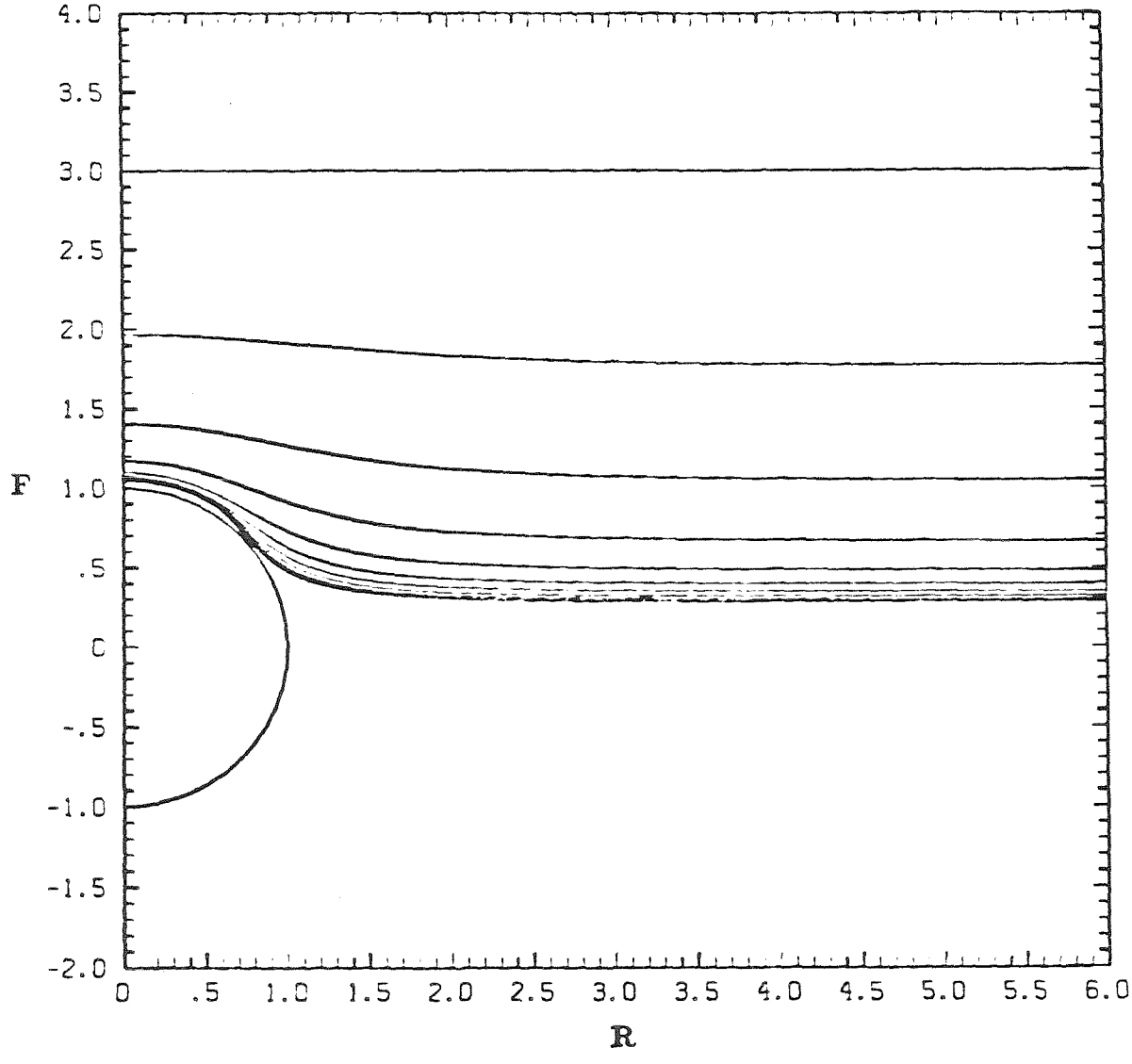

Figure 22. Interface shape as a function of sphere position with $\lambda = 0$, $Ca = 0.1$, $Cg = 10$, $l_o = -3$, $\Delta t_c = 0.25$.

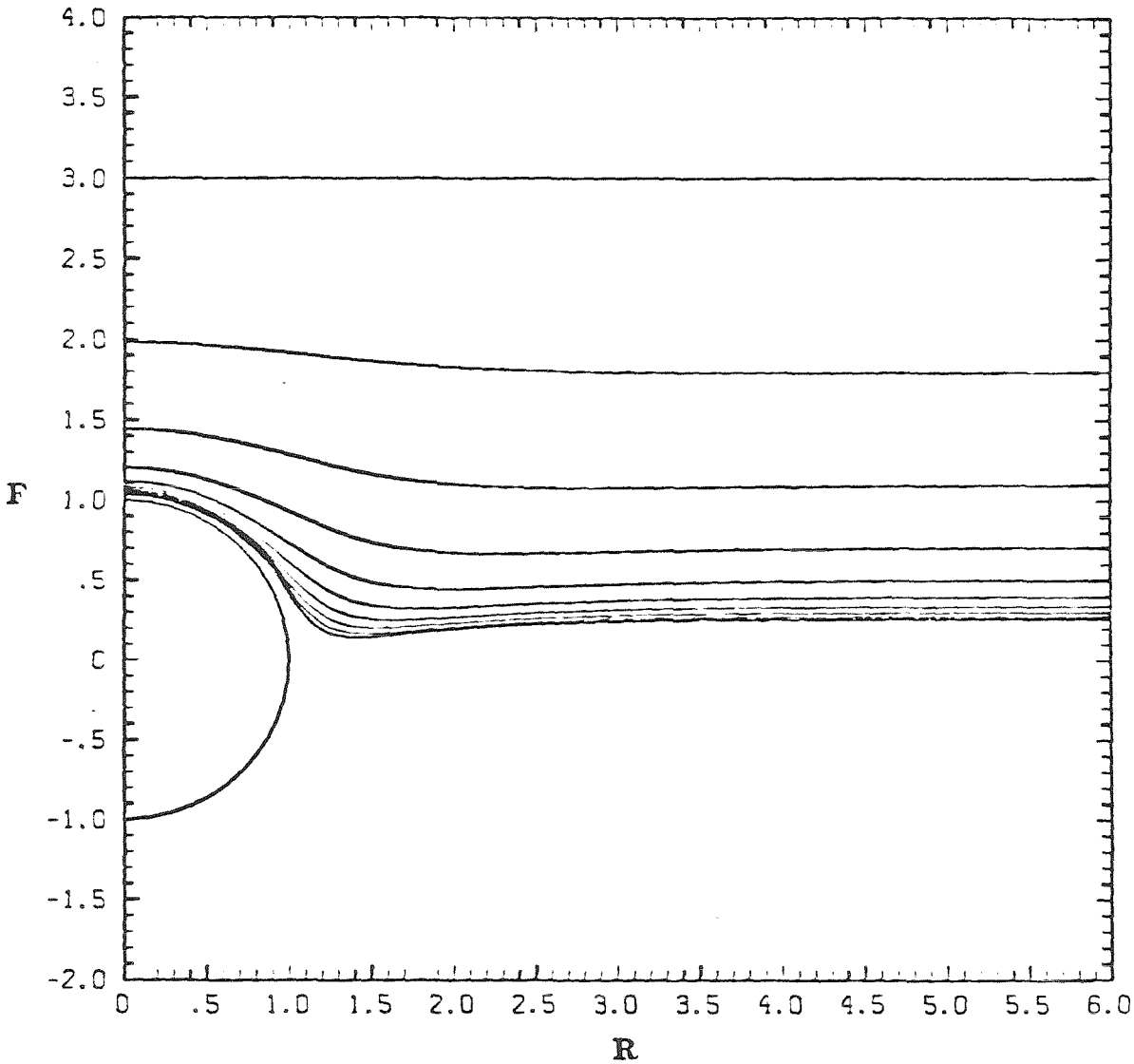

Figure 23. Interface shape as a function of sphere position with $\lambda = 0$, $Ca = 10$, $Cg = 0.1$, $l_o = -3$, $\Delta t_c = 0.25$.

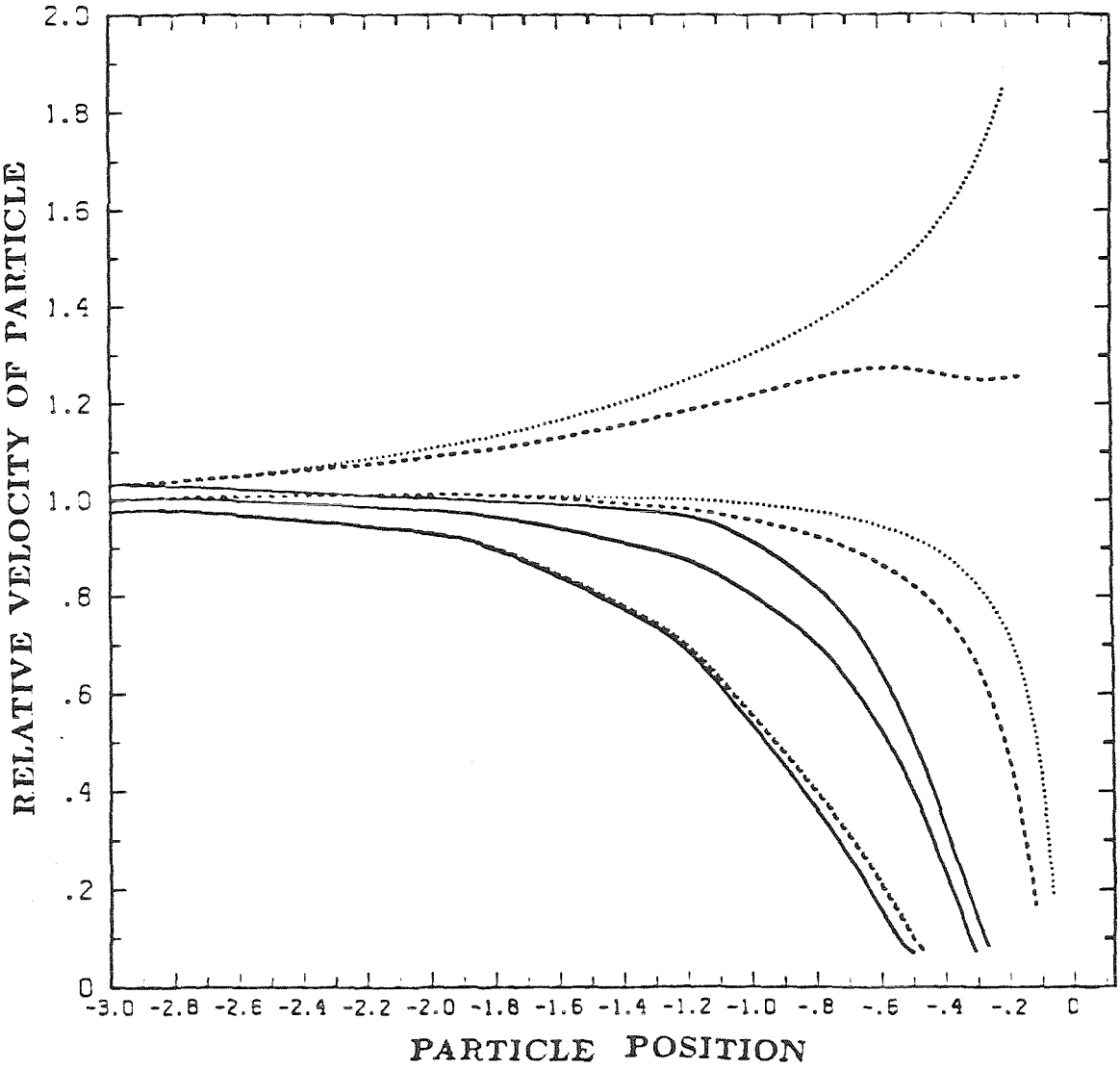

Figure 24. Relative velocity of the particle as a function of particle position, for $\lambda = 0$, 1, and 10, Ca = 1: ———, Cg = 0.1; - - - -, Cg = 1; · · · · ·, Cg = 10.

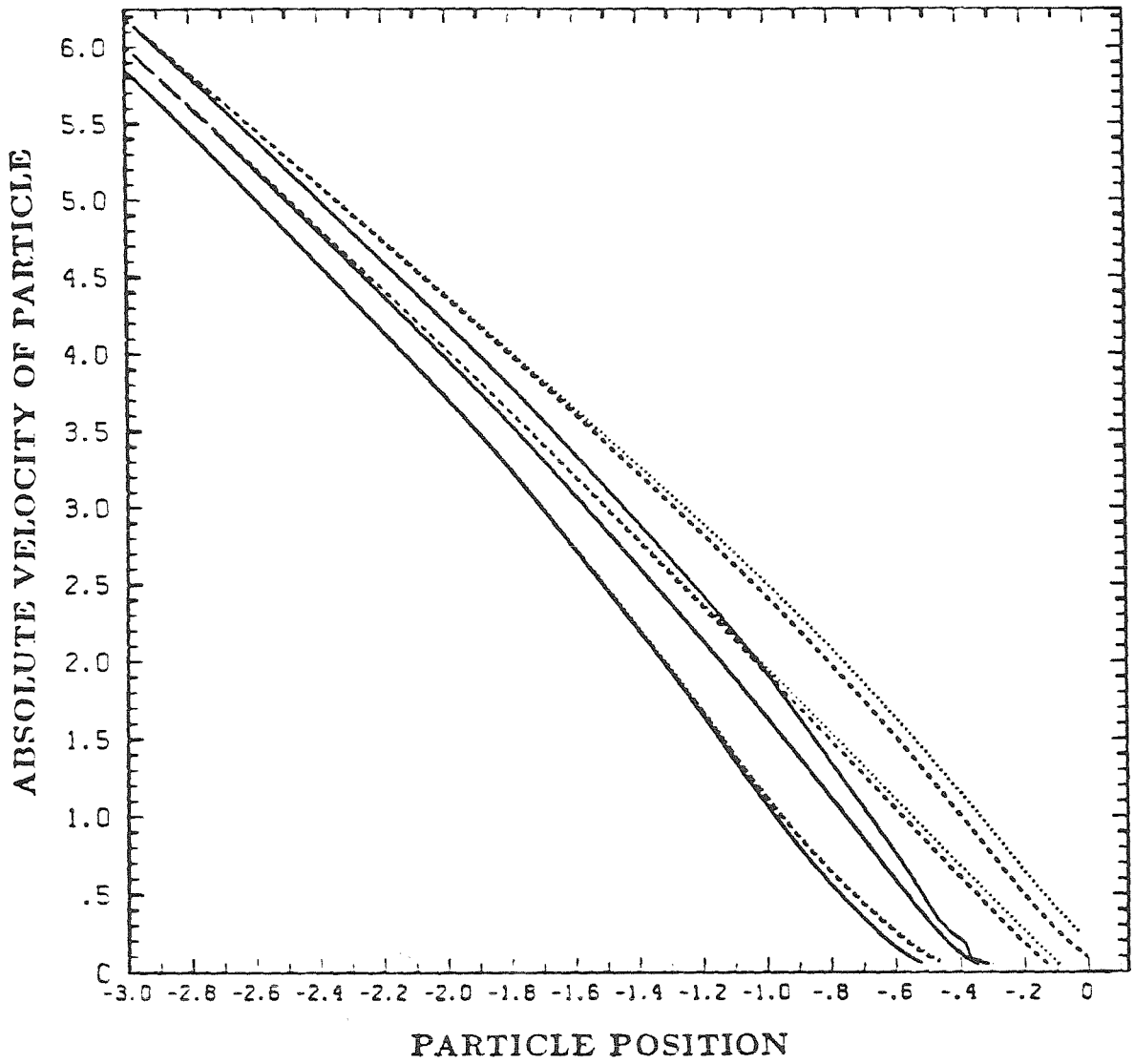

Figure 25. Absolute velocity of the particle as a function of particle position, for $\lambda = 0$, 1, and 10, Cg = 1: ———, Ca = 0.1; - - - -, Ca = 1; ·····, Ca = 10.

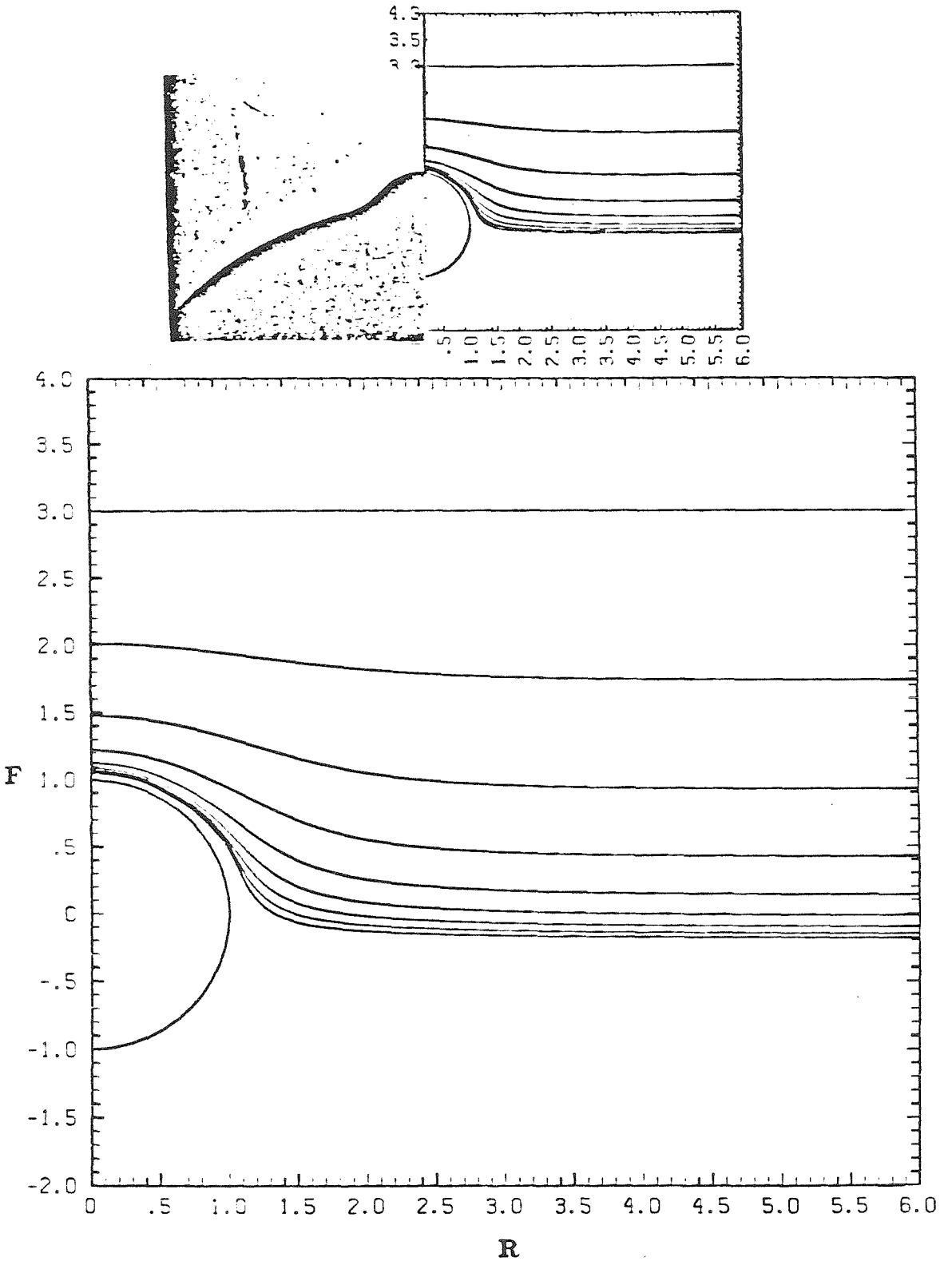

Figure 26. Interface shape as a function of sphere position with $\lambda = 0$, Ca = 22.1, Cg = 24.3, $l_o = -3$, $\Delta t_c = 0.25$. Also shown is the experimental results from Figure 12(c) of Hoffman (1985).

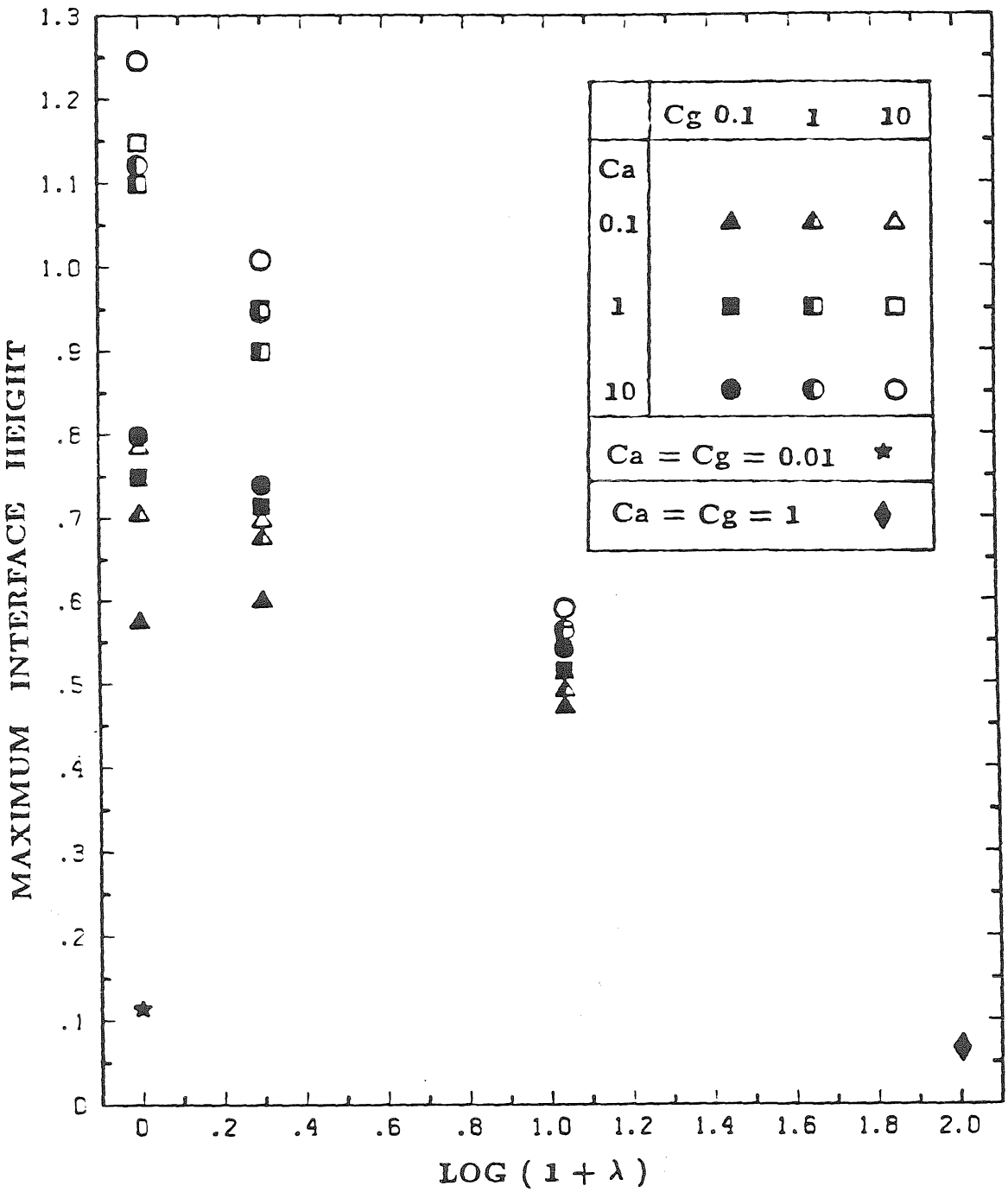

Figure 27. Maximum interface deformation as a function of λ, for all values of Ca and Cg considered.

Appendix

The following appendix contains several figures that have been referred to in the preceding text. These figures were not included in the preceding group because they are qualitatively similar to figures already contained there; however, they are presented here for completeness.

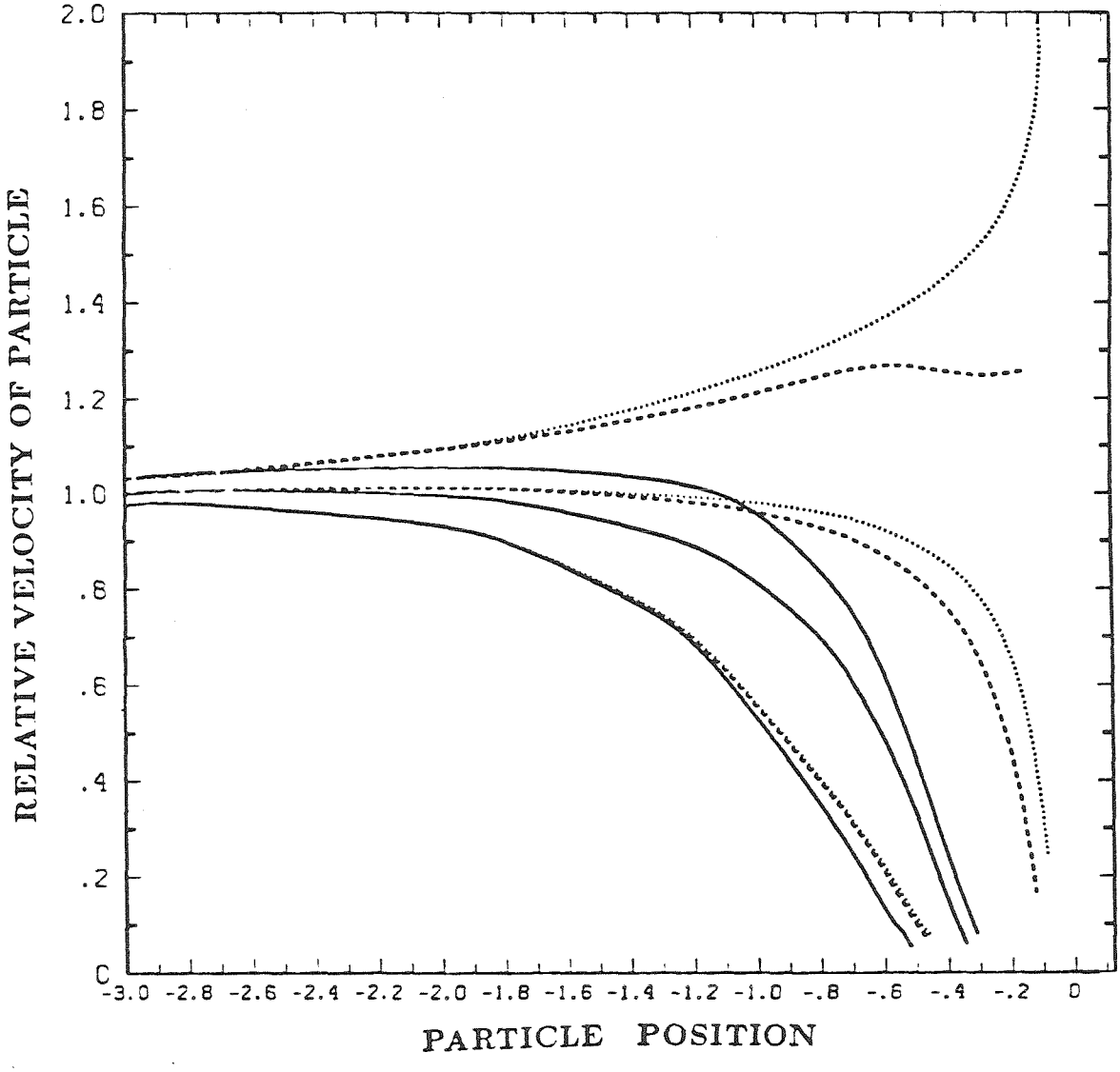

Figure 28. Relative velocity of the particle as a function of particle position, for $\lambda = 0$, 1, and 10, Cg = 1: ———, Ca = 0.1; - - - -, Ca = 1; · · · · ·, Ca = 10.

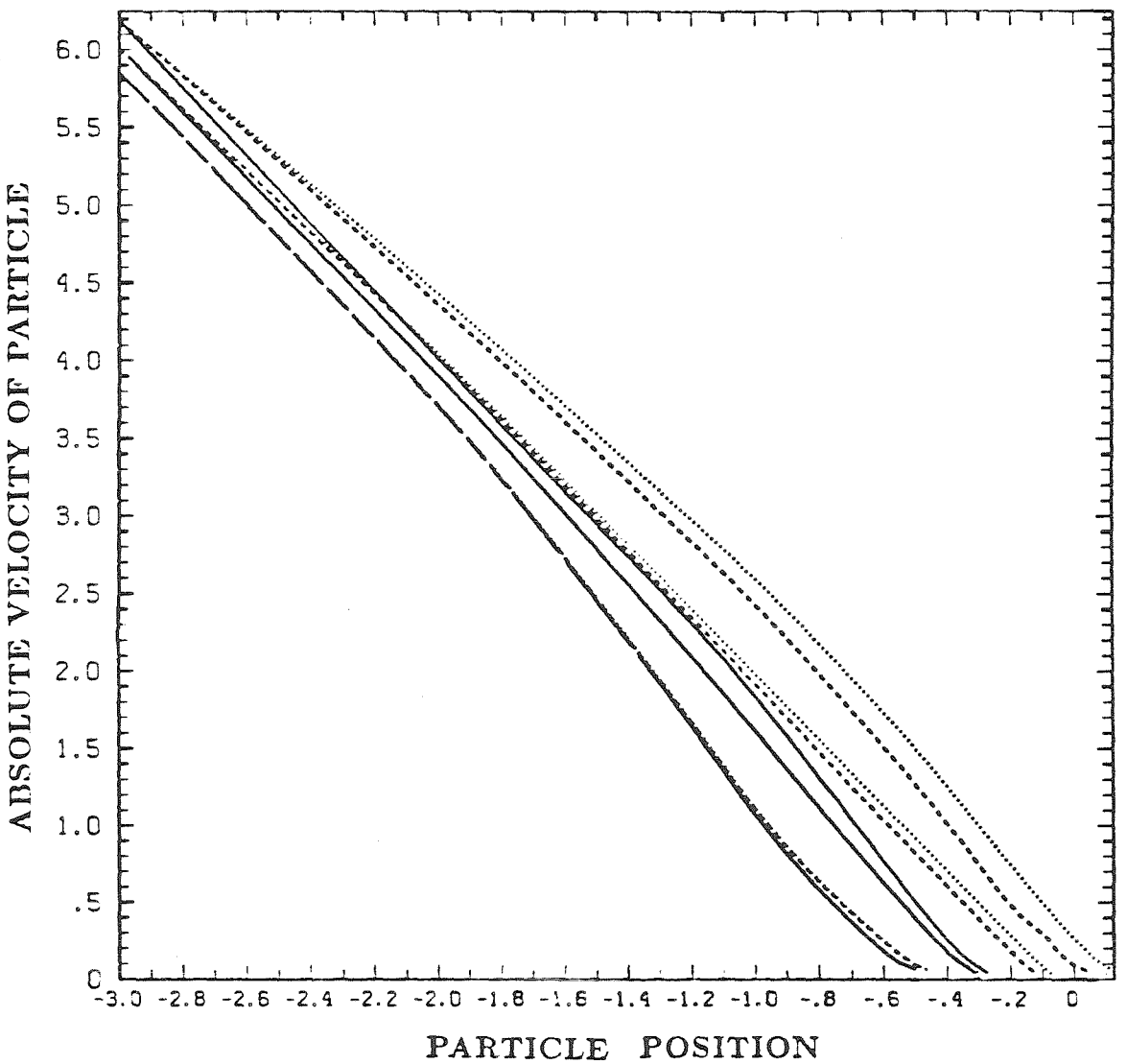

Figure 29. Absolute velocity of the particle as a function of particle position, for $\lambda = 0$, 1, and 10, Ca = 1: ———, Cg = 0.1; - - - -, Cg = 1; · · · · ·, Cg = 10.

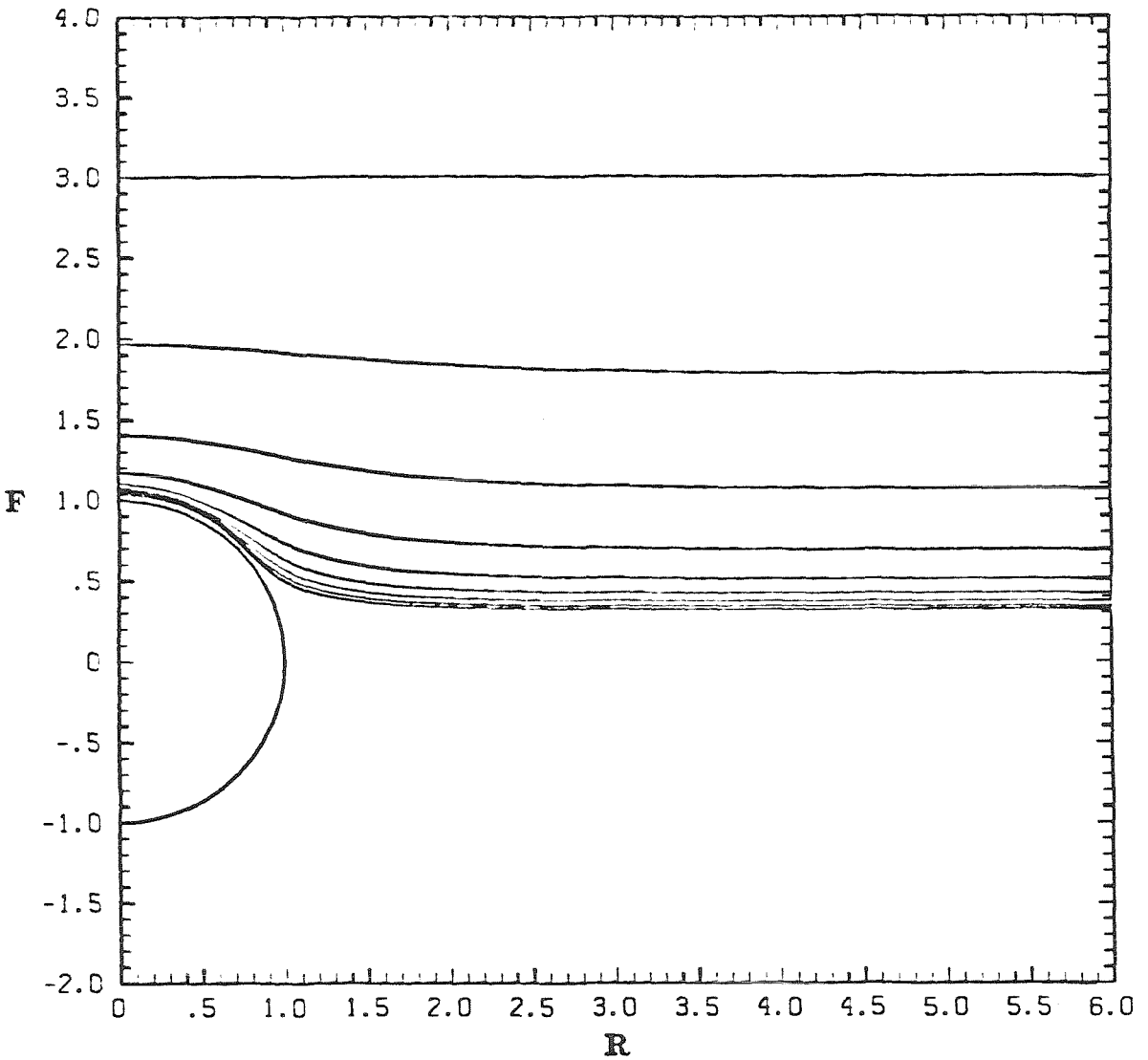

Figure 30. Interface shape as a function of sphere position with $\lambda = 0$, $Ca = 0.1$, $Cg = 1$, $l_o = -3$, $\Delta t_c = 0.25$.

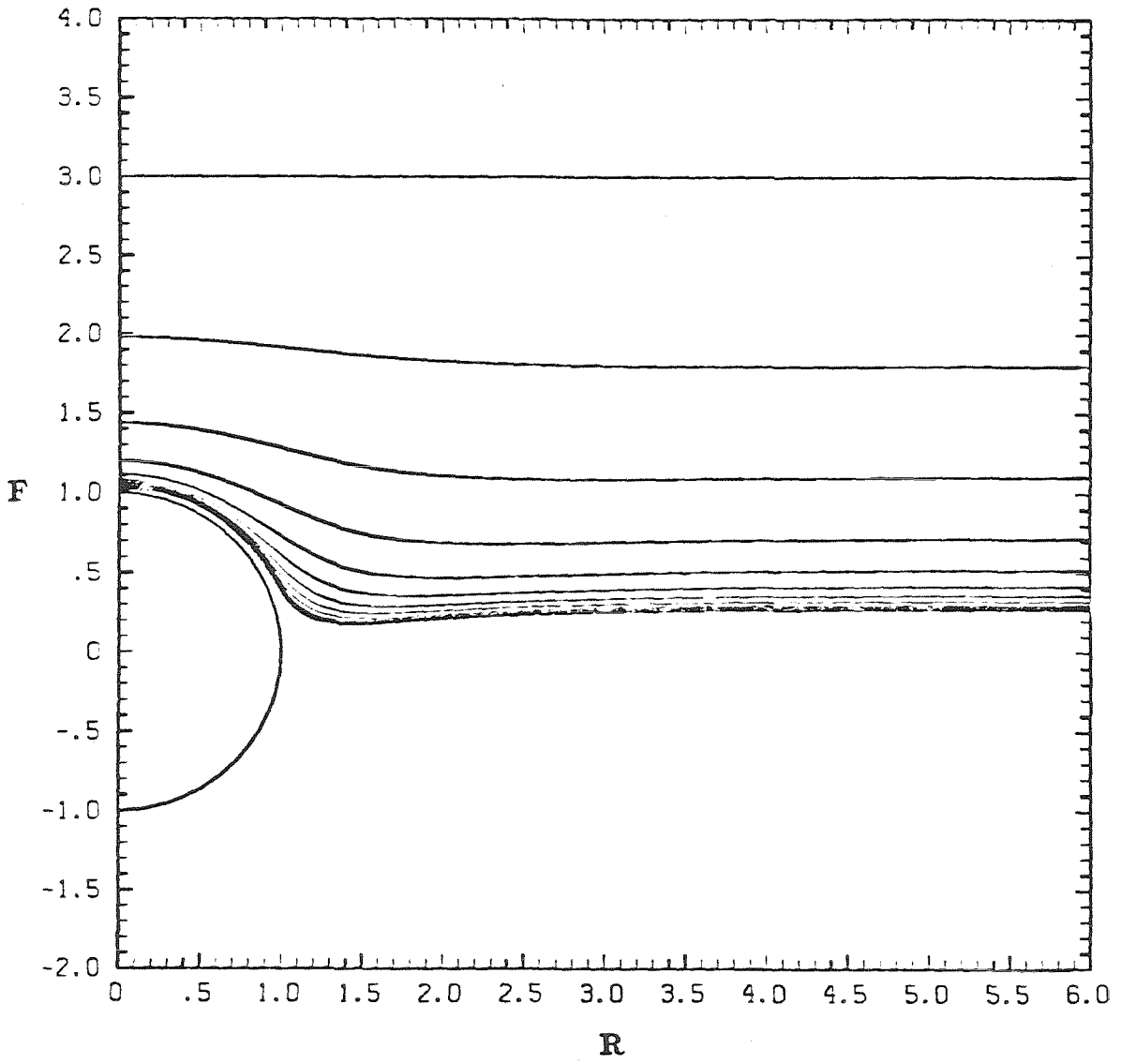

Figure 31. Interface shape as a function of sphere position with $\lambda = 0$, $Ca = 1$, $Cg = 0.1$, $l_o = -3$, $\Delta t_c = 0.25$.

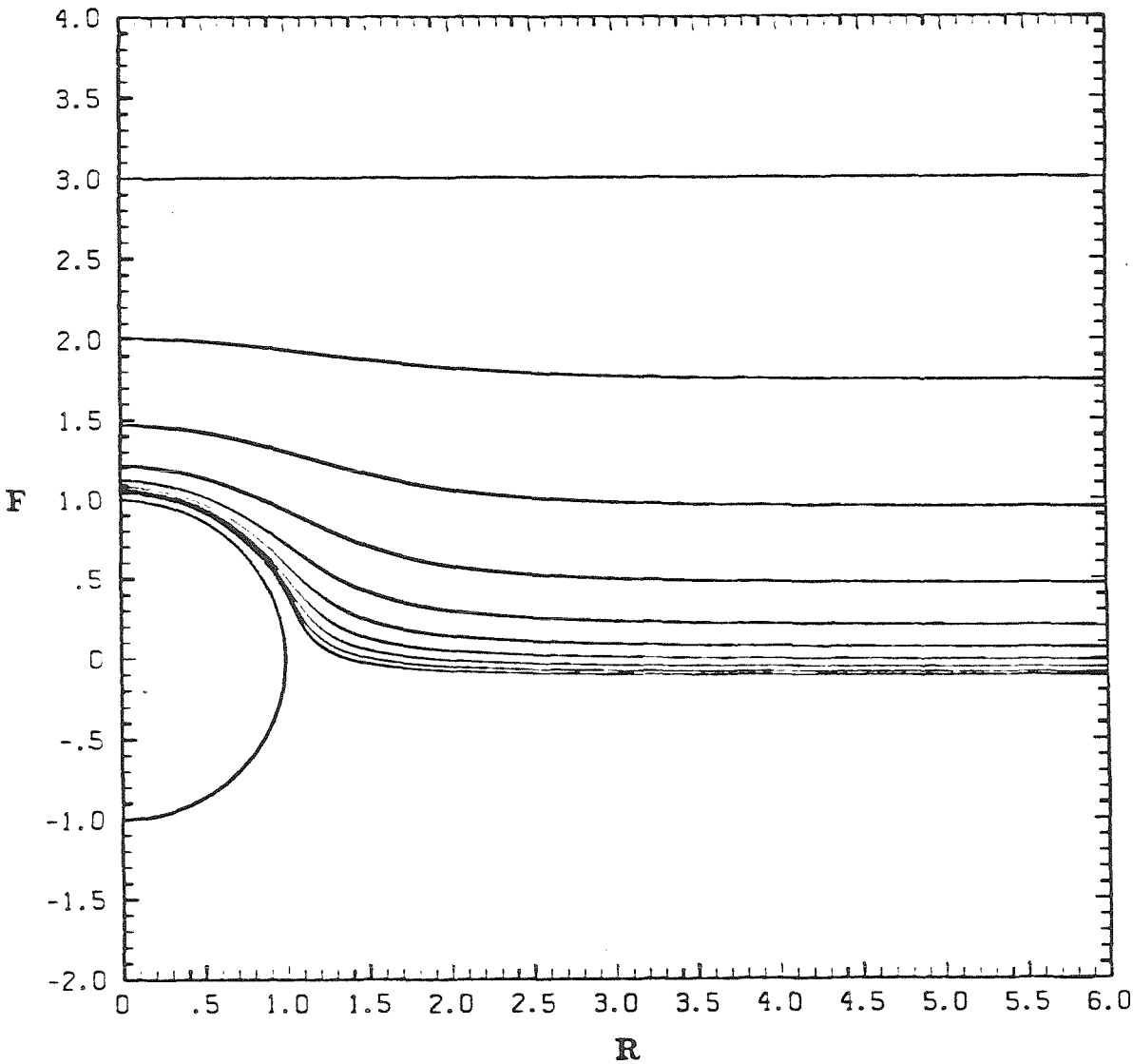

Figure 32. Interface shape as a function of sphere position with $\lambda = 0$, $Ca = 1$, $Cg = 10$, $l_o = -3$, $\Delta t_c = 0.25$.

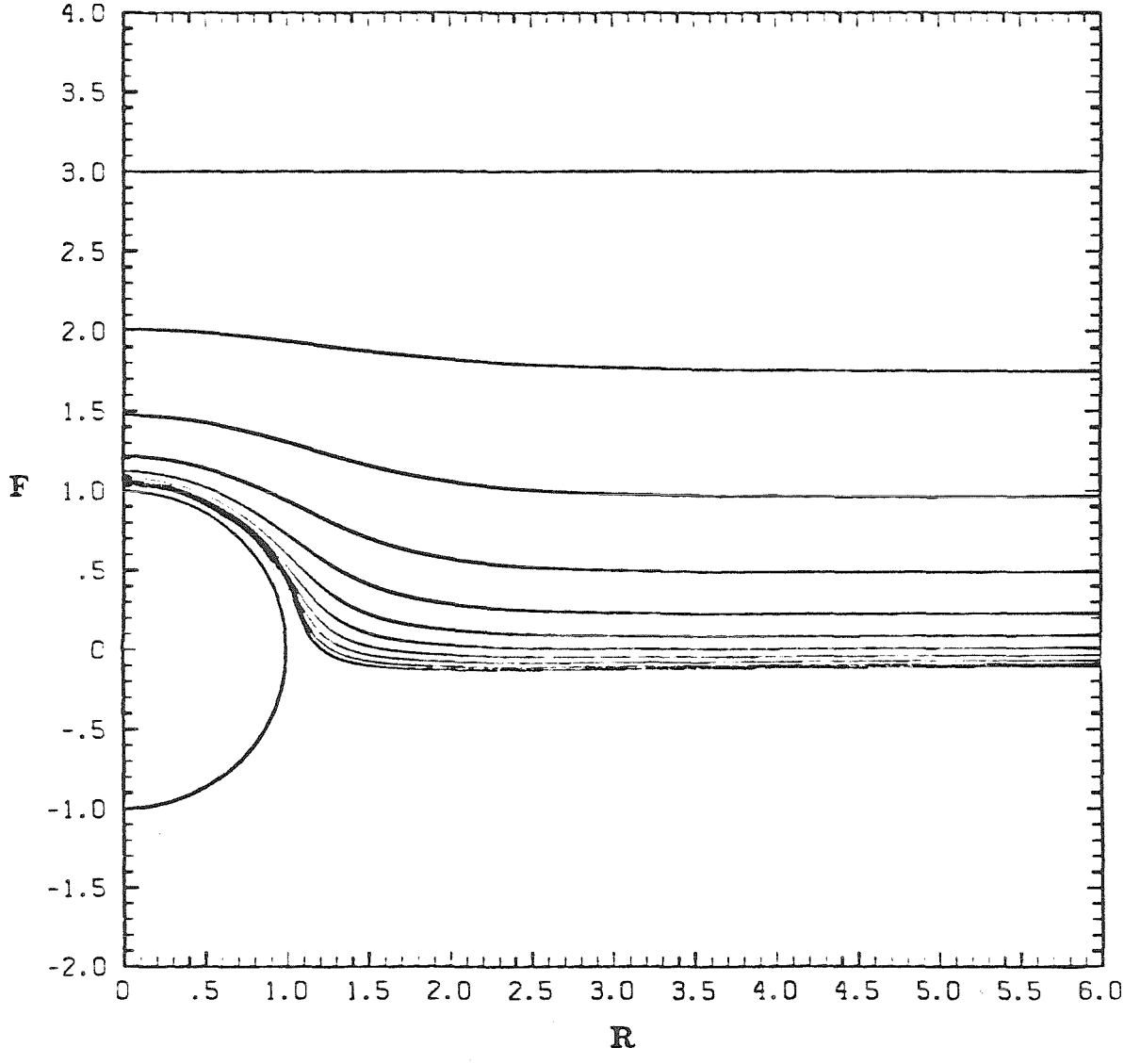

Figure 33. Interface shape as a function of sphere position with $\lambda = 0$, $Ca = 10$, $Cg = 1$, $l_o = -3$, $\Delta t_c = 0.25$.

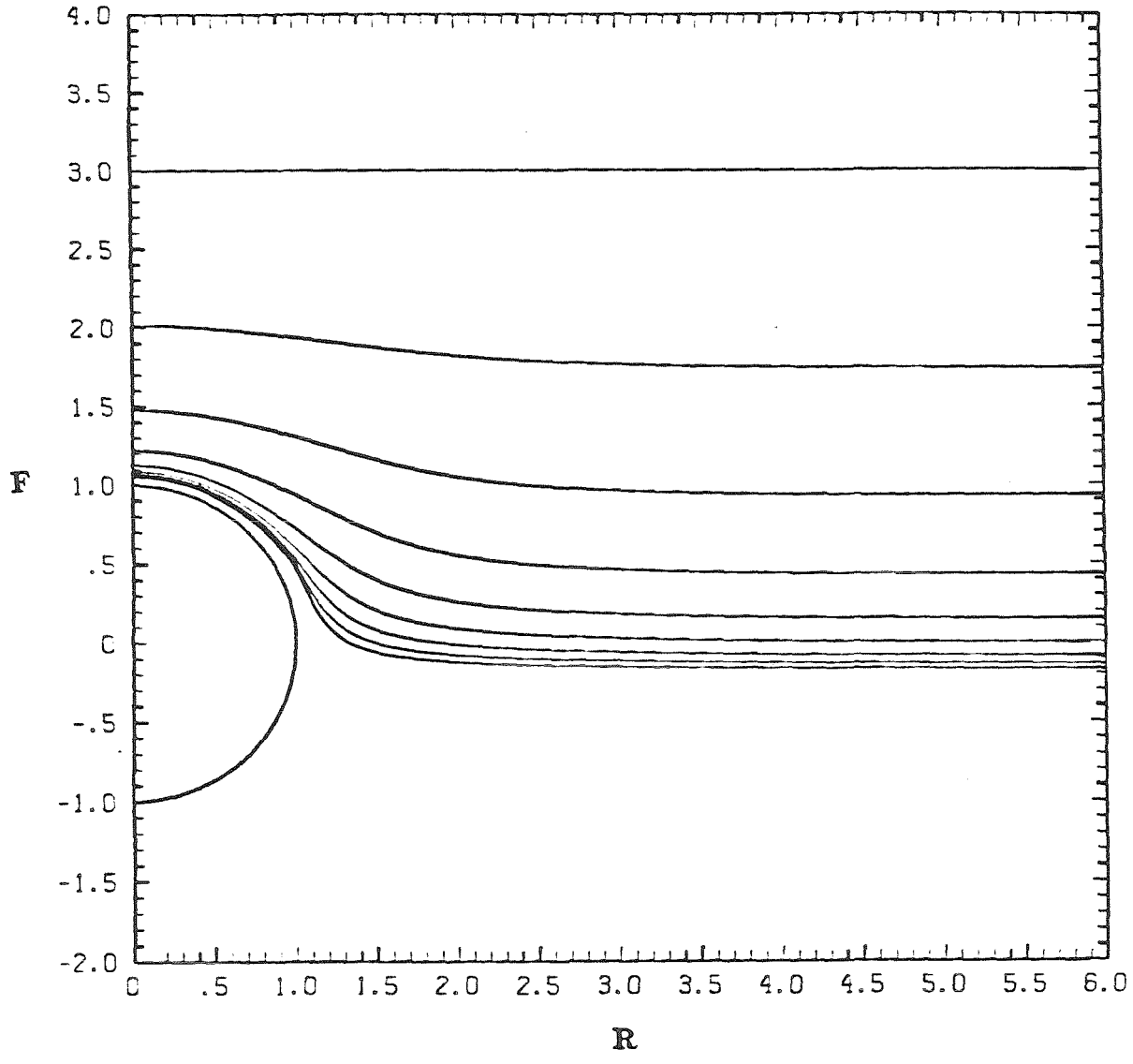

Figure 34. Interface shape as a function of sphere position with $\lambda = 0$, $Ca = 10$, $Cg = 10$, $l_o = -3$, $\Delta t_c = 0.25$.

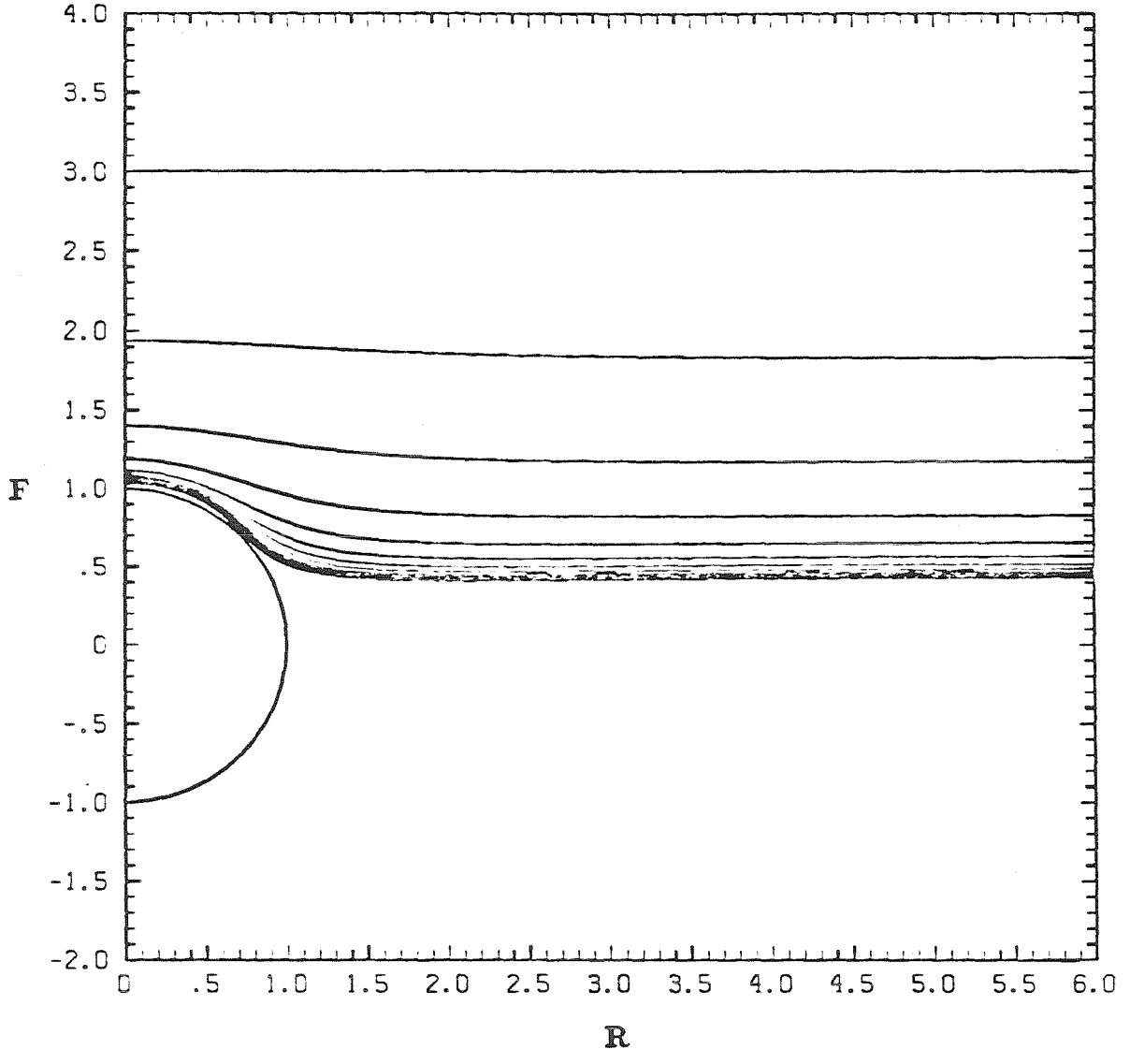

Figure 35. Interface shape as a function of sphere position with $\lambda = 1$, $Ca = Cg = 0.1$, $l_o = -3$, $\Delta t_c = 0.25$.

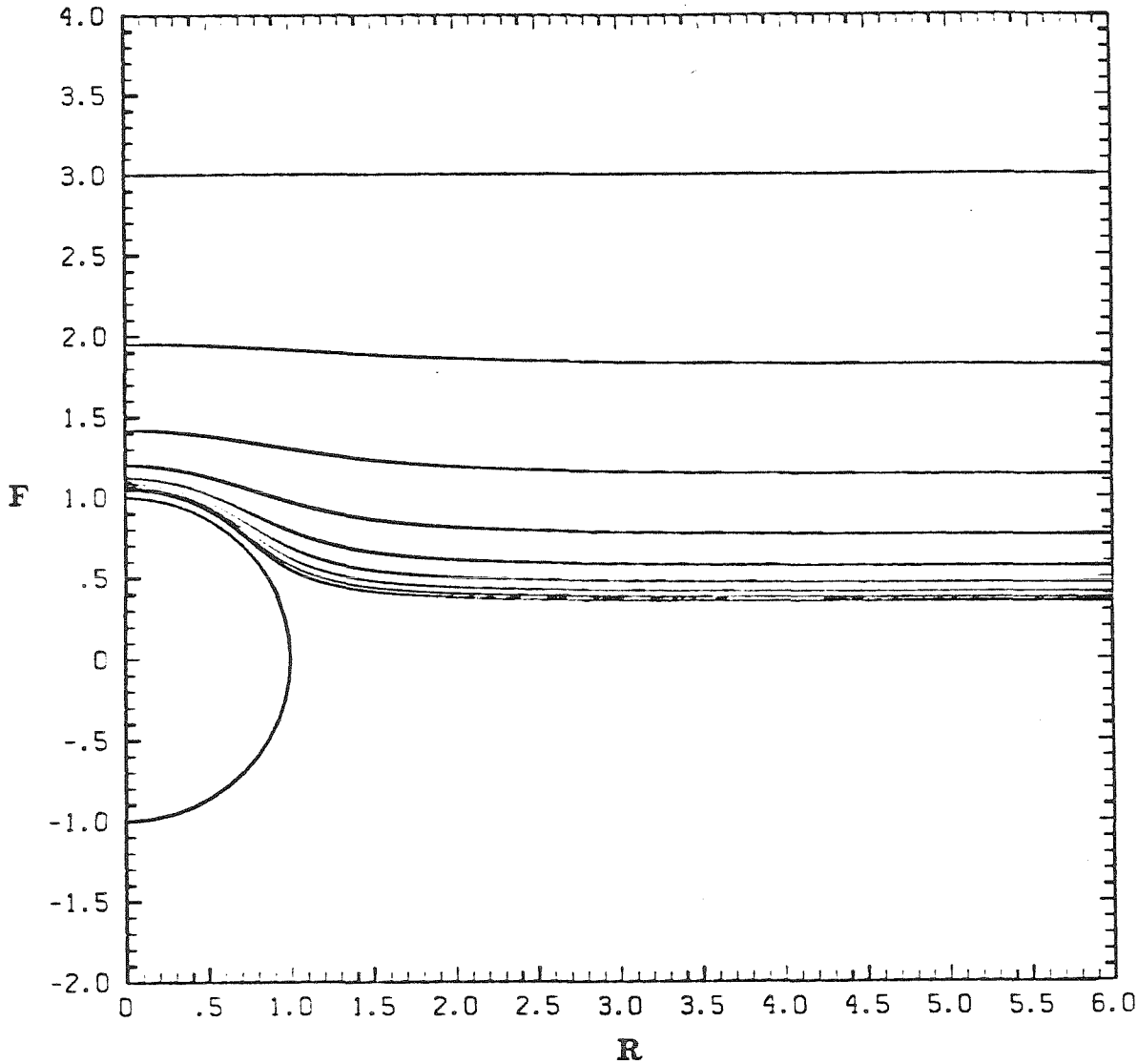

Figure 36. Interface shape as a function of sphere position with $\lambda = 1$, $Ca = 0.1$, $Cg = 10$, $l_o = -3$, $\Delta t_c = 0.25$.

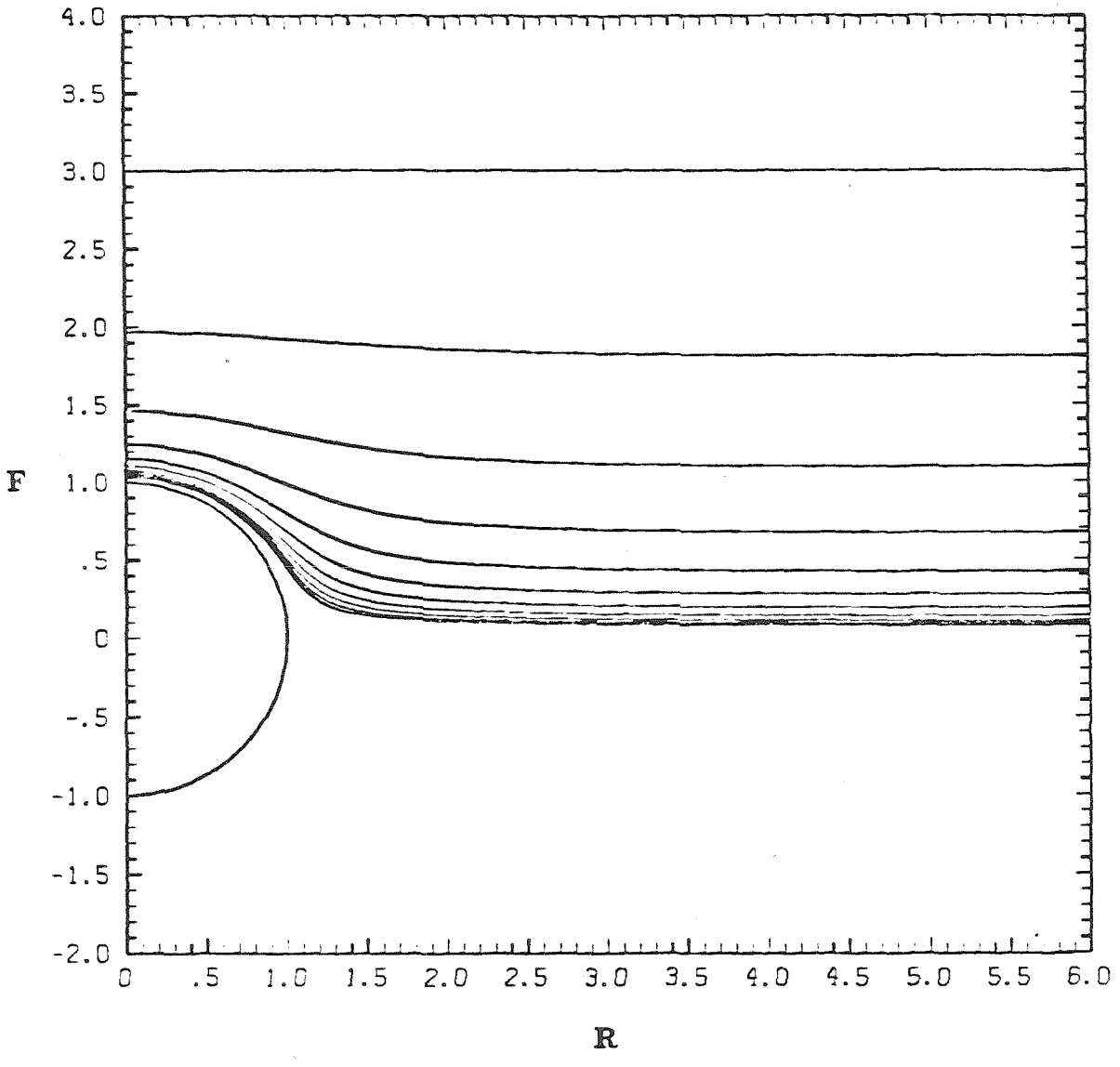

Figure 37. Interface shape as a function of sphere position with $\lambda = 1$, $Ca = 1$, $Cg = 10$, $l_o = -3$, $\Delta t_c = 0.25$.

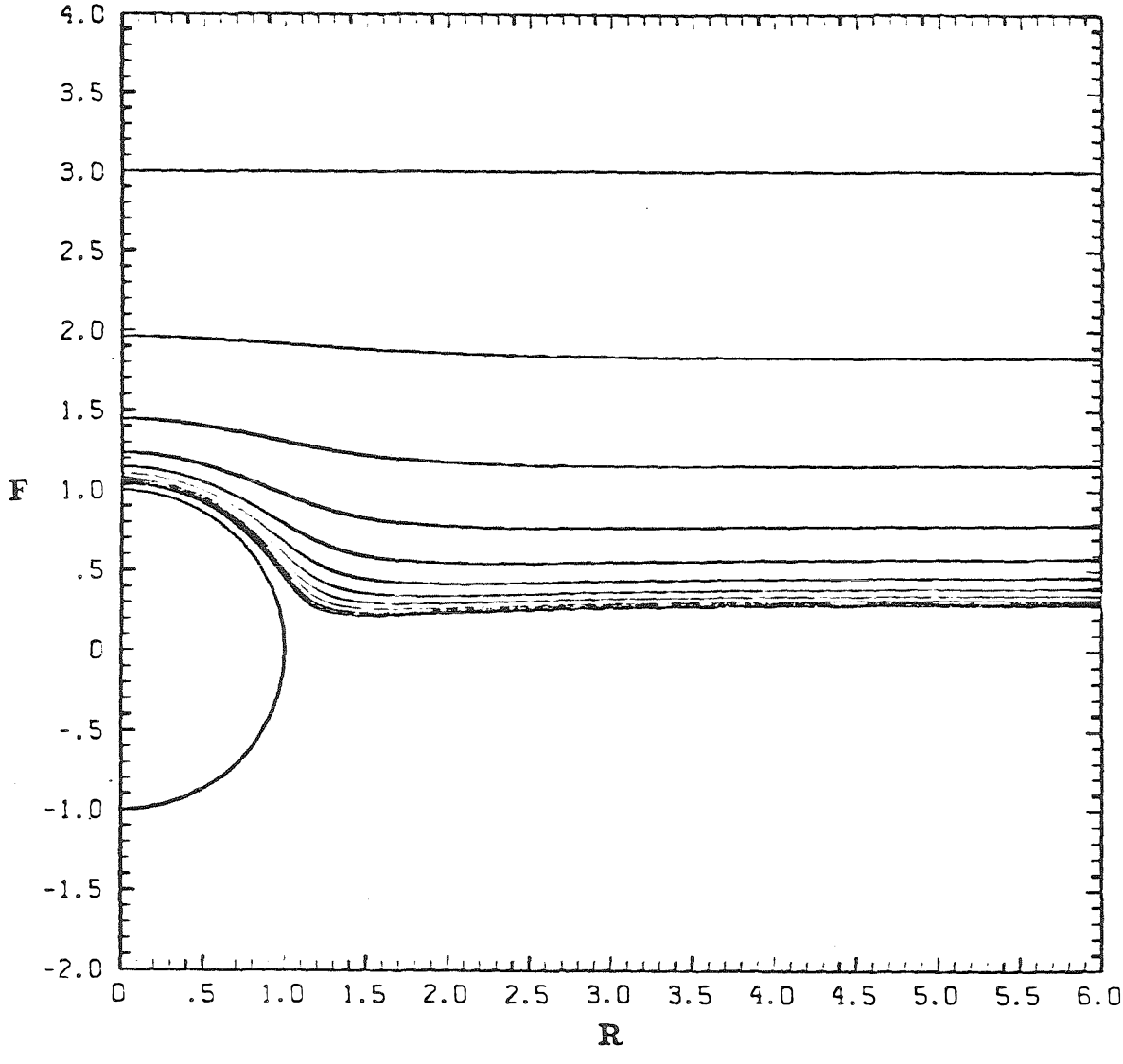

Figure 38. Interface shape as a function of sphere position with $\lambda = 1$, $Ca = 10$, $Cg = 0.1$, $l_o = -3$, $\Delta t_c = 0.25$.

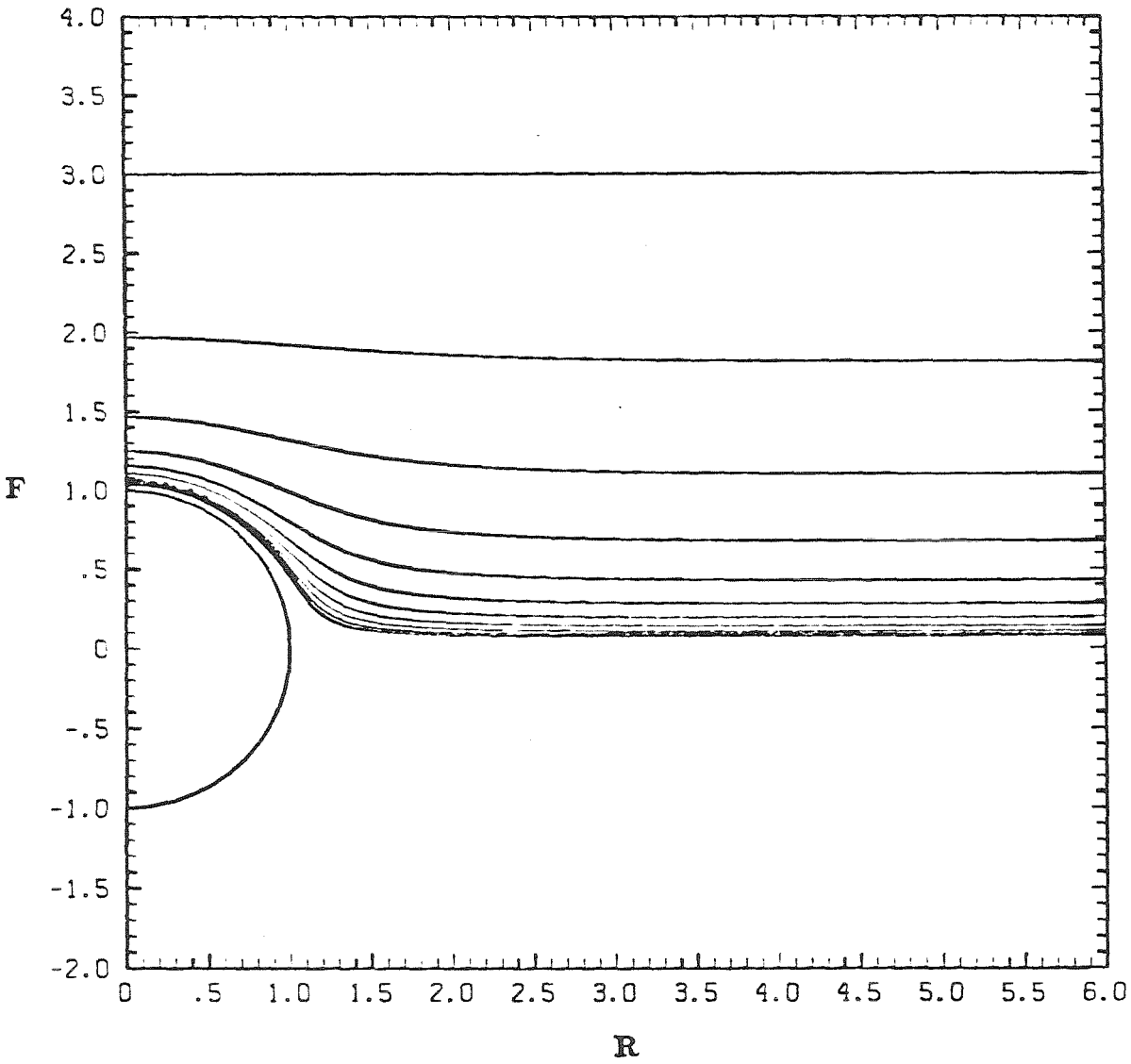

Figure 39. Interface shape as a function of sphere position with $\lambda = 1$, $Ca = 10$, $Cg = 1$, $l_o = -3$, $\Delta t_c = 0.25$.

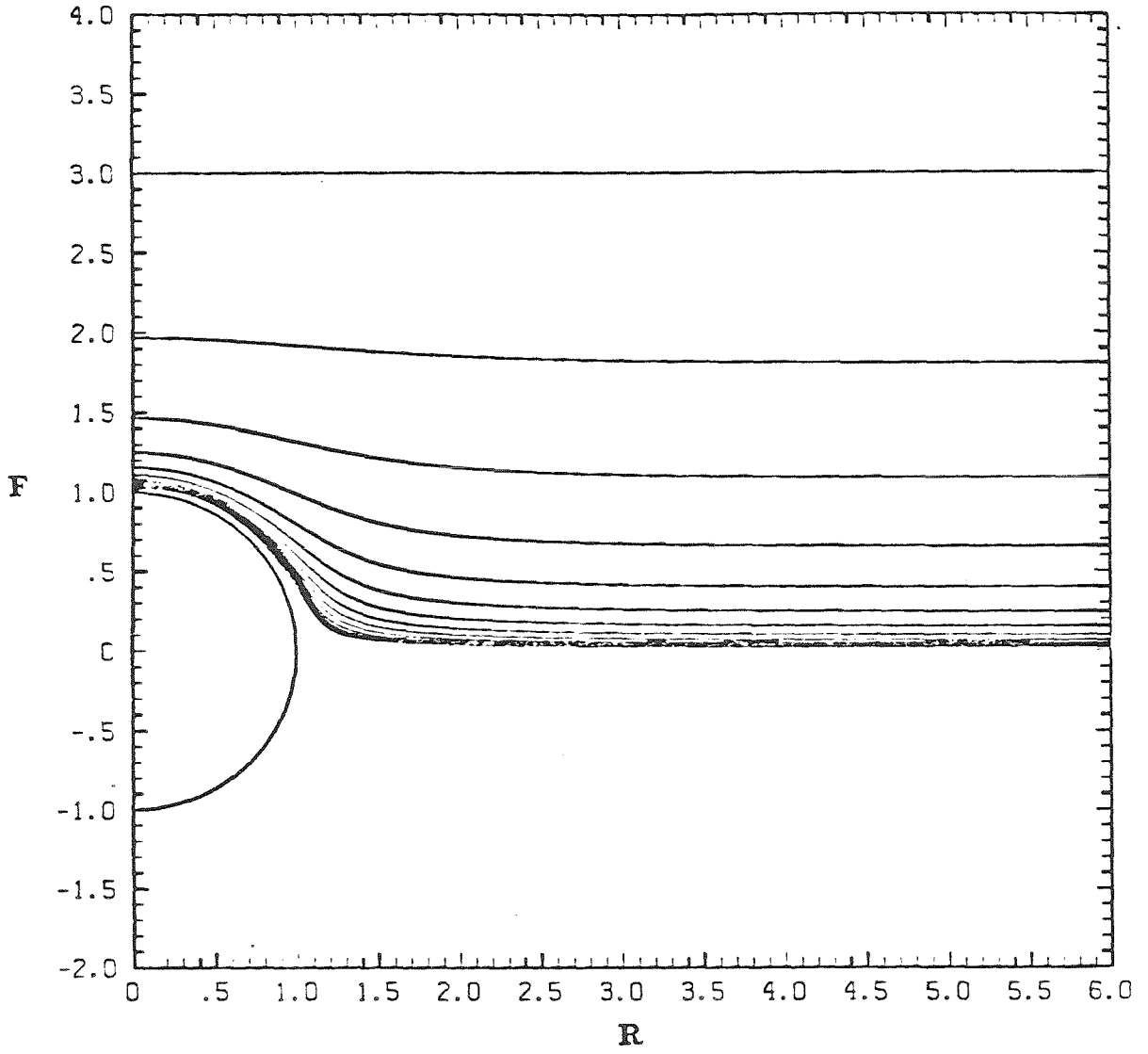

Figure 40. Interface shape as a function of sphere position with $\lambda = 1$, $Ca = 10$, $Cg = 10$, $l_o = -3$, $\Delta t_c = 0.25$.

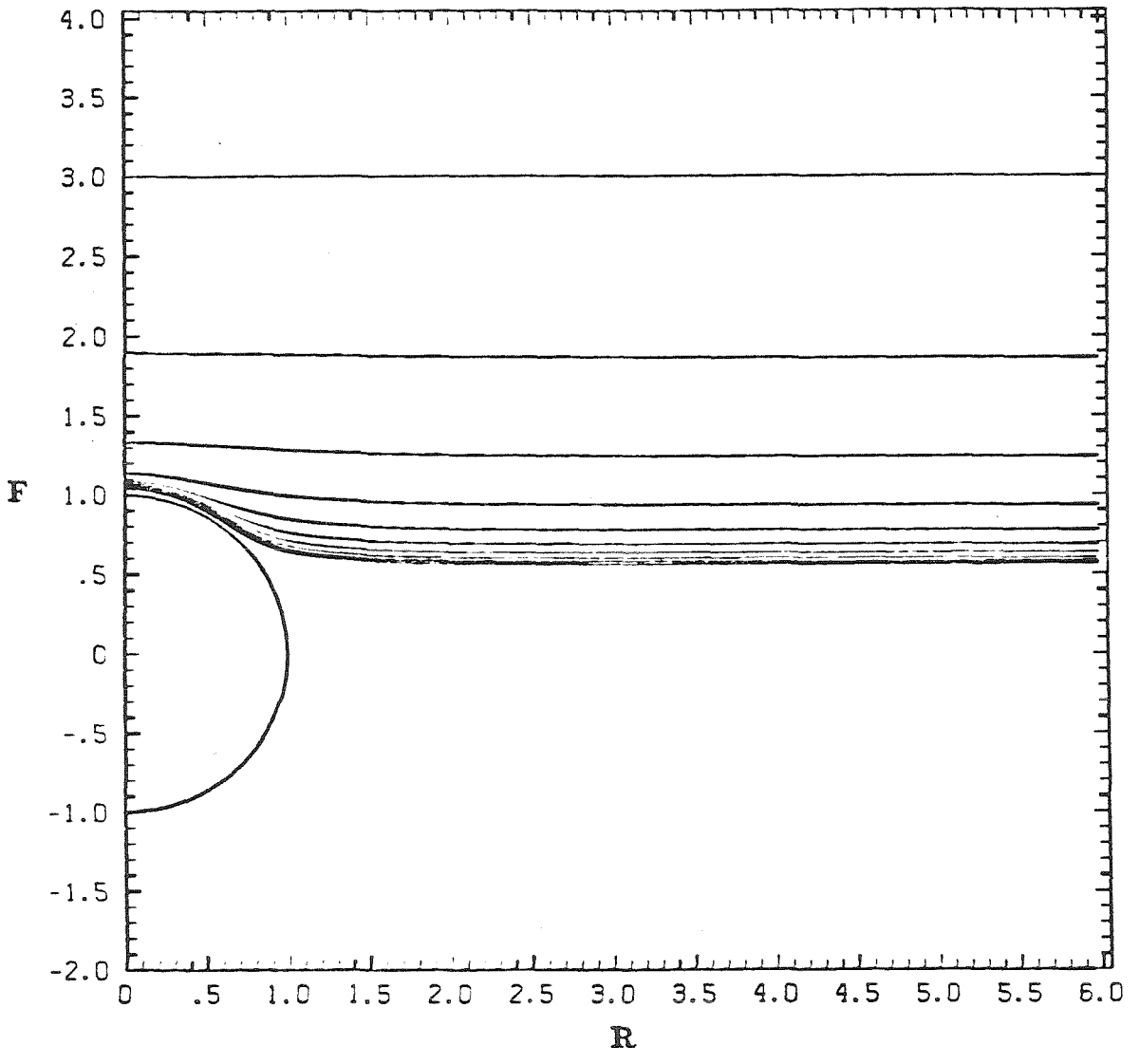

Figure 41. Interface shape as a function of sphere position with $\lambda = 10$, $Ca = Cg = 0.1$, $l_o = -3$, $\Delta t_c = 0.25$.

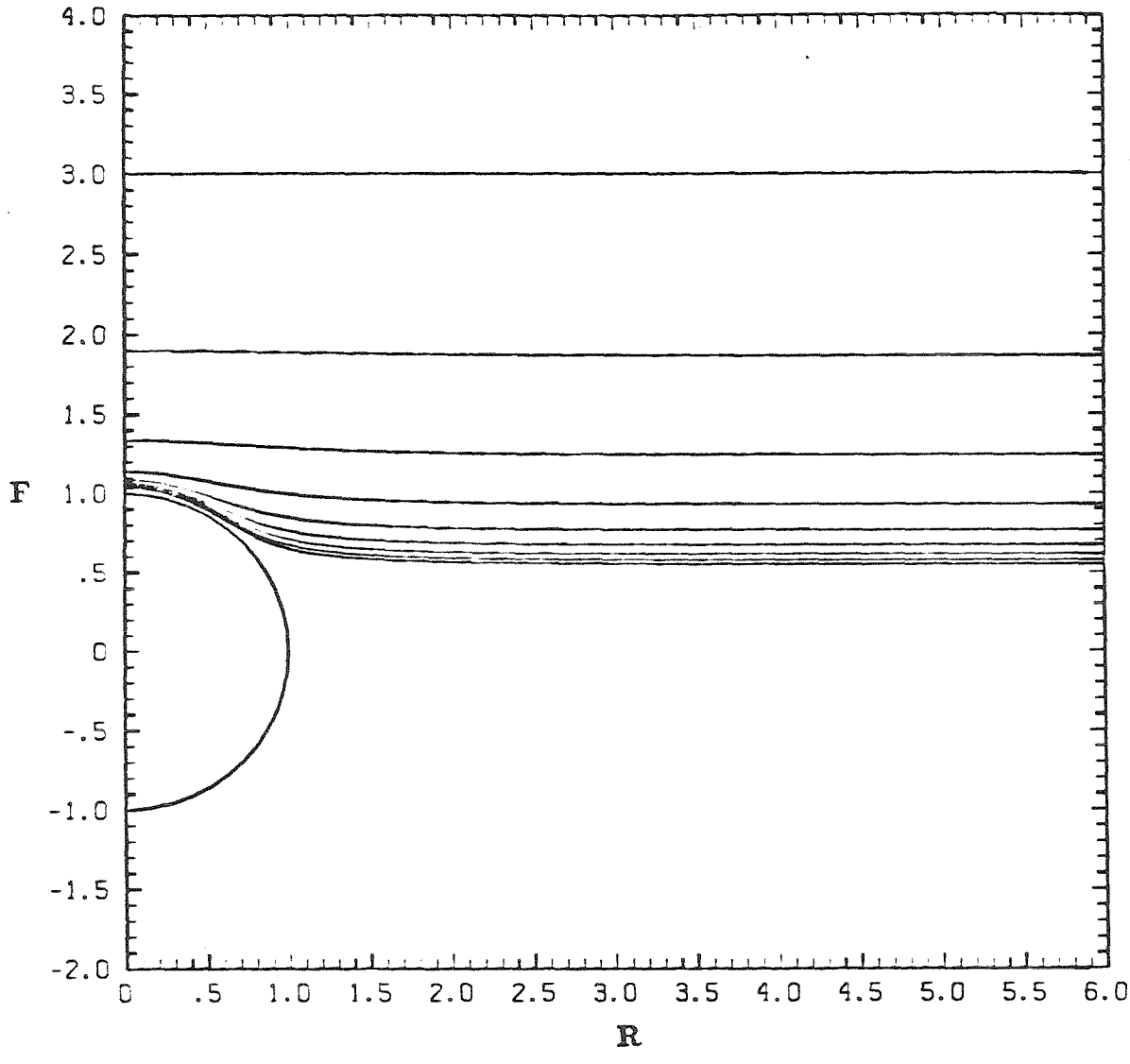

Figure 42. Interface shape as a function of sphere position with $\lambda = 10$, $Ca = 0.1$, $Cg = 1$, $l_o = -3$, $\Delta t_c = 0.25$.

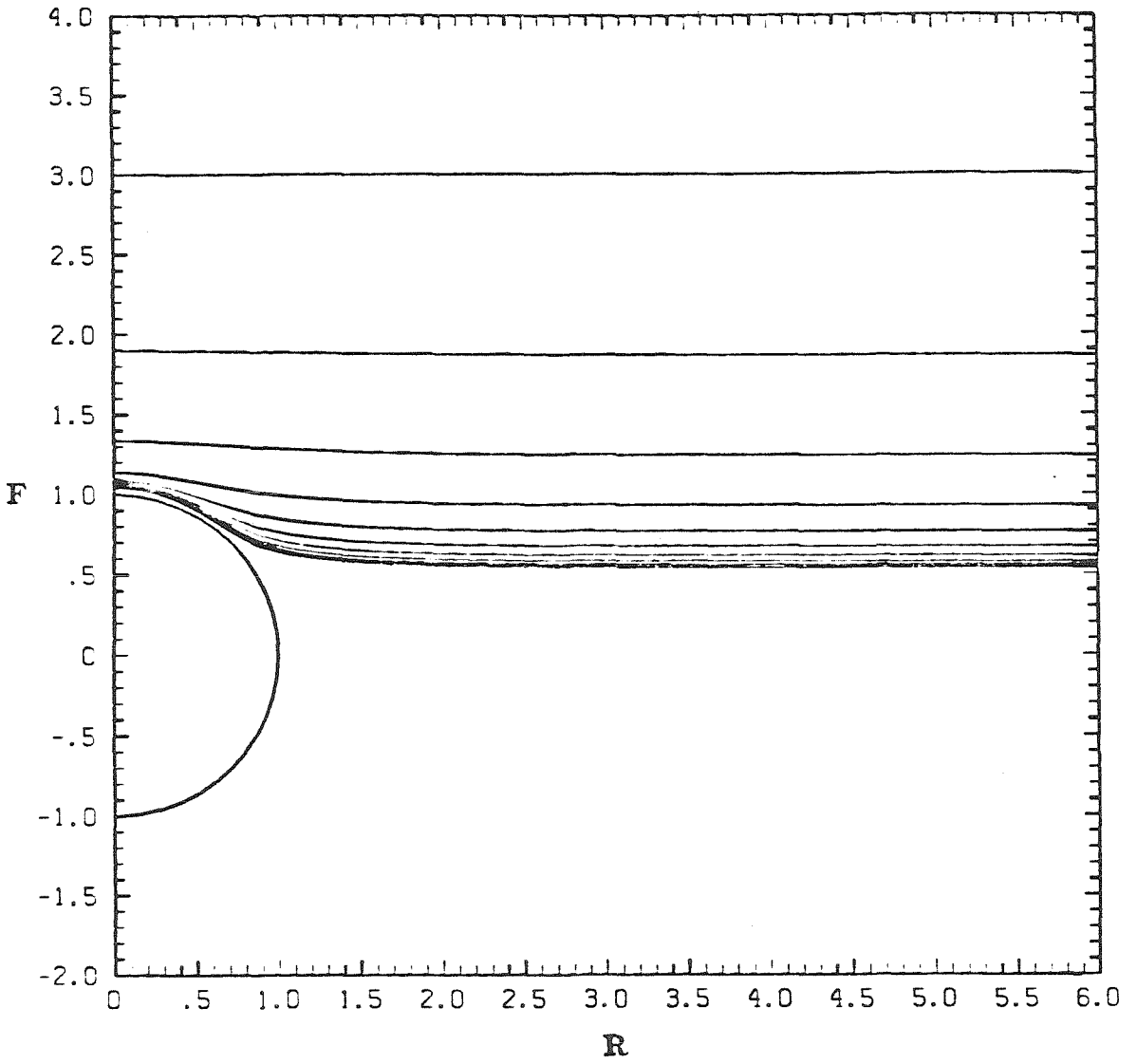

Figure 43. Interface shape as a function of sphere position with $\lambda = 10$, $Ca = 0.1$, $Cg = 10$, $l_o = -3$, $\Delta t_c = 0.25$.

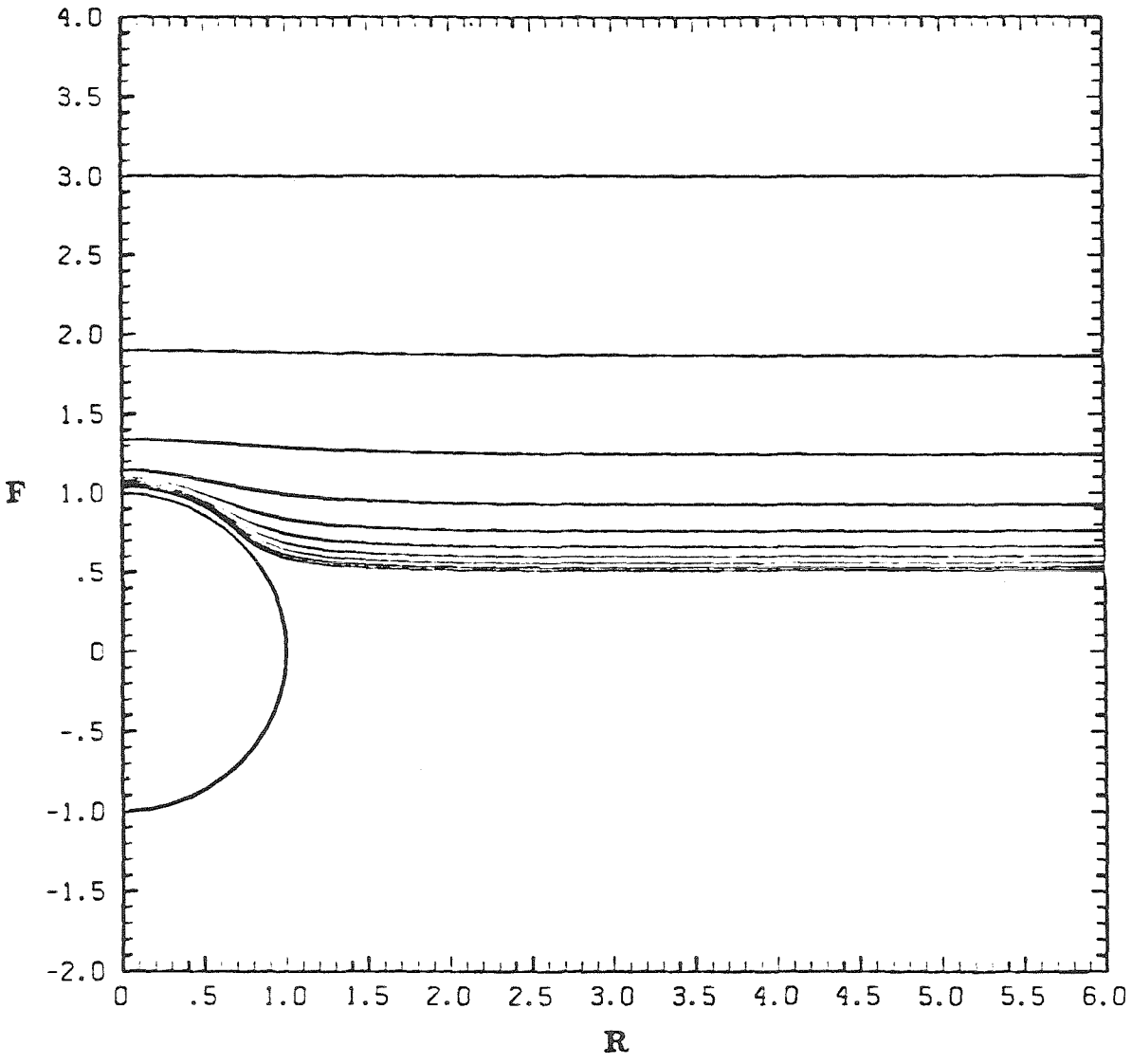

Figure 44. Interface shape as a function of sphere position with $\lambda = 10$, $Ca = 1$, $Cg = 0.1$, $l_o = -3$, $\Delta t_c = 0.25$.

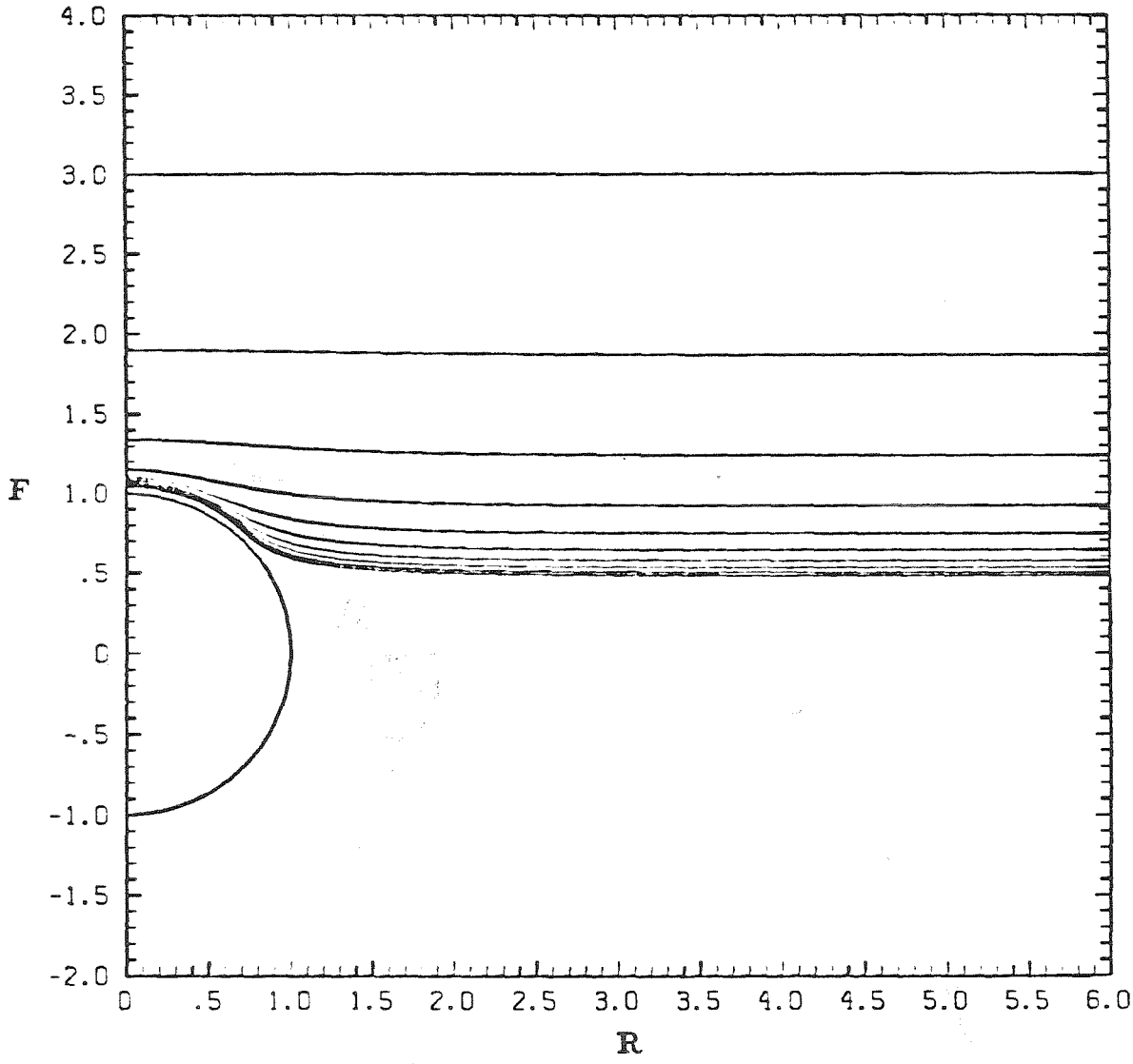

Figure 45. Interface shape as a function of sphere position with $\lambda = 10$, $Ca = 1$, $Cg = 10$, $l_o = -3$, $\Delta t_c = 0.25$.

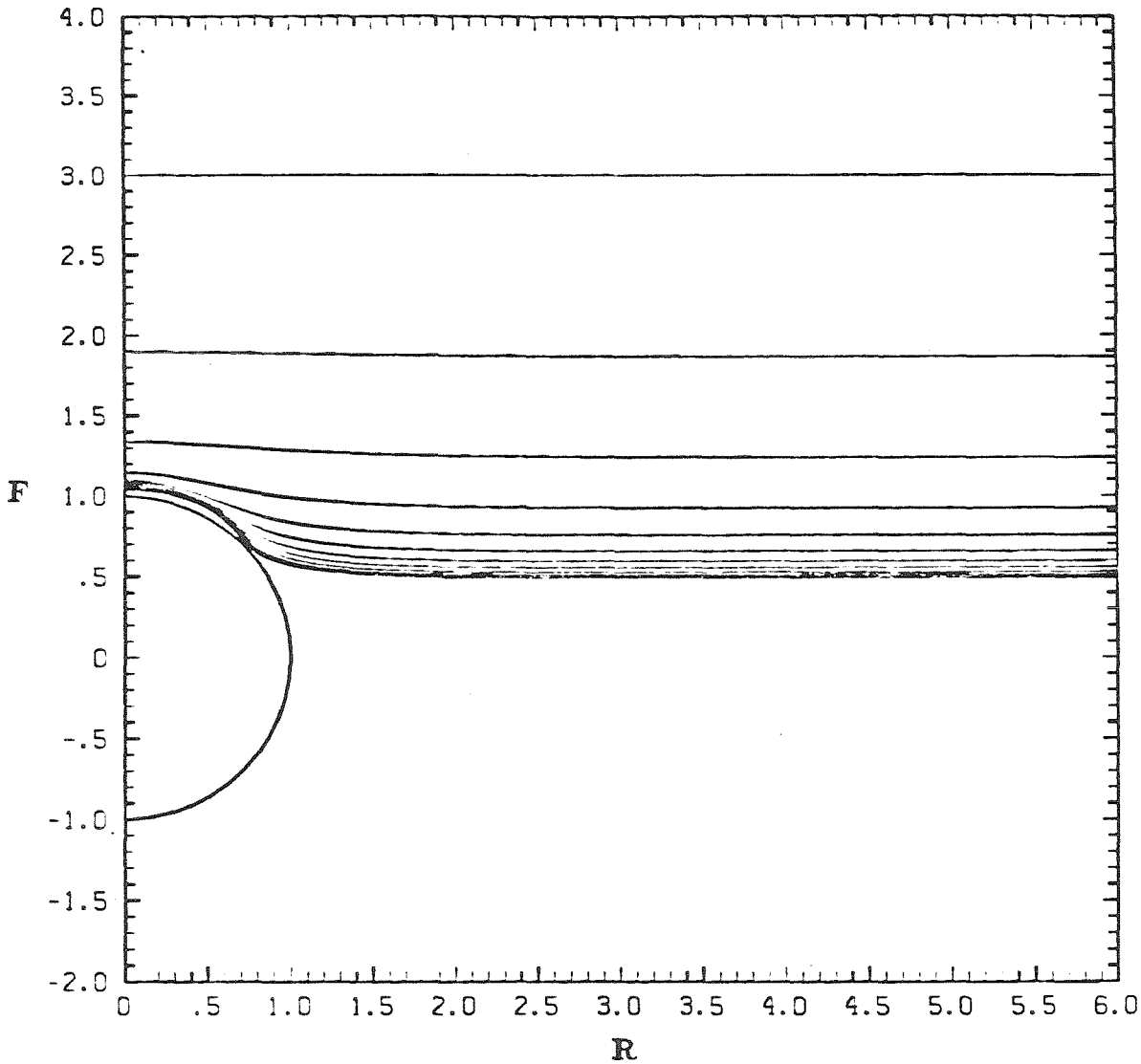

Figure 46. Interface shape as a function of sphere position with $\lambda = 10$, $Ca = 10$, $Cg = 0.1$, $l_o = -3$, $\Delta t_c = 0.25$.

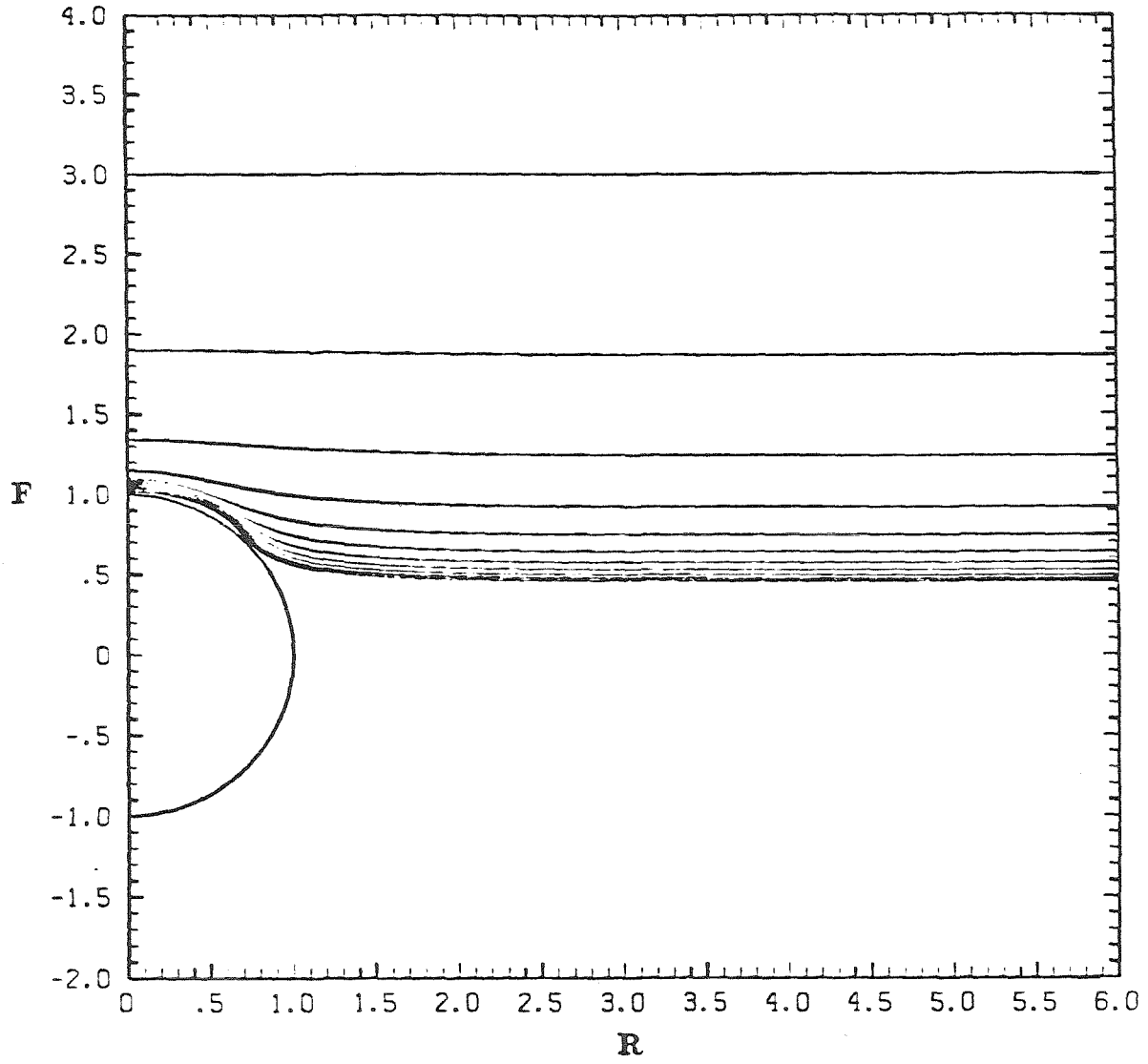

Figure 47. Interface shape as a function of sphere position with $\lambda = 10$, $Ca = 10$, $Cg = 1$, $l_o = -3$, $\Delta t_c = 0.25$.

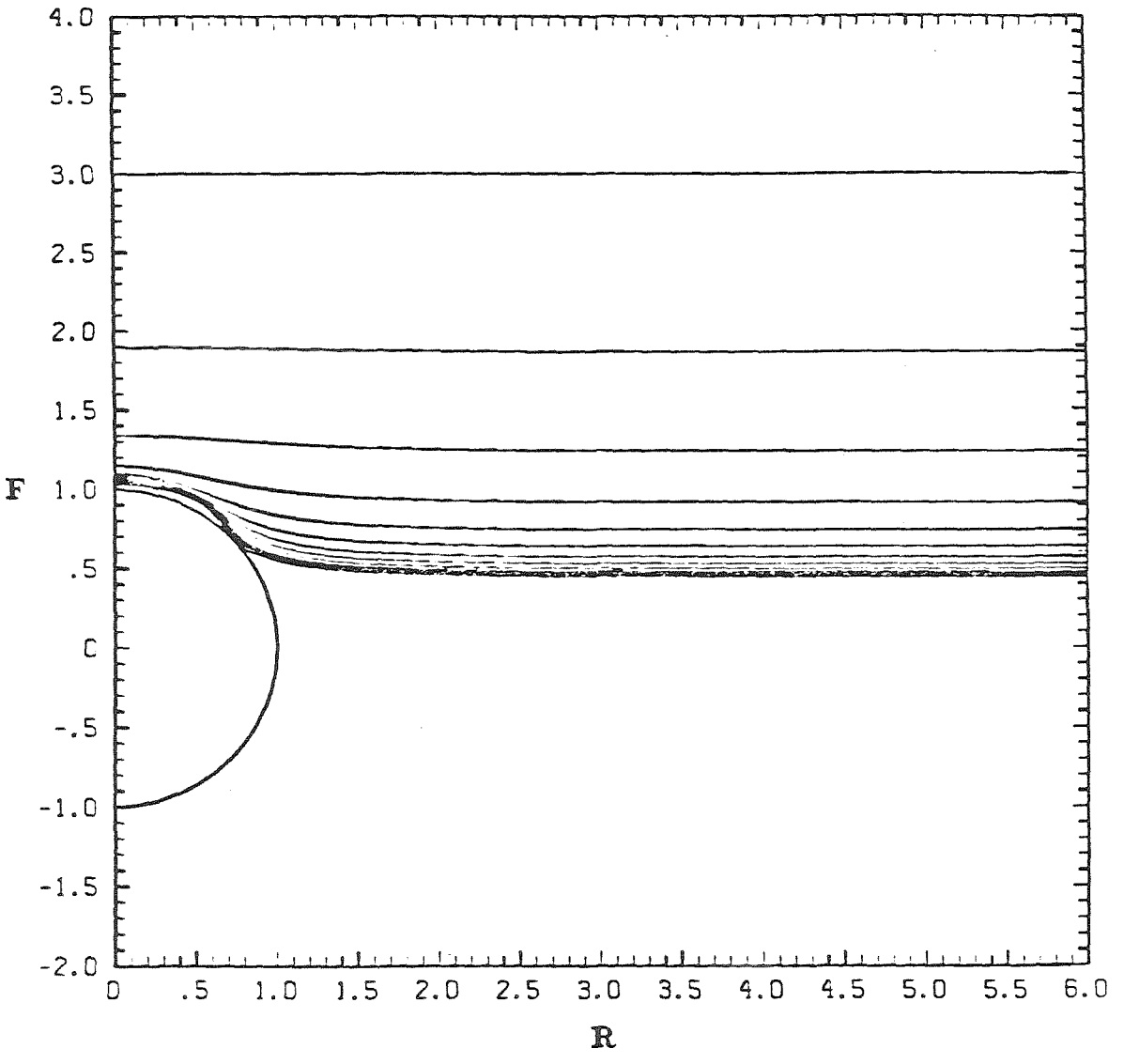

Figure 48. Interface shape as a function of sphere position with $\lambda = 10$, $Ca = 10$, $Cg = 10$, $l_o = -3$, $\Delta t_c = 0.25$.

Chapter II

A spherical particle contacting a deformable fluid/gas interface in an axisymmetric straining flow.

Abstract

Numerical solutions for the equilibrium particle-interface configuration for a neutrally buoyant spherical particle contacting a deformable fluid/gas interface in a linear axisymmetric straining flow at low Reynolds number are presented for a range of contact angles and capillary numbers. These solutions may have applications both in flotation separation processes and in contact angle and surface tension measurement. In addition, the accuracy of simply combining previous results for particle detachment due to particle buoyancy with the results for particle detachment due to viscous forces is considered. The equilibrium configuration is especially sensitive to the inclusion of a small amount of flow for small contact angles and for capillary numbers near the critical capillary number.

Introduction

The existence and form of solutions for the shape of a fluid interface contacting a solid boundary is important in a number of applications in fluid mechanics. For example, several methods of characterizing fluid/fluid interfacial tensions rely on the measurement of interface shapes or on the determination of the maximum external force at which an equilibrium interface shape exists in contact with a solid boundary (such as rings, plates, and spheres) exists. [Princen (1963), Princen and Mason (1965 I and II.), Huh and Scriven (1969), Huh and Mason (1974), Boucher and Evans (1975), Boucher et al. (1976), Boucher and Kent (1977), Hiemenz (1977), Girault et al. (1982, 1984), Rotenberg et al. (1984), Smith and Van de Ven (1984)]. Measurement of interfacial shapes is also an important tool in the determination of macroscopic contact angles, Rotenberg et al. (1983).

The study presented in this paper is motivated by the problem of capture stability for small particles at the surface of a bubble or drop in effluent and mineral flotation. The key question here is whether the hydrodynamic and body forces which act on the particle once it has been swept to the rear of the bubble or drop will overcome capillary forces and pull the particle off the bubble. A first step toward answering this question is to determine conditions when an equilibrium configuration exists for the particle in the interface where all of the forces balance. Several researchers, Princen and Mason (1965), Huh and Scriven (1969), Huh and Mason (1974), Rapacchietta and Neumann I and II (1977), Boucher and Kent (1978) Boucher and Jones (1981), have, in fact, already investigated this question in the approximate case of a sphere or spheroid in a *static* fluid contacting an unbounded fluid/fluid interface. Because of the nonlinear nature of the Young-Laplace equation governing interfacial statics and complications in achieving the prescibed flat interface shape at infinity, solutions were obtained either as asymptotic approximations for nearly flat interfaces or by numerical techniques employing iterative methods to ensure that the bound-

ary conditions and force balance on the particle were satisfied. These analyses offer one way of explaining quantitatively the selective separations achieved by flotation based both on the size and chemical nature (i.e., contact angle) of the particle, Sutherland and Wark (1955), Derjaguin and Dukhin (1979). Thus, it is possible to show that equilibrium configurations are possible for one component of a physical system but not for another component and to use this as a basis for evaluating the feasibility of selective separation of these components by flotation.

However, if the previous analyses are to model accurately the flotation problem, hydrodynamic effects must also be included. Although, hydrodynamic viscous forces are often significantly smaller than interfacial tension forces in effluent flotation, due to the small bubble sizes, viscous forces may be of the same order of magnitude or larger than forces arising from density differences between the particles and fluids since the particles being removed are often nearly neutrally bouyant (which is one reason why effluent flotation is used). Also in situations with small interfacial tension forces due to small contact angles and/or small contact line lengths no equilbrium solution may exist if a small viscous force is introduced, which tends to pull the particle from the interface. Thus hydrodynamic effects can promote selective separation and affect the separation efficiency in a manner similar to the effects of a density difference between the particle and the fluids.

In comparison to the many studies on the effects of density differences in the statics problem, the effects of viscous flow on the existence and form of solutions for flotation contact problems have received much less attention. Ranger (1978) and Falade (1982) investigated the motion of a disk straddling a flat interface in a creeping flow. Later, Davis (1982) considered a sphere contacting an unbounded interface in an extensional flow, but the interface was only allowed to undergo small deformations and solutions were obtained only for gravity and surface tension-dominated cases for small differences in fluid viscosities. Unfortunately,

none of these analyses is suitable for application to the flotation problem because of the severe restrictions that would be required on the magnitude of the viscous forces, the limited extent of the interface deformation and the small range of permissible contact angles ($\approx \frac{\pi}{2}$). The only other analysis which examines the role of viscous forces on the stability of captured particles, is due to French and Wilson (1980) who looked at the effects of viscous forces on a cap of particles on a bubble. However, their main conclusion that the action of the flow stabilizes the particles, rather than tends to pull the particles from the bubble surface, contradicts physical intuition. This conclusion also disagrees with observations made in our laboratory (Stoos 1987) on the stability of a cap of particles on a bubble that is held fixed on the tip of a syringe needle in flow through a capillary tube. The relative scarcity of theoretical investigations which include viscous effects is undoubtedly due to the complicated nature of the non-linear free boundary problem which must be solved. However, the solution of free boundary problems at low Reynolds number via boundary-integral methods has now become routine, c.f., Youngren and Acrivos (1975, 1976), Rallison and Acrivos (1978), Lee and Leal (1982) and Stone, Bentley and Leal (1986), and this lack of work does not currently seem justified. Therefore, in the present paper, we consider the prototype problem of a single spherical particle contacting a free deformable interface in the presence of a steady, uniaxial extensional flow.

For this initial investigation we consider only the conditions for existence of steady-state configurations. In particular, we do not attempt to analyze the dynamics of particle removal when a steady-state is not possible, nor do we concern ourselves with the transient regime prior to achieving a steady state. Thus, in spite of the fact that the related phenomena of contact line slip and dynamic contact angles, could be included in the boundary-integral analysis by using one of the many models available in the literature, c.f., Dussan (1979), these effects are not included in the present work. Also line tension effects, Ivanov et al. (1985 I-IV), which may be important for the very small particles

found in flotation applications, have not been included explicitly in this study since we are assuming a macroscopic contact angle and macroscopic surface tension that have been correctly measured or calculated, taking into account the possible presence of these effects. Of course, line tension or film tension effects would have to be included explicitly in an additional force balance at the contact line if the solid particle were replaced by a small drop or bubble. Finally, surfactant effects and associated complications due to interface surface blockage, interfacial viscosity and spatial variations in surface tension have not been included in this initial investigation.

Problem Statement

The same "flotation" approximations, based on the existence of two very different length scales, which have been used in the statics problem are also introduced in the flow peoblem, that is analyzed here. In particular, we assume that the radius of the particle a is very much smaller than the radius of the bubble R, so that the curvature of the bubble and any deformations of the bubble on the length scale R are not "seen" by the particle, and the bubble surface appears flat to leading order of approximation. Of course, deformations of the interface on a length scale a do influence the particle, and these must be considered explicitly to determine conditions for capture stability.

Upon contact, the particle is swept to the rear stagnation point of the bubble, where it is exposed to an axisymmetric flow that tends to pull it from the interface. By means of a "local" approximation of the undisturbed flow about this point, Stoos (1987) showed that, to leading order in $(\frac{a}{R})$, this flow is a linear uniaxial extensional flow. Approximating the full undisturbed flow as a linear uniaxial extensional flow centered at the rear stagnation point, amounts to solving the first inner problem of a matched asymptotic analysis. Since the disturbance flow in the first inner problem will decay like $\frac{1}{r}$, it will give rise to additional flows in the outer region at $O(\frac{a}{R})^2$, which, along with the deformation of the boundary shape resulting from the first inner problem, will modify the

outer problem. However, even the leading order "inner" inner problem is very difficult, requiring numerical solutions for the interface shape and the flow field and it is not practical to attempt to evaluate higher-order terms in the expansion. From a pragmatic point of view, it is likely that capture stability will be dominated by the lowest order $(\frac{a}{R})$ extensional flow contribution, rather than by the O $(\frac{a}{R})^2$ terms. The linear extensional flow may also have more general applicability to other contact problems, such as the effect of drainage flows on the measurement of interfacial tensions using "static" tensiometers.

Thus, as shown in Figure 1, we consider the problem of a spherical particle of density ρ_p and radius a straddling a free interface where the equilibrium contact angle is θ_c, the surface tension is a constant σ, and the density and viscosity of the incompressible Newtonian lower fluid are ρ and μ, respectively. In this axisymmetric problem the interface is represented by cylindrical coordinants (r,z) centered on the plane of the undeformed interface with the sphere center at (0,h). The position of the contact line on the sphere is designated by the angle ϕ, measured from the vertical axis. The convention, shown in Figure 1, of measuring ϕ from the *negative* z axis has been used to maintain consistency with the nomenclature from earlier investigations of the statics problem. The upper fluid is assumed to be a gas with negligible density and viscosity. Also, far from the particle the interface is assumed to be flat, the lower fluid velocity approaches a uniaxial extensional flow $\mathbf{u}_\infty = G(-r\mathbf{i}_r + 2z\mathbf{i}_z)$ (where G is the strain rate), and the dynamic pressure approaches zero. The strain rate, G is assumed to be small enough that the creeping motion approximation can be applied; i.e., the Reynolds number Re satisfies

$$Re = \frac{\rho G a^2}{\mu} \ll 1.$$

Thus, the equations of motion are linear. The problem remains nonlinear through the boundary conditions, however, because the interface shape, the sphere position h, and the position of the contact line ϕ, all remain unknown.

An excellent method of solution for this type of free boundary problem is

the boundary-integral method used previously in our group by Geller, Lee and Leal (1986), Lee and Leal (1982) and Chi and Leal (1987) following earlier work by Youngren and Acrivos (1975, 1976), Rallison and Acrivos (1978), and others. We refer the reader to these earlier papers for many of the details.

In the present problem, we nondimensionalize using the characteristic velocity Ga, length a and stress $G\mu$. The creeping motion equations in the lower fluid can thus be expressed in the form

$$\left.\begin{aligned} 0 &= -\nabla p + \nabla^2 \mathbf{u} \\ 0 &= \nabla \cdot \mathbf{u}. \end{aligned}\right\} \tag{1}$$

In addition to the condition stated previously at large distances from the particle, the boundary conditions at the interface are

$$\mathbf{u} \cdot \mathbf{n} = 0, \tag{2}$$

$$\mathbf{n} \cdot \mathbf{T} = \frac{1}{Ca}(\nabla \mathbf{n}) \cdot \mathbf{n} - \frac{1}{Cg} f \mathbf{n}, \tag{3}$$

$$\left.\begin{aligned} \mathbf{u}_p = 0, \end{aligned}\right\} \quad \text{at the particle surface} \tag{4}$$

In addition, the steady-state solution must satisfy the macroscopic condition of zero net force on the particle in the z direction (this condition is satisfied trivially in the r direction due to symmetry), i.e.,

$$F_z = 0 \tag{5a}$$

where

$$F_z = -\left(\frac{4}{3}\pi\frac{\rho_p}{\rho} + \pi h sin^2\phi + \frac{2}{3}\pi(-1 + cos^3\phi)\right)\frac{1}{Cg} - 2\pi sin\phi sin(\phi + \theta_c)\frac{1}{Ca}$$

$$+2\pi \int_{\pi-\phi}^{\pi} T^p_{nz} sin\theta d\theta$$

$$= F_{Buoy} + F_{Ca} + F_{Visc}. \tag{5b}$$

Finally, the interface must approach the particle surface with the prescibed macroscopic contact angle, θ_c. The three terms which appear in (5b) are, from

left to right, the net buoyancy force, the z-component of the capillary force at the contact line, and the hydrodynamic force due to the fluid motion. The parameters Ca and Cg appear in the first two terms because the force has been non-dimensionalized with the characteristic viscous force, $\mu G a^2$, in order to be consistent with the characteristic stress, μG, which was used in (1) - (3). Here, as in Lee and Leal, the interface shape is represented by z = f(r), and the outward pointing normal at the interface is $\mathbf{n} \equiv \frac{\nabla H}{|\nabla H|}$ where H = z - f(r).

The relevant dimensionless parameters which appear in (1) - (5) are the capillary number, $Ca = \frac{\mu G a}{\sigma}$, the ratio of capillary to bond numbers, $Cg = \frac{\mu G}{a g \rho}$, and the ratio of particle to fluid densities, $\frac{\rho_p}{\rho}$. It will be noted that Ca and Cg both appear twice, in the normal stress condition (3) and the macroscopic force balance (5). Thus, Ca may be viewed both as the ratio of viscous forces in the fluid that tend to pull the particle from the interface to interfacial tension forces, which tend to hold the particle on the interface, and also as the ratio of viscous forces tending to deform the interface to capillary forces which resist interface deformation. Likewise, Cg is the ratio of these viscous forces in the fluid to body forces that tend to pull the particle from the interface and also the ratio of viscous forces to body forces which tend to resist interface deformation. The ratio $\sqrt{Ca/Cg}$ can be viewed as the dimensionless particle radius scaled with an intrinsic measure of the interface curvature, i.e., $\frac{a}{\sqrt{\frac{\sigma}{\rho g}}}$, and is used frequently in the statics problem.

In the present work, we concentrate primarily upon the limiting case of neutrally buoyant particles, $\frac{\rho_p}{\rho} = 1$. Although non-neutrally buoyant particles could easily be treated by the same methodology, the case of nonzero density differences has been studied extensively in the statics problem, and we wish to maintain a manageable number of independent physical parameters. In addition, for $\rho_p = \rho$, there will always be an equilibrium solution for the statics problem, c.f., Boucher and Jones (1981). Thus, if a flow problem for $\rho_p = \rho$ is found to have no solution, this *must* be due to the presence of the flow. The solution

technique could also be modified slightly to consider an upper fluid of nonzero viscosity and density. However, the primary "flotation" case of interest has the "collector" as a gas bubble, and we thus limit our present solutions to the corresponding case in which the upper fluid is a gas.

The positions of the sphere center, h, and the contact line, ϕ, must be determined together with the shape of the interface f(r) such that the force balance on the sphere is satisfied, the normal velocity on the interface is zero, and the angle of the interface at the contact line agrees with the specified macroscopic contact angle, θ_c.

Solution Methodology

In the present work, the problem outlined above is solved via the boundary-integral method, for several values of θ_c and a range of values for Ca and Cg. The boundary-integral method for an unbounded domain requires that the flow variables decay to zero at infinity. Therefore, the velocity and stress are written in terms of disturbance variables, as in Rallison and Acrivos (1978), where $\mathbf{u}' \equiv \mathbf{u} - \mathbf{u}^\infty$ is the disturbance velocity and $\mathbf{T}' \equiv \mathbf{T} - \mathbf{T}^\infty$ is the disturbance stress. Ladyzhenskaya's (1963) general solution for the disturbance velocity and disturbance pressure at any point in the fluid $\mathbf{x}$ is

$$\mathbf{u}'(\mathbf{x}) = \frac{1}{8\pi}\int_S \left(\frac{\mathbf{I}}{R} + \frac{(\mathbf{x}-\eta)(\mathbf{x}-\eta)}{R^3}\right)\cdot\mathbf{T}'(\eta)\cdot\mathbf{n}dS_\eta$$
$$-\frac{3}{4\pi}\int_S \frac{(\mathbf{x}-\eta)(\mathbf{x}-\eta)(\mathbf{x}-\eta)}{R^5}\cdot\mathbf{u}'(\eta)\cdot\mathbf{n}dS_\eta \qquad (6)$$

$$p'(\mathbf{x}) = \frac{1}{2\pi}\int_S \left(\frac{\mathbf{I}}{R} - \frac{3(\mathbf{x}-\eta)(\mathbf{x}-\eta)}{R^5}\right)\cdot\mathbf{u}'(\eta)\cdot\mathbf{n}dS_\eta$$
$$+\frac{1}{4\pi}\int_S \frac{(\mathbf{x}-\eta)}{R^3}\cdot\mathbf{T}'(\eta)\cdot\mathbf{n}dS_\eta. \qquad (7)$$

Because the pressure associated with the undisturbed flow at infinity undergoes a jump across the interface $p_\infty - p_{\infty g} = 4G\mu$ (where p_∞ and $p_{\infty g}$ are the constant pressures in the lower fluid and the gas associated with the flow at

infinity), the disturbance pressures are defined as $p'_g \equiv p_g$ and $p' = p - 4G\mu$ or, in dimensionless terms, $p' = p - 4$ so that $p'_g, p' \to 0 \quad$ as $\quad |\mathbf{x}| \to \infty$.

The details of the derivation of the system of boundary-integral equations from (6) and (7) is similar to those of Lee and Leal (1982) with additional terms in the equations from the flow at infinity. After applying the double-layer jump condition, the velocity on the interface in the limit as $\mathbf{x} \to S_I$ from the lower fluid is given by

$$\frac{1}{2}\mathbf{u}^{I'}(\mathbf{x}) = -\frac{3}{4\pi}\int(\frac{\mathbf{rrr}}{R^5})\cdot\mathbf{u}^{I'}\cdot\mathbf{n}dS_I + \frac{1}{8\pi}\int(\frac{\mathbf{I}}{R}+\frac{\mathbf{rr}}{R^3})\cdot\mathbf{T}^{I'}\cdot\mathbf{n}dS_I$$
$$+\frac{1}{8\pi}\int(\frac{\mathbf{I}}{R}+\frac{\mathbf{rr}}{R^3})\cdot\mathbf{T}^{P}\cdot\mathbf{n}dS_P + \frac{3}{4\pi}\int(\frac{\mathbf{rrr}}{R^5})\cdot\mathbf{u}_\infty\cdot\mathbf{n}dS_P$$
$$-\frac{1}{8\pi}\int(\frac{\mathbf{I}}{R}+\frac{\mathbf{rr}}{R^3})\cdot\mathbf{T}^{P}_\infty\cdot\mathbf{n}dS_P. \qquad (8)$$

The velocity on the sphere surface, including the double-layer jump condition is given by

$$\mathbf{0} = -\frac{3}{4\pi}\int(\frac{\mathbf{rrr}}{R^5})\cdot\mathbf{u}^{I'}\cdot\mathbf{n}dS_I + \frac{1}{8\pi}\int(\frac{\mathbf{I}}{R}+\frac{\mathbf{rr}}{R^3})\cdot\mathbf{T}^{I'}\cdot\mathbf{n}dS_I$$
$$+\frac{1}{8\pi}\int(\frac{\mathbf{I}}{R}+\frac{\mathbf{rr}}{R^3})\cdot\mathbf{T}^{P}\cdot\mathbf{n}dS_P \quad + \quad \frac{1}{2}\mathbf{u}_\infty$$
$$+\frac{3}{4\pi}\int(\frac{\mathbf{rrr}}{R^5})\cdot\mathbf{u}_\infty\cdot\mathbf{n}dS_P - \frac{1}{8\pi}\int(\frac{\mathbf{I}}{R}+\frac{\mathbf{rr}}{R^3})\cdot\mathbf{T}^{P}_\infty\cdot\mathbf{n}dS_P. \qquad (9)$$

The disturbance stress on the interface, $\mathbf{T}^{I'}$, is defined as $\mathbf{n}\cdot\mathbf{T}^{I'} \equiv \mathbf{n}\cdot\mathbf{T}^{I} - \mathbf{n}\cdot\mathbf{T}^{I}_\infty$, where $\mathbf{n}\cdot\mathbf{T}^{I}$ may be evaluated from the interface shape via Equation (3) and the stress from the undisturbed flow at infinity may be evaluated from $\mathbf{n}\cdot\mathbf{T}_\infty = \mathbf{n}\cdot(-p_2\mathbf{I} + (-2\mathbf{i}_r\mathbf{i}_r + 4\mathbf{i}_z\mathbf{i}_z)) = -6n_r\mathbf{i}_r$, where the constant dynamic pressure associated with the undisturbed flow has been chosen to balance the

viscous stress of the undisturbed flow and maintain a flat interface (in the absence of the particle) in equilibrium, Stoos and Leal (1987)). In addition to the weighting functions $\mathbf{T}^{I'}$ and $\mathbf{T}^{P}_{\infty}$, the undisturbed flow in the above equations may also be evaluated, $\mathbf{u}_{\infty} = (r\mathbf{i}_r - 2z\mathbf{i}_z)$. Boundary condition (2) has already been incorporated into Equations (8) and (9). For a given interface and sphere configuration, i.e. f(r), h and ϕ, the Equations (8) and (9) can be solved simultaneously to determine the disturbance velocity on the interface and the net stress on the particle surface. The problem then, is to determine the configuration, i.e., f(r), h and ϕ, such that the boundary-condition (2) and the macroscopic balance (5) are satisfied for a given set of values for Ca, Cg and θ_c.

The method used to solve (8) and (9), for a given configuration, is essentially the same collocation scheme described by Geller, Lee and Leal (1986). The surface integrals in (8) and (9) are first reduced to line integrals by integrating analytically over the azimuthal angle, for this axisymetric problem. The infinite interface boundary is then truncated at some large but finite radius, R_o, and subdivided along with the portion of the particle surface that is exposed to the lower fluid into N_I and N_P small segments, respectively. The number of segments varied between 25 - 35 unequal-sized segments for N_I, with the highest concentration of segments being near the particle where the interface deformation is largest, and 15 - 25 evenly spaced segments for N_P. Because the undisturbed flow has a linear variation, the unknown basis functions for the velocity and stress are assumed to vary linearly over these small segments. Alternatively, high accuracy could also be maintained by increasing the number of boundary elements and assuming that the basis functions to be constant over the elements. However, the use of linear basis functions is numerically faster because the integrands for the additional integrals with linear weighting functions are already available from their evaluations for the terms with constant weighting functions, and the size of the matrix that must be inverted is not increased by assuming a linear variation in the unknown velocity and stress as

it would be for an increase in the number of boundary elements. Vector Equation (8) is evaluated at the N_I interface interval centers, and vector Equation (9) is evaluated at the N_P particle interval centers, thus generating a system of $2N_I + 2N_P$ linear algebraic equations (Kantorovich and Krylov 1958). For a given configuration (f(r), h and ϕ) these equations are solved for the $2N_I + 2N_P$ unknowns; $u_r'(N_I)$, $u_z'(N_I)$, $T^P_{nr}(N_P)$, and $T^P_{nz}(N_P)$. The normal vector to the interface and the local interface curvature, which appear in the integrands through the use of boundary condition (3) and the evaluation of the surface normals, are evaluated using a cubic spline to represent the interface shape as f(r). The azimuthal integration reduces the surface integrals to line integrals with integrands in terms of elliptic integrals (Lee and Leal (1982)). These final line integrals are evaluated numerically using a 7 point Gauss quadrature and the accuracy is checked by comparing to a 11 point Gauss quadruture. In doing this integration, a small line element is cut out around the singular point and evaluated analytically. In addition, the accuracy is improved by further subdividing the main segment into smaller segments near the singular points.

In general, with Ca, Cg and θ_c specified, the solutions for the interface velocities and the stress on the sphere will not satisfy boundary conditions (2) and (5), and the interface/particle configuration f(r), h and ϕ must be modified. Initially, attempts were made to modify the interface shape and particle position via an explicit, pseudo-time-dependent iteration, in which the positions of node points on the interface were stepped proportional to the calculated values for $\mathbf{u}^I \cdot \mathbf{n}$, and the position of the particle was incremented according to the imbalance in total force, from the sum of the three terms in (5). However, all such explicit iterative schemes were found to be slow and prone to numerical instability, leading to kinks in the interface shape and rapid divergence of the entire solution. Use of implicit stepping schemes stabilize the system somewhat but still result in very long computation times and occasional instabilities in the solutions.

Thus to speed convergence, to provide a more stable means of obtaining

equilibrium solutions, and to better determine when no solutions exist, a modified Newton's scheme similar to Youngren and Acrivos (1976) is used to obtain subsequent values of f(r), h and ϕ. It should be noted that the contact point (line) was *not* included as a node point in any of the schemes to determine a new geometric configuration. However, the first few node points were concentrated very near the contact point and a two-point right-handed difference scheme (see Appendix A) was used to set the position of the contact point to ensure that the contact angle has the required macroscopic value, to within an accuracy of 10^{-4} of the specified contact angle. Unlike the problem considered by Youngren and Acrivos (1976), the occurrence of neutral eigenvalue solutions does not cause difficulties in this study since the presence of the sphere boundary modifies the linear system. However, as already found by Youngren and Acrivos (1976), the radius of convergence of the Newton's method scheme in this problem is not very large. Therefore, a good initial guess for the interface shape and sphere position is required, and in this study the static configuration is used as a first guess for the interface shape and particle position for small flow strengths, i.e., small values of Ca and Cg. This static shape is calculated using a slight modification of the method of Rapacchietta and Neumann (1977b) (see Appendix B). From this shape, the normal velocity is calculated at the NI interface node points, and the net force on the particle is determined.

For convenience, let us define the vector x_j

$$x_j = \begin{cases} (\mathbf{u}\cdot\mathbf{n})_j, & \text{if } j \le NI; \\ F_{net}, & \text{if } j = NI+1, \end{cases} \tag{10}$$

which thus represents the deviation of the system from equilibrium, (at equilibrium all the elements of x_j would be zero). Similarly, the vector z_j

$$z_j = \begin{cases} f_j, & \text{if } j \le NI; \\ h, & \text{if } j = NI+1 \end{cases} \tag{11}$$

represents the interface shape at each r_j and the particle position. The Jacobian is evaluated by perturbing in turn each of the node points f(NI) and the sphere

position h, and calculating the new NI normal velocities and the new net force on the particle. This Jacobian has elements

$$A_{ij} = \begin{cases} \frac{\Delta(\mathbf{u}\cdot\mathbf{n})_i}{\Delta f_j}, & \text{if } i,j \le NI; \\ \frac{\Delta(\mathbf{u}\cdot\mathbf{n})_i}{\Delta h}, & \text{if } i \le NI,\ j = NI+1; \\ \frac{\Delta F_{net}}{\Delta f_j}, & \text{if } i = NI+1,\ j \le NI; \\ \frac{\Delta F_{net}}{\Delta h}, & \text{if } i = NI+1,\ j = NI+1. \end{cases} \tag{12}$$

A new interface shape and particle position is calculated based on the Jacobian according to (13), so that the NI normal velocities and net force on the particle are driven towards zero,

$$z_j^{n+1} \quad = \quad z_j^n \quad - \quad w \ A_{ij}^{n^{-1}} \ x_j^n. \tag{13}$$

It should be noted that we have followed Youngren and Acrivos (1976) and used under-relaxation in this calculation of shape change with an optimal relaxation factor $w \le 1$, which is chosen so that the maximum increment in shape is bounded by a specified limit. The use of $w \ne 1$ prevents divergence of the solution.

The Jacobian changes very little over the course of convergence for a particular choice of parameters Ca, Cg and θ_c, with a sufficiently close starting configuration. Thus, the Jacobian is not updated unless convergence is unusually slow, and the solution scheme is more accurately called a Picard iteration rather than a "modified" Newton scheme. The interface shape and sphere position is iterated until conditions (2) and (5) are satisfied to at least 10^{-4} in each normal velocity component and the net force. It will be noted that each iteration requires solution of the boundary-integral problem to determine x_j, even though the elements of the Jacobian are not changed. When the conditions (2) and (5) are satisfied, a measure of the change in shape at the n + 1^{th} iteration, as defined by Youngren and Acrivos (1976), W = $(z_j^{n+1} - z_j^n)(z_j^{n+1} - z_j^n)/w$ is always less than 10^{-10}, i.e., the configuration simultaneously reached a steady shape.

In many of the cases studied, the parameters Ca and Cg were increased, with the ratio, $\frac{Ca}{Cg}$, fixed, which is representative of the physical situation where the flow strength is increased, and the particle size (or ratio Ca/Cg) and fluid properties are held fixed. Changes in the flow strength would occur in the flotation problem through changes in the size of the collector bubble. We have also considered some cases in which Cg was held fixed (at its lowest value) while Ca was increased, which is representative of the physical situation where the flow strength, particle size and fluid densities are held fixed, while the surface tension is decreased, possibly due to the addition of a surfactant. The third possibility, of holding Ca fixed and varying Cg, was not explored because it corresponds to variation in the liquid density for a system with constant surface tension and flow strength, and thus would not be realized in any straightforward way in a flotation process.

For all of these investigations, after varying the parameters, a new Jacobian is calculated and the entire procedure is repeated until the solution has converged to a new steady shape satisfying the force balance on the particle and having the required macroscopic contact angle. Convergence of the interface shape is not obtained unless a sufficient number of segments on the interface are used, since the errors in calculating the interface curvature are very sensitive to the spatial resolution. However, even for the most deformed interface we consider, the final steady-state configuration is not affected by the number of intervals for N_I greater than 25. Also, in some instances convergence is accelerated by using a different (smaller) relaxation factor for the net force on the particle than for the normal velocities on the interface. This indicates, as might be expected, that the solution is more sensitive to variations in the particle position than to variations in the interface shape.

Finally, it should be recognized that steady-state solutions may exist only for a limited range of Ca and Cg values for a system with any fixed contact angle θ_c. In particular, if we follow one of the parameter pathways that was described

above beginning with the static limit Ca = Cg = 0, we will see that we reach a limit point for the particular branch of steady-state solutions which includes the static case. For larger values of Ca, and either the case of constant values of Cg or the case of larger values of Cg, a steady solution of this family does not exist, and we identify the limit point as the critical condition for capture stability. In order to explore the solution behavior in the vicinity of this limit point, where the configuration becomes increasingly sensitive to variations in Ca, it is more convenient to use a "continuation method", c.f., Kubicek and Marek (1983). In this procedure, we adopt the sphere position, h, as the independent parameter, and calculate the capillary number corresponding to a particular value of h as part of the solution. Thus, a new Jacobian is calculated as in (12), but with h replaced everywhere by Ca as an unknown. The dependence on Cg is included implicitly through the stress and force balances. In this way, we can easily achieve solutions for Ca values arbitrarily close to the critical capillary number, as well as exploring the nature of the limit point (for example, we can examine the unstable branch of steady solutions which emanates from the limit point in Ca).

The effects of interface truncation are shown in Figure 2, where the viscous drag on the particle at steady-state is plotted versus truncation distance for the parameters $\theta_c = \frac{\pi}{2}$, Ca=0.1, Cg=0.05 and $\theta_c = \frac{8\pi}{9}$, Ca=Cg=0.05. The viscous drag is seen to be relatively constant for truncation distances R_o greater than 10.0 particle radii. Since the meniscus depression, h, is generally O(1), and the truncation distance is found to be dependent on the distance from the particle to the interface, Stoos (1987), the truncation distance is smaller than in the problem of a particle approaching a deforming interface in an extensional flow. A truncation distance of 15 is used in all the calculations that are reported below.

Results

We begin by considering neutrally buoyant particles, i.e., $\frac{\rho_p}{\rho} = 1$, which will

form the primary focus of our investigation. In this case, steady-state configurations were determined for contact angles of $\theta_c = \frac{8\pi}{9}$, where the fluid does not preferentially wet the particle (representative of a hydrophobic particle which should be readily floated), $\theta_c = \frac{\pi}{2}$ where the fluid is intermediate between wetting and nonwetting the particle, and $\theta_c = \frac{\pi}{4}$ where the fluid preferentially wets the particle (representative of a hydrophylic particle which should *not* be readily floated). Solutions were also sought for $\theta_c = \frac{\pi}{9}$ (a fluid which wets the particle even more strongly), but it is advantageous to delay discussion of this case until we have presented and discussed our results for the other, more moderate values of θ_c. For the solutions that are presented below for $\theta_c = \frac{\pi}{4}$, $\frac{\pi}{2}$ and $\frac{8\pi}{9}$, the capillary number is increased either with the constraint Ca = Cg, or with Cg = constant, as indicated in the preceeding section.

The effects of flow on the steady-state shape of an interface contacting a particle is first investigated for the relatively small contact angle, $\theta_c = \frac{\pi}{4}$. The steady-state solutions for $\theta_c = \frac{\pi}{4}$ and flow strengths in terms of Ca = Cg ranging from 0.0 (static values) to 0.0327 are shown in Figure 3. For simplicity of presentation, the interface contours are plotted relative to a coordinate system that is fixed at the center of the particle. The absolute position of the particle center can be determined from its position relative to the plane of the flat, undisturbed part of the interface. Interface configurations which correspond to *stable* steady-state solutions are shown as solid contours. *Unstable* steady solutions are shown as dashed contours. We shall discuss the "mechanism" for instability shortly. The transition between stable and unstable steady solutions occurs at a limit point for the branch of steady solutions with Ca (=Cg=Ca_{crit}) that emanate from the origin, i.e., Ca = Cg = 0, and this corresponds to the critical value of Ca (=Cg) for capture stability, i.e.,in this cxase Ca_{crit} (=Cg)=0.0327. We will discuss the nature of the solution in the vicinity of the limit point below.

To do this, it is useful to better understand the mechanisms by which the system attempts to accomodate an increase in the flow strength (i.e., an in-

crease in Ca=Cg) through changes in the particle-interface configuration. For this purpose, it is informative to examine the details of these changes on a more quantitative basis, and especially to consider how the three force contributions (i.e., buoyancy, capillary, and hydrodynamic) vary with changes in the particle-interface configuration as Ca (=Cg) is gradually increased. In looking at Figure 3, we see that as the flow strength increases (i.e., Ca=Cg increases), thus increasing the magnitude of the hydrodynamic force on the particle, the interface curvature increases and the contact line moves closer to the top of the particle. Indeed, as we continue to increase Ca (=Cg) (restricting our discussion to the stable solutions for the moment) we can see in Figure 3 that the particle-interface configuration becomes more and more sensitive to small increases in Ca (=Cg) as we approach the final stable equilibrium solution (the limit point). This effect is seen clearly in Figure 4 where the equilibrium particle position, h, and the contact line position, ϕ, are shown as a function of the capillary number. As the "critical" capillary number is approached (Ca=Cg=0.0327) the solution reaches a true limit point beyond which (i.e., for larger Ca=Cg) no steady solutions exist, at least on the branch of solutions which includes the static limit, Ca = Cg = 0. However, the steady solution in the vicinity of the limit point is not unique, and we have integrated "around the corner" of the limit point using the continuation method that was described in the proceeding section to determine the form of the second branch of solutions which exist for larger $\|h\|$ and ϕ. The corresponding interface configurations are shown as the dashed contours in Figure 3. There is nothing particularly unusual in the appearance of the solutions, either in terms of the interface shape, or in terms of the sphere position, h, or the contact line position, ϕ. However, as expected on general mathematical grounds, the solutions which lie beyond the limit point (i.e., for which $h < h_{Ca=0.0327}$ and $\phi > \phi_{Ca=0.0327}$) are unstable, and the maximum value Ca (=Cg) = 0.0327 thus represents the *limit of stability* for particle capture.

In order to better understand wht these solutions are unstable, as well as

the nature of the limit point for particle capture, it is necessary to examine the changes in the varios types of forces which act on the sphere as the capillary number is increased. For this purpose, we can examine the three basic terms in Equation (5b). However, if we are to include the static limit, thje nondimensionalization that is built into (5b) is not a convenient choice. The problem is that in the static (no flow) limit, the characteristic scale $\mu G a^2$ that was used to nondimensionalize (5b) is zero, and this is reflected in the fact that the magnitudes of the buoyancy and capillary terms become unbounded in the limit Ca (=Cg) $\rightarrow$ 0. A more appropriate form of (5b) is obtained by multiplying this equation through by Cg, i.e.,

$$F_z^* = -\left(\frac{4}{3}\pi\frac{\rho_p}{\rho} + \pi h sin^2\phi + \frac{2}{3}\pi(-1+cos^3\phi)\right) - 2\pi sin\phi sin(\phi+\theta_c)\frac{Cg}{Ca}$$

$$+2\pi Cg\int_{\pi-\phi}^{\pi} T_{nz}^p sin\theta d\theta \qquad (14)$$

which corresponds to nondimensionalizing the force with respect to $F_c = a^3\rho g$. In this form, the buoyancy force changes only due to a change in the configuration, ϕ and h. The case considered above in which Ca is increased with $\frac{Ca}{Cg} = 1$ is most conveniently imagined as representing the changes in a system with fixed material properties due to an increase in G. With the scaling inherent in (14), both the buoyancy and capillary forces remain O(1) as Ca is increased, but the viscous term increases in proportion to Ca (=Cg), which is a qualitatively satisfactory representation of the physics. The other situation, considered below, is for Ca to increase with Cg fixed, which is most easily envisioned as corresponding to a decrease in σ for constant flow strength μG in a system with fixed ρ and a. In this case, as Ca is increased, the magnitude of the buoyancy and viscous contributions remain O(1), while the capillary forces decrease as Ca^{-1}, and this is again a qualitatively reasonable representation of the expected behavior.

In Figure 5 we have plotted the three contributions to the force on the sphere for the case $\theta_c = \frac{\pi}{4}$, Ca = Cg, that was shown in Figures 3 and 4. In the static limit, the viscous force is zero and there is a precise balance between

the buoyancy and capillary forces for the configuration shown in Figure 3 as Ca = Cg = 0. We have already seen that the interface curvature increases and the contact line moves toward the top of the sphere, as the flow strength and the viscous force increases with the increase of Ca=Cg. In terms of the buoyancy and capillary force contributions this change in the configuration has two primary effects, as shown in Figure 5. First, and most importantly, the magnitude of the capillary contribution in the positive z direction increases. Although the contact line becomes shorter with increasing Ca, this is compensated for some range of ϕ by the fact that the capillary force at the contact line is directed more in the vertical direction (clearly, however, the capillary force must eventually decrease as $\phi \rightarrow \pi$ since the length of the contact line goes to zero). Second, as Ca increases, the sphere is immersed farther into the liquid and also displaced further from the plane of the undeformed interface, and this causes the buoyancy force to change. For small contact angles, however, the neutrally buoyant sphere is almost completely submerged in the lower fluid and the magnitude of the net buoyancy force (for $\rho_p = \rho$) is quite small compared to capillary and viscous forces (except in the limit Ca = Cg = 0). Although the buoyancy force does contribute increasingly to supporting the particle as Ca is increased, and even changes sign from negative (tending to pull the particle off) to positive (tending to hold it on) as the meniscus depression more than compensates for the weight of the small portion of the particle above the interface, the large increase in the negative viscous force is mostly balanced by the increase in the capillary force.

Up to the limit point, Ca (=Cg) = 0.0327, which also appears in Figure 5 as a limit point for the various force components, the steady particle-interface configurations are stable. Beyond the critical capillary number, at which no new solutions can be found for larger Ca, the net force on the particle is always the largest component of x_j, i.e. the force balance on the particle is the relation which is not satisfied, and the particle position begins to diverge. The reason for this behavior is seen in Figure 6 where the dependence of the capillary force

on the contact line position, ϕ, is plotted for various contact angles with Ca = Cg. The contact line position at which the final stable equilibrium solution is obtained for $\theta_c = \frac{\pi}{4}$ coincides closely with the *maximum* in the capillary force. In fact, for small contact angles in general, the contact line position at which the final stable equilibrium solution is obtained coincides closely with the point of the maximum in the capillary contact force. Because the net buoyancy force is small for small contact angles, any increase in the viscous force must be essentially balanced by an increase in the capillary force. However, once the maximum value for the capillary force is reached at $\phi = \phi_{crit}$, any further increase in Ca must lead to instability since there is no mechanism available to balance any further increase in the viscous force. Thus the particle must be pulled from the interface if Ca is increased beyond the critical capillary number.

We have already seen that a second branch of steady-state solutions exists for $Ca < Ca_{crit}$, which correspond to increased displacement of the sphere (i.e., $h < h_{crit}$) and a contact line which is even closer to the top of the sphere (i.e., $\phi > \phi_{crit}$). However, these steady-state solutions are unstable, as is well-known from a knowledge of the general mathematical analysis of this type of limit point behavior. From a physical point-of-view, this instability is a consequence of the fact that the capillary "restoring" force, actually *decreases* with increased displacement (or increased ϕ), while the viscous destabilizing force increases.

Next, we investigate the equilibrium configurations for small contact angles ($\frac{\pi}{4}$), when the capillary number is increased with Cg fixed. As indicated above, this is most easily envisioned as corresponding to a decrease in surface tension, either due to the introduction of surfactants or to a change in the uniform solution temperature, with G and other material parameters held fixed. Figure 7 shows the interface contours for Cg=0.01 and Ca increasing from 0.0 to 0.0361 and then decreasing back to 0.034 by continuation. The shapes are quite similar to those obtained for the increase in flow strength; however, the interface curvature is slightly less in this case. As seen in Figure 8, the decrease in surface

tension causes the capillary force to drop slightly for increasing Ca, even though the contact line position is again moving towards the maximum capillary force configuration. This decrease in the capillary force and the simultaneous increase in the negative viscous force are both balanced in this case by the increase in the buoyancy force. It should be noted that the capillary and buoyancy force, if extrapolated for $Ca \rightarrow 0$, would not pass through the solutions obtained for the static limit since the correct limit for $Ca \rightarrow 0$, here, would be the situation of an interface (flat) due to infinite surface tension in a $non - zero$ flow and not the static case. Thus, the particle/interface configuration for the first nonzero values of Ca=Cg (and not the static case) is used as the starting configuration for the situation where the increase in Ca results from a decrease in σ, and thus Cg is held fixed. In general terms the buoyancy force is more important for decreases in surface tension (i.e., Ca increased with Cg fixed) than for increases in flow strength (i.e., Ca and Cg increased with Ca=Cg), although in the case of small contact angle, $\theta_c = \frac{\pi}{4}$, the capillary force still dominates the buoyancy force. The approach to the critical capillary number is again accompanied by rapid changes in the particle and interface position with small increments in Ca, as shown in Figure 5. Continuation is used to obtain additional solutions beyond the critical capillary number and to more exactly determine the exact value of the critical capillary number, which is 0.0361.

The effects of flow on the equilibrium shape of an interface contacting a particle is next investigated for large contact angles. The equilibrium shapes for $\theta_c = \frac{8\pi}{9}$ and increasing flow strengths with Ca = Cg ranging from 0.0 (static) to 0.304 are shown in Figure 9. As the flow strength increases, the interface curvature again increases and the contact line moves up the particle, thus increasing the capillary force in the positive z direction and decreasing the negative buoyancy force. The effects of increasing the flow strength (i.e., increase of Ca=Cg) are weaker for large contact angles (i.e. a larger change in the capillary number is required to obtain the same change in the contact line position ϕ), essentially

because the capillary restoring force is larger for large contact angles, and, since less of the particle is exposed to the lower fluid and the viscous force is *relatively* unimportant compared to cases for smaller θ_c. For large contact angles, as seen in Figure 10, the dominant balance over a considerable range of Ca values is between positive capillary forces and negative buoyancy forces. Only for larger Ca does the viscous force become of comparable magnitude, eventually leading again to a limit point, and a corresponding critical condition for capture stability. For large contact angles, the buoyancy force is always large and negative, although it gradually becomes less of a factor in trying to pull the particle off the interface for increasing Ca. The moderate interface depression for the small capillary numbers considered here produces only a small contribution to the buoyancy force, and the weight of the large portion of the particle above the interface is always large enough to yield a large negative net buoyant force.

As the limit point is approached in Figure 9, the particle/interface configuration again becomes more and more sensitive to small increases in Ca and Cg. This effect is seen in Figure 11 where the equilibrium particle position h and contact line position ϕ are shown as a function of the capillary number. As the critical capillary number is approached, the contact line position ϕ increases rapidly and the particle position h decreases rapidly, although the change in slope is more gradual than in the case of small contact angles. For large contact angles the buoyancy force is more important, and therefore the position of the contact line at the critical limit point does not coincide as closely with the point of a maximum in the capillary contact line force. However, the critical limit point does not coincide with a maximum in the buoyancy force either. The dependence of the general form of the buoyancy force on contact line position, ϕ, is shown for several values of interface depression in Figure 12. The buoyancy force reaches a plateau (or maximum depending on h) near $\phi = \frac{\pi}{2}$ in terms of ϕ, but for a given ϕ the buoyancy force always increases for an increasing negative value of h (increasing the meniscus depression). Thus, there is no simple relation

for the maximum of the net buoyancy force, h and ϕ are coupled through the solution for the interface shape. It is not obvious why the critical limit point occurs before either the capillary force or buoyant force reaches a maximum, on the other hand, there is no reason to expect that an equilibrium configuration will necessarily exist at which one of these forces reaches a maximum. In the force balance, these two "restoring" forces balance the viscous destabilizing force. For the case of large contact angles, $\theta_c = \frac{8\pi}{9}$, the viscous force increases in magnitude very rapidly near the limit point both because Ca (=Cg) becomes large (leading to significant interface deformation) and because of the change in configuration (a portion of the upper half of the sphere is exposed to the flow - providing a portion of the sphere for the flow to "push" against rather than just shearing). Therefore, because of the rapid increase of the effects of the flow with the change in the particle-interface configuration, Ca (the flow strength) must actually be decreased to reach the points of the maximum for the buoyancy or capillary forces. If Ca were increased, the magnitude of the buoyancy and capillary force (even if both at their maximum values) would be insufficient to hold the particle attached to the interface against the magnitude of the viscous force.

For large contact angles, the importance of the buoyancy force is even more evident in the case where Ca is increased by decreasing the surface tension (i.e., increasing Ca with Cg fixed). The equilibrium interface shapes for $\theta_c = \frac{8\pi}{9}$, Cg=0.05 and Ca increasing from 0.05 to 0.215 are shown in Figure 13. For this case, the limit point (corresponding to capture instability) occurs at a significantly smaller Ca (0.218, not shown) compared to the case where Ca=Cg, although the final contact line and particle positions are approximately the same in the two cases. This behavior can be explained partly by Figure 14, where the forces are shown for the increase in Ca with Cg fixed. As in Figure 8, the capillary force in this case is decreasing (which can be thought of as being because of a decrease in the surface tension). Thus, the buoyancy force must

balance both the decrease in the capillary force and the increase in the negative viscous force. Therefore, the interface *depression*, which is mainly responsible for the increase in the buoyancy force for intermediate ϕ (Figure 12), must be larger for the same values of Ca compared to the previous case where Ca = Cg. As a consequence, the final equilibrium particle/interface configuration is reached at a smaller Ca for a drop in surface tension. Because of the increased inportance of the buoyancy force in this case, the variation in h and ϕ (Figure 11) is smooth up until the maximum in the buoyancy force is reached, (shown on Figure 12), at which point the slopes of h and ϕ versus Ca diverge and continuation is again used to obtain further solutions. As before, for large contact angles the contact line position, ϕ, at the critical capillary number is smaller than the ϕ at which the capillary force reaches a maximum, since the buoyancy force has a significant effect in this case; i.e., the weight of the particle above the contact line plays a significant role in forcing the particle from the interface even for neutrally buoyant particles. It is interesting to note that the relatively small magnitude of the viscous force in Figure 14 is accompanied by large changes in the capillary and buoyancy forces, however, this is not a case of a small change in one variable producing a large change in two other variables. Rather, the large decrease in the capillary force results from the decrease in the surface tension (change in the weighting factor $\frac{Cg}{Ca}$ which appears in Equation (14)) and this is balanced by a large increase in the buoyancy force.

The final situation investigated in detail is the case where the contact angle is intermediate between wetting and nonwetting, $\theta_c = \frac{\pi}{2}$. The interface contours and magnitude of the forces acting on the particle for the situation where Ca is increased by increasing the flow strength (Cg=Ca) are shown in Figures 15 and 16, respectively. Also, the interface contours and magnitude of the forces acting on the particle for the situation where Ca is increased by decreasing the surface tension (Cg=0.05) are shown in Figures 18 and 19. The equilibrium interface shapes and final equilibrium configuration are very similar for the two cases.

However, the buoyancy force is more important in the case with decreasing surface tension since in this case the drop in capillary force and the increase in the negative viscous force must both be balanced by the buoyancy force. Compared to the situation with a large contact angle, the magnitude of the buoyancy force is small here (although less negative), since much of the particle is submerged in the lower fluid in this case. Therefore, the ϕ at which no solutions are found coincides more closely with the ϕ for a maximum in the contact force for $\theta_c = \frac{\pi}{2}$ compared to large contact angles. For increasing flow, the buoyancy force and capillary force again contribute approximately equally to balancing the increase in the negative viscous force. Similar to what we observe for large contact angles, the rate of change of ϕ and h with Ca shown in Figure 17 is initially significantly faster for increases in Ca arising from decreases in the surface tension compared to increases in Ca arising from increases in the flow strength. However, for large Ca, the behavior for Cg fixed is more similar to what is observed for small contact angles, since the capillary force has a more significant contribution compared to the buoyancy force at this point, because less of the particle is protruding above the interface meniscus for the smaller contact angle and the larger Ca. Therefore, it is not surprising that the critical capillary number at which no further solutions can be found coincides more closely with the contact line position at which the capillary force is a maximum.

Before concluding this section, we wish to briefly discuss two special cases; first, a case involving very small values of the contact angle (a fluid which strongly wets the particle surface and is therefore difficult to capture in a flotation process), and, second, a case involving a non-neutrally buoyant particle.

It was noted earlier that an attempt was made to obtain steady-state solutions, under flow conditions, for a contact angle, $\theta_c = \frac{\pi}{9}$. However, we are unable to obtain steady state solutions, even for extremely weak flows with Ca = Cg = 0.01. It had been noted earlier, by Boucher and Jones (1983), that only extremely small particles with a density very close to that of the fluid, i.e.,

$\frac{\rho_p}{\rho} \approx 1$, can achieve a stable equilibrium configuration, even in the static limit. The interface contours for Ca = Cg = 0 are plotted in Figure 3 for $\frac{\rho_p}{\rho} = 1$, and for $\frac{\rho_p}{\rho} = ???$. These interface contours are plotted relative to a coordinate system fixed at the center of the particle. For $\frac{\rho_p}{\rho} > ???$, no steady-state solutions could be attained. With the knowledge gained from the case $\theta_c = \frac{\pi}{4}$, discussed earlier, we can now understand this sensitivity to $\frac{\rho_p}{\rho}$ and the resultant difficulty of affecting separations by flotation for systems with small contact angle. The difficulty for small θ_c is that there is only a very small range of contact line positions, with $\phi \approx \pi$, where the capillary force acts in the positive z direction to support the particle against the net "buoyancy" force (or in the presence of flow, the viscous force) which acts to pull the particle from the interface, and even in this range the maximum magnitude of the capillary force is small. This can be seen most graphically by examining the variation in the capillary force contribution as a function of contact line position for $\theta_c = \frac{\pi}{9}$, as shown in Figure 6. The capillary force is positive only for $2.8 < \phi < 3.14$, and the maximum magnitude is smaller than 0.2. In this case, only infinitesimal flows can be withstood by a neutrally buoyant particle with Ca = Cg < 0.01.

An indication of the effect of particle density on the equilibrium configuration is shown in Figure 20, where equilibrium sphere-interface configurations are shown for a particle of density $\rho_p = 1.25\rho$ for increasing Ca = Cg and $\theta_c = \frac{8\pi}{9}$. These configurations can be compared with Figure 9, where the neutral density particle is considered. This comparison is purposely made for large contact angles, since we expect the changes in the particle surface area that is exposed to the flow, due to increases in the flow strength, to be largest for this case, thus presumably increasing the sensitivity of the results to changes in the particle density. In comparing Figures 9 and 20, we note that the critical capillary number falls from 0.3 to 0.2 with the increase in particle density. Also, the interface is significantly less curved near the particle for the large particle density case, no doubt, as a result of the lower critical flow rate. The difference

in the interface shapes in Figures 9 and 20 is one indication of the complicated interactions between the flow field, the interface shape, and the force balance on the particle. This interaction can be seen even more clearly in Figure 21, where the sphere position as a function of capillary number is plotted from Figures 9 and 20. Although the shapes of the curves are similar, if one were to attempt to extrapolate between the results for the neutral-density flow case and the dense static particle case to obtain the critical capillary number for a dense particle in a flow, the estimated value of Ca would be off by at least 0.05, as can be seen from the shifted form of the curve for $\rho_p = 1.25\rho$. Thus, we conclude that estimates of the combined effects of flow and particle density, obtained by a simple interpolation between the flow effects described in this paper and the effects of particle density described in Boucher and Jones (1981) will be in error because of the nonlinear interactions of these effects. However, it is not difficult to obtain solutions for various particle densities and flow strengths using the method outlined in this paper.

Finally, as a guide in calculating the range of selective separations that may be possible to obtain through use of the flow field, the critical capillary numbers for all cases considered in this paper with neutral density particles are shown in Figure 22. The critical capillary number falls rapidly for small contact angles because of the decreased effectiveness of the restoring capillary force. Also, there can be a significant spread in the critical capillary number between the cases where changes in Ca result from increased flow, and cases where changes in Ca result from decreased surface tension. This spread again points up the increased importance of buoyancy forces at large capillary number. From these critical capillary numbers, the maximum particle size which can be separated or the minimum contact angle for a particle of fixed size could be calculated for a given system with all other parameters specified.

Conclusions

Even a very small amount of flow can greatly affect the stability of particles

contacting fluid interfaces, especially for small contact angles. Even for large contact angles, corresponding to hydrophobic particles, the flow has a significant effect on the particle-interface configuration and the stability of captured particles, but the effects are seen at larger (although still small) capillary numbers. The effects of increasing the capillary number by increasing the flow strength (i.e., with Ca = Cg) or decreasing the surface tension (i.e., Cg fixed) are smaller for large contact angles because the capillary restoring force is larger for large contact angles and also because the viscous destabilizing force is smaller, since less of the particle is exposed to the lower fluid.

The configuration at which the critical capillary number is reached depends on the contact angle. For small contact angles, the contact line position, ϕ, at which the final equilibrium solution is found, coincides closely with the contact line position at which the capillary force reaches a maximum for the given contact angle. Since the net buoyancy force is small for small contact angles, the viscous force balances the capillary force for small contact angles. Beyond the critical (or limit) point, increases in the flow strength or decreases in the surface tension cannot be balanced by increases in the capillary force since this force is already at a maximum, and a steady state configuration is not possible. For large contact angles, on the other hand, the contact line position (as designated by ϕ) at the critical capillary number is smaller than the contact line position where the capillary force reaches a maximum. In this case the bouyancy force has a significant effect, as the weight of the particle above the contact line plays an important role in forcing the particle from the interface. As the critical capillary number is approached, small increases in the flow strength or small decreases in the surface tension produce large changes in the particle and contact line positions.

For large contact angles, the critical point occurs at a smaller Ca when decreasing the surface tension (i.e., holding Cg constant) than when increasing the flow strength (keeping Ca=Cg). This occurs because the decrease in the capil-

lary force and the increase in viscous forces which occurs when Ca is increased with Cg=constant, must *both* be balanced by the increase in buoyancy forces. This results in larger interface deformations and greater changes in the contact line position for a given increment in Ca than for a corresponding increase in Ca with Ca = Cg. When increasing the flow strength, (i.e., Ca with Ca = Cg) the increase in the viscous force is balanced approximately equally by an *increase* in both the capillary and buoyancy forces. At small contact angles, the buoyancy force is very small for neutrally buoyant particles, and the solutions exhibit approximately the same sensitivity to increases in flow strength and decreases in surface tension.

Appendix A: Contact Point Determination

A two point right handed difference scheme is used to determine the contact line position such that the contact angle has the desired macroscopic value. In the representation for the interface, z=f(r), the contact line radial position (which is undetermined) is denoted as r_0, the first node point on the interface is r_1, the second node point on the interface is r_2, and so on. The vertical positions of the interface at the first and second node points can be represented in terms of Taylor series expansions about the contact line position as

$$f(r_0 + \Delta r_1) = f(r_0) + \Delta r_1 f'(r_1) + \frac{\Delta r_1{}^2}{2} f''(r_0) + \cdots, \tag{1}$$

$$f(r_0 + \Delta r_1 + \Delta r_2) = f(r_0) + (\Delta r_1 + \Delta r_2) f'(r_1) + \frac{(\Delta r_1 + \Delta r_2)^2}{2} f''(r_0) + \cdots, \tag{2}$$

where, $\Delta r_1 = r_1 - r_0$, $\Delta r_2 = r_2 - r_1$. Combining these two equations, we obtain,

$$f(r_0) = \left[\left(\frac{\Delta r_1 + \Delta r_2}{\Delta r_1} \right)^2 f(r_1) - f(r_2) - (\Delta r_1 + \Delta r_2) f'(r_0) \frac{\Delta r_2}{\Delta r_1} \right] \left[\left(\frac{\Delta r_1 + \Delta r_2}{\Delta r_1} \right)^2 - 1 \right]^{-1}. \tag{3}$$

The slope of the interface at the contact line, $f'(r_0)$, is determined by the macroscopic contact angle and the geometry of the problem as,

$$f'(r_0) = tan(\phi + \theta_c) = \frac{tan\phi + tan\theta_c}{1 - tan\theta_c tan\phi}, \tag{4}$$

where, $tan\phi = \frac{r_0}{(1-r_0^2)^{\frac{1}{2}}}$. And the condition, that the first node point lies on the sphere is

$$f(r_0) = h + (1 - r_0^2)^{\frac{1}{2}}. \tag{5}$$

Substituting Equations (4) and (5) into Equation (3), we obtain a nonlinear algebraic equation for r_0, in terms of the known values h, r_1, r_2, $f(r_1)$, $f(r_2)$ and θ_c. The old value of r_0 is used as an initial guess along with a Newton's method scheme to solve this relation for r_0, the new contact line position on the sphere which satisfies the required macroscopic contact angle. method

Appendix B: Static Shape Determination

In the following Appendix, we describe our method for calculating the particle-interface configuration for the static (no-flow) case. Although the statics problem has been considered by a number of previous workers, our method involves some modifications which enable a straightforward calculation of the particle-interface configuration given the physical parameters of the system, rather than being forced to set one of these parameters (e.g., particle size) to satisfy the force balance on the particle.

The Young-Laplace equation represents the balance between the hydrostatic pressure difference across the interface because of different densities in the upper and lower fluids and the surface tension force because of the interface curvature. In terms of Figure 1, it can be expressed in the form

$$\sigma \left(\frac{\frac{d^2z}{dr^2}}{[1 + (\frac{dz}{dr})^2]^{\frac{3}{2}}} + \frac{\frac{dz}{dr}}{r[1 + (\frac{dz}{dr})^2]^{\frac{1}{2}}} \right) - g\rho z = 0. \tag{1}$$

Equation (1) is a second-order nonlinear ordinary differential equation for the interface shape, expressed as z=f(r), which must be solved subject to the boundary conditions

$$\frac{dz}{dr} = tan\beta_o \quad \text{at} \quad r = r_o \tag{2}$$

$$\left.\begin{array}{l} \frac{dz}{dr} \to 0 \quad \text{as} \quad r \to \infty \\ z \to 0 \quad \text{as} \quad r \to \infty \end{array}\right\} \tag{3}$$

In addition to the basic nonlinearity of the problem, the solution of (1) is complicated by the fact that boundary conditions (2) and (3) comprise a two-point boundary value problem with one of the boundaries at infinity. This must be solved numerically and the interface truncated at some large but finite value of r. The method used in the present work for the solution of the statics problem, is similar in many respects to that used by Rapacchietta and Neumann, and Huh and Scriven.

In the static problem it is convenient to nondimensionalize lengths by $l_c = \sqrt{\frac{\sigma}{g\rho}}$, so that y $\equiv \frac{z}{l_c}$ and $x \equiv \frac{r}{l_c}$. After parameterizing the interface in terms of the angle of inclination, β (shown in Figure 1), one obtains, Huh and Scriven (1969),

$$\frac{dx}{d\beta} = \frac{x cos\beta}{xy - sin\beta} \tag{4}$$

$$\frac{dy}{d\beta} = \frac{x sin\beta}{xy - sin\beta} \tag{5}$$

with boundary conditions

$$x = x_o, \quad y = y_o \quad \text{at} \quad \beta = \beta_o, \tag{6}$$

$$y \to 0, \quad x \to \infty \quad \text{as} \quad \beta \to 0. \tag{7}$$

The net force on the particle at equilibrium is given by

$$F_{\text{net}} = \left(-\frac{4}{3}\pi\frac{\rho_p}{\rho} - \pi\frac{h}{a}sin^2\phi - \frac{2}{3}\pi cos^3\phi + \frac{2}{3}\pi \right)$$

$$-2\pi sin\phi sin(\phi + \theta_c) \left\{ \frac{\sigma}{a^2 g\rho} \right\} = 0, \tag{8}$$

where the last term is the ratio $\frac{C_g}{C_a} = (\frac{l_c}{a})^2$, the ratio of surface tension forces to density forces, which is equivalent to the ratio of the two length scales in the problem. The relations arising from the geometry of the problem are

$$\phi = \beta_o + \pi - \theta_c, \tag{9}$$

$$x_o = \frac{a}{l_c}\, sin(\beta_o - \theta_c), \tag{10}$$

$$y_o = -\frac{h}{l_c} + \frac{a}{l_c} cos(\beta_o - \theta_c), \tag{11}$$

where x_o, y_o, and β_o are the values of x, y, and β at the contact line. With a $\hat{a}$, θ_c and $\frac{\rho_p}{\rho}$ specified, the physical problem is determined and the mathematical problem is well posed with h, β_o and the shape all determined as part of the solution.

This solution is obtained by the shooting method since interpolation via the tables of Huh and Scriven, combined with iteration on the force balance is inaccurate and slow. The method of Rapacchietta and Neumann is modified to calculate the full sphere position and interface shape, which satisfies the force balance on the sphere rather than calculates the net force with an assumed contact line position, and iterates on the particle size until the force balance is satisfied. A difficulty arises because the starting point x_o, y_o and shooting angle β_o are all unknown. The method of solution involves: guessing β_o; calculating ϕ from (9); with the value of ϕ just calculated the force balance is solved for $\frac{h}{l_c}h$, then x_o and y_o are determined from (10) and (11); finally, Equations (4) and (5) are integrated using a 4th order predictor- corrector method from β_o to some sufficiently small value of $\beta(=\beta_f)$ close to zero where boundary condition (7) is checked for y $\approx$ 0. If this condition is not satisfied, a new β_o is chosen. The new β_o is calculated using Newton's method such that the new values of β_o, x_o and y_o produce a y_f which is closer to zero. Since x and y are coupled, the effect of x_o, y_o and β_o on both x and y must be computed. Thus, since

$$\frac{dx}{d\beta} = f(x, y, \beta), \tag{12}$$

$$\frac{dy}{d\beta} = g(x, y, \beta). \tag{13}$$

We define

$$\epsilon \equiv \frac{\partial x}{\partial y_o}, \quad \gamma \equiv \frac{\partial x}{\partial \beta_o}, \quad \xi \equiv \frac{\partial x}{\partial x_o}, \tag{14}$$

$$\eta \equiv \frac{\partial y}{\partial y_o}, \quad \delta \equiv \frac{\partial y}{\partial \beta_o}, \quad \alpha \equiv \frac{\partial y}{\partial x_o}. \tag{15}$$

The dependence of x and y on x_o, y_o and β_o is given by

$$\frac{\partial}{\partial x_o}\left(\frac{dx}{d\beta}\right) = \frac{d}{d\beta}\left(\frac{\partial x}{\partial x_o}\right) = \frac{d\xi}{d\beta} = \frac{\partial f}{\partial x}\frac{\partial x}{\partial x_o} + \frac{\partial f}{\partial y}\frac{\partial y}{\partial x_o} = f_x\xi + f_y\alpha \qquad (16)$$

$$\frac{\partial}{\partial x_o}\left(\frac{dy}{d\beta}\right) = \frac{d}{d\beta}\left(\frac{\partial y}{\partial x_o}\right) = \frac{d\alpha}{d\beta} = \frac{\partial g}{\partial x}\frac{\partial x}{\partial x_o} + \frac{\partial g}{\partial y}\frac{\partial y}{\partial x_o} = g_x\xi + g_y\alpha \qquad (17)$$

$$\frac{\partial}{\partial y_o}\left(\frac{dx}{d\beta}\right) = \frac{d}{d\beta}\left(\frac{\partial x}{\partial y_o}\right) = \frac{d\epsilon}{d\beta} = \frac{\partial f}{\partial x}\frac{\partial x}{\partial y_o} + \frac{\partial f}{\partial y}\frac{\partial y}{\partial y_o} = f_x\epsilon + f_y\eta \qquad (18)$$

$$\frac{\partial}{\partial y_o}\left(\frac{dy}{d\beta}\right) = \frac{d}{d\beta}\left(\frac{\partial y}{\partial y_o}\right) = \frac{d\eta}{d\beta} = \frac{\partial g}{\partial x}\frac{\partial x}{\partial y_o} + \frac{\partial g}{\partial y}\frac{\partial y}{\partial y_o} = g_x\epsilon + g_y\eta \qquad (19)$$

$$\frac{\partial}{\partial \beta_o}\left(\frac{dx}{d\beta}\right) = \frac{d}{d\beta}\left(\frac{\partial x}{\partial \beta_o}\right) = \frac{d\gamma}{d\beta} = \frac{\partial f}{\partial x}\frac{\partial x}{\partial \beta_o} + \frac{\partial f}{\partial y}\frac{\partial y}{\partial \beta_o} = f_x\gamma + f_y\delta \qquad (20)$$

$$\frac{\partial}{\partial \beta_o}\left(\frac{dy}{d\beta}\right) = \frac{d}{d\beta}\left(\frac{\partial y}{\partial \beta_o}\right) = \frac{d\delta}{d\beta} = \frac{\partial g}{\partial x}\frac{\partial x}{\partial \beta_o} + \frac{\partial g}{\partial y}\frac{\partial y}{\partial \beta_o} = g_x\gamma + g_y\delta. \qquad (21)$$

The coefficients f_x, f_y, g_x and g_y are given by Rapacchietta and Neumann as

$$f_x(x,y,\beta) = \frac{(-sin\beta cos\beta)}{(xy - sin\beta)^2}, \qquad (22)$$

$$f_y(x,y,\beta) = \frac{(-x^2 cos\beta)}{(xy - sin\beta)^2}, \qquad (23)$$

$$g_x(x,y,\beta) = \frac{(-sin^2\beta)}{(xy - sin\beta)^2}, \qquad (24)$$

$$g_y(x,y,\beta) = \frac{(-x^2 sin\beta)}{(xy - sin\beta)^2}. \qquad (25)$$

Now the procedure is to integrate (4),(5) and (16)-(21) simultaneously from the initial conditions β_o with

$$\epsilon_o = 0,\ \eta_o = 1,\ \xi_o = 1,\ \alpha_o = 0,$$

$$\gamma_o = -\frac{a}{l_c}\, cos(\beta_o - \theta_c)$$

$$\delta_o = \frac{8\frac{a}{l_c}\rho_p cos(\beta_o - \theta_c)}{3\rho sin^3(\beta_o - \theta_c)} - \frac{2cos\beta_o}{\frac{a}{l_c}\, sin(\beta_o - \theta_c)} + \frac{2sin\beta_o cos(\beta_o - \theta_c)}{\frac{a}{l_c}\, sin^2(\beta_o - \theta_c)}$$

$$- \frac{2\frac{a}{l_c}\, cos^2(\beta_o - \theta_c)}{sin(\beta_o - \theta_c)} - \frac{4\frac{a}{l_c}\, cos^4(\beta_o - \theta_c)}{3sin^3(\beta_o - \theta_c)} - \frac{4\frac{a}{l_c}\, cos(\beta_o - \theta_c)}{3sin^3(\beta_o - \theta_c)}$$

to the point β_f. Then y_f is compared to zero and x_f is checked to see whether it is sufficiently large. If these conditions are not met Newton's method is used to increment β_o to β_o'

$$\beta_o' = \beta_o - w \frac{y(\beta_f)}{\frac{dy}{d\beta_o}\Big|_{\beta_f}},$$

$$\left.\frac{dy}{d\beta_o}\right|_{\beta_f} = \frac{\partial y}{\partial \beta_o} + \frac{\partial y}{\partial x_o}\frac{\partial x_o}{\partial \beta_o} + \left.\frac{\partial y}{\partial y_o}\frac{\partial y_o}{\partial \beta_o}\right|_{\beta_f},$$

where w is a relaxation factor ≤ 1, used to prevent divergence of the solution. The entire procedure is then repeated until $y_f \approx 0$ and $x_f > R_o$ the truncation distance.

References

Boucher, E.A. and Evans, M.J.B., 1975 Pendant drop profiles and related capillary phenomena. *Proc. R. Soc. A.* **346**, 349.

Boucher, E.A., Evans, M.J.B. and Kent, H.J., 1976 Capillary phenomena. II. Equilibrium and stability of rotationally symmetric fluid bodies. *Proc. R. Soc. A.* **349**, 81.

Boucher, E.A. and Kent, H.J., 1977 Capillary phenomena III. Properties of rotationally symmetric fluid bodies with one asymptote - holms. *Proc. R. Soc. A.* **356**, 61.

Boucher, E.A. and Kent, H.J., 1978 Capillary phenomena Part 6. - Behavior associated with the flotation and mechanical manipulation of solid spheres at fluid interfaces. *J. Chem. Soc. Faraday Trans. I* **74**, 846.

Boucher, E.A. and Jones, T.G.J., 1981 Empirical criteria for the flotation of a solid sphere at an interface in a gravitational field. *J. Coll. Int. Sci.* **83**, 645.

Chi, B. and Leal, L.G., 1987 A theoretical study of the motion of a viscous drop toward a fluid interface at low Reynolds number. *J. Colloid Interface Sci.* Accepted .

Davis, A.M.J. 1982 Two phase Stokes flows distorted by a sphere straddling the interface. *Int. J. Multiphase Flow* **8**, 361.

Derjaguin, B.V. and Dukhin, S.S. 1979 Kinetic theory of the flotation of fine particles. *Proceedings of 13th International Mineral Processing Congress, Warsaw*, (Elsevier, Amsterdam, 1981).

Dussan V., E.B. 1979 On the spreading of liquids on solid surfaces: static and dynamic contact lines. *Ann. Rev. Fluid Mech.* **11**, 371.

Falade, A. 1982 Arbitrary motion of an elliptic disc at a fluid interface. *Int. J. Multiphase Flow* **8**, 543.

French, R.M. and Wilson, D.J. 1980 Fluid mechanics - foam flotation interactions. *Sep. Sci. Tech.* **15**, 1213.

Geller, A.S., Lee, S.H. and Leal, L.G. 1986 The creeping motion of a spherical particle normal to a deformable interface. *J. Fluid Mech.* **169**, 27-69.

Girault, H.H.J., Schiffrin, D.J. and Smith, B.D.V. 1982 Drop image processing for surface and interfacial tension measurements. *J. Coll. Int. Sci.* **137**, 207.

Girault, H.H.J., Schiffrin, D.J. and Smith, B.D.V. 1984 The measurement of interfacial tension of pendent drops using a video image digitizer. *J. Electroanal. Chem.* **101**, 257.

Hiemenz, P.C. 1977 *Principles of Colloid and Surface Chemistry* Ch. 6., Dekker Press, New York, N.Y..

Huh, C. and Mason, S.G. 1974 The flotation of axisymmetric particles at horizontal liquid interfaces. *J. Coll. Int. Sci.* **47**, 271.

Huh, C. and Scriven, L.E. 1969 Shapes of axisymmetric fluid interfaces of unbounded extent. *J. Coll. Int. Sci.*, **30** 323.

Ivanov, I.B., Kralchevsky, P.A. and Nikolov, A.D. 1985 Film and line tension effects on the attachment of particles to an interface I. Conditions for mechanical equilibrium of fluid and solid particles at a fluid interface. *J. Coll. Int. Sci.* **112**, 97.

Kantorovich, L.V. and Krylov, V.I. 1958 *Approximate Methods of Higher Analysis*, Interscience, New York, N.Y..

Kralchevsky, P.A., Ivanov, I.B. and Nikolov, A.D. 1985 Film and line tension effects on the attachment of particles to an interface II. Shapes of the bubble (drop) and the external meniscus. *J. Coll. Int. Sci.* **112**, 108.

Kralchevsky, P.A., Nikolov, A.D. and Ivanov, I.B. 1985 Film and line tension effects on the attachment of particles to an interface IV. Experimental studies with bubbles in solutions of dodecyl sodium sulfate. *J. Coll. Int. Sci.* **112**, 132.

Kubicek, M. and Marek, M. 1983 *Computational methods in bifurcation theory and dissipative structures* Springer-Verlag, New York, N.Y..

Ladyzhenskaya, O.A. 1969 *The mathematical theory of viscous incompressible flow* Gordon and Breach, New York, N.Y..

Lee, S.H. and Leal, L.G. 1982 Motion of a sphere in the presence of a deformable interface. Part 2: numerical study of the translation of a sphere normal to an interface. *J. Colloid Int. Sci.* **87**, 81.

Nikolov, A.D., Kralchevsky, P.A. and Ivanov, I.B. 1985 Film and line tension effects on the attachment of particles to an interface III. a differential interferometric method for determination of the shapes of fluid surfaces. *J. Coll. Int. Sci.* **112**, 122.

Princen, H.M. 1963 Shape of a fluid drop at a liquid-liquid interface. *J. Colloid Sci.* **18**, 178.

Princen, H.M. and Mason, S.G. 1965 Shape of a fluid drop at a fluid-liquid interface I. extension and test of a two phase theory. *J. Colloid Sci.* **20**, 156.

Princen, H.M. and Mason, S.G. 1965 Shape of a fluid drop at a fluid-liquid interface II. theory for three-phase systems. *J. Colloid Sci.* **20**, 246.

Rallison, J.M. and Acrivos, A. 1978 A numerical study of the deformation and burst of a viscous drop in an extensional flow. *J. Fluid Mech.* **89**, 191.

Ranger, K.B. 1978 The circular disk straddling the interface of a two-phase flow. *Int. J. Multiphase Flow.* **4**, 263.

Rapacchietta, A.V., Neumann, A.W. and Omenyi, S.N. 1977 Force and free-energy analysis of small particles at fluid interfaces I. cylinders. *J. Colloid Interface Sci.* **59**, 541.

Rapacchietta, A.V., Neumann, A.W. 1977 Force and free-energy analysis of small particles at fluid interfaces II. spheres. *J. Colloid Interface Sci.* **59**, 555.

Rotenberg, Y., Boruvka, L. and Neumann, A.W. 1983 Determination of surface tension and contact angle from the shapes of axisymmetric fluid interfaces. *J. Colloid Interface Sci.* **93**, 169.

Rotenberg, Y., Boruvka, L. and Neumann, A.W. 1984 The shape of nonaxisymetric drops on inclined planar surfaces. *J. Colloid Interface Sci.* **102**, 424.

Smith, P.G. and Van de Ven, T.G.M. 1984 The effect of gravity on the drainage of a thin liquid film between a solid sphere interface and a liquid/fluid interface. *J. Colloid Interface Sci.* **100**, 456.

Stone, H.A., Bentley, B.J. and Leal, L.G. 1986 An experimental study of transient effects in the breakup of viscous drops. *J. Fluid Mech.* **173**, 131.

Stoos, J.A., 1987 Ph.D. dissertation. California Institute of Technology.

Sutherland, K.L. and Wark, I.W. 1955 *Principles of Flotation* Australian Institute of Mining and Metallurgy, Melbourne.

Youngren G.K. and Acrivos, A.A. 1975 Stokes flow past a particle of arbitrary shape: a numerical method of solution. *J. Fluid Mech.* **69**, 377.

Youngren G.K. and Acrivos, A.A. 1976 On the shape of a gas bubble in a viscous extensional flow. *J. Fluid Mech.* **76**, 433.

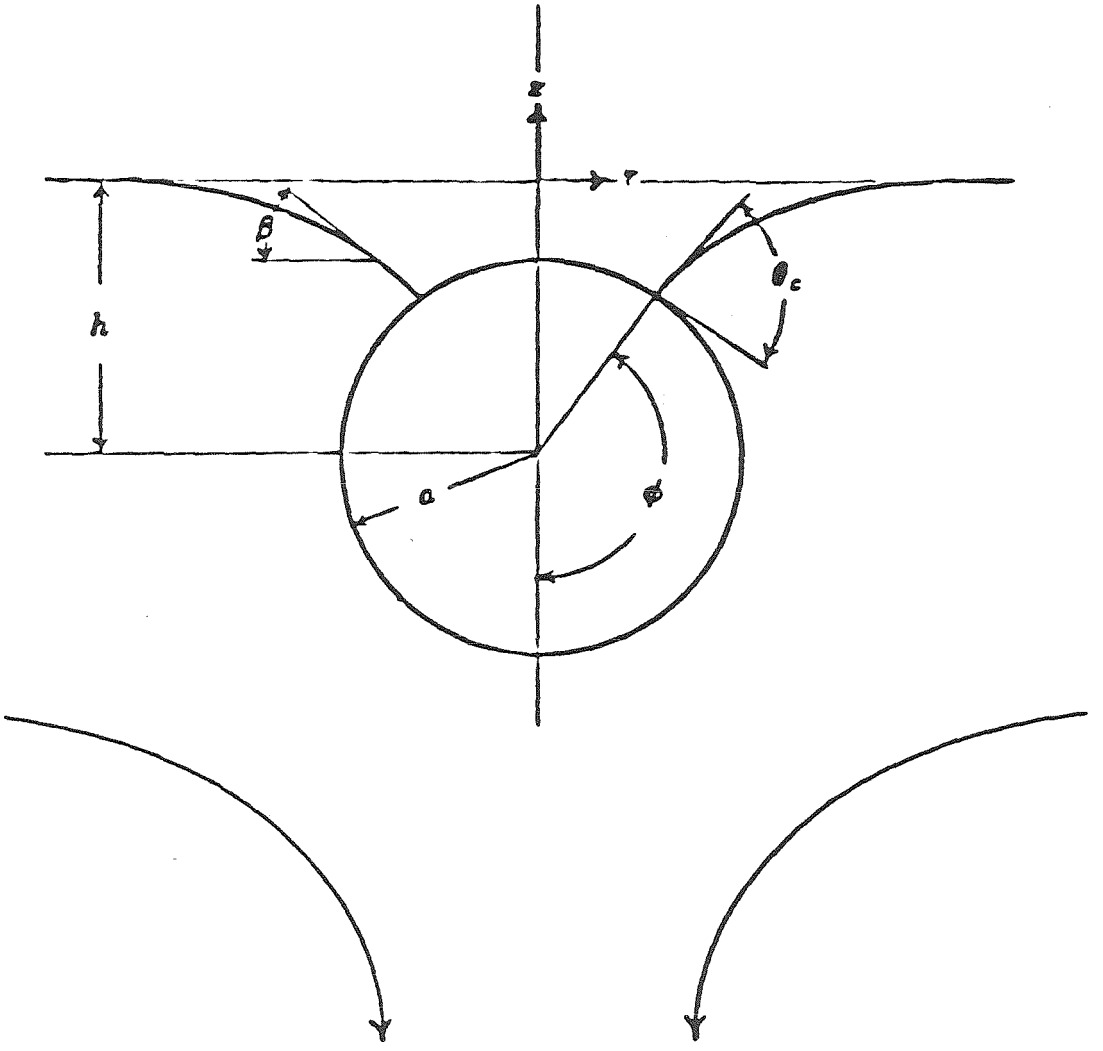

Figure 1. Schematic of problem.

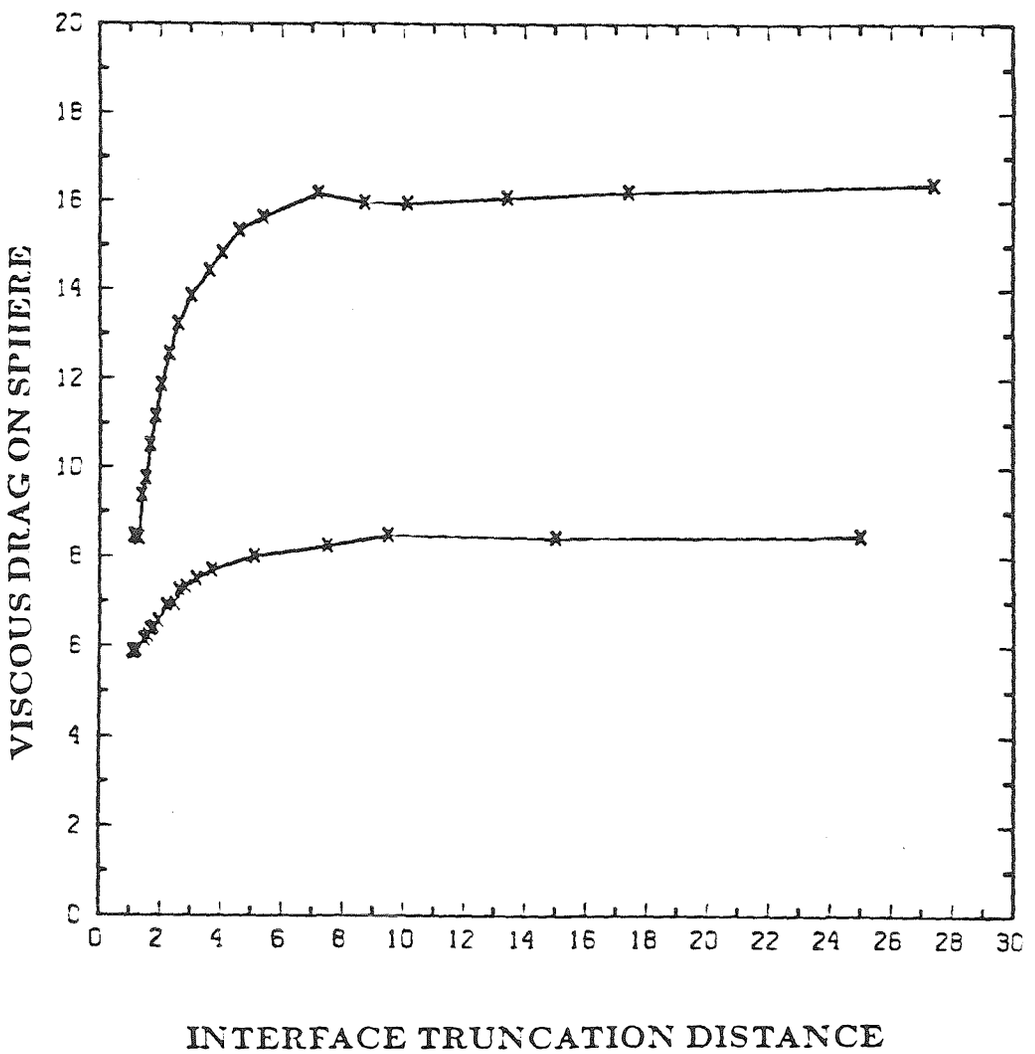

Figure 2. Viscous drag on sphere as a function of interface truncation for $\rho_p = \rho$: $\theta_c = \frac{\pi}{2}$, Ca = 0.1, Cg = 0.05; $\theta_c = \frac{8\pi}{9}$, Cg = Ca = 0.05.

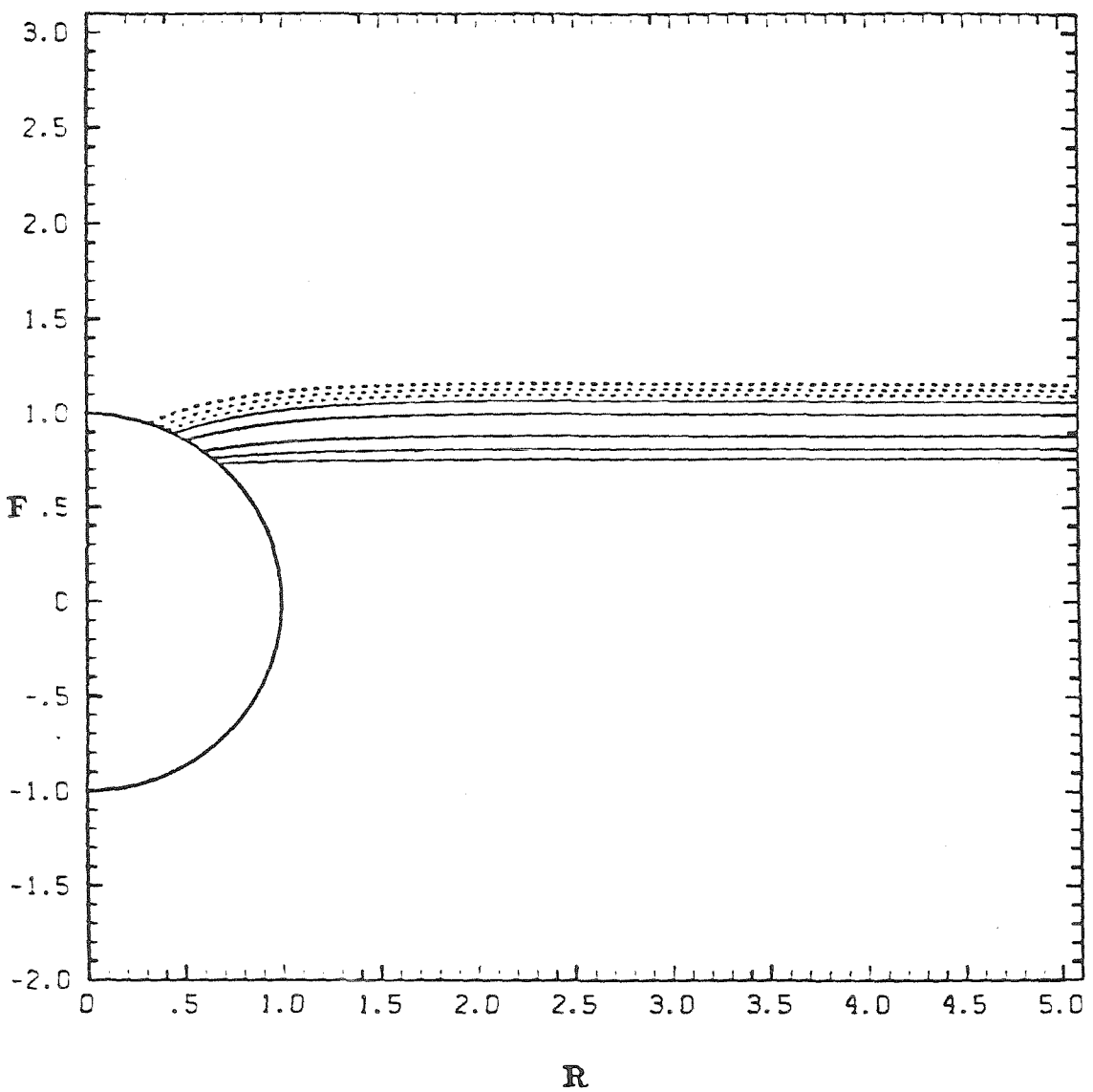

Figure 3. Equilibrium sphere/interface configuration for: $\theta_c = \frac{\pi}{4}$, $\rho_p = \rho$:——, Cg = Ca = 0, 0.01, 0.02, 0.03, 0.0325; - - - - - -, Cg = Ca = 0.0327, 0.0320, 0.0300 (obtained by continuation).

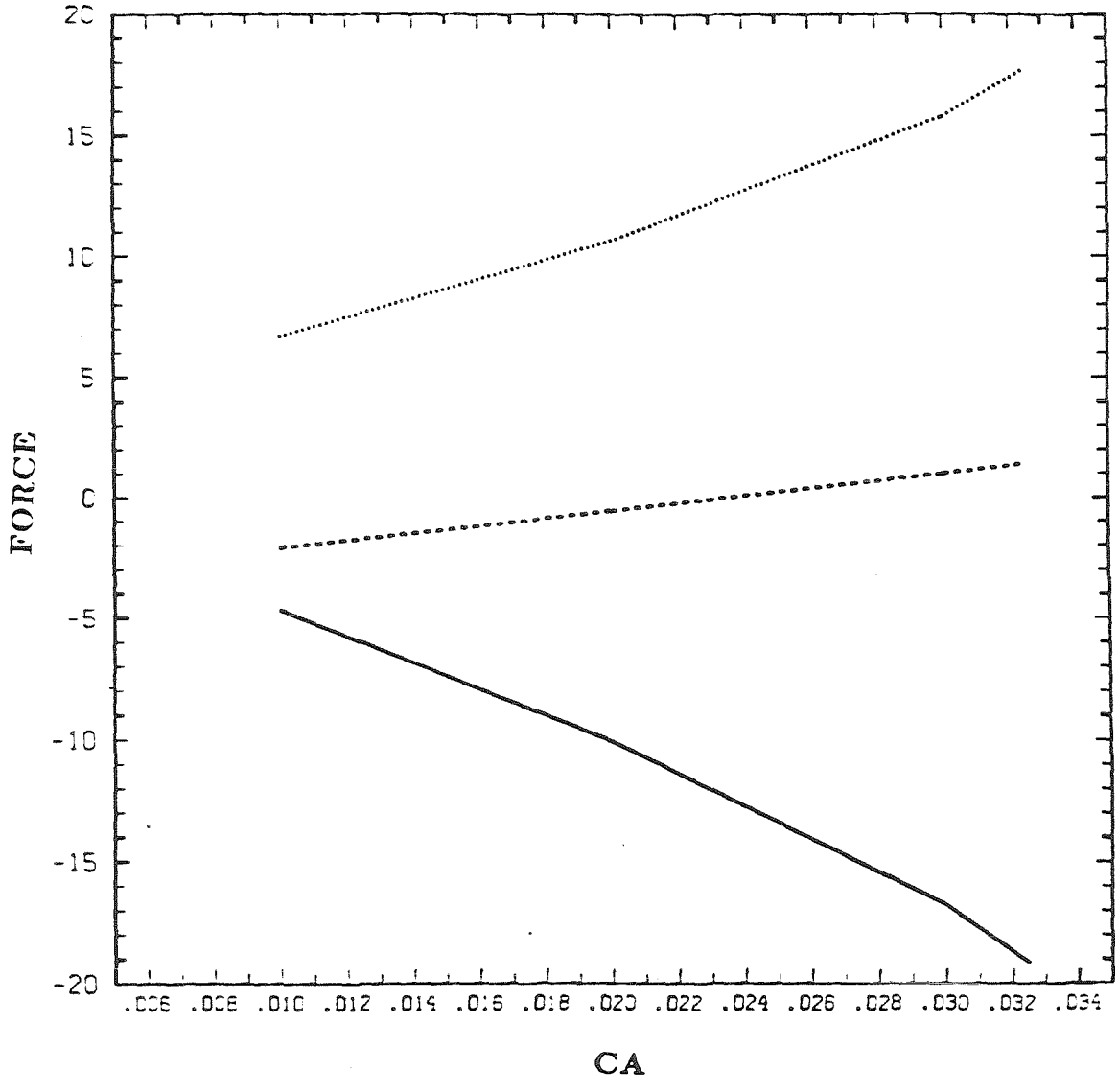

Figure 4. Components of net force acting on sphere as a function of capillary number for $\theta_c = \frac{\pi}{4}$, $\rho_p = \rho$, Cg = Ca: ———, viscous drag; - - - - - -, net buoyancy force; ·····, capillary force.

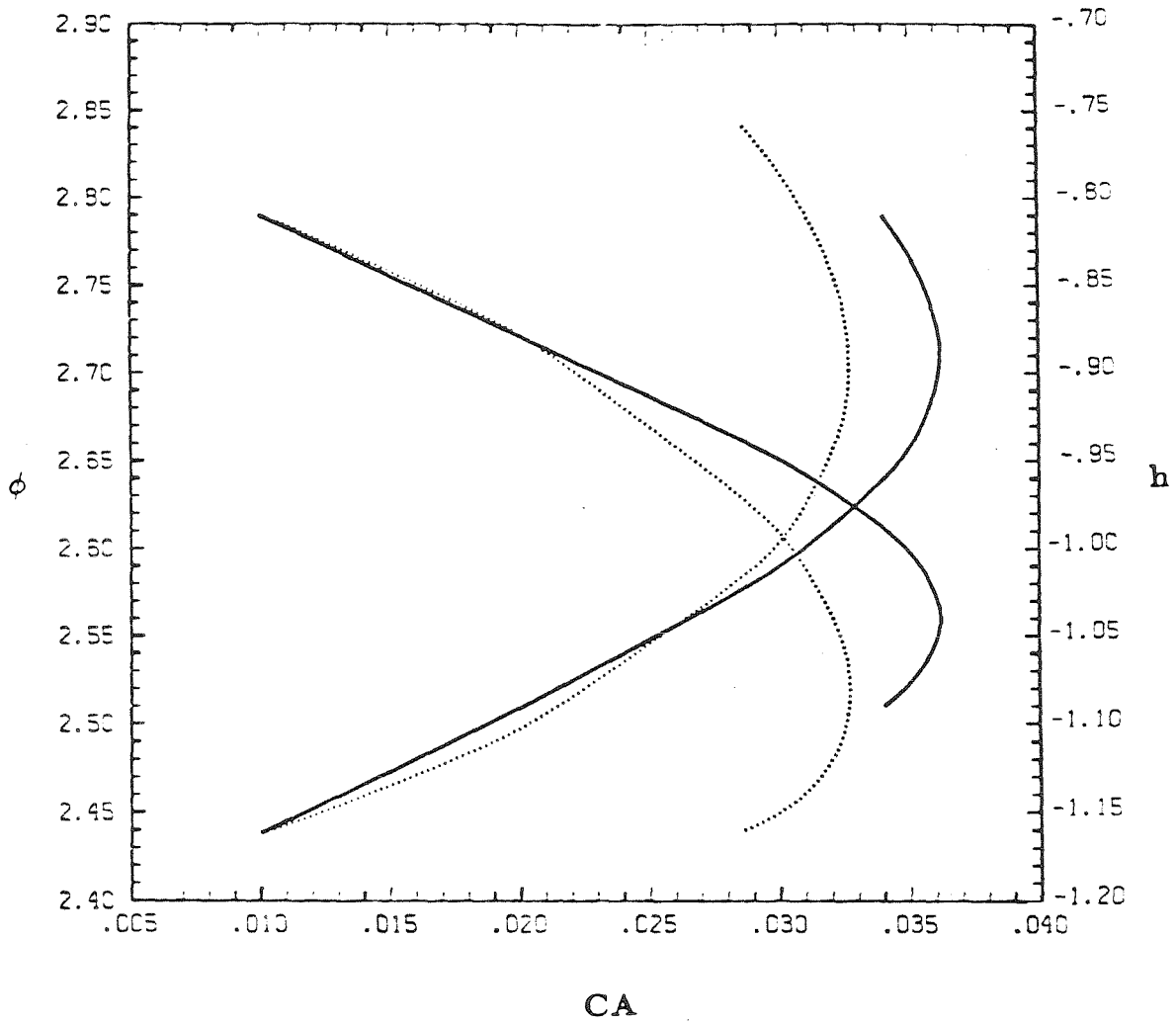

Figure 5. Sphere position, h, and contact line position ϕ as a function of capillary number for $\theta_c = \frac{\pi}{4}$, $\rho_p = \rho$: ———, Cg = 0.01; ·····, Cg = Ca.

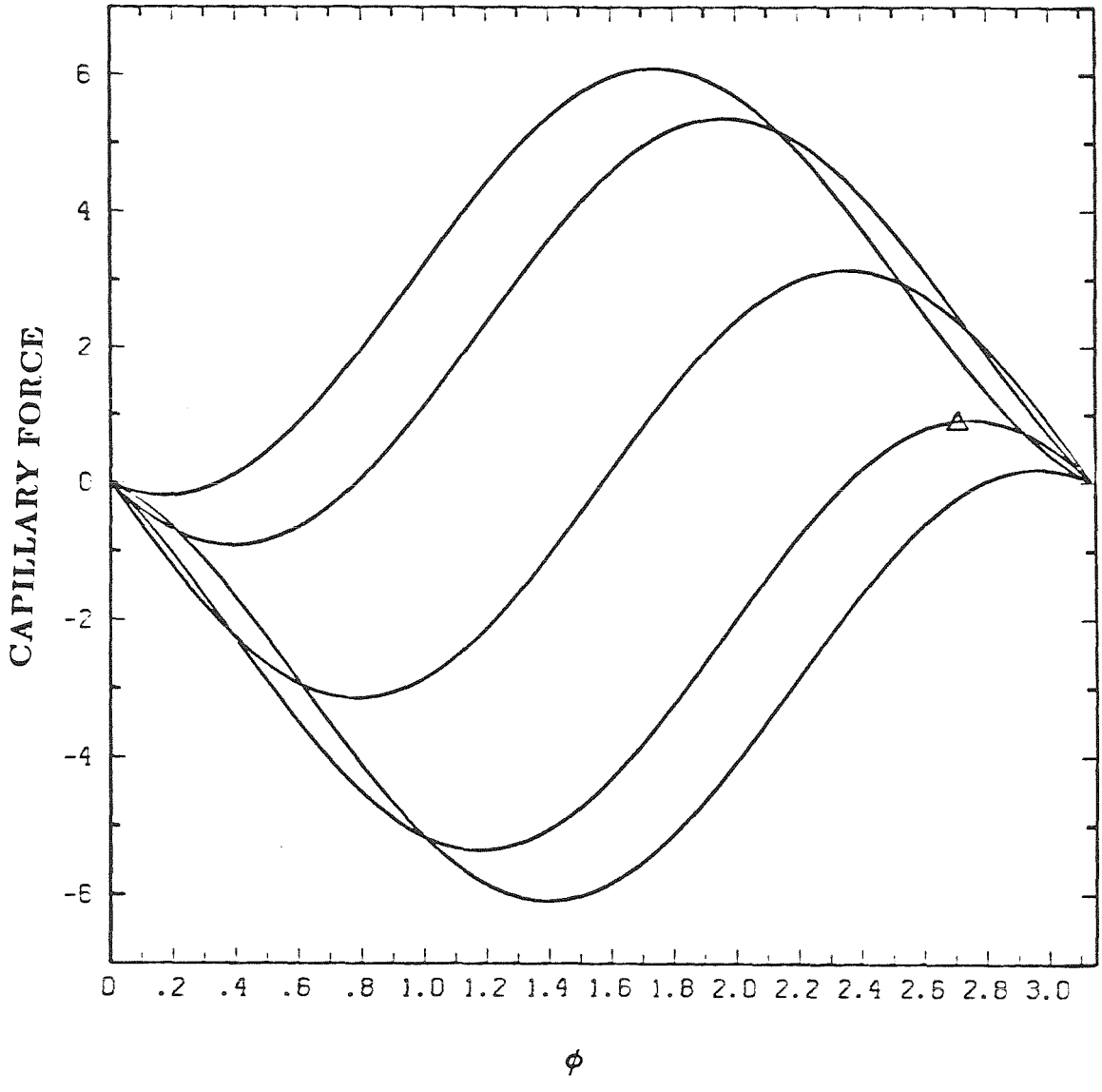

Figure 6. Capillary force as a function of contact line position for contact angles $\theta_c = \frac{\pi}{9}, \frac{\pi}{4}, \frac{\pi}{2}, \frac{3\pi}{4}, \frac{8\pi}{9}$; $\triangle$, contact line position at which critical capillary number occurs for $\theta_c = \frac{\pi}{4}$, Cg = Ca.

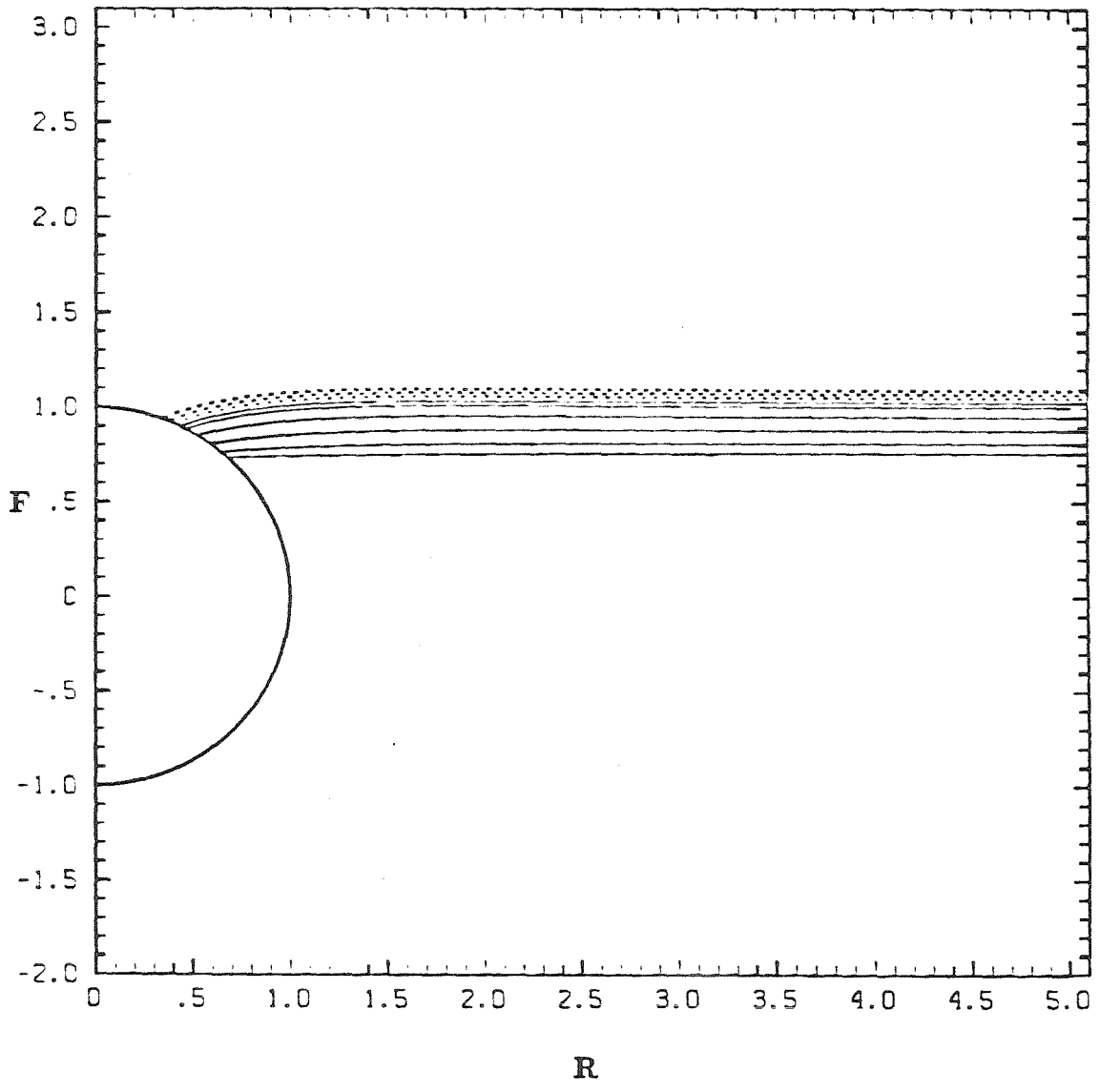

Figure 7 Equilibrium sphere/interface configuration for: $\theta_c = \frac{\pi}{4}$, $\rho_p = \rho$, Cg = 0.01: ———, Ca = 0, 0.01, 0.02, 0.03, 0.035, 0.036; - - - - - - Ca = 0.0361, 0.0354, 0.0340 (obtained by continuation).

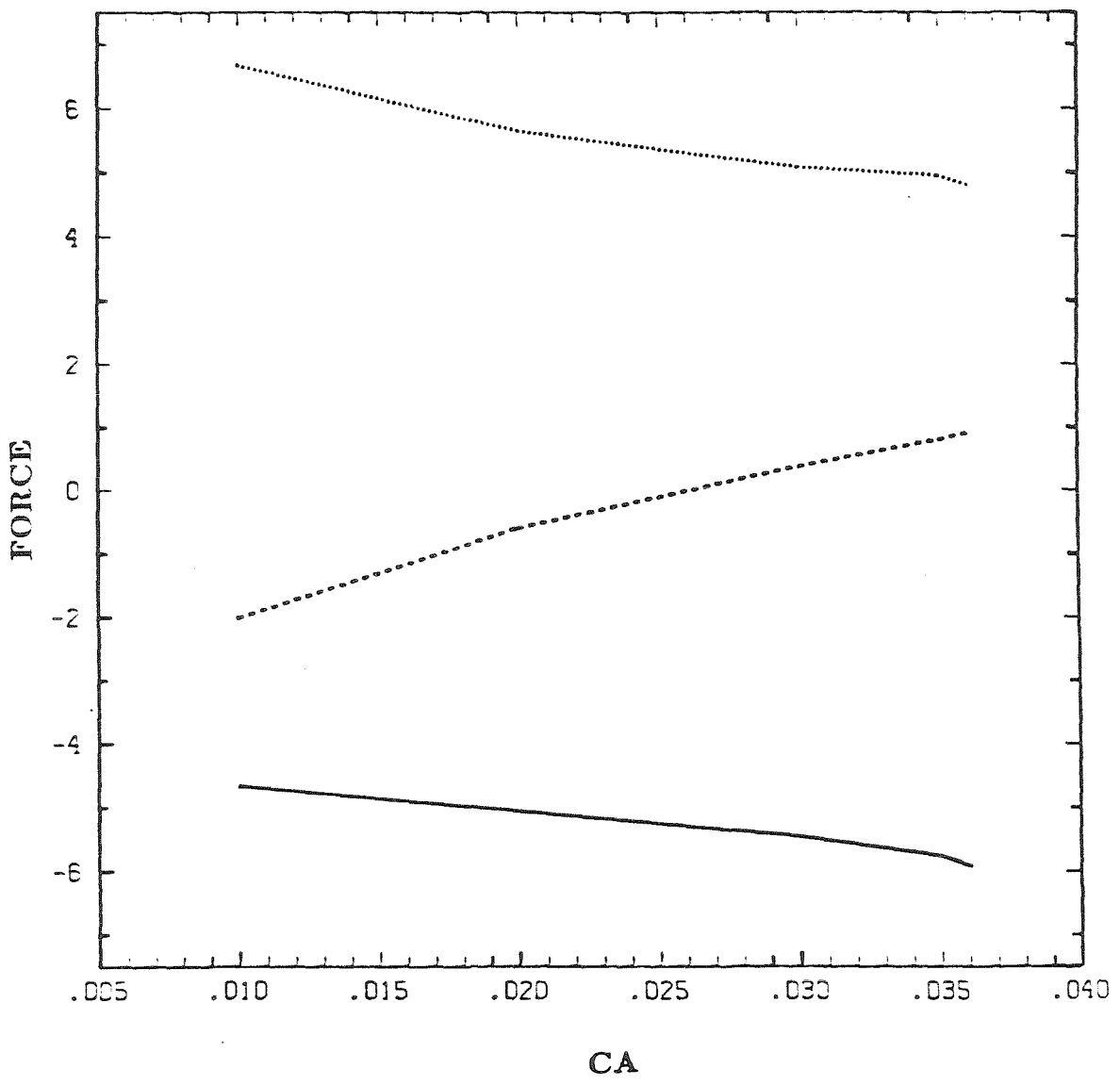

Figure 8. Components of net force acting on sphere for $\theta_c = \frac{\pi}{4}$, $\rho_p = \rho$, Cg = 0.01, as a function of capillary number: ———, viscous drag; - - - - - -, net buoyancy force; ·····, capillary force.

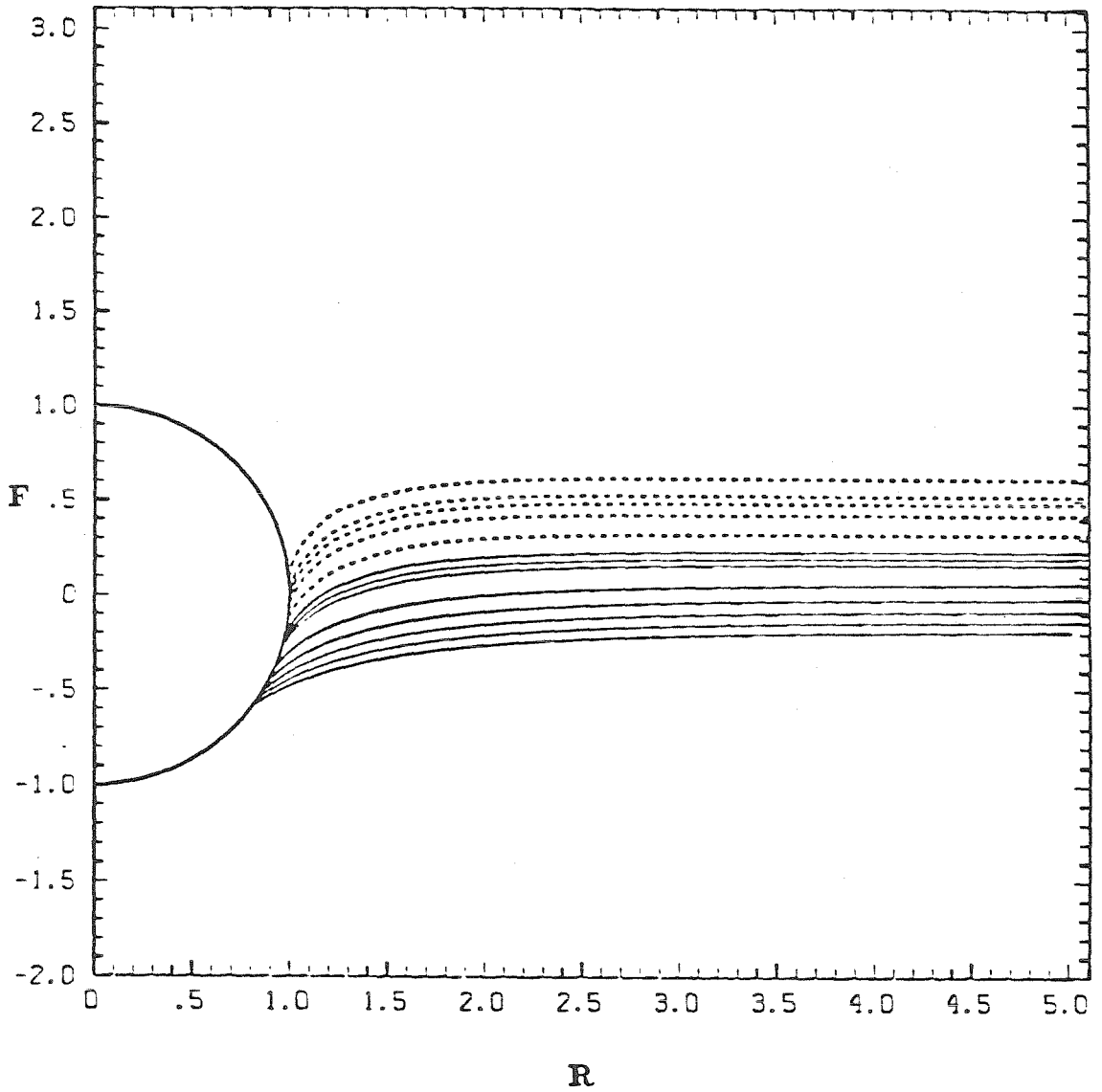

Figure 9. Equilibrium sphere/interface configuration for: $\theta_c = \frac{8\pi}{9}$, $\rho_p = \rho$:——, Cg = Ca = 0, 0.05, 0.1, 0.15, 0.2, 0.25, 0.26, 0.27; - - - - - -, Cg = Ca = 0.286, 0.297, 0.302, 0.304, 0.295 (obtained by continuation).

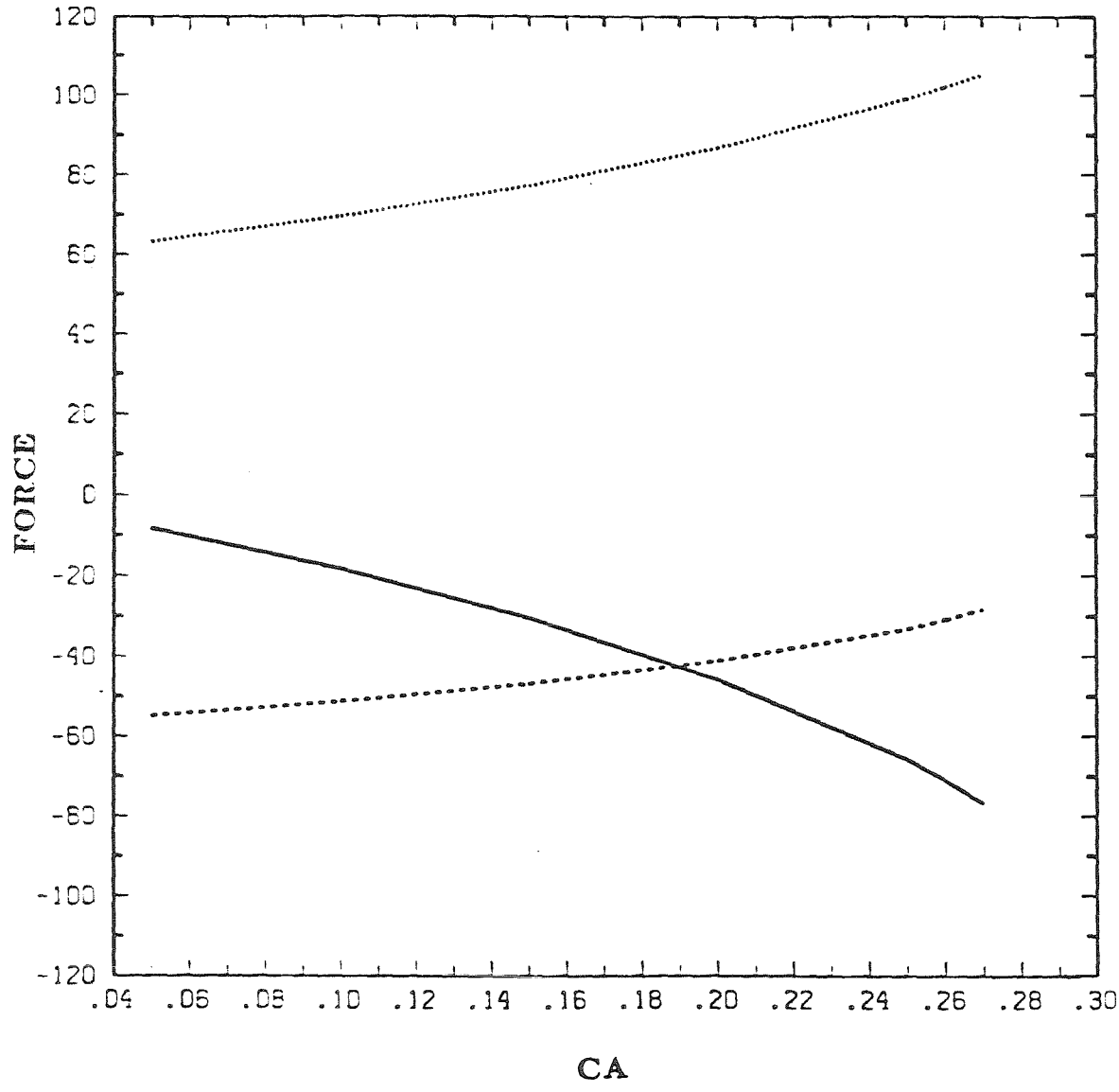

Figure 10. Components of net force acting on sphere for $\theta_c = \frac{8\pi}{9}$, $\rho_p = \rho$, Cg = Ca, as a function of capillary number: ———, viscous drag; - - - - - -, net buoyancy force; ·····, capillary force.

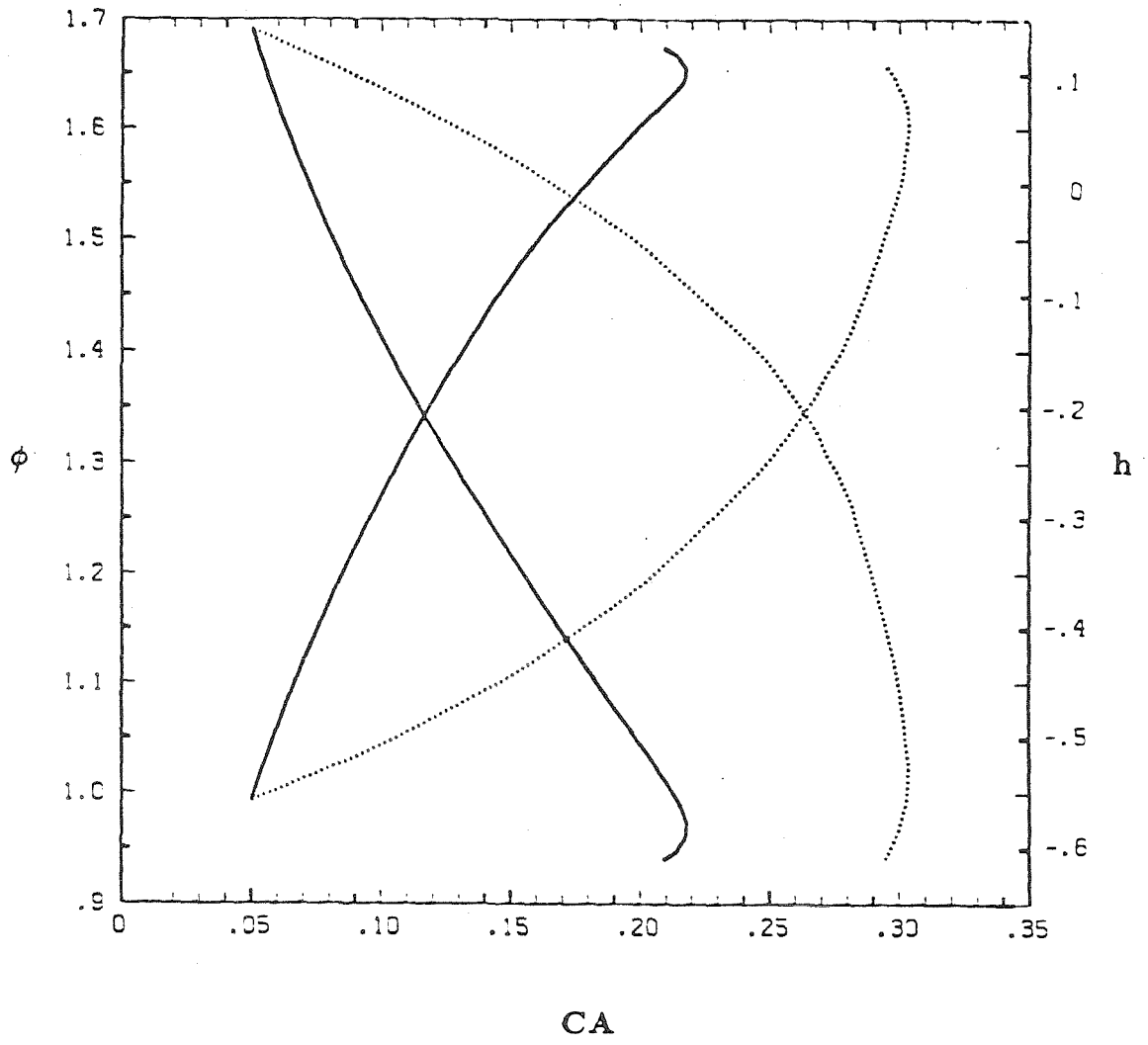

Figure 11. Sphere position, h, and contact line position ϕ as a function of capillary number for $\theta_c = \frac{8\pi}{9}$, $\rho_p = \rho$: ———, Cg = Fixed at minimum value of Ca; ·····, Cg = Ca.

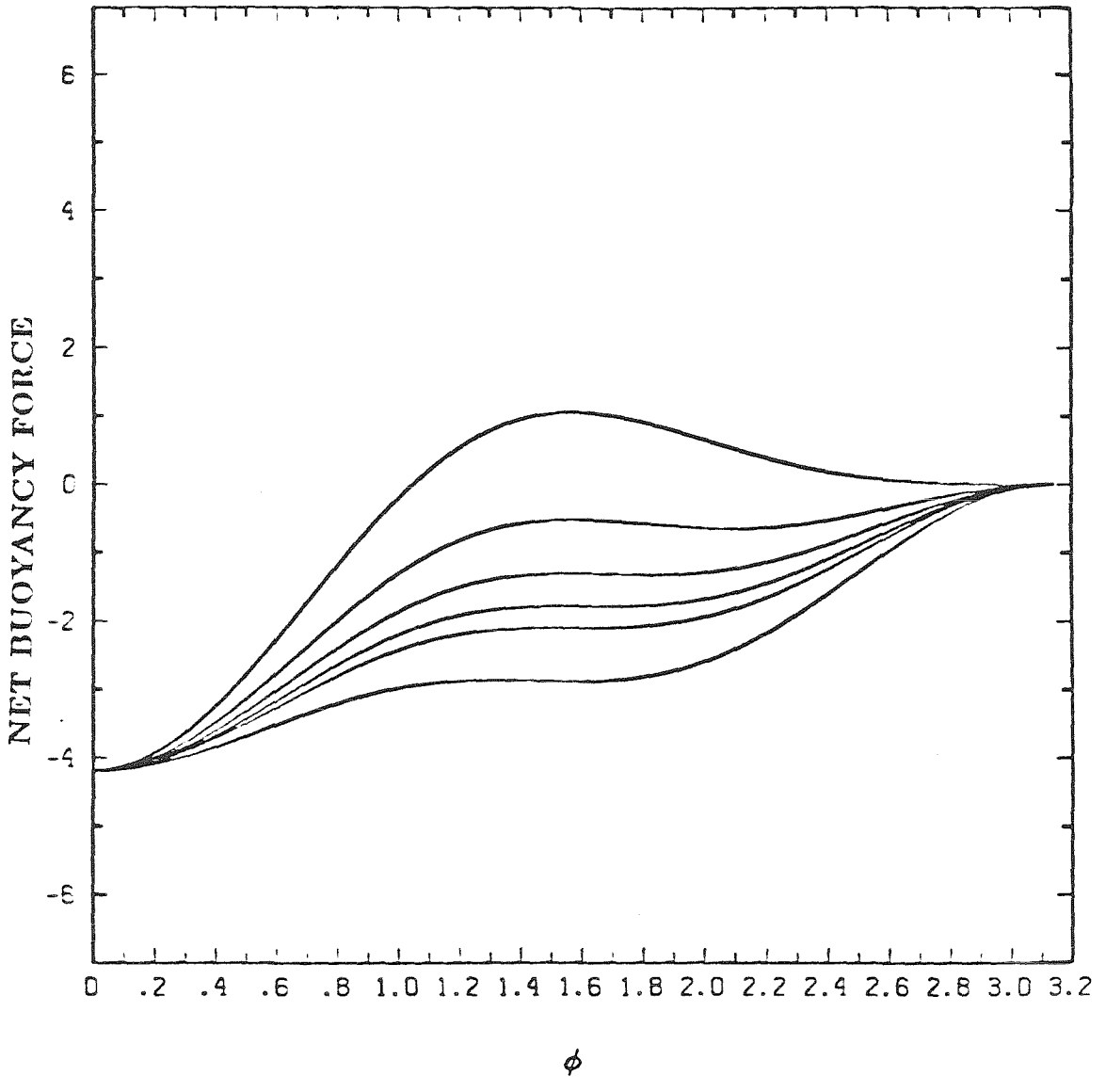

Figure 12. Net buoyancy force as a function of contact line position for sphere position, h = -1., -0.5, -0.25, -0.1, 0, 0.25.

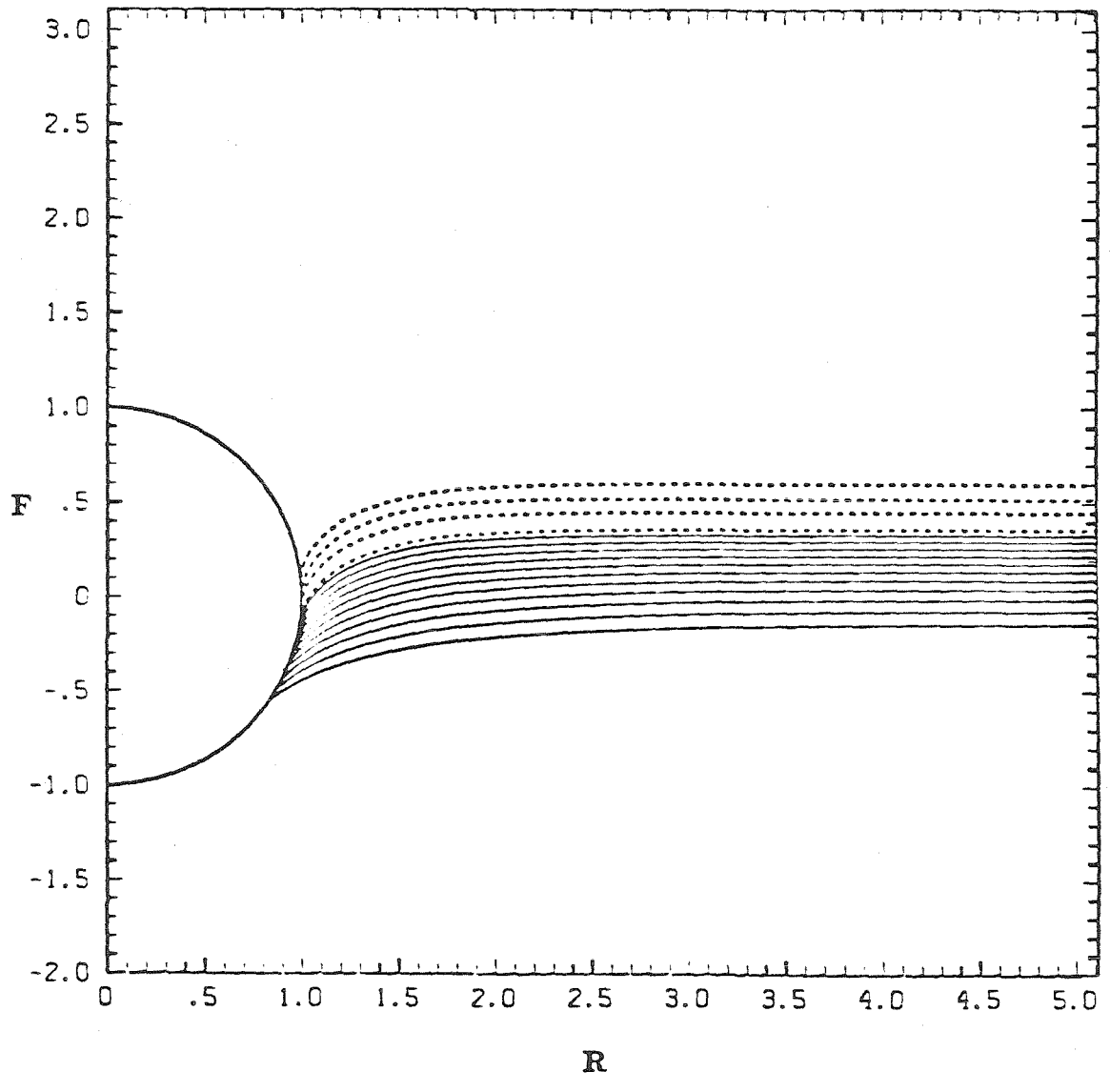

Figure 13. Equilibrium sphere/interface configuration for: $\theta_c = \frac{8\pi}{9}$, $\rho_p = \rho$, Cg = 0.05: ———, Ca = 0.05, 0.06, 0.07, 0.08, 0.09, 0.1, 0.11, 0.12, 0.13, 0.14, 0.15; Ca = 0.158, 0.184, 0.205, 0.215 (obtained by continuation).

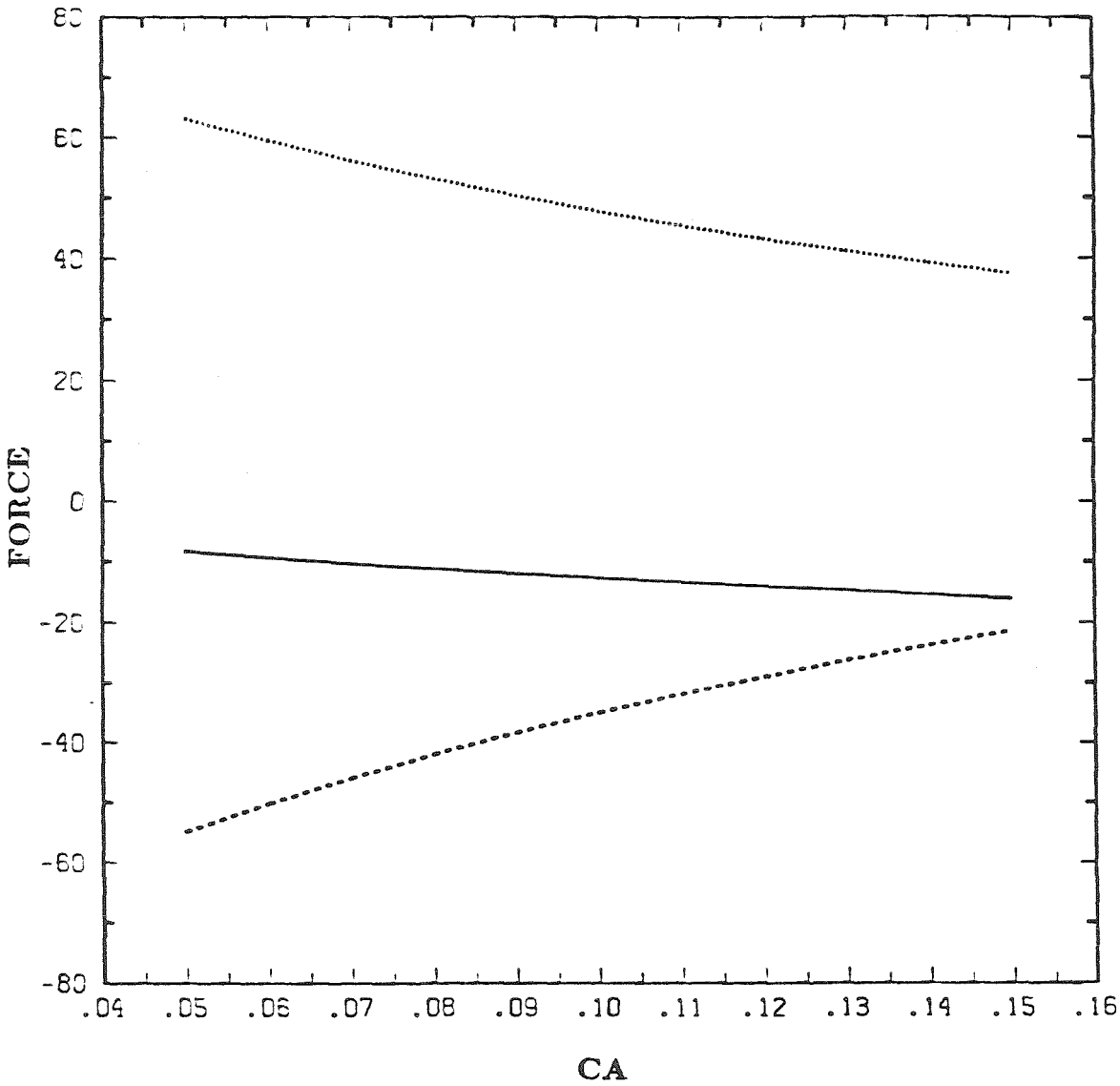

Figure 14. Components of net force acting on sphere for $\theta_c = \frac{8\pi}{9}$, $\rho_p = \rho$, $Cg = 0.05$, as a function of capillary number: ———, viscous drag; - - - - - -, net buoyancy force; ·····, capillary force.

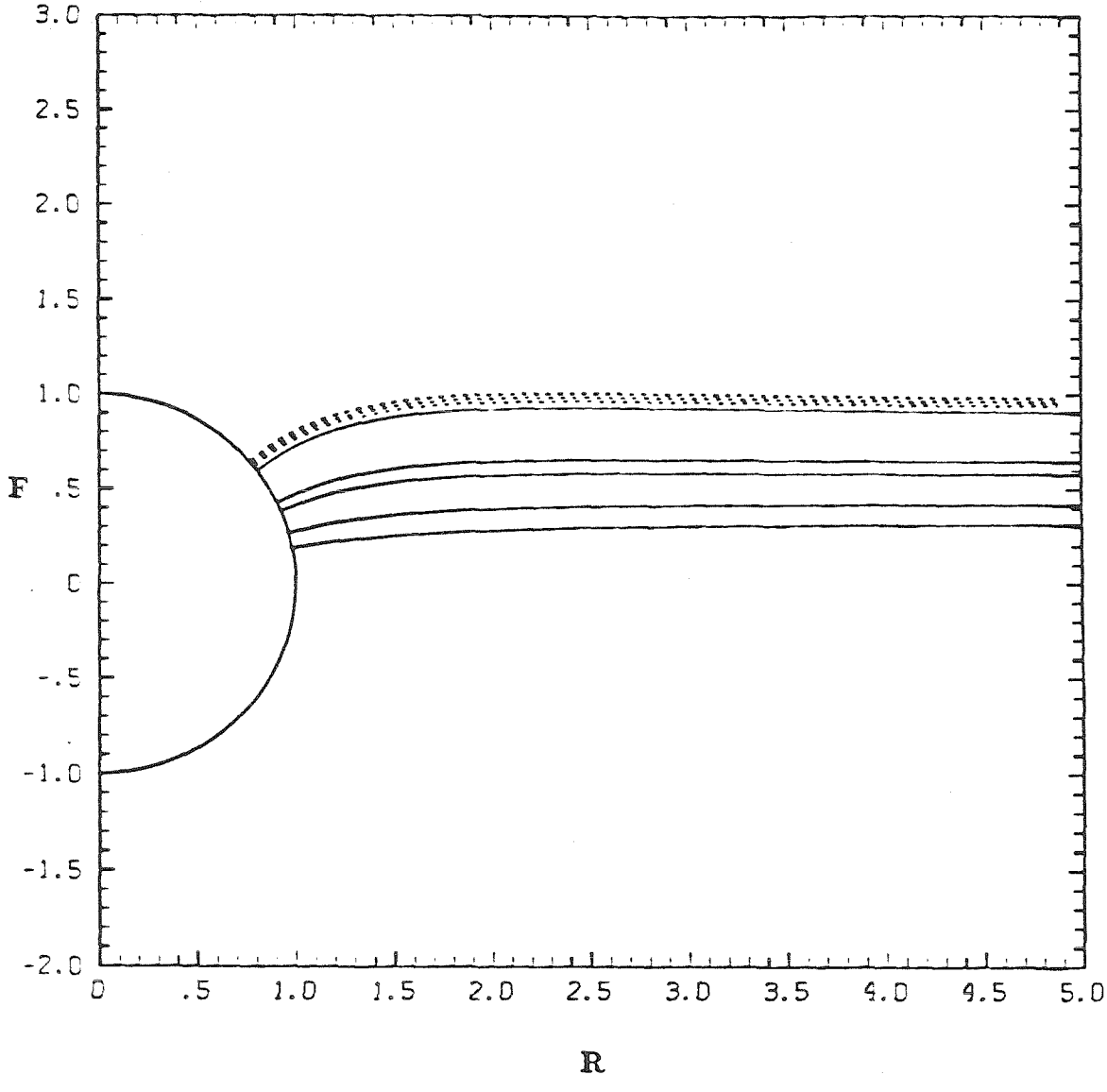

Figure 15. Equilibrium sphere/interface configuration for: $\theta_c = \frac{\pi}{2}$, $\rho_p = \rho$:—, Cg = Ca = 0, 0.05, 0.1, 0.11, 0.125; - - - - - -, Cg = Ca = 0.1253, 0.1255, 0.1250 (obtained by continuation).

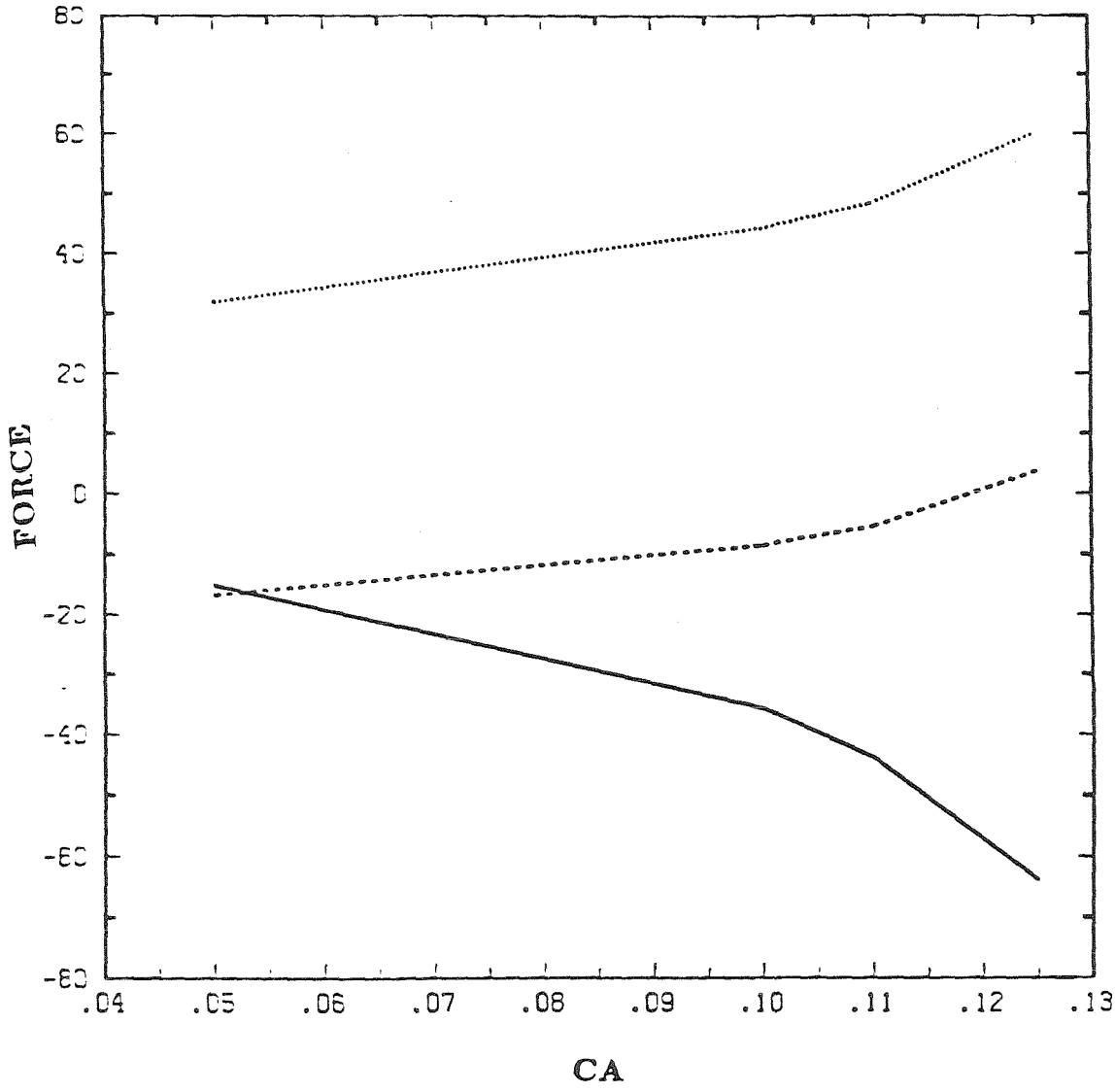

Figure 16. Components of net force acting on sphere for $\theta_c = \frac{\pi}{2}$, $\rho_p = \rho$, Cg = Ca, as a function of capillary number: ———, viscous drag; - - - - - -, net buoyancy force; ·····, capillary force.

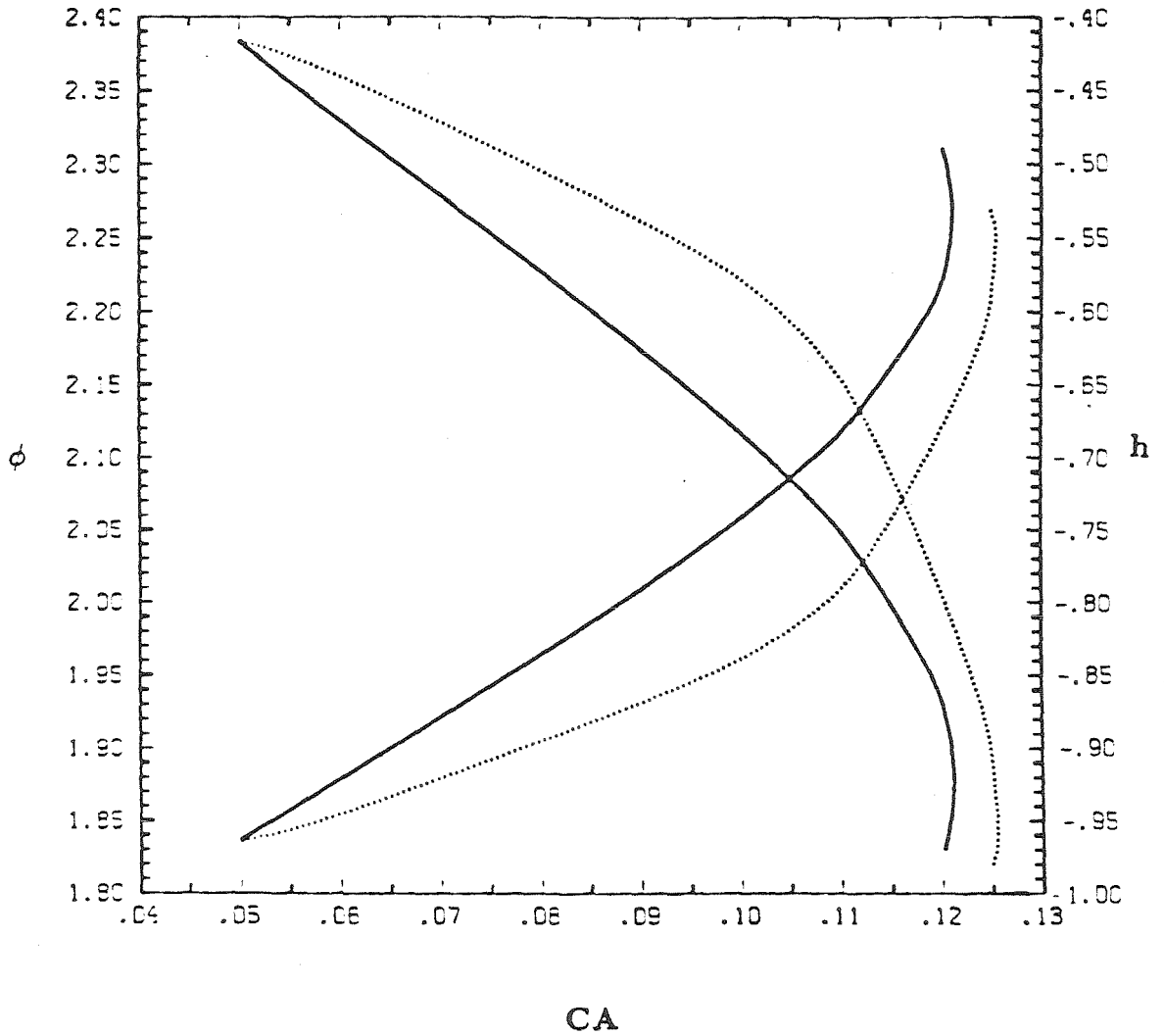

Figure 17. Sphere position, h, and contact line position ϕ as a function of capillary number for $\theta_c = \frac{\pi}{2}$, $\rho_p = \rho$: ———, Cg = Fixed at minimum value of Ca; ·····, Cg = Ca.

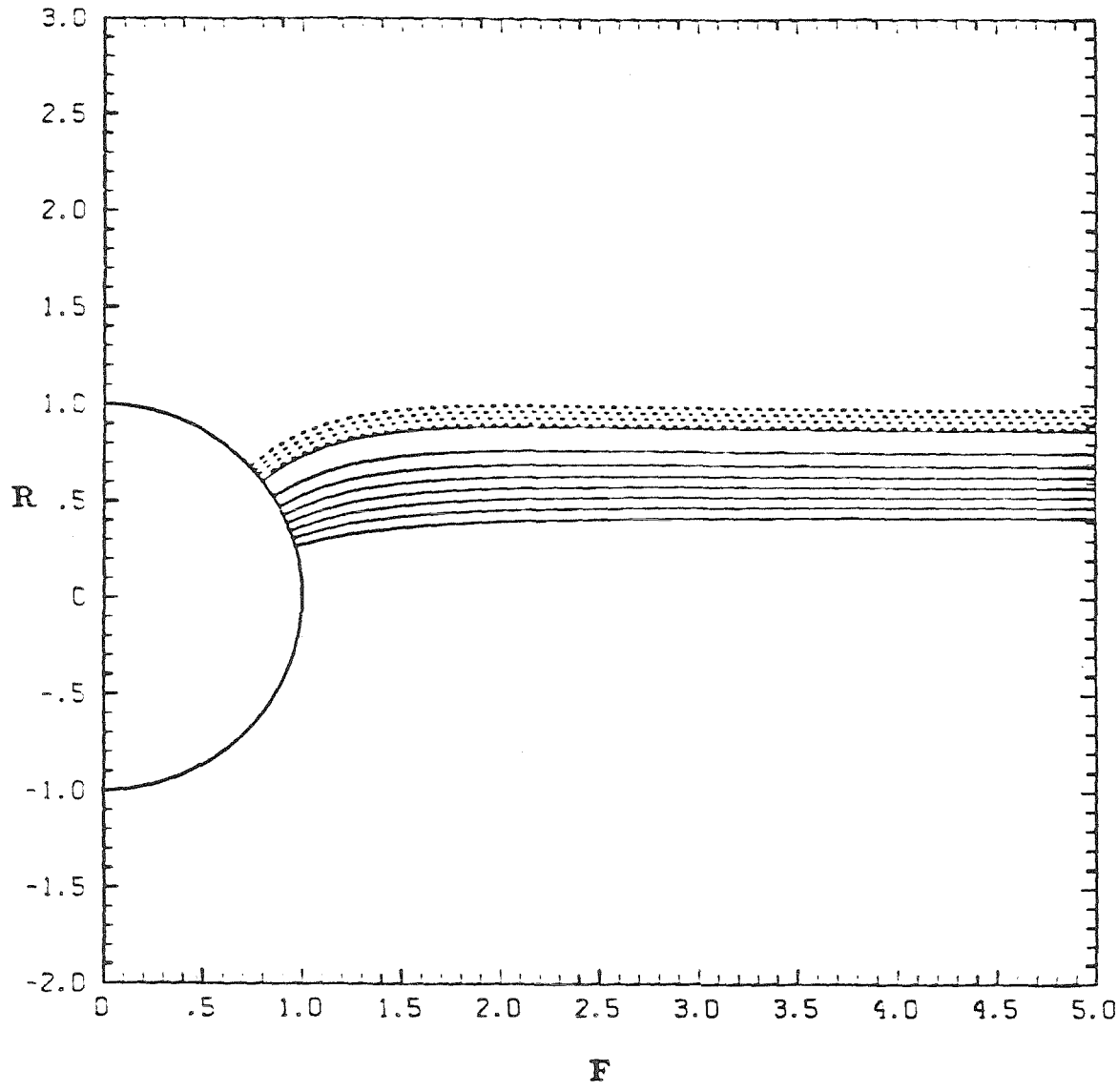

Figure 18. Equilibrium sphere/interface configuration for: $\theta_c = \frac{\pi}{2}$, $\rho_p = \rho$, Cg = 0.05: ——, Ca = 0.05, 0.06, 0.07, 0.08, 0.09, 0.1, 0.11, 0.12; - - - - -, Ca = 0.1205, 0.1211, 0.1210, 0.1202 (obtained by continuation).

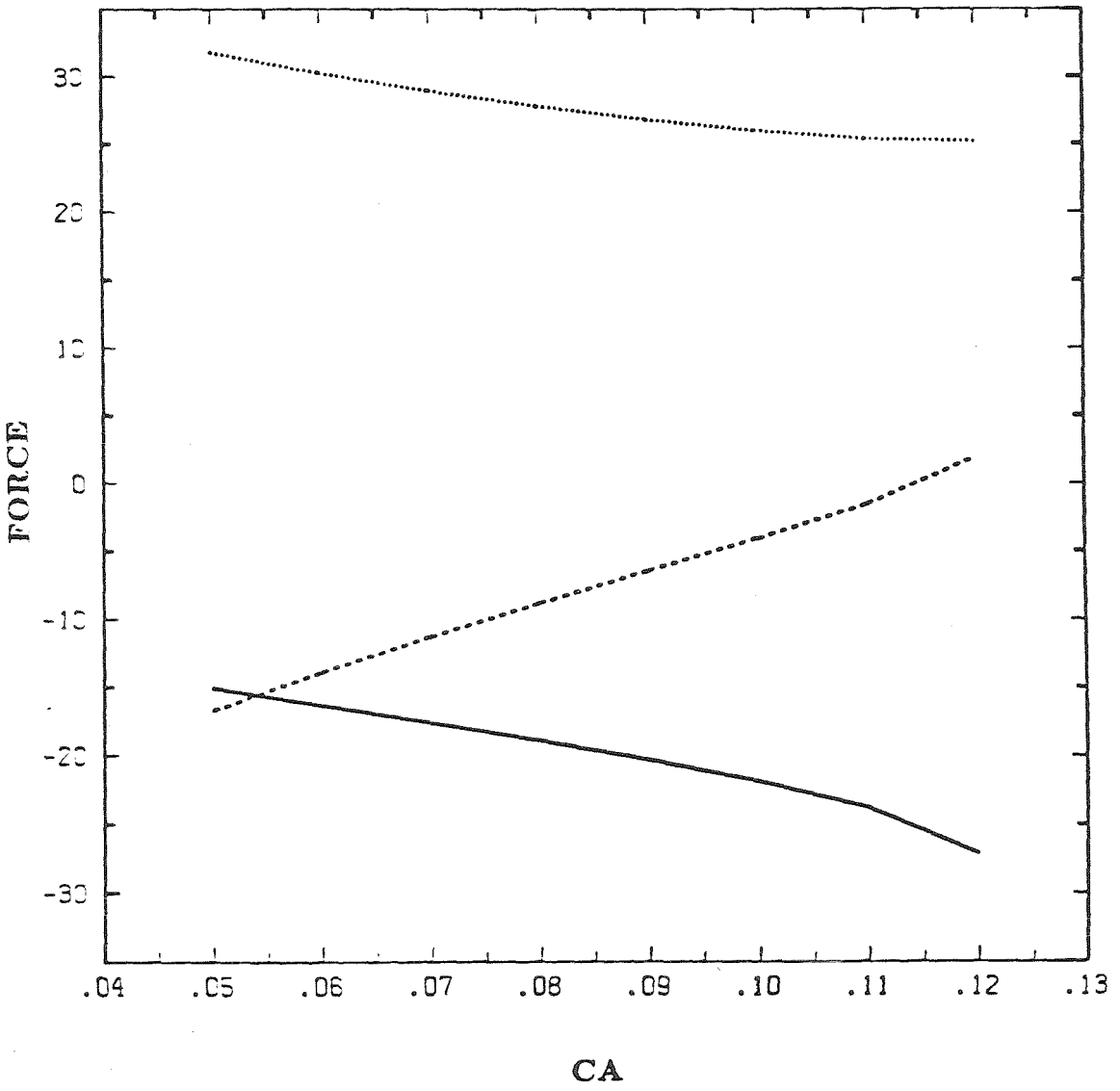

Figure 19. Components of net force acting on sphere for $\theta_c = \frac{\pi}{2}$, $\rho_p = \rho$, Cg = 0.05, as a function of capillary number: ———, viscous drag; - - -, net buoyancy force; ·····, capillary force.

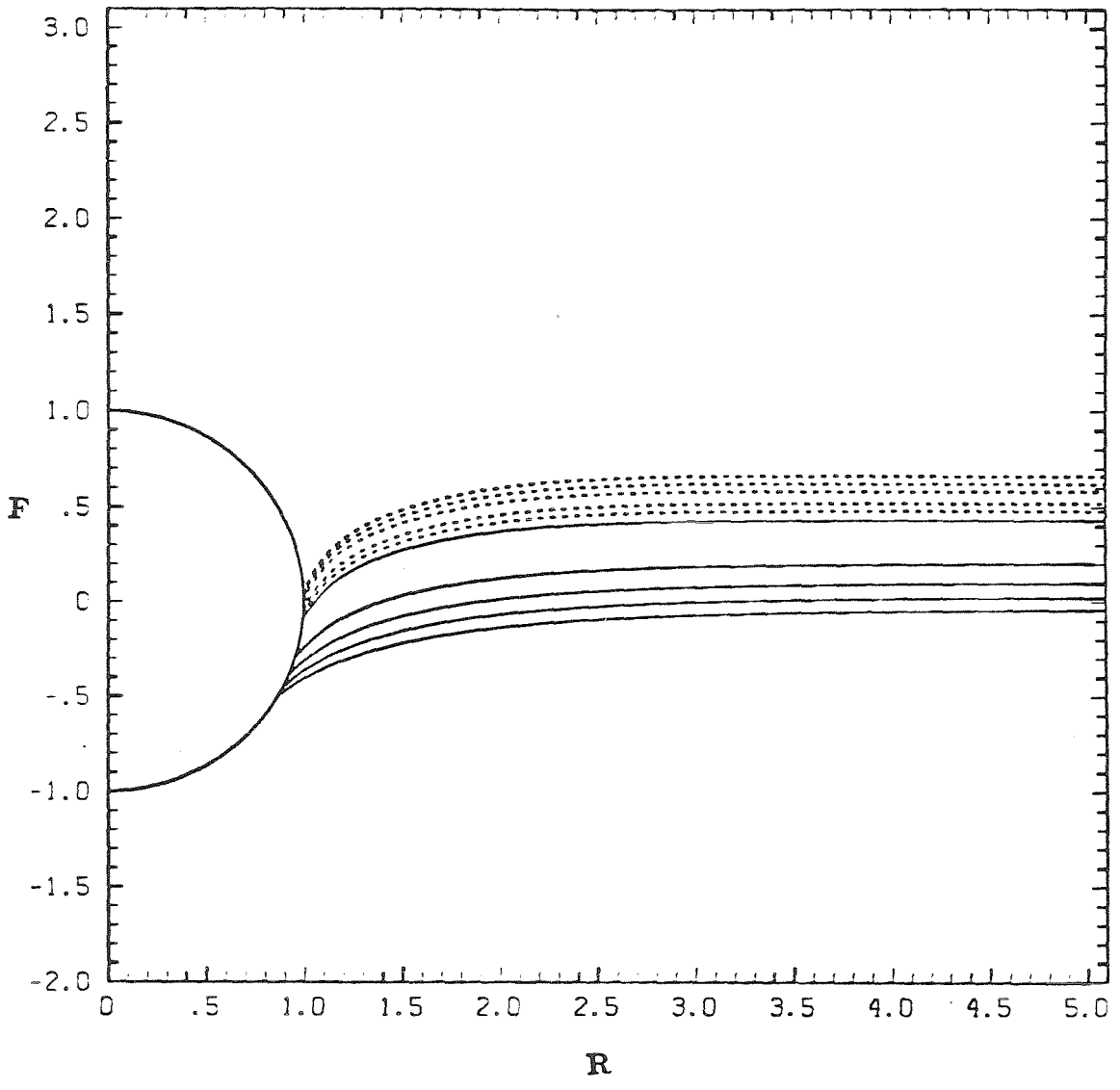

Figure 20. Equilibrium sphere/interface configuration for: $\theta_c = \frac{8\pi}{9}$, $\rho_p = 1.25\ \rho$: ———, Cg = Ca = 0.0, 0.05, 0.1, 0.15, 0.2; - - - - -, Cg = Ca = 0.2005, 0.2015, 0.2022, 0.2019 (obtained by continuation).

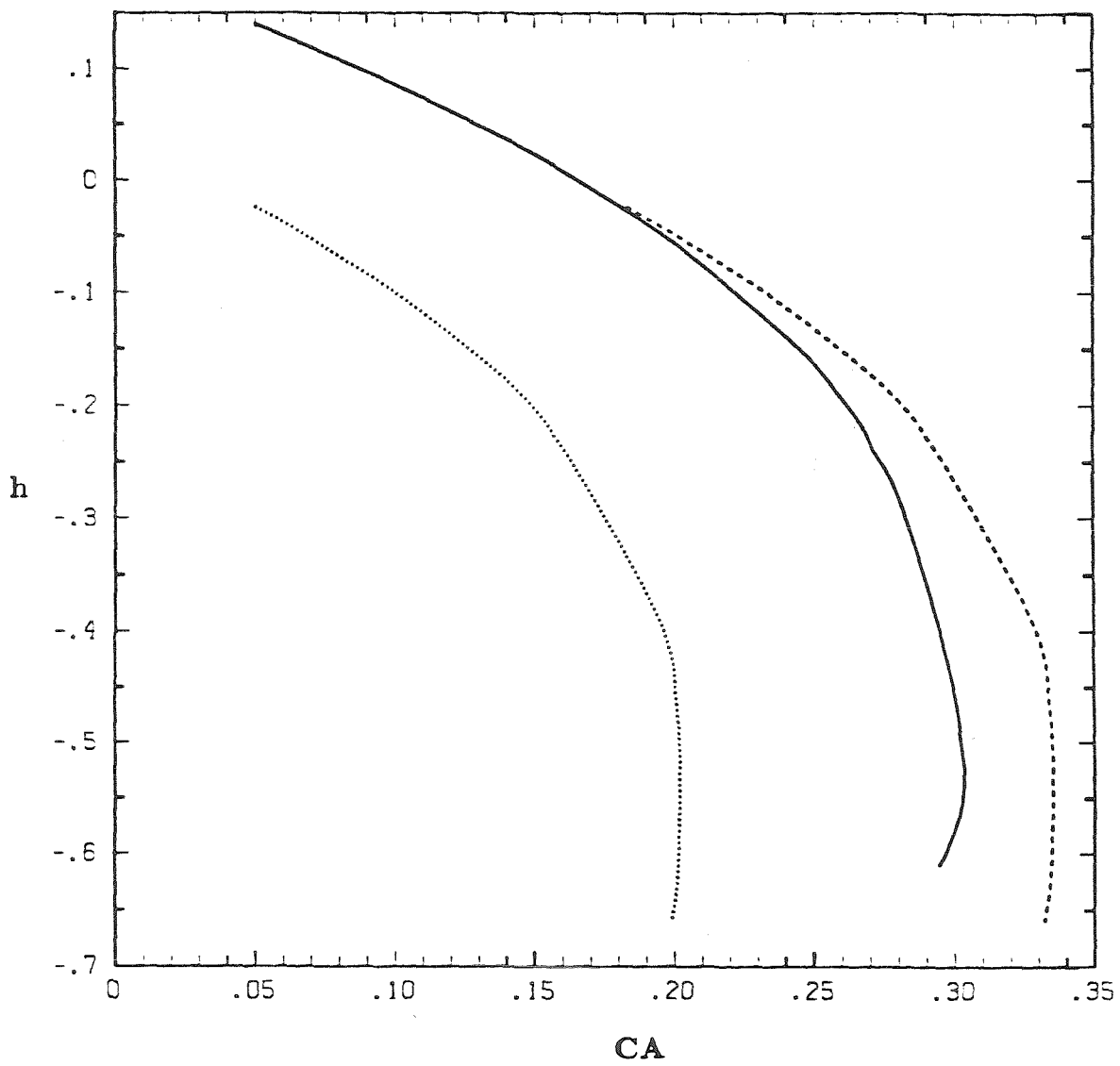

Figure 21. Sphere position, h, as a function of capillary number for $\theta_c = \frac{8\pi}{9}$, Cg = Ca:———, $\rho_p = \rho$; ·····, $\rho_p = 1.25\rho$; - - - - - - -, $\rho_p = 1.25\rho$ (shifted to compare with $\rho_p = \rho$).

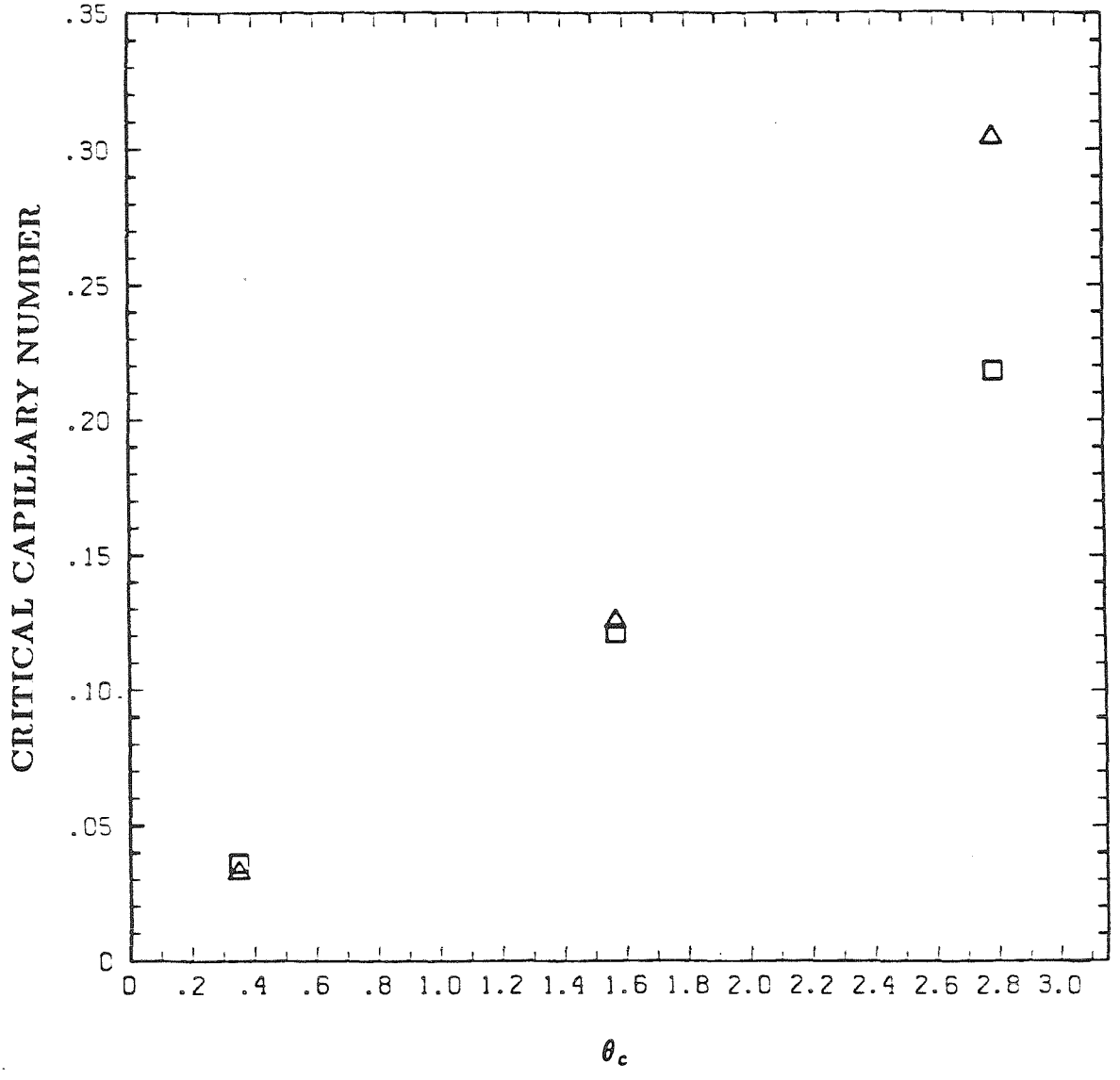

Figure 22. Critical capillary number as a function of contact angle for: △, Cg = Ca; □, Cg = constant (minimum value of Ca).

Chapter III

The trajectory of a small spherical particle around a spherical drop in low-Reynolds number flow.

Abstract

Trajectories of small spherical particles around a spherical drop (bubble and solid) are calculated from an approximate solution employing a matched asymptotic expansion. Viscous interaction is seen to have a large effect on the trajectory around a solid collector and a small effect on the trajectory around a bubble. Previous solutions are found to be in error in their prediction of a increase in the capture efficiency because of viscous interactions, the capture efficiency decreases significantly in this case. Also, the utility of the method of solution is demonstrated for nonspherical particles.

Introduction

Hydrodynamic interactions between particles and bubbles in flotation processes may greatly affect the efficiency of the separation process, as described in a review article by Jameson, Nam and Young (1977). The incorporation of these hydrodynamic interactions in theoretical calculations of particle trajectories for the flotation problem, (Spielman and Cukor (1973), Spielman and Fitzpatrick (1973), Spielman and Goren (1970), Prieve and Ruckenstein (1974), Deryaguin et al. (1976), Deryaguin and Dukhin (1979) and Dukhin and Rulev (1977), among others), has relied mainly on the solutions for the hydrodynamic interactions between a sphere (in several linear and quadratic flows) and a plane wall, obtained by Goren and O'Neill (1971). Recent relations for the resistance and mobility tensors developed by Jeffrey and Onishi (1984) for two solid spheres of arbitrary size ratio may represent a more accurate formulation for calculating trajectories of two solid spheres.

However, even though very small bubbles tend to rise with terminal velocities of equivalent solid spheres, Garner and Hammerton (1954), Rulev (1980), the observed mobility of captured particles on the surfaces of bubbles and the possible deformation of bubble surfaces accompanying the interaction of a bubble with a nearby particle (or other bubble) indicate that a bubble may not behave as a solid sphere when it interacts with particles, especially at small bubble/particle separations. This possibility is demonstrated in the experimental investigation of Yuu and Fukui (1981), where a significant deviation of the drag coefficient from the theoretical values is measured, for a sphere approaching both a solid wall and a fluid interface, when the separation between the sphere and the boundary becomes small. Also, in oil flotation or liquid-solid extraction processes, Goold et al. (1975) and Puddington and Sparks (1975), where a liquid drop is used as the collector instead of a bubble, the drop collectors are generally larger and thus may *not* behave as solid spheres even when not interacting with a solid particle. Part of the motivation for the present study is thus an evalua-

tion of the differences in hydrodynamic interaction when the collector is treated as a bubble or drop, rather than as a solid sphere. Another motivation is the development of more accurate and easily applied approximation techniques for evaluation of particle trajectories in the vicinity of a bubble/drop collector. For example, Anfruns and Kitchner (1977) demonstrated that collection efficiencies may vary greatly for different shapes of particles, i.e. rodlike particles versus spherical particles; therefore, a solution technique that could easily be applied to nonspherical particles is needed.

In the present chapter, we calculate trajectories of spherical particles near rising spherical drops using a method that could be applied to nonspherical particles. We have modeled our solution technique after the solution method of Goren and O'Neill, who approximated the flow experienced by a particle as it moves around a collector, by using a Taylor series expansion to decompose the local form of the undisturbed flow around the collector into a number of simpler component flows. However, unlike Goren and O'Neill, we solve a large number of component problems in the Taylor series expansion, rather than just the leading order parallel and normal terms, since we are interested in small but still finite-size particles, where the higher order terms may be important. Because of the large number of component problems we consider, and also the complication of a fluid interface rather than a solid interface, we are not able to solve all of these component problems exactly following Goren and O'Neill. Rather, we solve the component problems in a approximate manner based on the techniques used successfully by Lee, Chadwick and Leal (1979) and Yang and Leal (1984). Also, rather than using an ad-hoc (and incorrect) method to determine particle trajectories from the solutions of these component problems (as done by all other investigators who have performed trajectory calculations to calculate efficiencies of capture using the component solutions of Goren and O'Neill (cf. Spielman et al.; Derjaguin et al.; Collins)), we use a formalized matched expansion technique. Our solution technique specifically takes advantage of the

small size of the particles relative to the size of the collector, which is inherent in effluent flotation (and oil flotation) in calculating the trajectories through the use of singularity solutions and the method of matched asymptotic expansions. The formulas that are developed for the instantaneous particle velocities are integrated to obtain particle trajectories for several sample cases. The purpose of these sample trajectory calculations is not to develop an exhaustive tabulation, which could be used for every physical system, but rather to demonstrate the accuracy of the simple formulation that has been developed, thus validating its future use in capture efficiency calculations, and preparing the way for similar calculations for different particle shapes (e.g., rod-like particles). Furthermore, these formulas for the instantaneous particle velocity will be used to calculate trajectories, which can be compared to the experimentally measured trajectories in Chapter 5, thus answering the question of whether real bubbles behave more like solid spheres, gaseous bubbles, or some combination of these two limits, when these bubbles interact with particles.

Problem Formulation

The operating characteristics of effluent flotation warrant making several approximations that greatly simplify the analysis. Because of the very small concentrations of particles involved in effluent flotation, it is reasonable to neglect particle-particle interactions and consider only one particle at a time. A similar argument is not valid for the bubbles, since, at a fixed gas flow rate, a tendency to a large number of small bubbles should increase the process efficiency by increasing the surface area available for capture. However, as a first step, the flow around one bubble may be considered, and this may perhaps be modified at a later time to include disturbances produced by neighboring bubbles. Also, because of the very small particles generally encountered in effluent flotation, we will consider the asymptotic case in which the particle radius is very much smaller than the radius of the collection bubble; i.e., $(\frac{a}{R}) \ll 1$. Initially, we consider only hydrodynamic interactions between the particle and collector bubble

(drop) and neglect electroviscous forces, although later we will demonstrate how models for these forces could also be included.

Therefore, we consider the situation shown in Figure 1, where the centers of the drop and particle lie in the z-y plane, i.e., the plane of the paper. The coordinate system has its origin on the drop surface (and undergoes a quasi-static displacement as the particle-drop configuration changes) such that the z-axis points along the line of centers and the x-axis points out of the plane of the paper. By fixing the coordinate system on the drop, the equivalent problem of a drop at rest in a slow uniform flow at infinity, $\mathbf{u}_\infty$ (taken to be the terminal velocity of this same drop in an unbounded fluid), is considered. Note, $\mathbf{u}_\infty$ makes an angle of θ_p with the z-axis.

The drop-particle separation, h, is assumed to be intermediate between the length scales R and a, so that $R \gg h > a$. Although the method of solution that we adopt for the component problems is strictly valid only for h larger than a, we will apply these solutions to problems where $h \approx$O(a), and compare to the exact solution of Jeffrey and Onishi for two solid spheres as a check on the accuracy of this "ad hoc" procedure. The particle's disturbance to the uniform flow should be small compared to the drop's disturbance, except locally in the vicinity of the particle, for the case $(\frac{a}{R}) \ll 1$. In the region close to the particle, however, the particle's effect on the flow obviously cannot be neglected. Since the no slip condition must be satisfied on the particle's surface, the streamlines are different than they would be if the particle were not present. This local disturbance flow is significant over a distance from the particle of $O(a)$, but when the drop-particle separation is also of $O(a)$, interaction of this disturbance flow with the drop surface can significantly alter the particle trajectory. Clearly, the magnitude of this interaction will depend on the viscosity of the drop, both through the dependence of the magnitude of the "reflection" of the disturbance from the interface, and through the dependence of the form of the outer base flow around the drop.

Therefore, at least two characteristic length scales are involved in this process. The first, a, is a measure of the distance over which O(1) variations in the disturbance flow occur because of the presence of the particle, and we shall call this the "inner" region. The second, R, is a measure of the distance over which O(1) variations in the flow occur in the "outer" region, i.e., everything outside the immediate $O(a)$ vicinity of the particle. As mentioned earlier, the effect of changes in drop viscosity may be seen in both these regions. Hydrodynamic interactions, electroviscous interactions and interface deformation may be especially important in the "inner" region. In this chapter we will initially consider the hydrodynamic interaction and later include electroviscous effects. As mentioned earlier, the method of solution for these hydrodynamic interactions is based on the assumed relative magnitudes of the length scales, $(\frac{a}{R}) \ll (\frac{a}{h}) < 1$.

The very small bubbles and particles used in effluent flotation suggest considering the Reynolds number, Re, based on the bubble velocity and either the particle or bubble dimensions to be small. The terminal velocity of a 100 micron diameter air bubble in pure water at $20°C$ yields Re ≈ 3, whereas for a 20 micron air bubble, Re ≈ 0.025. Thus, although Stokes' approximation may not be valid for froth flotation, it should be valid for effluent flotation, where the bubble diameter is normally 50 microns or less.

In the "outer" region the characteristic velocity, length, pressure and time scales are, respectively, u_∞, R, $(\frac{\mu u_\infty}{R})$, $\frac{R}{u_\infty}$. The "inner" region has the same characteristic scales, except that the length scale a replaces R in the length pressure and time scales.

For Re small, the governing equations for a Newtonian incompressible fluid can be simplified to Stokes' equations and the continuity equation, which after appropriate nondimensionalization are

$$\nabla^2 \mathbf{u} = \nabla P, \qquad \nabla \cdot \mathbf{u} = 0. \tag{1}$$

The existence of two characteristic length scales and the small parameter

$(\frac{a}{R})$ suggests the utility of applying the method of matched asymptotic expansions to solve Equation (1).

Thus, applying the method of matched asymptotic expansions, we assume the following forms for the velocity and stress tensor in the "outer" region, outside the drop

$$\mathbf{u} = \mathbf{u}^{(0)} + (\frac{a}{R})\mathbf{u}^{(1)} + (\frac{a}{R})^2\mathbf{u}^{(2)} + \ldots, \tag{2}$$

$$\mathbf{T} = \mathbf{T}^{(0)} + (\frac{a}{R})\mathbf{T}^{(1)} + (\frac{a}{R})^2\mathbf{T}^{(2)} + \ldots, \tag{3}$$

and inside the drop,

$$\tilde{\mathbf{u}} = \tilde{\mathbf{u}}^{(0)} + (\frac{a}{R})\tilde{\mathbf{u}}^{(1)} + (\frac{a}{R})^2\tilde{\mathbf{u}}^{(2)} + \ldots, \tag{4}$$

$$\tilde{\mathbf{T}} = \tilde{\mathbf{T}}^{(0)} + (\frac{a}{R})\tilde{\mathbf{T}}^{(1)} + (\frac{a}{R})^2\tilde{\mathbf{T}}^{(2)} + \ldots . \tag{5}$$

Expansions (2) - (5) are substituted into Stokes' Equation (1), which after collecting like terms simply gives Stokes' and continuity equations at each order.

In the limit as $(\frac{a}{R}) \to 0$, a force balance shows that the disturbance flow due to the particle should be negligible in the outer region relative to the undisturbed flow produced by the drop. The balance between the force acting on the fluid because of the buoyancy of the particle and the hydrodynamic force exerted by the fluid on the particle is given by

$$\frac{4}{3}\pi a^3(\rho_p - \rho)\mathbf{g} + \mu u_\infty R \int\int_{S_p} (\mathbf{T}\cdot\mathbf{n}_p)dS = 0, \tag{6}$$

where ρ_p is the particle density, S_p indicates that the integration is to be performed over the surface of the particle, $\mathbf{n}_p$ is the unit normal to the particle surface and dS is a nondimensional differential surface element. Similarly, for the drop,

$$\frac{4}{3}\pi R^3(\rho_d - \rho)\mathbf{g} + \mu u_\infty R \int\int_{S_d} (\mathbf{T}\cdot\mathbf{n}_d)dS = 0, \tag{7}$$

where ρ_d is the drop density, S_d indicates integration over the surface of the drop and $\mathbf{n}_d$ is the unit normal to the drop surface. The ratio of the force exerted by the particle, on the fluid, relative to that exerted by the drop is

$$\frac{\mathbf{F_P}}{\mathbf{F_d}} = \frac{a^3(\rho_p - \rho)}{R^3(\rho_d - \rho)} \approx O(\frac{a}{R})^3. \tag{8}$$

Thus, to $O(\frac{a}{R})^3$ the force exerted by the particle on the fluid is negligible in its effect on the flow in the "outer" region so that, at least to O(1), the flow in the "outer" region should reduce to streaming flow around a drop with no particle present. Since the slowest decaying disturbance singularity decays like $\frac{1}{|\mathbf{x}|}$, and scales with the object size, the disturbance from the particle should be at most $O(\frac{a}{R})$, compared to O(1), $(O(\frac{R}{R}))$, for the drop.

As mentioned previously, for generality, in what follows we consider the interaction between a particle and a drop. Then, the particle-bubble problem with a clean interface is realized in the limit as the ratio of viscosities goes to zero and the particle-solid collector problem is realized in the limit as the ratio of viscosities goes to infinity. We denote the drop viscosity as $\tilde{\mu} = \lambda\mu$, and the internal velocity vector and stress tensor as $\tilde{\mathbf{u}}$ and $\tilde{\mathbf{T}}$, respectively. At the drop surface, the internal flow must match the external flow, and the stresses must balance. Again, to leading order, the "outer" flow inside the drop is assumed to be not directly influenced by the presence of the particle at O(1). Furthermore, for the present chapter, we neglect completely any flow-induced deformation of the drop.

Thus, the boundary conditions for the O(1) solution, in the "outer" region are:

$$\mathbf{u}^{(0)} \cdot \mathbf{n} = \tilde{\mathbf{u}}^{(0)} \cdot \mathbf{n} = 0, \tag{9}$$

$$\mathbf{t} \cdot \mathbf{n}\mathbf{T}^{(0)} = \mathbf{t}\mathbf{n}\tilde{\mathbf{T}}^{(0)}, \tag{10}$$

$$\mathbf{n} \cdot \mathbf{n} \cdot \mathbf{T}^{(0)} - \lambda \mathbf{n} \cdot \mathbf{n} \cdot \tilde{\mathbf{T}}^{(0)} = 2\frac{\sigma}{\mu u_\infty} = \frac{2}{Ca}, \tag{11}$$

$$\mathbf{u}^{(0)} = \tilde{\mathbf{u}}^{(0)}, \tag{12}$$

on the drop surface, and

$$\mathbf{u}^{(0)} \rightarrow 1 \text{ as } |\mathbf{x}| \rightarrow \infty. \tag{13}$$

Conditions (9) - (12) on the surface of the drop correspond to: zero normal velocity, continuity of tangential stress, the normal stress balance (only satisfied for a spherical drop for Re=0) and the continuity of velocity, respectively. The last condition (13) is the requirement that the solution "match" the streaming flow at large distances from the drop.

The Hadamard/Rybczynski solution given by Happel and Brenner (1965) for streaming flow past an undeformed drop satisfies conditions (9), (10), (12), and (13) and yields the O(1) velocity field in terms of spherical coordinates, (r, θ, ϕ), with origin at the drop center, for the "outer" region, outside the drop as

$$u_r = -cos\theta \left[1 - \frac{(3\lambda+2)}{2(\lambda+1)r} + \frac{\lambda}{2(\lambda+1)r^3}\right], \tag{14}$$

$$u_\theta = sin\theta \left[1 - \frac{(3\lambda+2)}{4(\lambda+1)r} + \frac{\lambda}{4(\lambda+1)r^3}\right], \tag{15}$$

and inside the drop

$$\tilde{u}_r = -cos\theta \left[\frac{r^2}{2(\lambda+1)} - \frac{1}{2(\lambda+1)}\right], \tag{16}$$

$$\tilde{u}_\theta = sin\theta \left[\frac{r^2}{(\lambda+1)} - \frac{1}{2(\lambda+1)}\right], \tag{17}$$

where, θ is measured from the upstream symmetry axis for the streaming flow. Note that this outer flow would have to be modified if the effects of neighboring bubbles were included. Also, a spherical drop in a flow with $Re \neq 0$ cannot satisfy the normal stress balance (11) and remain undeformed, but here we have considered only $Re = 0$. Neither can the drop remain spherical when interactions with the particle are taken exactly into account, and in Chapter 2 we considered the effects of interface deformation on the approach of the particle; however, in this investigation we are neglecting any possible interface deformation.

Now, the O(1) inner problem must be considered. Here the characteristic length scale is a, and for $h \approx O(a)$, the "inner" region is assumed to be composed of sections both inside and outside the drop. Analogous to Equations (2) - (5), the following "inner" domain velocity and stress tensor expansions are assumed, outside the drop,

$$\hat{\mathbf{u}} = \hat{\mathbf{u}}^{(0)} + (\frac{a}{R})\hat{\mathbf{u}}^{(1)} + (\frac{a}{R})^2\hat{\mathbf{u}}^{(2)} + \ldots, \tag{18}$$

$$\hat{\mathbf{T}} = \hat{\mathbf{T}}^{(0)} + (\frac{a}{R})\hat{\mathbf{T}}^{(1)} + (\frac{a}{R})^2\hat{\mathbf{T}}^{(2)} + \ldots, \tag{19}$$

and inside the drop,

$$\bar{\mathbf{u}} = \bar{\mathbf{u}}^{(0)} + (\frac{a}{R})\bar{\mathbf{u}}^{(1)} + (\frac{a}{R})^2\bar{\mathbf{u}}^{(2)} + \ldots, \tag{20}$$

$$\bar{\mathbf{T}} = \bar{\mathbf{T}}^{(0)} + (\frac{a}{R})\bar{\mathbf{T}}^{(1)} + (\frac{a}{R})^2\bar{\mathbf{T}}^{(2)} + \ldots . \tag{21}$$

The boundary conditions must also be arranged into a suitable form so that the O(1), $O(\frac{a}{R})$,...,terms can be isolated. To accomplish this, we note that the equation for the surface of the drop in terms of inner variables is

$$\hat{x}^2 + \hat{y}^2 + (\hat{z} + \frac{R}{a})^2 = (\frac{R}{a})^2. \tag{22}$$

This yields the following asymptotic expression for the normal to the drop surface,

$$\mathbf{n} = \mathbf{i}_z + (\frac{a}{R})(\hat{x}\mathbf{i}_x + \hat{y}\mathbf{i}_y) - \frac{1}{2}(\frac{a}{R})^2 (\hat{x}^2 + \hat{y}^2)\mathbf{i}_z + O(\frac{a}{R})^3. \tag{23}$$

Substituting Equation (23) into boundary condition (9) yields

$$\hat{\mathbf{u}} \cdot \mathbf{n} = \hat{u}_z^{(0)} + (\frac{a}{R})\left[\hat{x}\hat{u}_x^{(0)} + \hat{y}\hat{u}_y^{(0)} + \hat{u}_z^{(1)}\right] + (\frac{a}{R})^2\Big[-\frac{1}{2}(\hat{x}^2 + \hat{y}^2)\hat{u}_z^{(0)}$$

$$+ \hat{x}\hat{u}_x^{(1)} + \hat{y}\hat{u}_y^{(1)} + \hat{u}_z^{(2)}\Big] + O(\frac{a}{R})^3 = 0 \text{ at } \hat{z} = s, \tag{24}$$

where, $\hat{z} = s$ corresponds to the drop surface, which, according to (22), is

$$s = -\frac{1}{2}(\frac{a}{R})(\hat{x}^2 + \hat{y}^2) + O(\frac{a}{R})^3. \tag{25}$$

The right-hand side of Equation (24) contains the parameter $(\frac{a}{R})$ both explicitly and implicitly, since all the velocities are evaluated at s which is itself a function of $(\frac{a}{R})$. As in Van Dyke (1975), we perform a "domain perturbation" to remove the implicit dependence on the small parameter. This consists of utilizing a Taylor series expansion to obtain a boundary condition on the plane $\hat{z} = 0$, which is asymptotically equivalent to the boundary condition given by Equation (24) on the drop surface (25).

A Taylor series expansion for $\hat{\mathbf{u}} \cdot \mathbf{n}$ about $\hat{z} = 0$ yields

$$(\hat{\mathbf{u}} \cdot \mathbf{n})_s = \hat{u}_{z0}^{(0)} + (\frac{a}{R}) \Big[\hat{x}\hat{u}_{x0}^{(0)} + \hat{y}\hat{u}_{y0}^{(0)} + \hat{u}_{z0}^{(1)} + \frac{1}{2}(\hat{x}^2 + \hat{y}^2)\frac{\partial \hat{u}_{z0}^{(0)}}{\partial \hat{z}} \Big] + O(\frac{a}{R})^2 = 0, \tag{26}$$

where the subscript s indicates that the variable is evaluated on the drop surface, $\hat{z} = s$, and subscript 0 indicates that the variable is evaluated on the plane $\hat{z} = 0$. Note that the $O(\frac{a}{R})$ contribution to the normal velocity at s involves a z-derivative of the O(1) component of $\hat{u}_z$ evaluated at $\hat{z} = 0$. To simplify the presentation, the $O(\frac{a}{R})^2$ terms are omitted from Equation (26) (as well as in the similar equations derived below for the other boundary conditions). However, the form of these $O(\frac{a}{R})^2$ terms has been determined, and their representation will be considered when the $O(\frac{a}{R})^2$ "inner" problem is investigated later.

A similar analysis can now be performed for the shear stress balance. For the undeformed drop, one choice for the two tangent vectors $\mathbf{t}_1$ and $\mathbf{t}_2$ is simply the θ and ϕ spherical polar tangents to a sphere, i.e., $\mathbf{i}_\theta$ and $\mathbf{i}_\phi$, respectively. These vectors can be expressed in terms of the Cartesian coordinates $\hat{x}$, $\hat{y}$, and $\hat{z}$, and because condition (10) requires comparison of only two terms, both involving $\mathbf{t}_i$, the algebra can be simplified by dropping the normalization factors, so that

$$\mathbf{t}_1 \approx sin\theta_p \mathbf{i}_x + (\frac{a}{R})[\hat{y}cos\theta_p \mathbf{i}_x - \hat{x}cos\theta_p \mathbf{i}_y - \hat{x}sin\theta_p \mathbf{i}_z] + O(\frac{a}{R})^2, \tag{27}$$

$$\mathbf{t}_2 \approx sin\theta_p \mathbf{i}_y + (\frac{a}{R})[\hat{x}cos\theta_p \mathbf{i}_x + \hat{y}cos\theta_p \mathbf{i}_y - \hat{y}sin\theta_p \mathbf{i}_z] + O(\frac{a}{R})^2, \tag{28}$$

where, $\mathbf{t}_1$ and $\mathbf{t}_2$ are no longer necessarily unit vectors.

Utilizing Equations (22), (25), (26) and the symmetry of the stress tensor, $\mathbf{T}_{xy} = \mathbf{T}_{yx}$, the tangential stress components at $\hat{z} = s$ are

$$\mathbf{t}_1 \cdot \mathbf{n} \cdot \hat{\mathbf{T}} = sin\theta_p \hat{\mathbf{T}}^{(0)}_{xz} + (\frac{a}{R})\Big[sin\theta_p \hat{\mathbf{T}}^{(1)}_{xz} + \hat{x}sin\theta_p \hat{\mathbf{T}}^{(0)}_{xx} + \hat{y}sin\theta_p \hat{\mathbf{T}}^{(0)}_{xy}$$

$$+ \hat{y}cos\theta_p \hat{\mathbf{T}}^{(0)}_{xz} - \hat{x}cos\theta_p \hat{\mathbf{T}}^{(0)}_{yz} - \hat{x}sin\theta_p \hat{\mathbf{T}}^{(0)}_{zz}\Big] + O(\frac{a}{R})^2, \qquad (29)$$

$$\mathbf{t}_2 \cdot \mathbf{n} \cdot \hat{\mathbf{T}} = sin\theta_p \hat{\mathbf{T}}^{(0)}_{yz} + (\frac{a}{R})\Big[sin\theta_p \hat{\mathbf{T}}^{(1)}_{yz} + \hat{x}sin\theta_p \hat{\mathbf{T}}^{(0)}_{xy} + \hat{y}sin\theta_p \hat{\mathbf{T}}^{(0)}_{yy}$$

$$+ \hat{y}cos\theta_p \hat{\mathbf{T}}^{(0)}_{yz} + \hat{x}cos\theta_p \hat{\mathbf{T}}^{(0)}_{xz} - \hat{y}sin\theta_p \hat{\mathbf{T}}^{(0)}_{zz}\Big] + O(\frac{a}{R})^2. \qquad (30)$$

Again, the method of domain perturbations is used to remove the implicit dependence on $(\frac{a}{R})$, so that

$$(\mathbf{t}_1 \cdot \mathbf{n} \cdot \hat{\mathbf{T}})_s = sin\theta_p \hat{\mathbf{T}}^{(0)}_{xz0} + (\frac{a}{R})\Big[sin\theta_p \hat{\mathbf{T}}^{(1)}_{xz0} + \hat{x}sin\theta_p \hat{\mathbf{T}}^{(0)}_{xx0} + \hat{y}sin\theta_p \hat{\mathbf{T}}^{(0)}_{xy0}$$

$$+ \hat{y}cos\theta_p \hat{\mathbf{T}}^{(0)}_{xz0} - \hat{x}cos\theta_p \hat{\mathbf{T}}^{(0)}_{yz0} - \hat{x}sin\theta_p \hat{\mathbf{T}}^{(0)}_{zz0}$$

$$-\frac{1}{2}(\hat{x}^2 + \hat{y}^2)sin\theta_p \frac{\partial \hat{\mathbf{T}}^{(0)}_{xz0}}{\partial \hat{z}}\Big] + O(\frac{a}{R})^2, \qquad (31)$$

$$(\mathbf{t}_2 \cdot \mathbf{n} \cdot \hat{\mathbf{T}})_s = sin\theta_p \hat{\mathbf{T}}^{(0)}_{yz0} + (\frac{a}{R})\Big[sin\theta_p \hat{\mathbf{T}}^{(1)}_{yz0} + \hat{x}sin\theta_p \hat{\mathbf{T}}^{(0)}_{xy0} + \hat{y}sin\theta_p \hat{\mathbf{T}}^{(0)}_{yy0}$$

$$+ \hat{y}cos\theta_p \hat{\mathbf{T}}^{(0)}_{yz0} + \hat{x}cos\theta_p \hat{\mathbf{T}}^{(0)}_{xz0} - \hat{y}sin\theta_p \hat{\mathbf{T}}^{(0)}_{zz0}$$

$$-\frac{1}{2}(\hat{x}^2 + \hat{y}^2)sin\theta_p \frac{\partial \hat{\mathbf{T}}^{(0)}_{yz0}}{\partial \hat{z}}\Big] + O(\frac{a}{R})^2. \qquad (32)$$

Since the drop is treated as spherical in the present analysis, the normal stress balance is not used.

The requirement that the "inner" solution match with the "outer" solution in the overlap region provides the final boundary conditions; i.e.,

$$\lim_{|\hat{\mathbf{x}}|\to\infty} \hat{\mathbf{u}} \Leftrightarrow \lim_{|\mathbf{x}|\to\infty} \mathbf{u}, \qquad (33)$$

$$\lim_{|\hat{\mathbf{x}}|\to\infty} \bar{\mathbf{u}} \Leftrightarrow \lim_{|\mathbf{x}|\to\infty} \tilde{\mathbf{u}}. \tag{34}$$

To utilize these matching conditions at leading order in $(\frac{a}{R})$, the form of the solution in the "outer" region, (14) and (15) (outside the drop), and (16) and (17) (inside the drop) is determined, as $\mathbf{x} \to 0$ via a Taylor series expansion around the point (x,y,z)=(0,0,0). The result, outside the drop, is

$$\mathbf{u}^{(0)} = \frac{sin\theta_p}{2(\lambda+1)}\mathbf{i}_y + \frac{cos\theta_p}{2(\lambda+1)}(x\mathbf{i}_x + y\mathbf{i}_y - 2z\mathbf{i}_z)$$

$$+\frac{sin\theta_p(3\lambda+1)}{2(\lambda+1)}z\mathbf{i}_y - \frac{sin\theta_p}{2(\lambda+1)}y\mathbf{i}_z + \ldots, \tag{35}$$

and inside the drop,

$$\tilde{\mathbf{u}}^{(0)} = \frac{sin\theta_p}{2(\lambda+1)}\mathbf{i}_y + \frac{cos\theta_p}{2(\lambda+1)}(x\mathbf{i}_x + y\mathbf{i}_y - 2z\mathbf{i}_z)$$

$$+\frac{sin\theta_p}{2(\lambda+1)}4z\mathbf{i}_y - \frac{sin\theta_p}{2(\lambda+1)}y\mathbf{i}_z + \ldots . \tag{36}$$

The first term in this expression represents a uniform flow that is strongest when $\theta_p = \frac{\pi}{2}$ and the drop is a bubble, $\lambda = 0$. This term vanishes for a solid sphere because of the no slip condition, and for a drop or bubble at $\theta_p = 0$, because of symmetry.

The second term corresponds to a uniaxial extensional or stagnation point flow. As would be expected, this term is a maximum for $\lambda = 0$ and $\theta_p = 0$, the impinging flow case. Again, the surface of a solid sphere cannot support this flow because of the no-slip requirement.

Finally, the last two terms are linear shear flows. The first, and most intuitively expected, is largest when $\theta_p = \frac{\pi}{2}$ and, although larger for a solid sphere, is the same order of magnitude for both a bubble and a solid sphere. The second shear flow term in Equation (35) is a result of the finite curvature of the drop. Because (x,y,z) are defined such that x corresponds locally to ϕ, and the outer flow is independent of ϕ, there is no linear shear flow component in the $\mathbf{i}_x$ direction. Because the analysis is limited to a small area around the point

(0,0,0), the form of the flow inside and outside the drop is remarkably similar. Note that relation (36) satisfies the condition of no flow inside a solid sphere (i.e., $\lambda \to \infty$).

i. Solution at O(1)

The O(1) inner problem both inside and outside the drop must be solved simultaneously because of the coupling of the boundary conditions. Expansions (26), (31) and (32) are used to extract the O(1) boundary conditions for the "inner" problem,

$$\hat{\mathbf{u}}_{z0}^{(0)} = \bar{\mathbf{u}}_{z0}^{(0)} = 0, \tag{37}$$

$$\hat{\mathbf{T}}_{xz0}^{(0)} = \bar{\mathbf{T}}_{xz0}^{(0)}, \tag{38}$$

$$\hat{\mathbf{T}}_{yz0}^{(0)} = \bar{\mathbf{T}}_{yz0}^{(0)}, \tag{39}$$

$$\hat{\mathbf{u}}_{0}^{(0)} = \bar{\mathbf{u}}_{0}^{(0)},, \tag{40}$$

$$\lim_{|\hat{\mathbf{x}}|\to\infty} \hat{\mathbf{u}}^{(0)} \Leftrightarrow \lim_{|\mathbf{x}|\to\infty} \mathbf{u}^{(0)} = \frac{sin\theta_p}{2(\lambda+1)}\mathbf{i}_y, \tag{41}$$

$$\lim_{|\hat{\mathbf{x}}|\to\infty} \bar{\mathbf{u}}^{(0)} \Leftrightarrow \lim_{|\mathbf{x}|\to\infty} \tilde{\mathbf{u}}^{(0)} = \frac{sin\theta_p}{2(\lambda+1)}\mathbf{i}_y., \tag{42}$$

$$\hat{\mathbf{u}}^{(0)} = \hat{\mathbf{u}}_p^{(0)} + \hat{\Omega}_p^{(0)} \times \mathbf{r}_p \quad \mathbf{x} \in S_p. \tag{43}$$

The right-hand sides of conditions (41) and (42) are the leading O(1) contributions from (35) and (36), which is easily seen by expressing (35) and (36) in terms of "inner" variables and then letting $(\frac{a}{R}) \to 0$.

The resulting motion of the particle $\hat{\mathbf{u}}_p^{(0)}$ and $\hat{\Omega}_p^{(0)}$is not known, but must be such that the force and the torque balance on the particle are satisfied. The force balance, Equation (6) can be rewritten, after substitution of the Hadamard-Rybzynski result for the terminal velocity, u_∞, of a small spherical drop in an unbounded fluid, in the form

$$K(\frac{a}{R})^2 = \int\int_{S_p} (\hat{\mathbf{T}} \cdot \mathbf{n}_p) dS, \tag{44}$$

where K is a constant dependent on the viscosity and density of the two phases. The torque balance on the particle is

$$0 = \int\int_{S_p} \mathbf{r}_p \times (\hat{\mathbf{T}} \cdot \mathbf{n}_p) dS, \tag{45}$$

where, $\mathbf{r}_p$ is the radial vector of the particle.

The solution in the "inner" region satisfying the boundary conditions (37)-(43) is simply

$$\hat{\mathbf{u}}^{(0)} = \bar{\mathbf{u}}^{(0)} = \frac{sin\theta_p}{2(\lambda+1)} \mathbf{i}_y. \tag{46}$$

Since at this order the particle is subjected to a simple "uniform" flow, it simply moves with the local velocity of the fluid without disturbing the flow; i.e., the disturbance velocity due to the presence of the particle, $\hat{\mathbf{u}}_d$, is zero. The disturbance velocity is related to the actual velocity field and the velocity field at infinity, $\hat{\mathbf{u}}_\infty$ (i.e., the matching velocity field from the outer region flow), by $\hat{\mathbf{u}}_d = \hat{\mathbf{u}} - \hat{\mathbf{u}}_\infty$. The use of the disturbance velocity field will be important in the $O(\frac{a}{R})$ and $O(\frac{a}{R})^2$ inner problems. Although the results from the O(1) inner problem are trivial, it is still instructive to formulate the composite expansion from the O(1) "inner" and "outer" solutions, as in Van Dyke (1975). This is done by adding the outer solution to the inner solution and subtracting the part that the two solutions already have in common; i.e., the inner expansion of the outer solution is subtracted. The inner expansion of the outer solution is simply the uniform flow given in Equation (46). Thus, the uniformly valid composite solution at O(1) is simply the Hadamard/Rybczynski solution. Also, since the governing equations are linear, the motion of the particle arising from this flow can be superposed on the motion of the particle resulting from the higher order flows.

ii. Solution at $O(\frac{a}{R})$

Now, we turn to the more interesting contributions to the flow fields at $O(\frac{a}{R})$. The leading O(1) solution, (14)-(17), in the outer region already satisfies exactly the inhomogeneous boundary-conditions (41) and (42). Furthermore,

the simple "inner" solution (46) matches exactly with this outer solution at O(1); i.e., no mismatch is generated between the two O(1) solutions. Thus, the outer problem at $O(\frac{a}{R})$ is homogeneous with solution $\mathbf{u}^{(1)} = \tilde{\mathbf{u}}^{(1)} = 0$, both inside and outside the drop. This simply confirms the earlier suggestion that the particle produces no direct contribution to the flow at leading order, except locally in the region within $O(a)$ of the particle. It follows that the flow field in the "inner" region at $O(\frac{a}{R})$, is just that driven by the terms of the O(1) outer solution, (35) and (36), which are linear in x,y and z.

The governing equations for the inner region at $O(\frac{a}{R})$ are just Stokes' equations. The boundary conditions obtained from expansions (26), (31) and (32) are

$$\hat{\mathbf{u}}_{z0}^{(1)} = \bar{\mathbf{u}}_{z0}^{(1)} = -\hat{y}\frac{sin\theta_p}{2(\lambda+1)}, \tag{47}$$

$$\hat{\mathbf{T}}_{xz0}^{(1)} = \bar{\mathbf{T}}_{xz0}^{(1)}, \tag{48}$$

$$\hat{\mathbf{T}}_{yz0}^{(1)} = \bar{\mathbf{T}}_{yz0}^{(1)}, \tag{49}$$

$$\hat{\mathbf{u}}_{0}^{(1)} = \bar{\mathbf{u}}_{0}^{(1)}, \tag{50}$$

$$\lim_{|\hat{\mathbf{x}}|\to\infty} \hat{\mathbf{u}}^{(1)} \Leftrightarrow \frac{cos\theta_p}{2(\lambda+1)}(\hat{x}\mathbf{i}_x + \hat{y}\mathbf{i}_y - 2\hat{z}\mathbf{i}_z) + \frac{sin\theta_p(3\lambda+1)}{2(\lambda+1)}\hat{z}\mathbf{i}_y - \frac{sin\theta_p}{2(\lambda+1)}\hat{y}\mathbf{i}_z, \tag{51}$$

$$\lim_{|\hat{\mathbf{x}}|\to\infty} \bar{\mathbf{u}}^{(0)} \Leftrightarrow \frac{cos\theta_p}{2(\lambda+1)}(\hat{x}\mathbf{i}_x + \hat{y}\mathbf{i}_y - 2\hat{z}\mathbf{i}_z) + \frac{sin\theta_p}{2(\lambda+1)}(4\hat{z}\mathbf{i}_y - \hat{y}\mathbf{i}_z), \tag{52}$$

$$\hat{\mathbf{u}}^{(1)} = \hat{\mathbf{u}}_p^{(1)} + \hat{\Omega}_p^{(1)} \times \mathbf{r}_p \quad \mathbf{x} \in S_p. \tag{53}$$

The above problem for the inner region at $O(\frac{a}{R})$ can be simplified by using linearity to obtain a solution as the superposition of the disturbance stress and velocity fields for a stationary sphere near a flat interface in the linear flows (51) and (52), and the disturbance fields for a translating and rotating sphere in an otherwise quiescent fluid near a flat interface. The total hydrodynamic force and

torque on the sphere are zero at this level of approximation. Hence, the unknown translational and rotational velocities, $\mathbf{u}_p$ and $\mathbf{\Omega_p}$, must be chosen so that the *nonzero* contribution to the force and torque associated with a stationary sphere in the linear flows is exactly balanced by the contributions from translation and rotation in a quiescent fluid. The quasi-steady force and torque for translation and rotation of a sphere near a flat interface in a quiescent fluid can be expressed in the general form

$$\mathbf{F}^* = \mathbf{K}_T \cdot \mathbf{u}_p + \mathbf{K}_C \cdot \mathbf{\Omega_p},$$

$$\mathbf{T}^* = \mathbf{K}_C^T \cdot \mathbf{u}_p + \mathbf{K}_R \cdot \mathbf{\Omega_p},$$

and asymptotic forms for the resistance tensors in the expressions have been obtained by Lee, Chadwick and Leal (1979) and Yang and Leal (1984). If we denote the contributions to the force and torque for a stationary particle in the linear flows, (51) and (52), as $\mathbf{F}^{(1)}$ and $\mathbf{T}^{(1)}$, respectively, the contribution to the particle velocity at $O(\frac{a}{R})$, i.e., $\mathbf{u}_p^{(1)}$ and $\Omega_p^{(1)}$, can be obtained by solving the equations

$$\mathbf{F}^{(1)} + \mathbf{F}^{*(1)} = \mathbf{0},$$

$$\mathbf{T}^{(1)} + \mathbf{T}^{*(1)} = \mathbf{0},$$

with the result

$$\mathbf{u}_p^{(1)} = \begin{pmatrix} (F_x^{(1)} - K_C^{xy} T_y^{(1)}/K_R^{yy})/(K_T^{yy} - K_C^{xy^2}/K_R^{yy}) \\ (F_y^{(1)} + K_C^{xy} T_x^{(1)}/K_R^{yy})/(K_T^{yy} - K_C^{xy^2}/K_R^{yy}) \\ F_z^{(1)}/K_T^{zz} \end{pmatrix},$$

$$\mathbf{\Omega}_p^{(1)} = \begin{pmatrix} (T_x^{(1)} + K_C^{xy} u_y^{(1)}/K_R^{yy}) \\ (T_y^{(1)} - K_C^{xy} u_x^{(1)}/K_R^{yy}) \\ T_z^{(1)}/K_R^{zz} \end{pmatrix}, \tag{54}$$

where K_T^{yy}, K_T^{zz}, K_R^{yy}, K_R^{zz}, K_C^{xy} are the hydrodynamic resistance tensors for: translation parallel and normal to the interface, rotation about an axis parallel and normal to the interface and coupling between force and torque for motion

parallel to the interface, respectively. The asymptotic forms for these functions are given in Lee, Chadwick and Leal (1979) and Yang and Leal (1984).

It remains to solve for the disturbance flows associated with a stationary sphere near an interface with the linear velocity fields (51) and (52) imposed at "infinity". Now, however, the velocity field, plus the force and torque, on a stationary sphere near a flat interface in an arbitrary linear flow has been determined by Yang and Leal (1984), as the first terms in a power series in $\epsilon = \frac{1}{h}$, by using the method of reflections (with reflected solutions obtained by the relations of Lee, Chadwick and Leal), in conjunction with the appropriate fundamental disturbance singularities at the particle center. Note that the disturbance flow arising from a shear flow normal to the interface can be shown to be identical to the disturbance flow arising from a shear flow parallel to the interface that was obtained by Yang and Leal since the same singularities are used to cancel the two flows on the particle surface. Thus, as was shown in Chwang and Wu (1975), the force and torque on a stationary particle due to the $O(\frac{a}{R})$ matching flows from Equation (51) can be calculated by simply determining the magnitude of the "stokeslet" and "rotlet" singularities at the particle center that are necessary to cancel these "matching flows" (51) (and the reflections from the interface) on the particle surface. The result is

$$F_x^{(1)} = 0,$$

$$F_y^{(1)} = -\pi(\frac{a}{R})\frac{(9\lambda+6)(5\lambda-2)sin\theta_p}{16(\lambda+1)^2}\epsilon^2\left[1-\frac{3(2-3\lambda)}{16(1+\lambda)}\epsilon\right]+O(\epsilon^4),$$

$$F_z^{(1)} = \pi(\frac{a}{R})\frac{15(2+3\lambda)cos\theta_p}{16(\lambda+1)^2}\epsilon^2\left[1+\frac{3(2+3\lambda)}{8(1+\lambda)}\epsilon\right]+O(\epsilon^4),$$

$$T_x^{(1)} = \pi(\frac{a}{R})\frac{(6\lambda+4)sin\theta_p}{(\lambda+1)}\left[-1+\frac{3}{8(1+\lambda)}\epsilon^3\right]+O(\epsilon^4),$$

$$T_y^{(1)} = T_z^{(1)} = 0. \qquad (55)$$

It should be noted that there is a small algebra error in Yang and Leal. The stokeslet and potential dipole strengths given in their Equation (21) should each

be multiplied by a factor of two and the drag ratio given in Equation (25) must be appropriately modified. The force and torque in Equation (54) are obtained by dividing the matching flows into extensional and shear flows centered around the particle, and uniform flows. As we showed for the O(1) inner problem, the particle simply translates in a uniform flow with no disturbance velocity. Because these uniform flows with particle translation are already included in the outer solution, when the composite expansion is formed, they would be included twice if they were not subtracted off. Thus, to reduce some of the considerable algebra, rather than add and then subtract the contributions from the uniform flows, the force and torque from the uniform flows are simply not included in the inner expansions. Thus, only the particle translational and rotational *disturbance* velocities are included from the "inner" expansion.

The $O(\frac{a}{R})$ contributions to the translational and rotational velocity of the particle are now obtained by substituting (55) into (54).

Since the particle is force-free and torque-free, at $O(\frac{a}{R})$ its translational and rotational motion at $O(\frac{a}{R})$, i.e., (50), must generate stokeslets and rotlets that exactly cancel the stokeslets and rotlets produced at the center of a stationary particle in the linear flows (51) (which correspond to the force and torque expressions (54)). Thus, at $O(\frac{a}{R})$, the net disturbance velocity field corresponds to stresslet singularities,

$$(\frac{a}{R})\frac{5cos\theta_p}{4(\lambda+1)}\left[1+\frac{5(2\lambda+1)}{16(\lambda+1)}\epsilon^3+O(\epsilon^4)\right]\mathbf{u}_{SS}(\mathbf{x}_-,\mathbf{i}_z,\mathbf{i}_z),$$

$$(\frac{a}{R})\frac{5(3\lambda+2)sin\theta_p}{12(\lambda+1)}\left[-1+\frac{(-9\lambda+1)}{16(\lambda+1)}\epsilon^3+O(\epsilon^4)\right]\mathbf{u}_{SS}(\mathbf{x}_-,\mathbf{i}_y,\mathbf{i}_z), \qquad (57)$$

and potential quadrupole singualarities,

$$(\frac{a}{R})\frac{cos\theta_p}{4(\lambda+1)}\left[1+\frac{5(2\lambda+1)}{16(\lambda+1)}\epsilon^3+O(\epsilon^4)\right]\frac{\partial \mathbf{u}_D(\mathbf{x}_-,\mathbf{i}_z)}{\partial \hat{z}},$$

$$(\frac{a}{R})\frac{(3\lambda+2)sin\theta_p}{12(\lambda+1)}\left[-1+\frac{(-9\lambda+1)}{16(\lambda+1)}\epsilon^3+O(\epsilon^4)\right]\frac{\partial \mathbf{u}_D(\mathbf{x}_-,\mathbf{i}_y)}{\partial \hat{z}}, \qquad (58)$$

at the particle center, $(\mathbf{x}_-)$. The stresslet velocity fields, $\mathbf{u}_{SS}$ (Chwang and Wu (1975)), decay like $\frac{1}{r^2}$ and the potential quadrupole velocity fields decay like $\frac{1}{r^4}$. Thus, these singularities produce disturbance flows in the matching region with the outer solution, which are of $O(\frac{a}{R})^3$ and $O(\frac{a}{R})^5$, respectively (since the strength of the singularities is $O(\frac{a}{R})$). Thus, the first nonzero term in the outer solution would appear to be $O(\frac{a}{R})^3$, as was, in fact, suggested earlier via an overall force balance argument.

iii. Solution at $O(\frac{a}{R})^2$

For a solid collector, the first component of the undisturbed flow, Equation (35), which produces a contribution in the inner solution that forces the particle towards the interface, occurs at $O(\frac{a}{R})^2$. Thus, to obtain accurate trajectories over the whole range of viscosity ratios for the collector, we must consider the $O(\frac{a}{R})^2$ inner problem. We may note, as indicated above, that the first two terms at $O(1)$ and $O(\frac{a}{R})$ in the inner region have produced no disturbance flow contribution in the matching region that is larger than $O(\frac{a}{R})^3$ and thus, the outer solution remains the undisturbed flow field (35) at the present level of approximation. It is the quadratic terms that were originally omitted from the undisturbed outer velocity fields, (35) and (36), which produce contributions to the inner problem at $O(\frac{a}{R})^2$ through the matching conditions. Indeed, when (35) and (36) are expressed in terms of inner variables we see

$$\mathbf{u}^{(0)} = \{O(1) \text{ and } O(\frac{\mathrm{a}}{\mathrm{R}}) \text{ terms from (33)}\} + (\frac{a}{R})^2\Big[-\frac{cos\theta_p}{(\lambda+1)}(\hat{x}^2+\hat{y}^2)\mathrm{i}_z$$

$$+\frac{(3\lambda-2)cos\theta_p}{2(\lambda+1)}\hat{z}(\hat{x}\mathrm{i}_x+\hat{y}\mathrm{i}_y-\hat{z}\mathrm{i}_z) - \frac{(3\lambda-2)sin\theta_p}{2(\lambda+1)}\hat{y}(\hat{x}\mathrm{i}_x-\hat{y}\mathrm{i}_y+\hat{z}\mathrm{i}_z)$$

$$+\frac{sin\theta_p}{4(\lambda+1)}[(3\lambda+1)\hat{x}^2-(9\lambda+2)\hat{z}^2]\mathrm{i}_y+(3\lambda-3)\hat{y}[2\hat{x}\mathrm{i}_x-\hat{y}\mathrm{i}_y]\Big] + O(\frac{a}{R})^3, \quad (59)$$

outside the drop, and

$$\tilde{\mathbf{u}}^{(0)} = \{O(1) \text{ and } O(\frac{\mathrm{a}}{\mathrm{R}}) \text{ terms from (34)}\} + (\frac{a}{R})^2\Big[-\frac{cos\theta_p}{(\lambda+1)}(\hat{x}^2+\hat{y}^2)\mathrm{i}_z$$

$$+\frac{cos\theta_p}{2(\lambda+1)}\hat{z}(\hat{x}\mathrm{i}_x+\hat{y}\mathrm{i}_y-\hat{z}\mathrm{i}_z)-\frac{sin\theta_p}{2(\lambda+1)}\hat{y}(\hat{x}\mathrm{i}_x-\hat{y}\mathrm{i}_y+\hat{z}\mathrm{i}_z)$$

$$+\frac{sin\theta_p}{(\lambda+1)}(\hat{x}^2+\hat{z}^2)\mathrm{i}_y\Big]+O(\frac{a}{R})^3, \tag{60}$$

inside the drop. Additional contributions to the inner disturbance flow at $O(\frac{a}{R})^2$ are generated by the translational and rotational velocity contributions to the particle motion at $O(\frac{a}{R})^2$, and by the nonhomogeneous contributions that arise from the domain perturbation approximation at the drop surface. These latter contributions are obtained by substituting the forms for the $O(1)$ and $O(\frac{a}{R})$ velocity and stress fields into the domain perturbation terms at $O(\frac{a}{R})^2$: i.e., zero normal velocity,

$$\hat{u}_{z0}^{(2)}+\hat{x}\hat{u}_{x0}^{(1)}+\hat{y}\hat{u}_{y0}^{(1)}-\frac{1}{2}(\hat{x}^2+\hat{y}^2)\frac{\partial\hat{u}_{z0}^{(1)}}{\partial\hat{z}}$$

$$=\bar{u}_{z0}^{(2)}+\hat{x}\bar{u}_{x0}^{(1)}+\hat{y}\bar{u}_{y0}^{(1)}-\frac{1}{2}(\hat{x}^2+\hat{y}^2)\frac{\partial\bar{u}_{z0}^{(1)}}{\partial\hat{z}}=0; \tag{61}$$

continuity of tangential stress,

$$sin\theta_p\hat{T}_{zx0}^{(2)}+\hat{x}sin\theta_p\hat{T}_{xx0}^{(1)}+\hat{y}sin\theta_p\hat{T}_{yx0}^{(1)}-\hat{x}sin\theta_p\hat{T}_{zz0}^{(1)}$$

$$-\frac{1}{2}(\hat{x}^2+\hat{y}^2)sin\theta_p\frac{\partial\hat{T}_{zx0}^{(1)}}{\partial\hat{z}}=sin\theta_p\bar{T}_{zx0}^{(2)}+\hat{x}sin\theta_p\bar{T}_{xx0}^{(1)}$$

$$+\hat{y}sin\theta_p\bar{T}_{yx0}^{(1)}-\hat{x}sin\theta_p\bar{T}_{zz0}^{(1)}-\frac{1}{2}(\hat{x}^2+\hat{y}^2)sin\theta_p\frac{\partial\bar{T}_{zx0}^{(1)}}{\partial\hat{z}}; \tag{62}$$

and

$$sin\theta_p\hat{T}_{zy0}^{(2)}+\hat{x}sin\theta_p\hat{T}_{xy0}^{(1)}+\hat{y}sin\theta_p\hat{T}_{yy0}^{(1)}-\hat{y}sin\theta_p\hat{T}_{zz0}^{(1)}$$

$$-\frac{1}{2}(\hat{x}^2+\hat{y}^2)sin\theta_p\frac{\partial\hat{T}_{zy0}^{(1)}}{\partial\hat{z}}=sin\theta_p\bar{T}_{zy0}^{(2)}+\hat{x}sin\theta_p\bar{T}_{xy0}^{(1)}$$

$$+\hat{y}sin\theta_p\bar{T}_{yy0}^{(1)}-\hat{y}sin\theta_p\bar{T}_{zz0}^{(1)}-\frac{1}{2}(\hat{x}^2+\hat{y}^2)sin\theta_p\frac{\partial\bar{T}_{zy0}^{(1)}}{\partial\hat{z}}; \tag{63}$$

and continuity of velocity,

$$\hat{\mathbf{u}}_0^{(2)} - \frac{1}{2}(\hat{x}^2 + \hat{y}^2)\frac{\partial \hat{\mathbf{u}}_0^{(1)}}{\partial \hat{z}} = \bar{\mathbf{u}}_0^{(2)} - \frac{1}{2}(\hat{x}^2 + \hat{y}^2)\frac{\partial \bar{\mathbf{u}}_0^{(1)}}{\partial \hat{z}}. \tag{64}$$

Note that the $O(\frac{a}{R})$ and $O(\frac{a}{R})^2$ *undisturbed* flows from the outer region satisfy (61) - (64) identically; i.e., the expansion of the solution to the original problem satisfies the expansion of the boundary conditions of the original problem. Thus, in the boundary conditions there remain contributions from three sources: the $O(\frac{a}{R})$ disturbance flows from the singularities in Equations (57) and (58) (i.e., the nonhomogeneous terms generated in boundary conditions (61)-(64) from singularities in Equations (57) and (58)); the $O(\frac{a}{R})^2$ disturbance flows for a stationary particle in the $O(\frac{a}{R})^2$ flows (59), and the disturbance flows arising from a particle translating and rotating in an otherwise quiescent fluid to satisfy the force balance on the particle. To reduce the complexity of the individual problems, we will consider each of these three cases separately.

First, we will consider the disturbance flows for a stationary particle in the $O(\frac{a}{R})^2$ flows from matching, (59) and (60). Since the undisturbed flows (59) and (60) satisfy boundary conditions (61)-(64) exactly, the disturbance flows are required to satisfy only the no-slip condition on the surface of a stationary sphere and the simpler boundary conditions at $\hat{z} = 0$,

$$\hat{\mathbf{u}}_{z0}^{(2)} = \bar{\mathbf{u}}_{z0}^{(2)} = 0, \tag{65}$$

$$\hat{\mathbf{T}}_{xz0}^{(2)} = \bar{\mathbf{T}}_{xz0}^{(2)}, \tag{66}$$

$$\hat{\mathbf{T}}_{yz0}^{(2)} = \bar{\mathbf{T}}_{yz0}^{(2)}, \tag{67}$$

$$\hat{\mathbf{u}}_0^{(2)} = \bar{\mathbf{u}}_0^{(2)}, \tag{68}$$

in addition to the requirement that the disturbance velocities decay to zero as $|\hat{\mathbf{x}}| \to \infty$, so that the net velocity matches the outer solution.

Thus, we follow the same method as Yang and Leal (1984), and Lee, Chadwick and Leal (1979), to obtain solutions for the net disturbance singularities at

the particle center. Because the method is straightforward and similar to that of the preceding section, we will not repeat the details of the analysis. However, since the solutions are new and are not reported elsewhere, we will describe the initial singularities that are required for each base flow and the final forms of the force and torque on the sphere, which are obtained after applying the method of reflections using the relations of Lee, Chadwick and Leal.

Thus, we first consider the disturbance flow produced by a stationary particle near a flat interface in a parabolic shear flow, i.e., $\hat{\mathbf{u}}^{\infty} = \bar{\mathbf{u}}^{\infty} = -(\frac{a}{R})^2 \frac{cos\theta_p}{(\lambda+1)}(\hat{x}^2 + \hat{y}^2)\mathbf{i}_z$. This disturbance flow must satisfy the boundary condition on the particle's surface, $\hat{\mathbf{u}}_d = (\frac{a}{R})^2 \frac{cos\theta_p}{(\lambda+1)}(\hat{x}^2 + \hat{y}^2)\mathbf{i}_z$, to ensure that the net flow satisfies the no-slip condition on the particle surface, $\hat{\mathbf{u}} = 0$. Also, the disturbance velocity field must vanish at infinity and satisfy boundary conditions (65)-(68) on the interface. The method of reflections is used to obtain an approximation to the solution that satisfies the boundary conditions both on the sphere and on the interface. Thus, we first determine the unbounded domain solution, which satisfies the boundary conditions on the sphere. Then the solution is added that modifies this flow to satisfy the boundary conditions on the interface using the relations of Lee, Chadwick and Leal. Next, this additional flow (or reflection) is canceled on the surface of the particle by adding additional, weaker, singularities at the particle center, then the flow from these additional singularities is again reflected from the interface, and so on up to $O(\epsilon^3)$. The first disturbance flow solution that cancels the parabolic shear base flow on the particle surface has been determined in Section 9 of Chwang and Wu (1975) as

$$-(\frac{a}{R})^2 \frac{cos\theta_p}{(\lambda+1)}\Big[(\hat{x}^2 + \hat{y}^2)\mathbf{i}_z - \frac{1}{2}\mathbf{u}_S(\mathbf{x}_-, \mathbf{i}_z) + \frac{5}{12}\mathbf{u}_D(\mathbf{x}_-, \mathbf{i}_z) + \frac{7}{24}\frac{\partial^2}{\partial \hat{z}^2}\mathbf{u}_S(\mathbf{x}_-, \mathbf{i}_z) - \frac{1}{24}\frac{\partial^2}{\partial \hat{z}^2}\mathbf{u}_D(\mathbf{x}_-, \mathbf{i}_z)\Big]. \tag{69}$$

Here $\mathbf{u}_S$, $\mathbf{u}_D$, $\mathbf{u}_R$, are "stokeslet", "potential dipole" and "rotlet" velocity fields, which represent force and force dipole singularities at the particle center. The form of these fundamental solutions is given by Chwang and Wu (1975). After

reflecting this solution several times from the interface using relations (8)-(13) from Lee, Chadwick and Leal (1979), the force exerted on a stationary sphere near a flat interface in this parabolic flow is found to be

$$\mathbf{F} = -\pi(\frac{a}{R})^2 \frac{4cos\theta_p}{(\lambda+1)}\left[1 + \frac{3(3\lambda+2)}{8(\lambda+1)}\epsilon + \left(\frac{3(3\lambda+2)}{8(\lambda+1)}\right)^2\epsilon^2 \right.$$

$$\left. + \left\{\left(\frac{3(3\lambda+2)}{8(\lambda+1)}\right)^3 - \frac{(4\lambda+1)}{8(\lambda+1)} - \frac{(19\lambda+10)}{32(\lambda+1)}\right\}\epsilon^3 + O(\epsilon^4)\right]\mathbf{i}_z. \qquad (70)$$

Because of symmetry there is no torque exerted on the particle by this flow.

The second quadratic matching flow in Equations (59) and (60) is rewritten into three terms that are positioned about the particle center. This is done both to separate out the flows that are nonzero at the particle center and to simplify the process of finding the disturbance singularities at the particle center. Thus, we consider the disturbance flows arising from a stationary particle in the three flows

$$(\frac{a}{R})^2 \frac{cos\theta_p(3\lambda-2)}{2(\lambda+1)}\left[(\hat{z}-h)(\hat{x}\mathbf{i}_x+\hat{y}\mathbf{i}_y-(\hat{z}-h)\mathbf{i}_z)+h(\hat{x}\mathbf{i}_x+\hat{y}\mathbf{i}_y-2(\hat{z}-h)\mathbf{i}_z)-h^2\mathbf{i}_z\right]. \qquad (71)$$

The last term in Equation (71) is a uniform flow at the particle center, when forming the composite solution the particle will simply move with this flow and generate no disturbance. The motion of the particle in this flow is already contained in the outer solution and will be included in the composite expansion through the outer solution. Thus, the disturbance velocity field and the accompanying force and torque on a stationary particle in this uniform flow are not determined. The second term in (71) is a uniaxial extensional flow, for which the solution has been determined by Yang and Leal up to $O(\epsilon^3)$. However, the flow strength for this term is $\frac{1}{\epsilon}$ and thus the previous solution must be extended to $O(\epsilon^4)$. In performing this extension, a small algebra error in Yang and Leal was discovered. The net force on a stationary particle in the second flow of (71) is

$$\mathbf{F} = \pi(\frac{a}{R})^2 \frac{5cos\theta_p(3\lambda-2)}{(\lambda+1)}\left[\frac{3(3\lambda+2)}{8(\lambda+1)}\epsilon + \left(\frac{3(3\lambda+2)}{8(\lambda+1)}\right)^2\epsilon^2\right.$$

$$+\left\{\left(\frac{3(3\lambda+2)}{8(\lambda+1)}\right)^3-\frac{(45\lambda+12)}{40(\lambda+1)}\right\}\epsilon^3+O(\epsilon^4)\Big]\mathbf{i}_z. \tag{72}$$

Again, because of symmetry there is no torque exerted on the particle by the uniaxial extensional flow. The first term in Equation (71) is a quadratic extensional flow towards the interface, which has not been considered before. The sum of this term and the fundamental solutions shown below satisfy the no-slip condition on the sphere surface for a stationary particle,

$$(\frac{a}{R})^2\frac{cos\theta_p(3\lambda-2)}{2(\lambda+1)}\Big[(\hat{z}-h)(\hat{x}\mathbf{i}_x+\hat{y}\mathbf{i}_y-(\hat{z}-h)\mathbf{i}_z)+\frac{1}{4}\mathbf{u}_S(\mathbf{x}_-,\mathbf{i}_z)+\frac{1}{12}\mathbf{u}_D(\mathbf{x}_-,\mathbf{i}_z)$$

$$+\ \frac{7}{12}\frac{\partial^2}{\partial\hat{z}^2}\mathbf{u}_S(\mathbf{x}_-,\mathbf{i}_z)-\frac{1}{12}\frac{\partial^2}{\partial\hat{z}^2}\mathbf{u}_D(\mathbf{x}_-,\mathbf{i}_z)\Big], \tag{73}$$

which after reflecting from the interface several times gives the force on the particle as

$$\mathbf{F}=-\pi(\frac{a}{R})^2\frac{cos\theta_p(3\lambda-2)}{(\lambda+1)}\Big[1+\frac{3(3\lambda+2)}{8(\lambda+1)}\epsilon+\left(\frac{3(3\lambda+2)}{8(\lambda+1)}\right)^2\epsilon^2$$

$$+\left\{\left(\frac{3(3\lambda+2)}{8(\lambda+1)}\right)^3-\frac{(4\lambda+1)}{8(\lambda+1)}-\frac{(11\lambda+8)}{8(\lambda+1)}\right\}\epsilon^3+O(\epsilon^4)\Big]\mathbf{i}_z. \tag{74}$$

Note that this term yields an $O(\frac{a}{R})^2$ force on the particle towards the interface because of the finite size of the particle; i.e., even without interaction of the disturbance flow with the interface ("wall" effects) this flow would exert a force on the particle. There is no torque exerted on the particle from this flow.

The third quadratic matching flow in Equations (59) and (60), is also most conveniently expressed in terms of coordinate axes positioned about the particle center as

$$-(\frac{a}{R})^2\frac{sin\theta_p(3\lambda-2)}{2(\lambda+1)}[\hat{y}(\hat{x}\mathbf{i}_x-\hat{y}\mathbf{i}_y+(\hat{z}-h)\mathbf{i}_z)+h\hat{y}\mathbf{i}_z]. \tag{75}$$

The final term in Equation (75) is a simple shear flow, which was considered by Yang and Leal. However, again, the flow strength is $O(\frac{1}{\epsilon})$, and the force and

torque must be calculated to a higher order than originally obtained by Yang and Leal. The resulting net force and torque obtained from this calculation are

$$\mathbf{F} = \pi(\frac{a}{R})^2 \frac{sin\theta_p(3\lambda-2)}{2(\lambda+1)}\left[\frac{-3(5\lambda-2)}{8(\lambda+1)}\left\{\epsilon + \frac{3(3\lambda-2)}{16(\lambda+1)}\epsilon^2 + \left(\frac{3(3\lambda-2)}{16(\lambda+1)}\right)^2\epsilon^3\right\} + \frac{(9\lambda+4)}{8(\lambda+1)}\epsilon^3 + O(\epsilon^4)\right]\mathbf{i}_y \tag{76}$$

$$\mathbf{T} = 2\pi(\frac{a}{R})^2 \frac{sin\theta_p(3\lambda-2)}{(\lambda+1)}\left[-\frac{1}{\epsilon} + \frac{3}{8(\lambda+1)}\epsilon^2 + \frac{3(5\lambda-2)}{128(\lambda+1)^2}\epsilon^3 + O(\epsilon^4)\right]\mathbf{i}_x. \tag{77}$$

It may be noted that the above flow induces an $O(\frac{1}{\epsilon})$ torque on the particle; however, this still has a weak effect on the particle trajectory, since the coefficient of T_x in (54a) for the translational velocity is K_C^{xy}, which is $O(\epsilon^2)$. The first term in Equation (75) is a quadratic extensional flow, with the extension axis parallel to the interface. The terms that satisfy the no slip condition on the sphere surface before reflecting from the interface are

$$-(\frac{a}{R})^2 \frac{sin\theta_p(3\lambda-2)}{2(\lambda+1)}\left[\hat{y}(\hat{x}\mathbf{i}_x - \hat{y}\mathbf{i}_y + (\hat{z}-h)\mathbf{i}_z) + \frac{1}{4}\mathbf{u}_S(\mathbf{x}_-,\mathbf{i}_y) + \frac{1}{12}\mathbf{u}_D(\mathbf{x}_-,\mathbf{i}_y) + \frac{7}{12}\frac{\partial^2}{\partial\hat{y}^2}\mathbf{u}_S(\mathbf{x}_-,\mathbf{i}_y) - \frac{1}{12}\frac{\partial^2}{\partial\hat{y}^2}\mathbf{u}_D(\mathbf{x}_-,\mathbf{i}_y)\right]. \tag{78}$$

After reflecting from the interface several times, the force and torque on a stationary particle from the quadratic extensional contribution to (75) is

$$\mathbf{F} = \pi(\frac{a}{R})^2 \frac{sin\theta_p(3\lambda-2)}{(\lambda+1)}\left[1 + \frac{3(3\lambda-2)}{16(\lambda+1)}\epsilon + \left(\frac{3(3\lambda-2)}{16(\lambda+1)}\right)^2\epsilon^2 + \left\{\left(\frac{3(3\lambda-2)}{16(\lambda+1)}\right)^3 - \frac{(2\lambda+1)}{16(\lambda+1)} - \frac{(41\lambda+10)}{64(\lambda+1)}\right\}\epsilon^3 + O(\epsilon^4)\right]\mathbf{i}_y, \tag{79}$$

$$\mathbf{T} = -\pi(\frac{a}{R})^2 \frac{sin\theta_p(3\lambda-2)}{4(\lambda+1)}\left[\epsilon^2 + \frac{3(3\lambda-2)}{16(\lambda+1)}\epsilon^3 + O(\epsilon^4)\right]\mathbf{i}_x. \tag{80}$$

The next matching flow in Equations (59) and (60) is a parabolic shear flow parallel to the interface, which requires the following singularities to satisfy the no slip condition on the surface of a stationary sphere,

$$(\frac{a}{R})^2 \frac{sin\theta_p(3\lambda+1)}{4(\lambda+1)}\left[\hat{x}^2\mathbf{i}_y - \frac{1}{4}\mathbf{u}_S(\mathbf{x}_-,\mathbf{i}_y) - \frac{5}{24}\frac{\partial^2}{\partial\hat{x}^2}\mathbf{u}_D(\mathbf{x}_-,\mathbf{i}_y)\right.$$

$$- \frac{1}{12}\frac{\partial^2}{\partial\hat{x}\partial\hat{y}}\mathbf{u}_S(\mathbf{x}_-,\mathbf{i}_x) + \frac{1}{24}\frac{\partial^2}{\partial\hat{x}^2}\mathbf{u}_D(\mathbf{x}_-,\mathbf{i}_y)\Big]. \qquad (81)$$

Again, after reflecting from the interface several times the force and torque on a stationary particle in these flows is given by

$$\mathbf{F} = \pi(\frac{a}{R})^2\frac{sin\theta_p(3\lambda+1)}{2(\lambda+1)}\Big[1 + \frac{3(3\lambda-2)}{16(\lambda+1)}\epsilon + \left(\frac{3(3\lambda-2)}{16(\lambda+1)}\right)^2\epsilon^2$$

$$+\left\{\left(\frac{3(3\lambda-2)}{16(\lambda+1)}\right)^3 - \frac{(2\lambda+1)}{16(\lambda+1)} - \frac{(19\lambda-10)}{128(\lambda+1)}\right\}\epsilon^3 + O(\epsilon^4)\Big]\mathbf{i}_y, \qquad (82)$$

$$\mathbf{T} = \pi(\frac{a}{R})^2\frac{sin\theta_p(9\lambda+2)}{8(\lambda+1)^2}\Big[\epsilon^2 + \frac{3(3\lambda-2)}{16(\lambda+1)}\epsilon^3 + O(\epsilon^4)\Big]\mathbf{i}_x. \qquad (83)$$

The next-to-the-last matching term from Equations (59) and (60) is a parabolic shear flow parallel to the interface, which has the flow strength varying in the direction normal to the interface, i.e., in the z-direction (rather than varying in the direction parallel to the interface which was considered in Equation (69)). This term again is transposed relative to the particle center, which generates the following three flows,

$$-(\frac{a}{R})^2\frac{sin\theta_p(9\lambda+2)}{4(\lambda+1)}[(\hat{z}-h)^2\mathbf{i}_y + 2(\hat{z}-h)h\mathbf{i}_y + h^2\mathbf{i}_y]. \qquad (84)$$

The last term of Equation (84) is a uniform flow, which is included in the composite expansion through the outer flow and thus is neglected in the inner region. The second term is a shear flow, which produces the same form of disturbance flow as the last term in Equation (75), and the force and torque from this flow follow directly from Equations (76) and (77) as

$$\mathbf{F} = -\pi(\frac{a}{R})^2\frac{sin\theta_p(9\lambda+2)}{2(\lambda+1)}\Big[\frac{-3(5\lambda-2)}{8(\lambda+1)}\Big\{\epsilon + \frac{3(3\lambda-2)}{16(\lambda+1)}\epsilon^2$$

$$+\left(\frac{3(3\lambda-2)}{16(\lambda+1)}\right)^2\epsilon^3\Big\} + \frac{(9\lambda+4)}{8(\lambda+1)}\epsilon^3 + O(\epsilon^4)\Big]\mathbf{i}_y, \qquad (85)$$

$$\mathbf{T} = -2\pi(\frac{a}{R})^2\frac{sin\theta_p(9\lambda+2)}{(\lambda+1)}\Big[-\frac{1}{\epsilon} + \frac{3}{8(\lambda+1)}\epsilon^2 + \frac{3(5\lambda-2)}{128(\lambda+1)^2}\epsilon^3 + O(\epsilon^4)\Big]\mathbf{i}_x. \qquad (86)$$

The first term in Equation (84) requires the following singularities to satisfy the no slip condition on a stationary particle,

$$-(\frac{a}{R})^2\frac{sin\theta_p(9\lambda+2)}{4(\lambda+1)}\Big[(\hat{z}-h)^2\mathbf{i}_y-\frac{1}{4}\mathbf{u}_S(\mathbf{x}_-,\mathbf{i}_y)-\frac{5}{24}\frac{\partial^2}{\partial\hat{z}^2}\mathbf{u}_S(\mathbf{x}_-,\mathbf{i}_y)$$

$$-\frac{1}{12}\frac{\partial^2}{\partial\hat{z}\partial\hat{y}}\mathbf{u}_S(\mathbf{x}_-,\mathbf{i}_z)+\frac{1}{24}\frac{\partial^2}{\partial\hat{z}^2}\mathbf{u}_D(\mathbf{x}_-,\mathbf{i}_y)\Big]. \qquad (87)$$

After reflection, the force and torque on the particle are found to be

$$\mathbf{F}=-2\pi(\frac{a}{R})^2\frac{sin\theta_p(9\lambda+2)}{4(\lambda+1)}\Big[1+\frac{3(3\lambda-2)}{16(\lambda+1)}\epsilon+\left(\frac{3(3\lambda-2)}{16(\lambda+1)}\right)^2\epsilon^2$$

$$+\left\{\left(\frac{3(3\lambda-2)}{16(\lambda+1)}\right)^3-\frac{(2\lambda+1)}{16(\lambda+1)}+\frac{(11\lambda-2)}{32(\lambda+1)}\right\}\epsilon^3+O(\epsilon^4)\Big]\mathbf{i}_y, \qquad (88)$$

$$\mathbf{T}=\pi(\frac{a}{R})^2\frac{sin\theta_p(9\lambda+2)}{8(\lambda+1)^2}\Big[\epsilon^2+\frac{3(3\lambda-2)}{16(\lambda+1)}\epsilon^3+O(\epsilon^4)\Big]\mathbf{i}_x. \qquad (89)$$

The final matching flow from Equations (59) and (60), and the singularities required to satisfy the no-slip condition on the surface of a stationary sphere in this flow are,

$$(\frac{a}{R})^2\frac{sin\theta_p(3\lambda-3)}{4(\lambda+1)}\Big[-\hat{y}^2\mathbf{i}_y+2\hat{x}\hat{y}\mathbf{i}_x+\frac{1}{4}\mathbf{u}_S(\mathbf{x}_-,\mathbf{i}_y)-\frac{1}{3}\mathbf{u}_D(\mathbf{x}_-,\mathbf{i}_y)$$

$$+\frac{7}{24}\frac{\partial^2}{\partial\hat{y}^2}\mathbf{u}_S(\mathbf{x}_-,\mathbf{i}_y)-\frac{1}{24}\frac{\partial^2}{\partial\hat{y}^2}\mathbf{u}_D(\mathbf{x}_-,\mathbf{i}_y)-\frac{2}{3}\frac{\partial}{\partial\hat{x}}\mathbf{u}_R(\mathbf{x}_-,\mathbf{i}_z)$$

$$+\frac{5}{12}\frac{\partial^2}{\partial\hat{x}^2}\mathbf{u}_S(\mathbf{x}_-,\mathbf{i}_y)+\frac{1}{12}\frac{\partial^2}{\partial\hat{x}^2}\mathbf{u}_D(\mathbf{x}_-,\mathbf{i}_y)-\frac{1}{6}\frac{\partial^2}{\partial\hat{x}\partial\hat{y}}\mathbf{u}_S(\mathbf{x}_-,\mathbf{i}_x)\Big]. \qquad (90)$$

After reflection, this produces the force and torque

$$\mathbf{F}=-\pi(\frac{a}{R})^2\frac{sin\theta_p(3\lambda-3)}{2(\lambda+1)}\Big[1+\frac{3(3\lambda-2)}{16(\lambda+1)}\epsilon+\left(\frac{3(3\lambda-2)}{16(\lambda+1)}\right)^2\epsilon^2$$

$$+\left\{\left(\frac{3(3\lambda-2)}{16(\lambda+1)}\right)^3-\frac{(2\lambda+1)}{16(\lambda+1)}+\frac{(135\lambda-106)}{128(\lambda+1)}\right\}\epsilon^3+O(\epsilon^4)\Big]\mathbf{i}_y, \qquad (91)$$

$$\mathbf{T}=\pi(\frac{a}{R})^2\frac{sin\theta_p(3\lambda-3)}{8(\lambda+1)^2}\Big[\epsilon^2+\frac{3(3\lambda-2)}{16(\lambda+1)}\epsilon^3+O(\epsilon^4)\Big]\mathbf{i}_x \qquad (92)$$

on a stationary sphere.

Next, we will consider the additional $\hat{\mathbf{u}}^{(2)}$ and $\bar{\mathbf{u}}^{(2)}$ flows that arise from the domain perturbation conditions (61) - (64) when the nonhomogeneous terms are evaluated using the $O(\frac{a}{R})$ disturbance flow solutions that are represented by the singularities in Equations (57) and (58). We thus require solutions that satisfy inhomogeneous boundary conditions at the plane $\hat{z} = 0$ from (61) - (64) and the no-slip condition on the surface of a stationary sphere. This velocity field, generated by nonhomogenous terms on the plane $\hat{z} = 0$, is, in some respects, similar to the corrections associated with application of the original boundary conditions on the flat interface. The solution technique is similar to the method used by Lee (1980) to derive the general lemma used in Lee, Chadwick and Leal (1979). The problems, corresponding to each term in (57) and (58), are repetitive and exceedingly tedious; thus, only the first example will be worked through in detail here. This is the velocity field $\hat{\mathbf{u}}^{(2)}$ and $\bar{\mathbf{u}}^{(2)}$ corresponding to the stresslet normal to the interface, $\mathbf{u}_{SS}(\mathbf{x}_-, \mathbf{i}_z, \mathbf{i}_z)$, in (57). For simplicity of presentation, we drop the multiplicative coefficient that appears in (57), since the problem is linear and we can multiply by any constant at the end. Upon substitution into (61) - (64), the "normalized" stresslet velocity field, $\mathbf{u}_{SS}(\mathbf{x}_-, \mathbf{i}_z, \mathbf{i}_z)$, produces the following nonhomogeneous boundary conditions at $O(\epsilon^3)$ on the surface $\hat{z} = 0$,

$$\hat{\mathbf{u}}^{(2)}_{z0} = \bar{\mathbf{u}}^{(2)}_{z0} = -\frac{8(\hat{x}^2 + \hat{y}^2)}{(\lambda+1)}\epsilon^3 + O(\epsilon^4) \tag{93}$$

$$\hat{\mathbf{T}}^{(2)}_{xz0} = \bar{\mathbf{T}}^{(2)}_{xz0} - \frac{24(\lambda-1)\hat{x}}{(\lambda+1)}\epsilon^3 + O(\epsilon^4) \tag{94}$$

$$\hat{\mathbf{T}}^{(2)}_{yz0} = \bar{\mathbf{T}}^{(2)}_{yz0} - \frac{24(\lambda-1)\hat{y}}{(\lambda+1)}\epsilon^3 + O(\epsilon^4) \tag{95}$$

$$\hat{\mathbf{u}}^{(2)}_{0} = \bar{\mathbf{u}}^{(2)}_{0} + O(\epsilon^4). \tag{96}$$

As stated above, we require a solution that satisfies (93) - (96), the no-slip condition on the surface of a stationary sphere, and decays to zero as one moves far from the interface, i.e., into the outer region, since the outer flow already matches with the inner flow.

To solve the above problem, we assume a solution of the form

$$\hat{u}_z^{(2)} = -\frac{8(\hat{x}^2+\hat{y}^2)}{(\lambda+1)(\hat{z}+h)^3} + \hat{z}\hat{F}(\hat{x},\hat{y},zh) + \hat{z}^2\hat{G}(\hat{x},\hat{y},\hat{z}), \tag{97}$$

$$\bar{u}_z^{(2)} = \frac{8(\hat{x}^2+\hat{y}^2)}{(\lambda+1)(\hat{z}-h)^3} + \hat{z}\bar{F}(\hat{x},\hat{y},zh) + \hat{z}^2\bar{G}(\hat{x},\hat{y},\hat{z}), \tag{98}$$

which will satisfy the normal velocity condition (93) on the interface, and

$$\hat{u}_x^{(2)} = -\frac{8\hat{x}\hat{z}}{(\lambda+1)(\hat{z}+h)^3} + \hat{z}^2\hat{E}(\hat{x},\hat{y},\hat{z}), \tag{99}$$

$$\hat{u}_y^{(2)} = -\frac{8\hat{y}\hat{z}}{(\lambda+1)(\hat{z}+h)^3} + \hat{z}^2\hat{H}(\hat{x},\hat{y},\hat{z}), \tag{100}$$

$$\bar{u}_x^{(2)} = \frac{8\hat{x}\hat{z}}{(\lambda+1)(\hat{z}-h)^3} + \hat{z}^2\bar{E}(\hat{x},\hat{y},\hat{z}), \tag{101}$$

$$\bar{u}_y^{(2)} = \frac{8\hat{y}\hat{z}}{(\lambda+1)(\hat{z}-h)^3} + \hat{z}^2\bar{H}(\hat{x},\hat{y},\hat{z}), \tag{102}$$

which satisfies the continuity of tangential stress on the interface. From the continuity equation and the symmetry of the problem, appropriate choices for the unknown functions are made. The base velocity field, which vanishes at infinity and satisfies boundary conditions (93)-(96), is found to be

$$\hat{u}_x = -\frac{8\hat{x}\hat{z}}{(\lambda+1)(\hat{z}+h)^3} + \hat{z}^2\left\{\frac{12\hat{x}}{(\lambda+1)(\hat{z}+h)^4} - \frac{60\hat{x}(\hat{x}^2+\hat{y}^2)}{(\lambda+1)(\hat{z}+h)^6}\right\}, \tag{103}$$

$$\hat{u}_y = -\frac{8\hat{y}\hat{z}}{(\lambda+1)(\hat{z}+h)^3} + \hat{z}^2\left\{\frac{12\hat{y}}{(\lambda+1)(\hat{z}+h)^4} - \frac{60\hat{y}(\hat{x}^2+\hat{y}^2)}{(\lambda+1)(\hat{z}+h)^6}\right\}, \tag{104}$$

$$\begin{aligned}\hat{u}_z = &-\frac{8(\hat{x}^2+\hat{y}^2)}{(\lambda+1)(\hat{z}+h)^3} - \hat{z}\frac{24(\hat{x}^2+\hat{y}^2)}{(\lambda+1)(\hat{z}+h)^4} \\ &+\hat{z}^2\left\{\frac{8}{(\lambda+1)(\hat{z}+h)^3} - \frac{48(\hat{x}^2+\hat{y}^2)}{(\lambda+1)(\hat{z}+h)^5}\right\},\end{aligned} \tag{105}$$

$$\bar{u}_x = \frac{8\hat{x}\hat{z}}{(\lambda+1)(\hat{z}-h)^3} + \hat{z}^2\left\{\frac{-12\hat{x}}{(\lambda+1)(\hat{z}-h)^4} + \frac{60\hat{x}(\hat{x}^2+\hat{y}^2)}{(\lambda+1)(\hat{z}-h)^6}\right\}, \tag{106}$$

$$\bar{u}_y = \frac{8\hat{y}\hat{z}}{(\lambda+1)(\hat{z}-h)^3} + \hat{z}^2\left\{\frac{-12\hat{y}}{(\lambda+1)(\hat{z}-h)^4} + \frac{60\hat{y}(\hat{x}^2+\hat{y}^2)}{(\lambda+1)(\hat{z}-h)^6}\right\}, \tag{107}$$

$$\bar{u}_z = \frac{8(\hat{x}^2+\hat{y}^2)}{(\lambda+1)(\hat{z}-h)^3} + \hat{z}\frac{24(\hat{x}^2+\hat{y}^2)}{(\lambda+1)(\hat{z}-h)^4}$$

$$+\hat{z}^2\left\{\frac{-8}{(\lambda+1)(\hat{z}-h)^3} + \frac{48(\hat{x}^2+\hat{y}^2)}{(\lambda+1)(\hat{z}-h)^5}\right\}. \qquad (108)$$

This solution does *not* satisfy boundary conditions on the surface of the sphere. Hence, the next step is to add a disturbance velocity field so that the sum satisfies the no-slip condition on the surface of a stationary sphere. This is accomplished by expanding the above flow in a Taylor series expansion about the center of the sphere for small ϵ, and introducing singularities at the particle center to cancel the component flows from this expansion at the sphere surface. These singularities are then reflected from the interface, using the relations of Lee, Chadwick and Leal. The resulting force arising from the domain perturbation of the net stresslet normal to the interface at $O(\frac{a}{R})$ (i.e., including the coefficient from (57)) is

$$\mathbf{F} = \pi(\frac{a}{R})^2\frac{15cos\theta_p}{(\lambda+1)^2}\left[\epsilon + \frac{3(3\lambda+2)}{8(\lambda+1)}\epsilon^2 + \left\{-\frac{17}{16} + \left(\frac{3(3\lambda+2)}{8(\lambda+1)}\right)^2\right\}\epsilon^3 + O(\epsilon^4)\right]\mathbf{i}_z. \qquad (109)$$

It will be noted that the ϵ^3 contribution from the stresslet to the boundary conditions (93) - (96) requires a flow field that produces an ϵ force on the particle. This appears surprising at first, since an ϵ^2 point force at the particle center will produce an ϵ^3 normal velocity on the interface. However, the ϵ^3 stress difference on the interface, Equation (94), requires an ϵ^2 tangential velocity on the interface. To satisfy the continuity equation, a component of the normal velocity, although zero on the interface, has a strength of ϵ at the particle center. Thus, the contribution to the force on the particle is $O(\epsilon)$. Following the same line of reasoning, it is apparent that the $O(\epsilon^4)$ contribution from the stresslet through the domain perturbation conditions may contribute to the force at $O(\epsilon^2)$, while the $O(\epsilon^5)$ term may contribute to the force at $O(\epsilon^3)$. Thus, to obtain the complete force expression to $O(\epsilon^3)$, as required to be compatible with the force contributions calculated earlier, it is necessary to include the stresslet contributions to the

domain perturbation conditions at both $O(\epsilon^4)$ and $O(\epsilon^5)$. A stresslet normal to the interface, $\mathbf{u}_{SS}(\mathbf{x}_-, \mathbf{i}_z, \mathbf{i}_z)$, generates the following boundary conditions at $O(\epsilon^4)$,

$$\hat{\mathbf{u}}^{(2)}_{z0} = \bar{\mathbf{u}}^{(2)}_{z0} = 0 + O(\epsilon^5), \tag{110}$$

$$\hat{\mathbf{T}}^{(2)}_{xz0} = \bar{\mathbf{T}}^{(2)}_{xz0} + O(\epsilon^5), \tag{111}$$

$$\hat{\mathbf{T}}^{(2)}_{yz0} = \bar{\mathbf{T}}^{(2)}_{yz0} + O(\epsilon^5), \tag{112}$$

$$\hat{\mathbf{u}}^{(2)}_{0} = \bar{\mathbf{u}}^{(2)}_{0} - \frac{18(\lambda-1)(\hat{x}^2+\hat{y}^2)(\hat{x}\mathbf{i}_x+\hat{y}\mathbf{i}_y)}{(\lambda+1)}\epsilon^4 + O(\epsilon^5). \tag{113}$$

The $O(\epsilon^4)$ terms can be shown to yield a net force on a stationary particle,

$$\mathbf{F} = -\pi(\frac{a}{R})^2 \frac{45cos\theta_p\lambda}{(\lambda+1)^2}\left[\epsilon^3 + O(\epsilon^4)\right]\mathbf{i}_z. \tag{114}$$

Similarly, the net force on a stationary particle arising from the $O(\epsilon^5)$ terms is

$$\mathbf{F} = \pi(\frac{a}{R})^2 \frac{15cos\theta_p}{2(\lambda+1)^2}\left[\epsilon^3 + O(\epsilon^4)\right]\mathbf{i}_z. \tag{115}$$

The $O(\epsilon^6)$ and $O(\epsilon^7)$ boundary conditions produce only $o(\epsilon^4)$ contributions to the force on the particle.

The other terms in (57) and (58) can be treated in a similar manner. The net force and torque on a stationary particle arising from the stresslet parallel to the interface, $\mathbf{u}_{SS}(\mathbf{x}_-, \mathbf{i}_z, \mathbf{i}_z)$, is

$$\mathbf{F} = \pi(\frac{a}{R})^2 \frac{5sin\theta_p(3\lambda+2)(5\lambda-4)}{16(\lambda+1)^2}\left[\epsilon^3 + O(\epsilon^4)\right]\mathbf{i}_y, \tag{116}$$

$$\mathbf{T} = \pi(\frac{a}{R})^2 \frac{5sin\theta_p(3\lambda+2)(5\lambda+6)}{8(\lambda+1)^2}\left[\epsilon^2 + O(\epsilon^3)\right]\mathbf{i}_x, \tag{117}$$

where the torque is determined to a lower order in ϵ, because the contribution of the torque to the translational velocity has a coefficient K_C^{xy} (a component of the coupling tensor), which is $O(\epsilon^2)$.

The net force on a stationary particle arising from the derivative of the potential quadrupole normal to the interface, $\frac{\partial}{\partial \hat{z}}\mathbf{u}_D(\mathbf{x}_-, \mathbf{i}_z)$, is

$$\mathbf{F} = -\pi(\frac{a}{R})^2 \frac{3cos\theta_p}{2(\lambda+1)^2}\left[\epsilon^3 + O(\epsilon^4)\right]\mathbf{i}_z. \tag{118}$$

The net force and torque on a stationary particle arising from the derivative of the potential quadrupole parallel to the interface, $\frac{\partial}{\partial \tilde{z}}\mathbf{u}_D(\mathbf{x}_-, \mathbf{i}_y)$ are,

$$\mathbf{F} = \pi(\frac{a}{R})^2 \frac{3(3\lambda+2)sin\theta_p}{32(\lambda+1)^2}\left[\epsilon^3 + O(\epsilon^4)\right]\mathbf{i}_y, \tag{119}$$

$$\mathbf{T} = O(\epsilon^4)\mathbf{i}_x. \tag{120}$$

From the preceding expressions for the forces and torques at $O(\frac{a}{R})^2$, the contribution to the particle motion can be calculated at the same order such that the force balance and torque balance on the particle are satisfied by use of Equations (55) and (56). In effect, the particle motion is calculated that will generate additional viscous forces and torques that exactly cancel the forces and torques imposed on a stationary particle from the "outer" region matching flows. Thus, the net force and torque on the particle are zero, as required by the overall force balance. Also, if external forces are acting on the sphere, these can be included simply at the present order if their contribution is $O(\frac{a}{R})^2$. One such force is the buoyancy of the particle. The nondimensional buoyant force acting on the particle is

$$F_B = \frac{\frac{4}{3}\pi a^3(\rho_p - \rho)\mathbf{g}}{\mu \mathbf{u}_\infty a}. \tag{121}$$

After substituting for the terminal velocity of a drop in an unbounded fluid, the buoyancy force in terms of inner variables is

$$F_B = 4\pi \frac{(\rho_p - \rho)}{(\rho - \rho_d)} \frac{(3\lambda+2)}{2(\lambda+1)}(\frac{a}{R})^2 \left[sin\theta_p \mathbf{i}_y - cos\theta_p \mathbf{i}_z\right], \tag{122}$$

which is $O(\frac{a}{R})^2$ and can be included in the present analysis. Similarly, approximate forms for the unretarded London attractive force between a sphere and a plane wall, as in Hamaker (1937), or Spielman and Cukor (1973) should also be included at this level, if they are to be treated in the analysis; i.e.,

$$F_L = \frac{-Q}{a^4 g(\rho - \rho_d)} \frac{(3\lambda+2)}{(\lambda+1)}(\frac{a}{R})^2 \frac{1}{(h+1)^2(h-1)^2}, \tag{123}$$

where Q is the Hamaker constant, characteristic of the attractive forces between the two bodies. Also, double-layer forces can be included using the approximate relations of Hogg, Healy and Fuerstenau (1966) and Spielman and Cukor (1973),

$$F_{DL} = \frac{3\varepsilon\zeta_p\zeta_d}{2a^4 g(\rho-\rho_d)} \frac{(3\lambda+2)}{(\lambda+1)} (\frac{a}{R})^2 \tau \frac{e^{-\tau(h-1)}}{(1 \mp e^{-\tau(h-1)})}, \qquad (124)$$

where ε, ζ_p, , ζ_d, τ are the outer fluid dielectric constant, zeta potentials for the particle and drop and dimensionless reciprical double-layer length.

Combining all the previous results, the net disturbance force and torque on the particle, which are used in Equation (55) to determine the instantaneous particle velocity, are given by

$$F_z = 6\pi cos\theta_p \Big[s21\epsilon^2(\frac{a}{R}) + s31\epsilon^3(\frac{a}{R}) + s02(\frac{a}{R})^2 + s12\epsilon(\frac{a}{R})^2 + s22\epsilon^2(\frac{a}{R})^2 + s32\epsilon^3(\frac{a}{R})^2 \Big] + F_{Bz} + F_{Lz} + F_{DLz} + O\left((\frac{a}{R})\epsilon^4\right) + O(\frac{a}{R})^3, \quad (125)$$

$$F_y = 6\pi sin\theta_p \Big[p21\epsilon^2(\frac{a}{R}) + p31\epsilon^3(\frac{a}{R}) + p02(\frac{a}{R})^2 + p12\epsilon(\frac{a}{R})^2 + p22\epsilon^2(\frac{a}{R})^2 + p32\epsilon^3(\frac{a}{R})^2 \Big] + F_{By} + F_{Ly} + F_{DLy} + O\left((\frac{a}{R})\epsilon^4\right) + O(\frac{a}{R})^3, \quad (126)$$

$$\frac{T_x \cdot K_C^{xy}}{K_R^{yy}} = \frac{sin\theta_p}{8\pi} \Big[t21\epsilon^2(\frac{a}{R}) + t31\epsilon^3(\frac{a}{R}) + t02(\frac{a}{R})^2 + t12\epsilon(\frac{a}{R})^2 + t22\epsilon^2(\frac{a}{R})^2 + t32\epsilon^3(\frac{a}{R})^2 + O\left((\frac{a}{R})\epsilon^4\right) + O(\frac{a}{R})^3, \quad (127)$$

where the contribution from the torque has been expanded with the components of the coupling tensor and the rotation tensor and terms of $O(\epsilon^4)$ or smaller are truncated. The form of the coefficients, s02, s12,..., t22, in Equations (124), (125) and (126) may be found in Appendix A, where the simple computer code, which was used to calculate particle trajectories, is given. The forms for the resistance tensors are also given in the computer code.

Using the preceding analysis, the instantaneous disturbance velocity of the particle can be calculated to $O(\frac{a}{R})^2(\epsilon)^3$, with terms of $O(\epsilon^4)$ truncated at both

$O(\frac{a}{R})$ and $O(\frac{a}{R})^2$, and terms of $O(\frac{a}{R})^3$ also neglected in the particle disturbance velocities. Adding the "inner" disturbance velocity to the "outer" streaming flow results in a uniformly valid composite solution for the particle velocity. Particle trajectories are calculated by integrating these particle velocities from an initial point. The code in Appendix A begins with the system parameters and an initial starting point supplied by the user. The initial starting point is relative to a Cartesian coordinate system (xp,yp,zp) with origin at the drop center (particle motion in the yp × zp plane, and $\mathbf{i}_{zp}$ pointing in the negative g direction). The program transforms the particle position in "outer" coordinates to a position in "inner" coordinates, calculates the expressions given in (124)-(126), and uses these to calculate the particle disturbance velocity. The outer streaming flow velocity is added to the disturbance velocity to form the composite velocity, which is transformed to "outer" coordinates. The ratio of the composite particle velocities in the two outer coordinate directions is integrated using a 4^{th} order predictor-corrector method (IMSL routine DGEAR) to obtain a parameterized particle trajectory.

Results

The main purpose for calculating particle trajectories in "flotation" applications is to determine the limiting trajectory for capture. Expressions for the London dispersion force, double layer repulsive force, buoyancy force and hydrodynamic force could be used to calculate an equilibrium position of the particle at the back of the drop where the forces would balance (if such a position exists). At separations smaller than this equilibrium separation, the dispersive attractive force grows faster than the repulsive forces, and the particle will be pulled into the drop. At larger separations the dispersive attractive force falls off rapidly, and generally the flow will sweep the particle away from the drop. From this equilibrium point the particle position could be integrated backward to obtain the limiting trajectory; i.e., the trajectory which forms the boundary of the region, inside which, all particles (with the same physical and chemical

characteristics as the test particle) would be captured by the drop.

The purpose of the present study, however, is the development of accurate approximations for the hydrodynamic interaction in particle capture configurations, not the tabulation of capture efficiencies for all possible combinations of physical parameters. Furthermore, it is desired to use our solutions to explore the qualitative effects of hydrodynamic interaction on capture. Because the inclusion of dispersive and double-layer forces will mask the effects due to hydrodynamic interaction, we assume that dispersion and double-layer forces are negligible except insofar as they determine the critical point for capture, which can be used to determine a limiting trajectory. If the earlier investigations of Spielman et al. and Derjaguin et al. had first investigated the hydrodynamic interactions alone rather than including all the external forces in the trajectory equations, they might have noticed some peculiar results from the efficiency calculations. Thus, to the extent that dispersive and double-layer forces are relevant at all to the present results, we effectively assume that they act in a yes/no fashion, as described by Derjaguin and Dukhin (1979). Essentially, it is assumed that the particle will be captured if the distance between the particle and the collector ("drop") decreases below a critical separation. Thus, to evaluate the influence of hydrodynamic interaction on capture, we start with a pre-determined "critical" separation at the minimum separation configuration ($\theta_v = \frac{\pi}{2}$) and then integrate backward to determine the outer boundary of the capture "cross-section" (which can then be compared with the capture cross-section from the undisturbed streamlines). In reality, of course, the critical separation depends on the chemical nature of the system. As a nominal value, however, Jameson, Nam and Young (1977) estimate that molecular forces become important at separations of about 1000 nm.. Hence, for a 10 micron particle, this suggests a critical gap of 0.05 of the particle radius at the minimum separation point (the equator or $\theta_p = \frac{\pi}{2}$). This value was used for the majority of the present calculations.

The trajectories calculated from the asymptotic solutions for a solid collector ($\lambda \rightarrow \infty$) will be compared to trajectories calculated from Jeffrey and Onishi's (1984) solutions rather than the solutions of Goren and O'Neill (1971). The Jeffrey and Onishi solutions are an improvement on the solutions of Goren and O'Neill in three ways. First, the Jeffrey and Onishi solutions include more terms in the outer solution (also the motion normal and parallel to the boundary are all solved to the same order; i.e., the particle motion parallel to the the solid collector surface is not truncated at $O(\frac{a}{R})$, while including the $O(\frac{a}{R})^2$ motion normal to the surface). Second, Jeffrey and Onishi's solutions include a better representation of the singular force between the particle and solid collector for small separations, i.e., in the lubrication regime. The final and most important reason for using the solutions of Jeffrey and Onishi is that these solutions contain a very formalized method of calculating *uniformly valid* solutions for the instantaneous particle velocity. This can be seen to be important by noting the results obtained by Collins (1975), where the hydrodynamic interaction between the particle and collector was reported to have *increased* the effectiveness of the separation process. This behavior seems contrary to physical intuition; i.e., the hydrodynamic interaction would be normally expected to decrease the efficiency, since the hydrodynamic interaction tends to keep the two solid bodies apart (if originally apart), and together (if originally together). The results of Collins were "explained" in the review article of Jameson, Nam and Young (1977) as occurring because the increased hydrodynamic resistance of the particle motion, because of the proximity of the solid collector boundary, prevents the particle from moving out of the way of the collector. However, we will show that the results of Collins are simply incorrect (along with the results from Spielman et al. (1970-1973) and Derjaguin et al. (1976)). The error occurs in the application of Goren and O'Neill's solutions to represent the particle trajectory far from the collector. When integrating out to large particle/collector separations to calculate the cross section of the limiting streamline for capture, one cannot simply

use the local expansion of the undisturbed flow field about the drop surface; e.g., the inner flow field begins to look like a flow radially away from the collector, not like a flow in the u_∞ direction. A typical particle trajectory obtained by this incorrect method of applying Goren and O'Neill's solutions is shown in Figure 2, along with the actual full fluid streamlines and the streamlines given by the "inner" approximation to the undisturbed flow. As the particle trajectory is integrated backwards from the critical separation (gap = 0.05), the hydrodynamic interaction keeps the particle close to the collector initially, which would result in a decrease in the capture cross section and the separation efficiency if it extended out to infinity. However, once the separation becomes large, the particle trajectory begins to follow the incorrect "inner" streamline approximation resulting in an apparent *increase* in efficiency relative to that based upon the actual undisturbed flow. For a qualitative study of the effects of hydrodynamic interactions, ad hoc methods of including these interactions may give the correct trends; however, the purpose of most previous investigations appears to have been a quantitative evaluation of capture efficiencies, in which case the efficiency calculated by this method would be in error by over 100% for a critical gap of 0.05, when compared to the actual particle trajectory shown in Figure 3.

In order to check the accuracy of the trajectories calculated from our approximate solutions, as in Figure 3, we use the forms of the resistance and mobility tensors determined by Jeffrey and Onishi to calculate "exact" trajectories for two solid particles. Since the method of Jeffrey and Onishi, using twin multipole expansions, is described very well in their article, we will simply outline our method of calculating trajectories using their results and refrain from a detailed discussion of their method. To calculate trajectories using Jeffrey and Onishi's solutions, we switch between the expansions for the mobility terms in their "outer" region given in Jeffrey and Onishi and the mobility terms given in their "inner" region by the inverse of of the resistance tensor for the inner region. We extrapolate between these two forms for intermediate separations as

suggested by Jeffrey and Onishi. Thus, Figure 3 shows the actual fluid streamlines along with particle trajectories calculated from our solutions and from Jeffrey and Onishi's solutions, both for a minimum separation of 0.05 particle radii. The excellent agreement between our approximate trajectories and Jeffrey and Onishi's "exact" trajectories is most likely due, in part, to cancellation of errors in our approximations for the normal and parallel translation cases. Also, even though the minimum separation is extremely small in Figure 3, much smaller separations could be required for weak attractive molecular forces or strong double-layer repulsive forces, and for these smaller separations the comparison between our solutions and the exact solutions for two solid spheres is expected to be worse. The point is that the approximate hydrodynamic force and torque expressions that we use are based on a "far-field" approximation, where the spheres are not close together. Hence, in spite of the fact that comparisons with exact results (c.f. Yang and Leal (1984)) show excellent agreement down to unexpectedly small separations, the final "lubrication" singularity cannot be precisely simulated and thus particle trajectories for extremely small minimum separations cannot be accurately reproduced by the present approximate theory. However, one result is qualitatively clear from Figure 3; if a collector bubble behaves as a solid, hydrodynamic interactions will have a pronounced effect on the capture process, tending to keep the two bodies apart and thus will *reduce* the capture efficiency, rather than increase it as reported earlier.

In addition to the previous works already mentioned, there also exists at least one other analysis that may be applied to the flotation problem. The hydrodynamic interaction of two spherical drops of arbitrary sizes and viscosity ratios is calculated by Hetsroni and Haber (1978), using the method of reflections and Lamb's general solution of Stokes' equations in spherical harmonics. However, this analysis may not be well suited to the flotation problem, the case when one of the drops is a smaller solid body, for several reasons. First, the complexity of the problem is increased because expansions have been performed

for the insides of both drops, this part of the analysis is wasted on the solid particle. Second, the authors have considered expansions from both body centers, i.e., expansions in $\alpha = \frac{a}{(R+a+h)}$ and $\beta = \frac{R}{(R+a+h)}$, which is better suited for cases where $R = O(a)$, and loses accuracy in the flotation problem where these two length scales are quite different, $R \gg a$. Also, when comparing the results of Hetsroni and Haber to the results in Happel and Brenner for two solid spheres, we note that the relation between the torque on the small particle and the particle translation velocity is not included in the limit as the particle becomes a solid; i.e., the particle is assumed to translate without rotating. The effect of this approximation may be especially pronounced on the small particle, since Happel and Brenner list the error involved in this approximation for two solid spheres as $O(\frac{aR^3}{h^4})$, which may be large in the flotation problem. Finally, it should be noted that when comparing the results of Hetsroni and Haber to those of Happel and Brenner several typographic errors in Hetsroni and Haber were discovered along with the more serious difficulty that the relations describing the resistance functions in Hetsroni and Haber are truncated at different orders, $O(\alpha^m)(\beta^n)$, m+n=3,4,5, for the different resistance functions. Because of the uncertainty about what the form of these truncated terms should be, we simply apply the results of Happel and Brenner to determine the suitability of applying Hetsroni and Haber's formulation to the flotation problem. Thus, in Figures 4 and 5, trajectories calculated from formulas (6-3.51), (6-3.91) and (6-3.96) of Happel and Brenner are compared to trajectories calculated from our asymptotic solution and from Jeffrey and Onishi's forms. Because the approximate forms of Happel and Brenner yield divergent trajectories for small gaps, the gap chosen for this comparison is relatively large, 0.5 for $(\frac{a}{R}) = \frac{1}{7}$ and $\frac{1}{2}$. However, even at this uncharacteristically large critical gap, the trajectories calculated from the resistance functions of Happel and Brenner deviate significantly from both the "exact" trajectories and the fluid streamlines for small ratios of $(\frac{a}{R})$. However, the solutions of Happel and Brenner work significantly better than our asymp-

totic solutions for large values of $(\frac{a}{R})$, as is shown in Figure 5. The influence of the inhibition of rotation of the particle on the particle trajectory is found to be small for the system in Figure 4; i.e., the trajectories for a rotating and non-rotating particle are almost identical. Thus, the deviation of the particle trajectory from the "exact" solution must come from the error in the expansion for these small values of $(\frac{a}{R})$; particularly, terms of $O(\beta^m)$ which are dropped may not be small and may be what is significantly affecting the particle trajectory. Thus, the method of Hetsroni and Haber is judged to be not well suited for application to the flotation problem, although these authors' analysis would undoubtedly be valuable for application to many problems of great interest, e.g., coalescence of two fluid drops of similar sizes.

Additional comparisons between our asymptotic expansions for small $((\frac{a}{R}))$, the undisturbed streamlines, and the solutions of Jeffrey and Onishi are shown in Figures 6-9 for two solid spheres. Figure 6 shows the limiting trajectories for $(\frac{a}{R}) = \frac{1}{4}$. For this relatively large value of $(\frac{a}{R})$, our approximate solutions significantly overpredict the effects of hydrodynamic interaction and yield limiting cross sections that are significantly smaller that those calculated from Jeffrey and Onishi's solutions. The sensitivity to $(\frac{a}{R})$ that is evident in comparing figures 3 and 6 is surprising in the sense that a large error appears for a quite modest $(\frac{a}{R})$, while seemingly accurate solutions are obtained for "large" values of ϵ in spite of the fact that ϵ is the second small parameter in the solutions. It is, in fact, well known that the expansion in ϵ works surprisingly well for "large" ϵ; for example, the hydrodynamic force on a sphere near an interface in a linear extensional flow calculated by Yang and Leal is in good agreement with exact results obtained by Dukhin and Rulev (1977) using bipolar coordinate solutions for ϵ as large as 0.99. The relatively large deviation of the trajectories from the exact results for moderate values of $(\frac{a}{R})$ is probably because, for large $(\frac{a}{R})$, the errors occur in both the outer and inner terms rather than just in the inner term, as the disturbance from the particle begins to influence the outer flow.

Also for large $(\frac{a}{R})$, the curvature of the collector is no longer large compared to the particle curvature, and errors in the expansion arising from the domain perturbation may become especially important.

The trajectories for $(\frac{a}{R}) = \frac{1}{5}$ are shown in Figure 7. For $(\frac{a}{R}) = \frac{1}{5}$, the agreement between the results from the asymptotic solutions and the exact solutions is much better. Furthermore, for $(\frac{a}{R}) \leq \frac{1}{5}$ the exact trajectories and the approximate trajectories are almost identical, as can be seen in Figures 3,8 and 9. It should be noted, however, that for $(\frac{a}{R})$ less than 0.04 the agreement between the exact and asymptotic solutions begins to deteriorate. This disagreement may be partly because, for very small $(\frac{a}{R})$, the particle spends a much larger relative portion of its trajectory very near the boundary where the asymptotic solutions are not a very good approximation to the real solution, since, relative to the larger collector, the 0.05 gap represents a closer particle; also, the solutions of Jeffrey and Onishi begin to lose accuracy for very small size ratios, $(\frac{a}{R})$. Finally, in any application with particles this small compared to 100 micron bubbles, Brownian motion effects (along with dispersion forces) begin to become important.

We have already noted that, for smaller critical gap sizes, the approximate solutions fail to capture the singular behavior of the hydrodynamic resistance tensors, which diverge like $\frac{1}{(\epsilon-1)}$ for approach along the axis of the two bodies and prevent two solid bodies from touching in the absence of dispersion forces. The consequences of this behavior can be seen in Figure 10, where trajectories are shown for $(\frac{a}{R}) = \frac{1}{7}$, with gaps of 0.25, 0.05, 0.01 and 0.0001. The agreement between the asymptotic solutions and the exact solutions is good for gaps larger than 0.01; however, for a 0.0001 gap the disagreement is quite large. For extremely weak dispersion forces or strong double-layer forces, the particle must come very close to the surface of the collector in order to be captured. At these small critical separations the hydrodynamic interaction between the two solid bodies is very large, and this leads to a pronounced decrease in the efficiency

of capture. The results based on the "inner" solutions of Goren and O'Neill would fail to capture this large decrease in the efficiency because of the errors in approximating the entire trajectory by the "inner" solution alone.

The effect of particle buoyancy is shown in Figure 11, where trajectories are shown for $(\frac{a}{R}) = \frac{1}{7}$ and particle-to-bubble density difference ratios, $\frac{(\rho_p - \rho)}{(\rho - \rho_d)}$, of -0.5, 0.0 and 0.5. The efficiency increases significantly for O(1) positive values of this density difference ratio, as the settling of the heavy particle moves it closer to the collector and somewhat offsets the effects of hydrodynamic interaction, which tend to keep the two bodies apart. In this case, the results of Jeffrey and Onishi yield the same efficiency as our asymptotic solutions, because the increased separation leads to a decreased effect of the hydrodynamic interactions which the asymptotic solutions capture well. For O(1) negative values of the density difference ratio, the efficiency decreases significantly, as the particle rises away from the collector, thus reducing the particle velocity normal to the collector compared to the particle velocity parallel to the collector surface. However, in this case the results of Jeffrey and Onishi give a much weaker dependence on the particle density; because their hydrodynamic resistance tensors grow very rapidly for small separations, they dominate the settling effect, or effect of particle rising after the collector. Thus, the results for particles with significant buoyancy will not be as accurate for our asymptotic solutions, because this trajectory is dominated by the singular resistance terms in the exact solution.

Since, for two solid spheres the asymptotic results agree reasonably well with the exact results for small $(\frac{a}{R})$ and gaps of 0.01 or larger, we have some confidence in applying these relations to the case when the collector is a drop. In fact, the asymptotic forms are expected to work even better for a drop, since the singular resistance to approach between the two bodies is not as severe in this case. Thus, we next consider the effects of hydrodynamic interaction on the trajectory of a spherical particle relative to a "collector" drop of an immiscible fluid that has the same viscosity as the suspending fluid. The results

are shown in Figures 12 - 16. The fluid streamlines around a spherical drop with a viscosity ratio of 1 are much flatter and less curved than the streamlines around a solid sphere. Because of this, the particle spends a much smaller portion of its trajectory in the vicinity of the drop, and so the hydrodynamic interaction and the deviation of the particle trajectory from the fluid streamlines is much less. Also, any deviation of the particle trajectory from the fluid streamline while the particle is near the collector is not amplified by the curvature of the streamlines to result in larger displacements towards the axis of symmetry as in the solids case. For large ratios of $(\frac{a}{R})$, i.e., $(\frac{a}{R}) = \frac{1}{4}$, shown in Figure 12, the error in the expansion is the same order of magnitude as the effects of the hydrodynamic interaction, and the result is a prediction of a very small *increase* in efficiency because of the effects of hydrodynamic interaction. However, for smaller ratios of $(\frac{a}{R})$, as in Figures 14, 15 and 16, the hydrodynamic interaction leads to a decrease in the efficiency as it should. The actual deviation of the particle trajectory from the streamline at infinity is two to five times larger for two solids than for the drop of fluid with viscosity ratio of 1 that we consider here. The resultant fractional change in the *efficiency* due to hydrodynamic interactions is even more significant for a solid than for a drop, since the efficiency for a drop is significantly higher in the first place.

The final case that we consider is the particle trajectories around a spherical bubble (i.e. $\lambda = 0$). Particle trajectories and fluid streamlines around a bubble are shown for various ratios of particle to bubble sizes in Figures 17 - 21. The magnitude of the deviation of the particle trajectory from the streamlines is slightly greater for a bubble than for a drop of viscosity ratio 1; however, the trajectories around a bubble are even flatter then the trajectories around a drop and thus this interaction leads to a smaller decrease in efficiency for a bubble than for a drop.

The capture efficiency, or ratio of the cross-sectional area of fluid that contains particles that will be captured relative to the cross-sectional area that the

collector sweeps out is shown in Figure 22, for $\lambda = \infty$, 1.0, and 0.0 and various ratios of particle to collector sizes. Based upon the results for a solid collector, it appears that the exact solutions and the present asymptotic solutions are quite good for size ratios, $(\frac{a}{R})$, of $\frac{1}{7}$ or less. It will be noted that the efficiency falls only slightly for smaller ratios of $(\frac{a}{R})$ for solid collectors, compared to a much larger drop in efficiency for drops and bubbles. The decrease in efficiency for these latter two cases is due mainly to the streamlines' themselves lying closer to the axis of symmetry. Thus, the separation efficiency is increased for smaller bubbles both because the area available for capture is increased and because the efficiency per bubble is increased with a tendency towards a larger number of smaller bubbles.

Conclusions

Previous application of particle trajectory calculations to determine capture efficiencies has incorrectly applied the available solutions for the hydrodynamic interactions between the two bodies to a region, (the "outer" region), where these ("inner") solutions no longer accurately represent the particle motion. In contrast, we have used a formal matched asymptotic expansion to obtain solutions that are uniformly valid over the entire range of the particle trajectories.

From these calculations it is shown that viscous interaction can significantly alter the capture efficiency, especially for solidlike collectors. However, unlike the incorrect results obtained by previous investigators, we find that hydrodynamic interactions tend to *decrease* the efficiency of the separation process.

The present asymptotic solutions for $(\frac{a}{R}) \ll 1$ and $\epsilon \ll 1$ work fairly well for small $(\frac{a}{R})(\leq \frac{1}{7})$ and dimensionless gaps as small as 0.05. However, for smaller gaps the asymptotic solutions do *not* agree as closely with the exact results for two solid spheres. However, in the real problem the fluid collector or bubble will most likely not behave as a solid sphere at small bubble/particle separations, and it is not clear whether the actual particle trajectories will be closer to trajectories around a solid sphere or a fluid sphere (this should be answered in the

experiments discussed in Chapter 4). If the trajectories are close to the results for solid spheres, the "exact" solutions of Jeffrey and Onishi or the approximate solutions of the current paper, rather than the solutions of Goren and O'Neill, should be used to calculate trajectories. If the measured trajectories are similar to those for a bubble (or drop), on the other hand, the present solutions provide the best approach, though it should be noted that even the undisturbed streamlines provide a reasonable approximation in this case. Clearly, an important experimental objective should be to determine conditions when the collector acts like a solid. For nonspherical particles, however, the approximate method of solution outlined in this chapter represents a straightforward, although tedious method, of calculating the effects of hydrodynamic interaction on the particle trajectories. Exact solutions of the Jeffrey-Onishi type are not a practical objective in this case. An attempt to model the collection of nonspherical particles may be important, especially in light of the observed differences between capture efficiencies for spherical and nonspherical particles, Anfruns and Kitchner (1977).

The magnitude of the deviation of the particle trajectory from the streamlines is less for a fluid collector than for a solid. This is primarily a consequence of the form of the undisturbed streamlines. Because these streamlines are relatively straight for a bubble or drop, the particle spends a smaller portion of the trajectory in the immediate vicinity of the bubble and so has less hydrodynamic interaction with the bubble surface. Futhermore, the small deviations of the particle trajectory from a streamline while in the vicinity of the collector are not magnified by the streamline curvature as in the solid case.

Although the magnitude of the deviation of the particle trajectory from the undisturbed streamlines is approximately the same for both bubbles and solids, the relative decrease in the efficiency because of this interaction is much smaller for a bubble than for a solid, since the bubble efficiency is quite large to begin with.

References

Anfruns, J.F. and Kitchener, J.A., 1977 Rate of capture of small particles in flotation. *Inst. Mining Metal.* **86**, C9.

Chwang, A.T. and Wu, T. Y.-T., 1975 Hydromechanics of low-Reynolds number flow. Part 2. singularity method for Stokes flows. *J. Fluid Mech.* **67**, 787.

Collins, G.L., 1975 Dispersed air flotation of fine particles. *Ph.D. thesis*, Imperial College, University of London.

Derjaguin, B.V., Dukhin, S.S. and Rulev, N.N., 1976 Importance of hydrodynamic interaction in the flotation of fine particles. *Coll. J. U.S.S.R.* **38**, 227.

Derjaguin, B.V. and Dukhin, S.S., 1979 Kinetic theory of the flotation of fine particles. *Proceedings of 13th International Mineral Processing Congress, Warsaw* (Elsevier, Amsterdam, 1981).

Dukhin, S.S. and Rulev, N.N., 1977 Hydrodynamic interaction between a solid spherical particle and a bubble in the elementary act of flotation. *Coll. J. U.S.S.R.* **39**, 231.

Garner, F.H. and Hammerton, D., 1954 Circulation inside gas bubbles. *J. Chem. Eng. Sci.* **3**, 1.

Goold, L.A., Lin, I.J., Lovell, V.M. and Finkelstein, N.P., 1975 Oil-levitation extraction - a variation of flotation. *J. S. African Inst. Mining Metallurgy.* **76**, 132.

Goren, S.L. and O'Neill, M.E., 1971 On the hydrodynamic resistance to a particle of a dilute suspension when in the neighbourhood of a large obstacle. *Chem. Eng. Sci.* **26**, 325.

Hamaker, H.C., 1937 The London-van der Waals attraction between spherical particles. *Physica* **4**, 1058.

Happel, J. and Brenner, H., 1965 *Low Reynolds Number Hydrodynamics.* Prentice - Hall, Inc., Eaglewood Cliffs, N.J..

Hetsroni, G. and Haber, S. 1978 Low Reynolds number motion of two drops submerged in an unbounded arbitrary velocity field. *Int. J. Multiphase Flow* **4**, 1.

Hogg, R., Healy, T.W. and Fuerstenau, D.W., 1966 *Trans. Faraday Soc.* **63**, 1638.

Jameson, G.J., Nam, S. and Young, M.M., 1977 Physical factors affecting recovery rates in flotation. *Minerals Sci. Engng.* **9**, 103.

Jeffrey, D.J. and Onishi, Y. 1984 Calculation of the resistance and mobility functions for two unequal rigid spheres in low-Reynolds number flow. *J. Fluid Mech.* **139**, 261.

Lee, S.H. 1980 Ph.D. dissertation. California Institute of Technology.

Lee, S.H., Chadwick, R.S. and Leal, L.G. 1979 Motion of a sphere in the presence of a plane interface. Part 1: An approximate solution by generalization of the method of Lorentz. *J. Fluid Mech.* **93**, 705.

Prieve, D.C. and Ruckenstein, E., 1974 Effect of London forces upon the rate of deposition of Brownian particles. *J. A.I.Ch.E.* **20**, 1178.

Puddington, I.E. and Sparks, B.D., 1975 Spherical agglomeration processes. *Miner. Sci. Engng.* **17**, 282.

Rulev, N.N., 1977 Efficiency of particle capture by bubbles in noninertial flotation. *Coll. J. U.S.S.R.* **40**, 747.

Rulev, N.N., 1980 Hydrodynamics of a rising bubble. *Coll. J. U.S.S.R.* **42**, 210.

Spielman, L.A. and Cukor, P.M., H.J., 1973 Deposition of nonbrownian particles under colloidal forces. *J. Coll. Int. Sci.* **43**, 51.

Spielman, L.A. and Fitzpatrick, J.A., 1973 Theory for particle collection under London and gravity forces. *J. Colloid Int. Sci.* **42**, 607.

Spielman, L.A. and Goren, S.L., 1970 Capture of small particles by London forces from low-speed flows. *Environ. Sci. Technol.* **4**, 135.

Stoos, J.A., 1987 Ph.D. dissertation. California Institute of Technology.

Sutherland, K.L. and Wark, I.W. 1955 Principles of Flotation. Australian Institute of Mining and Metallurgy, Melbourne.

Van Dyke, M., 1975 *Perturbation Methods in Fluid Mechanics*, Parabolic Press, Stanford, Ca.,

Yang, S.-M. and Leal, L.G. 1984 Particle motion in Stokes flow near a plane fluid-fluid interface. Part 2. Linear shear and axisymmetric straining flows. *J. Fluid Mech.* **149**, 275.

Yuu, S. and Fukui, Y., 1981 Measurement of fluid resistance correction factor for a sphere moving through a viscous fluid toward a plane surface. *J. A.I.Ch.E.* **27**, 168.

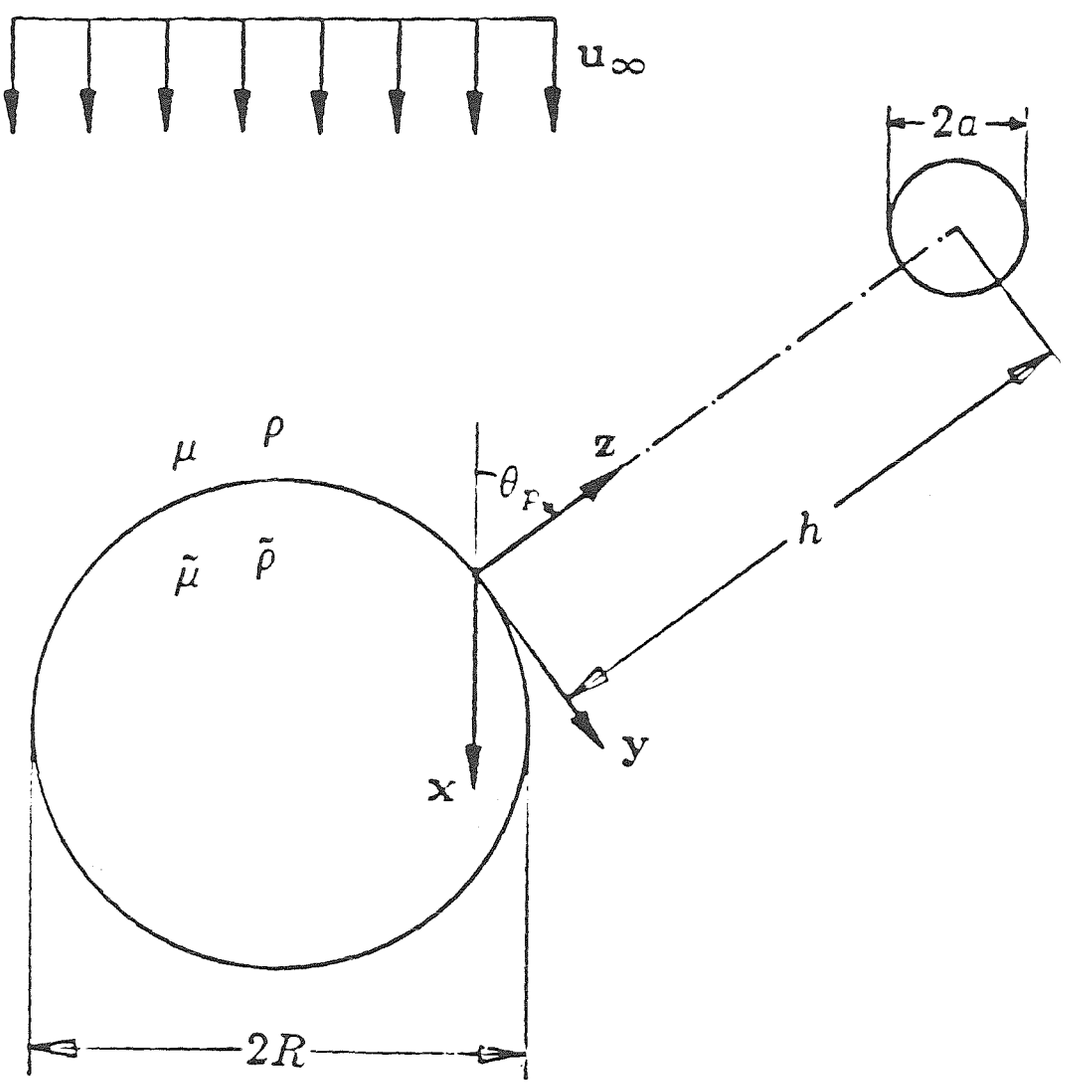

Figure 1. Schematic of problem.

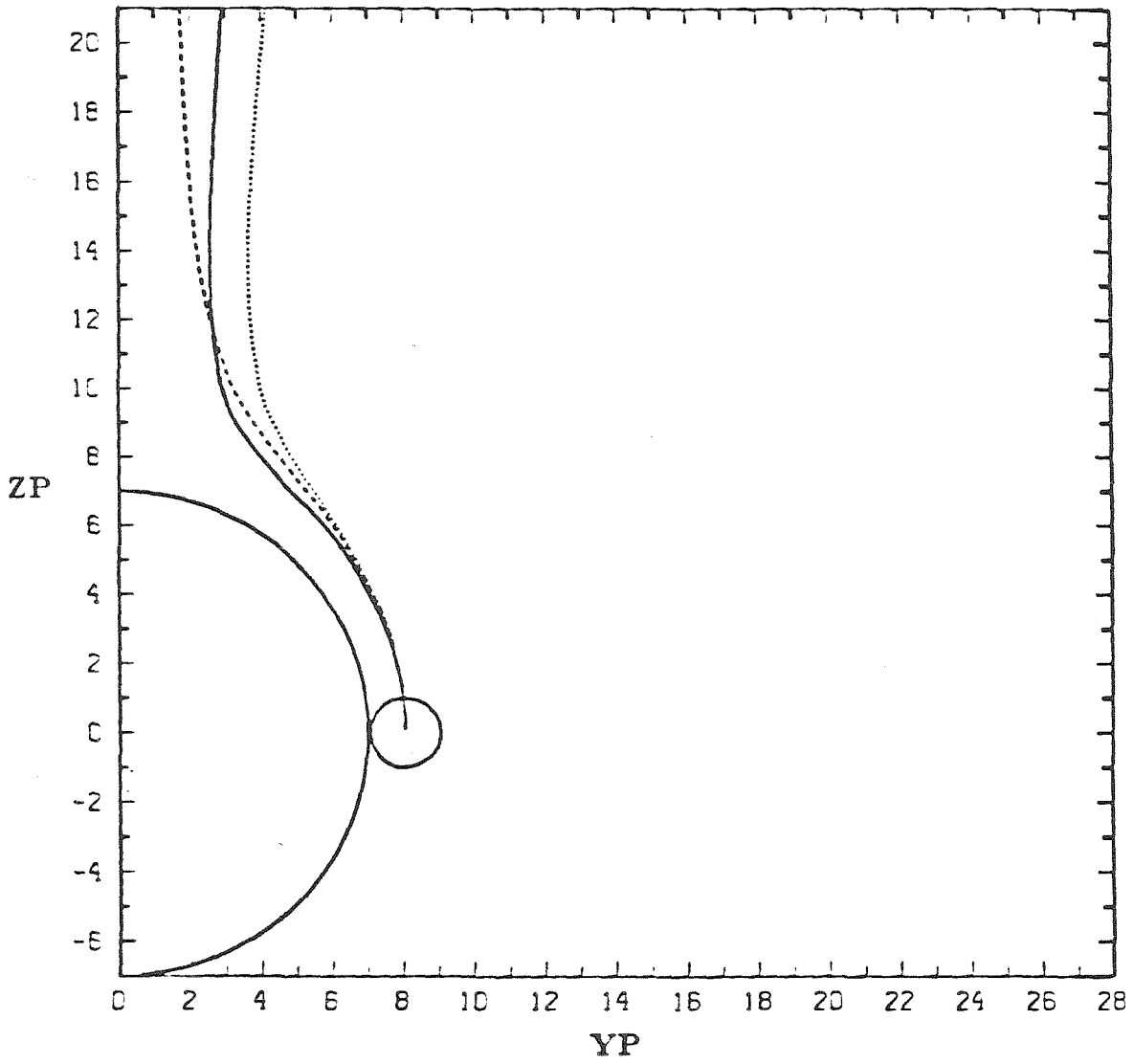

Figure 2. Effects of hydrodynamic interaction on particle trajectory for $\lambda = \infty$, $\frac{a}{R} = \frac{1}{7}$, critical gap = 0.05 a: ———, particle trajectory using Goren and O'Neill's "inner" solution only; - - - - - -, actual fluid streamlines; ·····, Goren and O'Neill's "inner" expansion of streamlines.

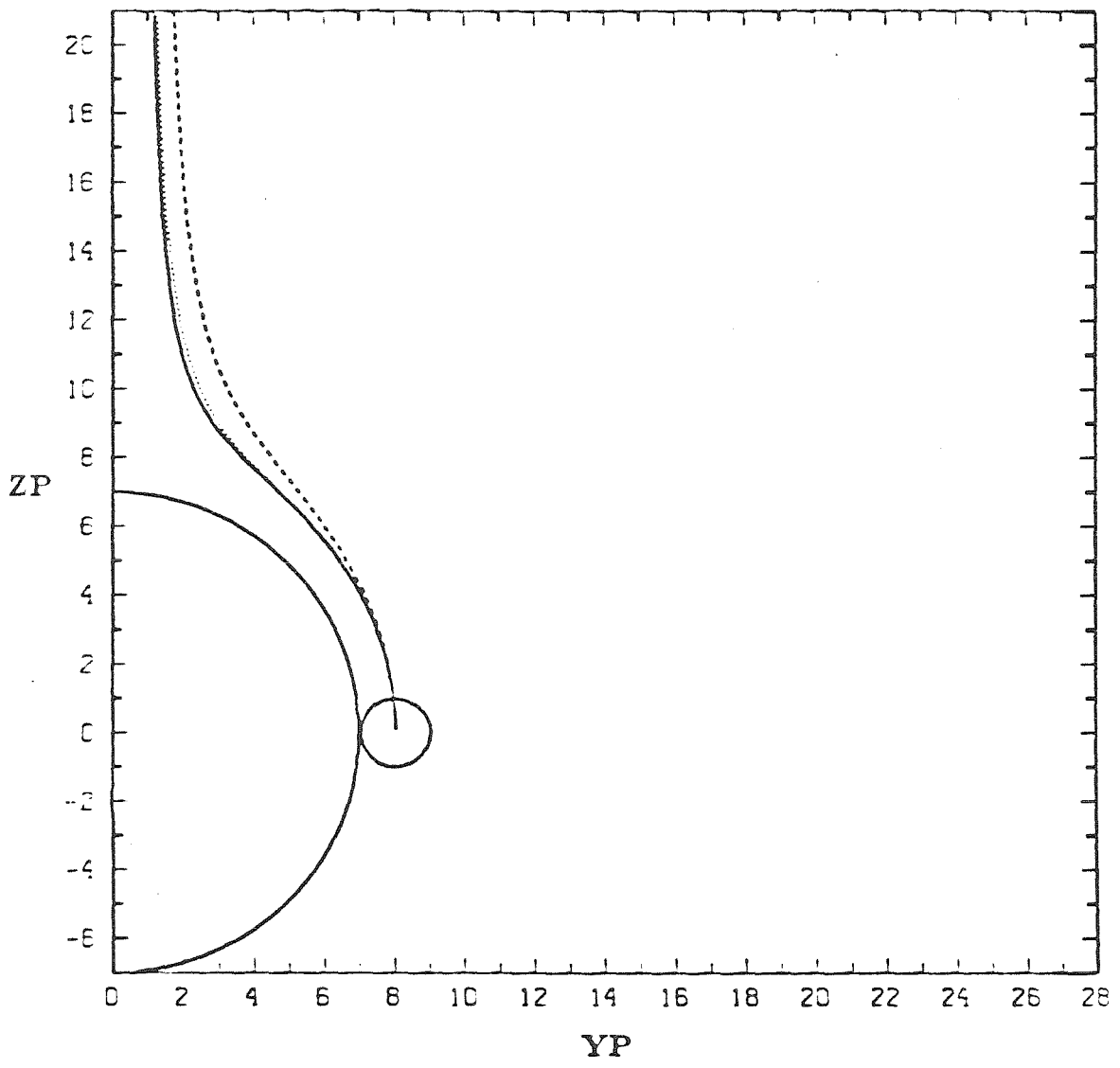

Figure 3. Effects of hydrodynamic interaction on particle trajectory for $\lambda = \infty, \frac{a}{R} = \frac{1}{7}$, critical gap = 0.05 a: ———, particle trajectory using matched asymptotic solution ; - - - - - -, fluid streamlines; ·····, particle trajectory using Jeffrey and Onishi's "exact" solutions.

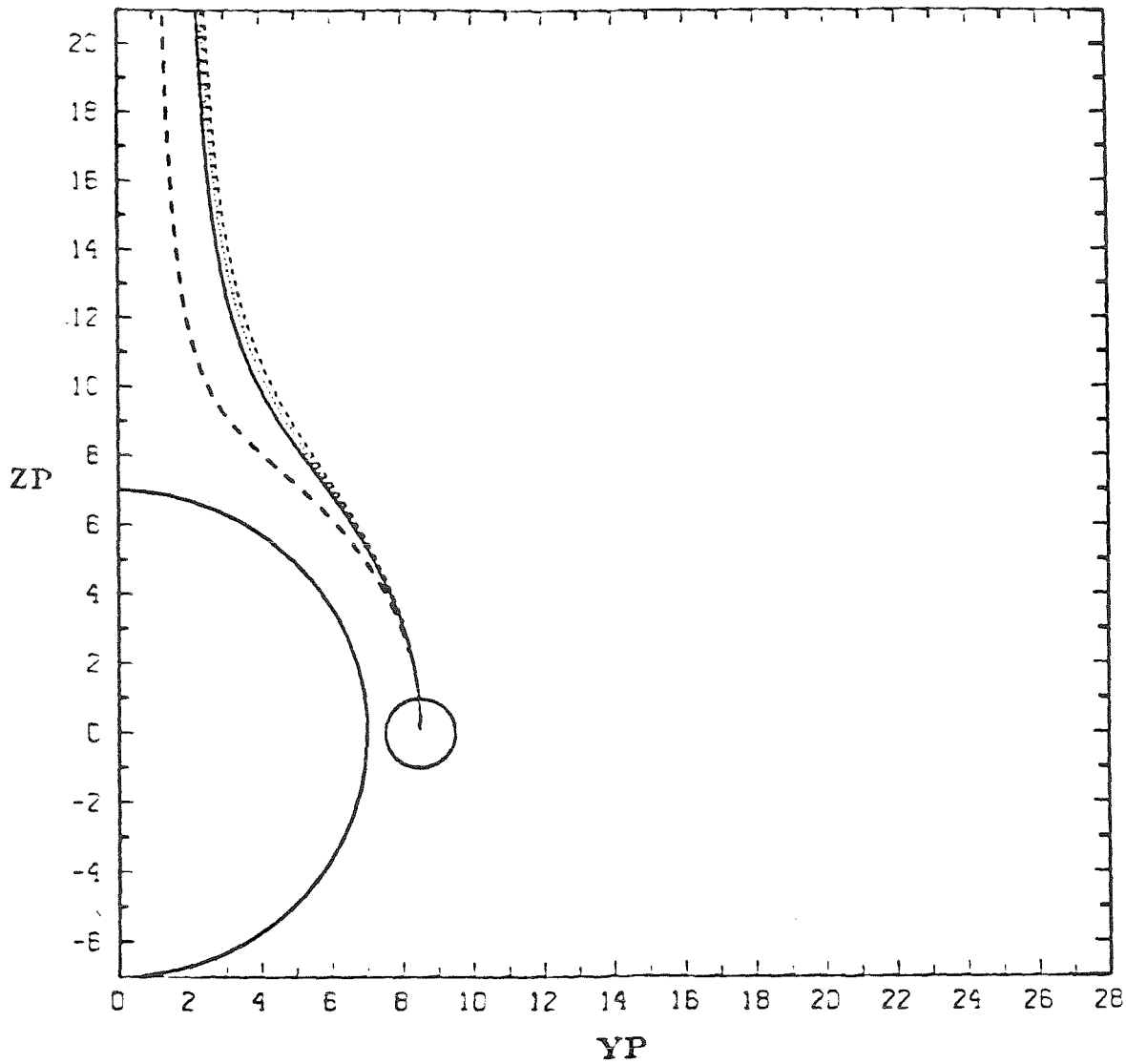

Figure 4. Comparison with reflection solutions where reflection is about both sphere centers for $\lambda = \infty, \frac{a}{R} = \frac{1}{7}$, critical gap = 0.5 a: ——, particle trajectory using matched asymptotic solution ; - - - - - -, fluid streamlines; ·····, particle trajectory using Jeffrey and Onishi's "exact" solutions; – – – –, Happel and Brenner's reflection about both sphere centers.

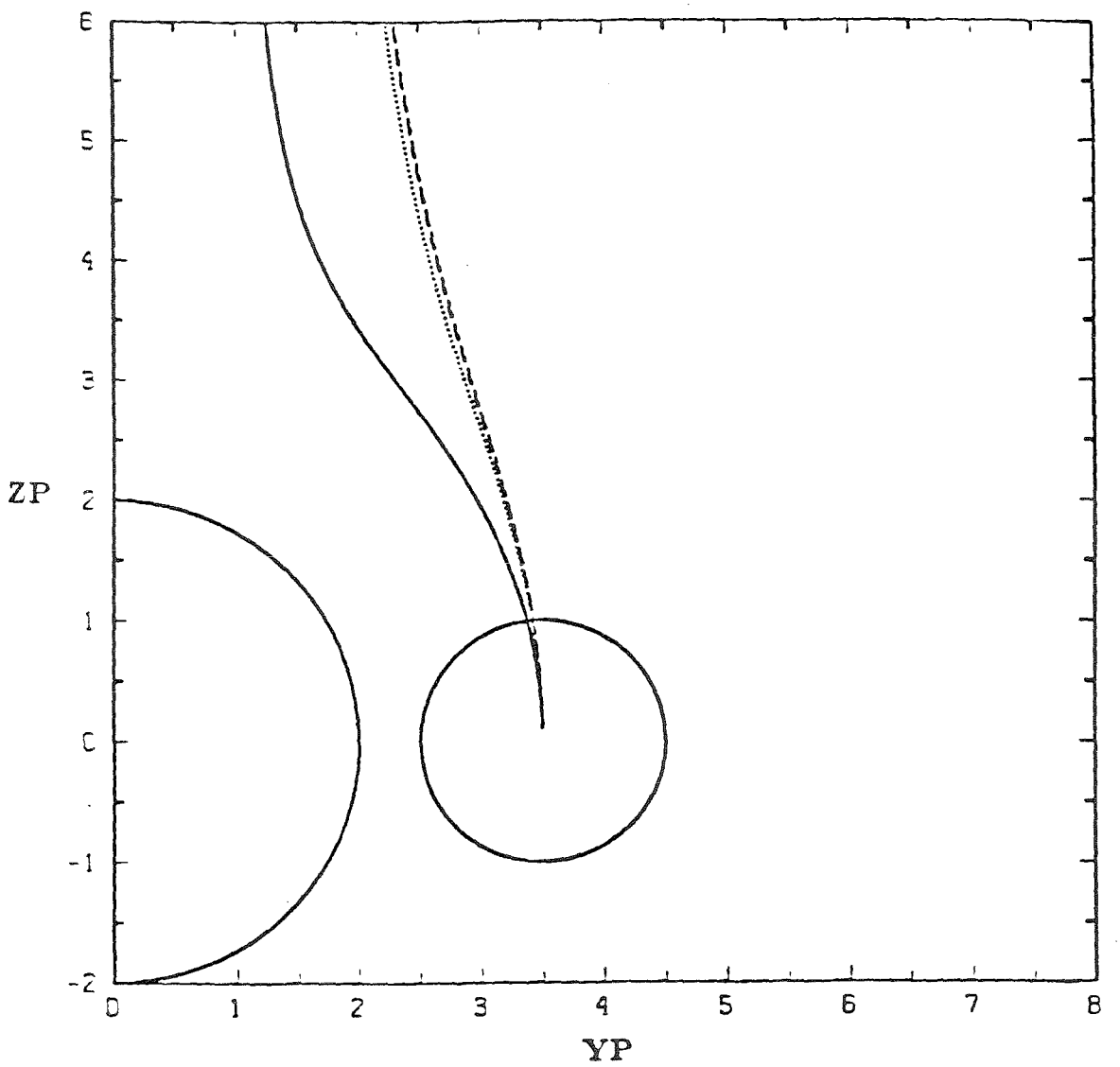

Figure 5. Comparison with reflection solutions where reflection is about both sphere centers for $\lambda = \infty, \frac{a}{R} = \frac{1}{2}$, critical gap = 0.5 a: ——, particle trajectory using matched asymptotic solution ; - - - - - -, fluid streamlines; ·····, particle trajectory using Jeffrey and Onishi's "exact" solutions; – – – –, Happel and Brenner's reflection about both sphere centers.

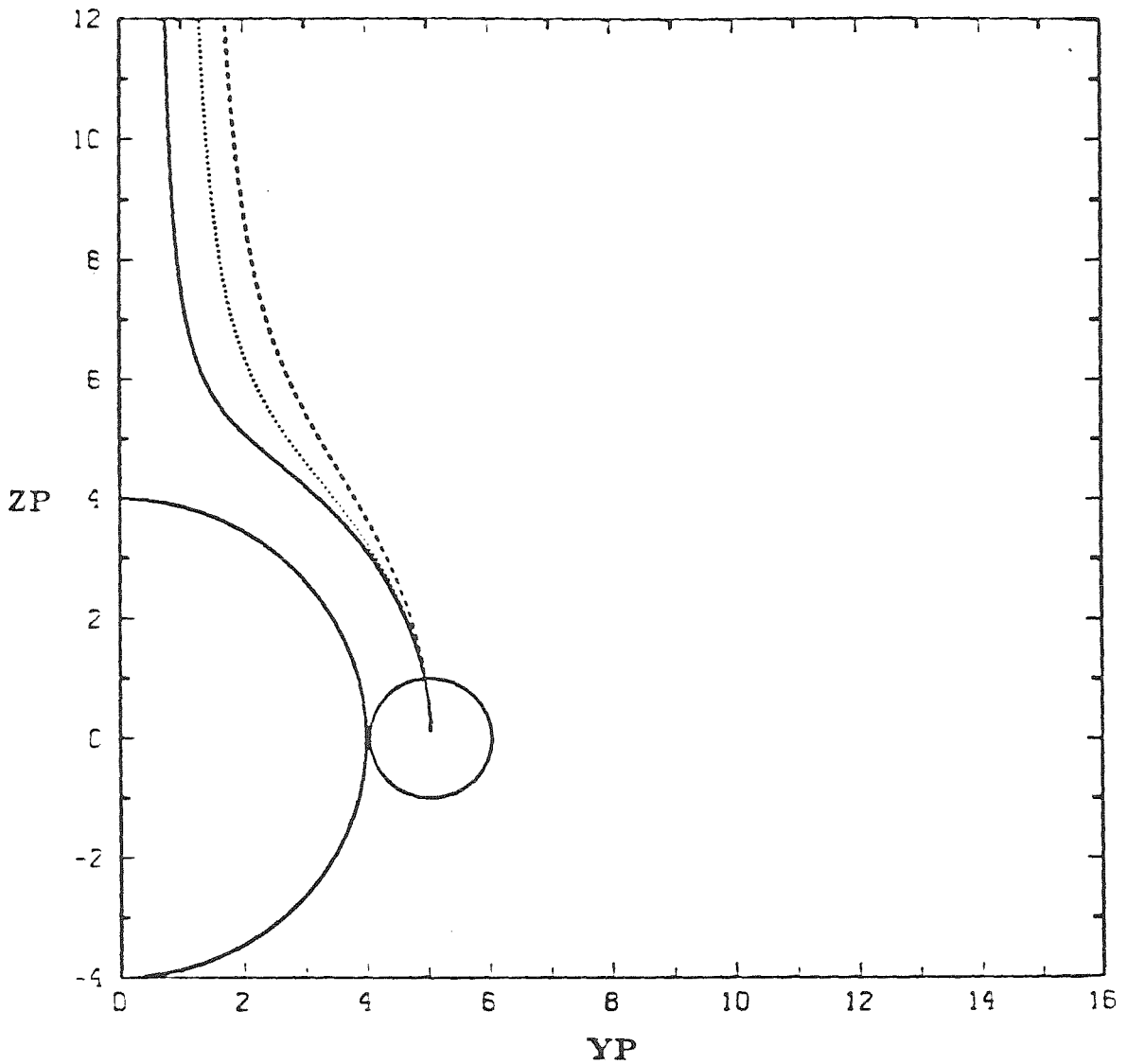

Figure 6. Effects of hydrodynamic interaction on particle trajectory for $\lambda = \infty, \frac{a}{R} = \frac{1}{4}$, critical gap = 0.05 a: ———, particle trajectory using matched asymptotic solution ; - - - - - -, fluid streamlines; ·····, particle trajectory using Jeffrey and Onishi's "exact" solutions.

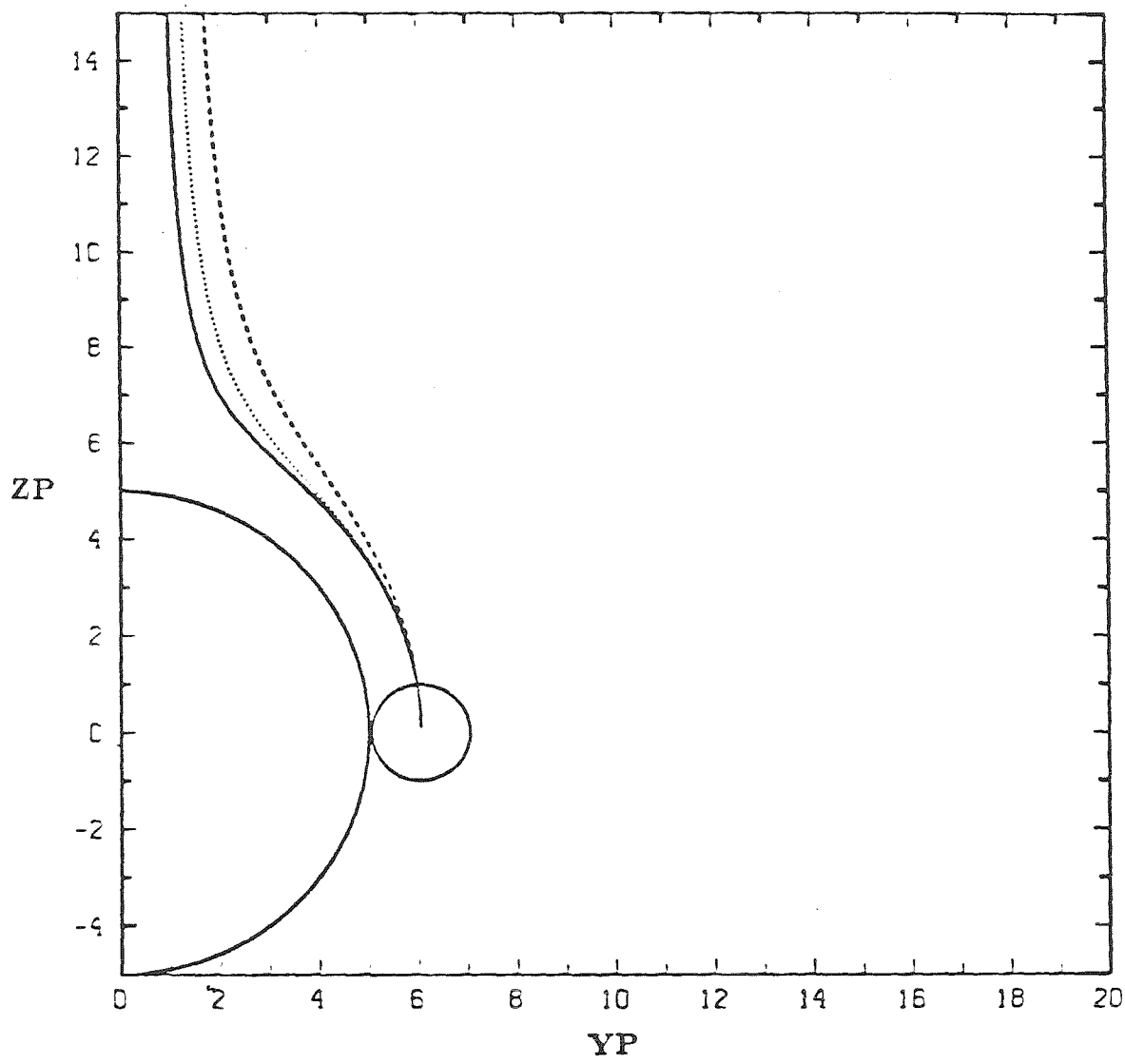

Figure 7. Effects of hydrodynamic interaction on particle trajectory for $\lambda = \infty, \frac{a}{R} = \frac{1}{5}$, critical gap = 0.05 a: ———, particle trajectory using matched asymptotic solution ; - - - - - -, fluid streamlines; ·····, particle trajectory using Jeffrey and Onishi's "exact" solutions.

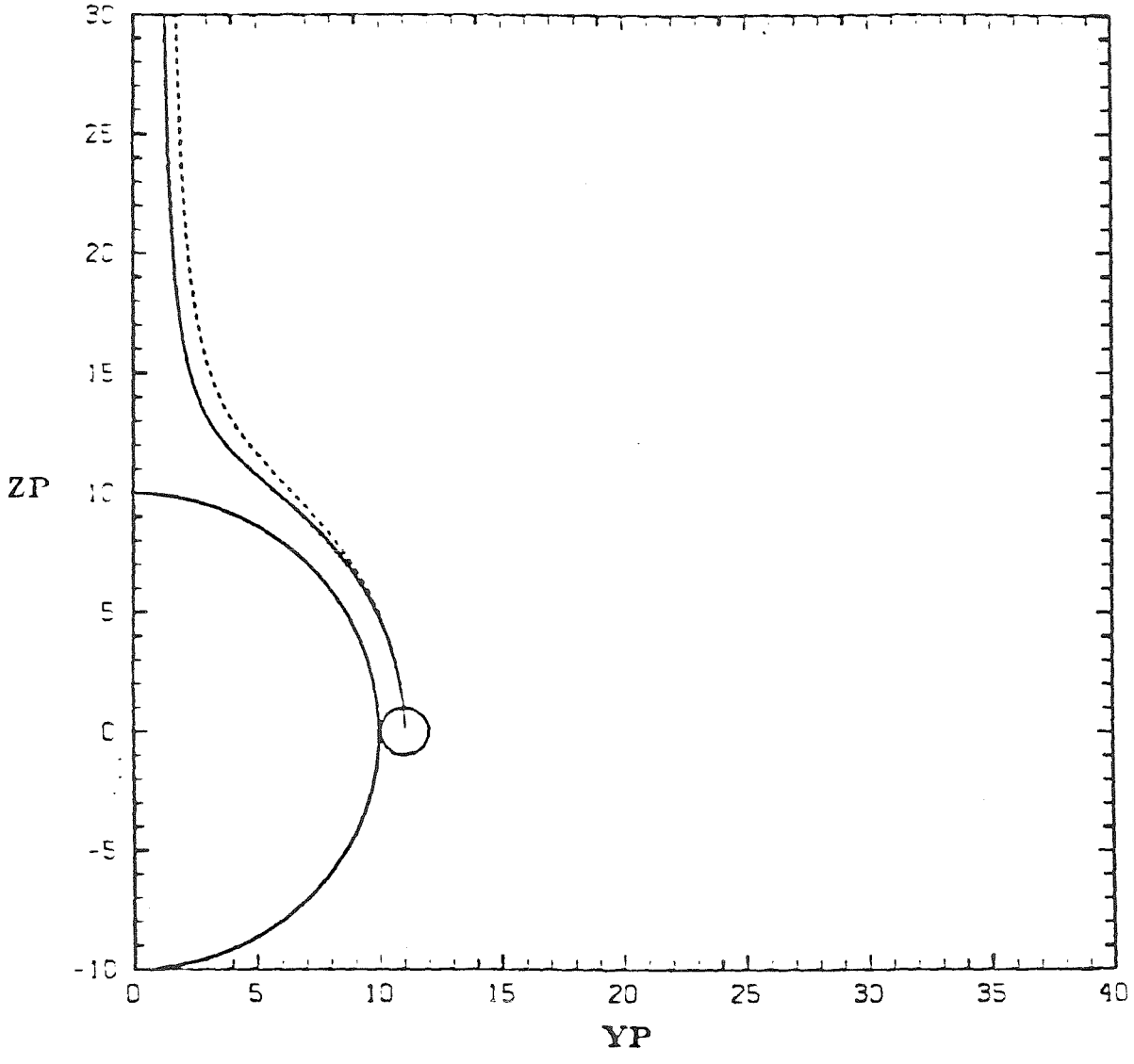

Figure 8. Effects of hydrodynamic interaction on particle trajectory for $\lambda = \infty, \frac{a}{R} = \frac{1}{10}$, critical gap = 0.05 a: ———, particle trajectory using matched asymptotic solution ; - - - - - -, fluid streamlines; ·····, particle trajectory using Jeffrey and Onishi's "exact" solutions.

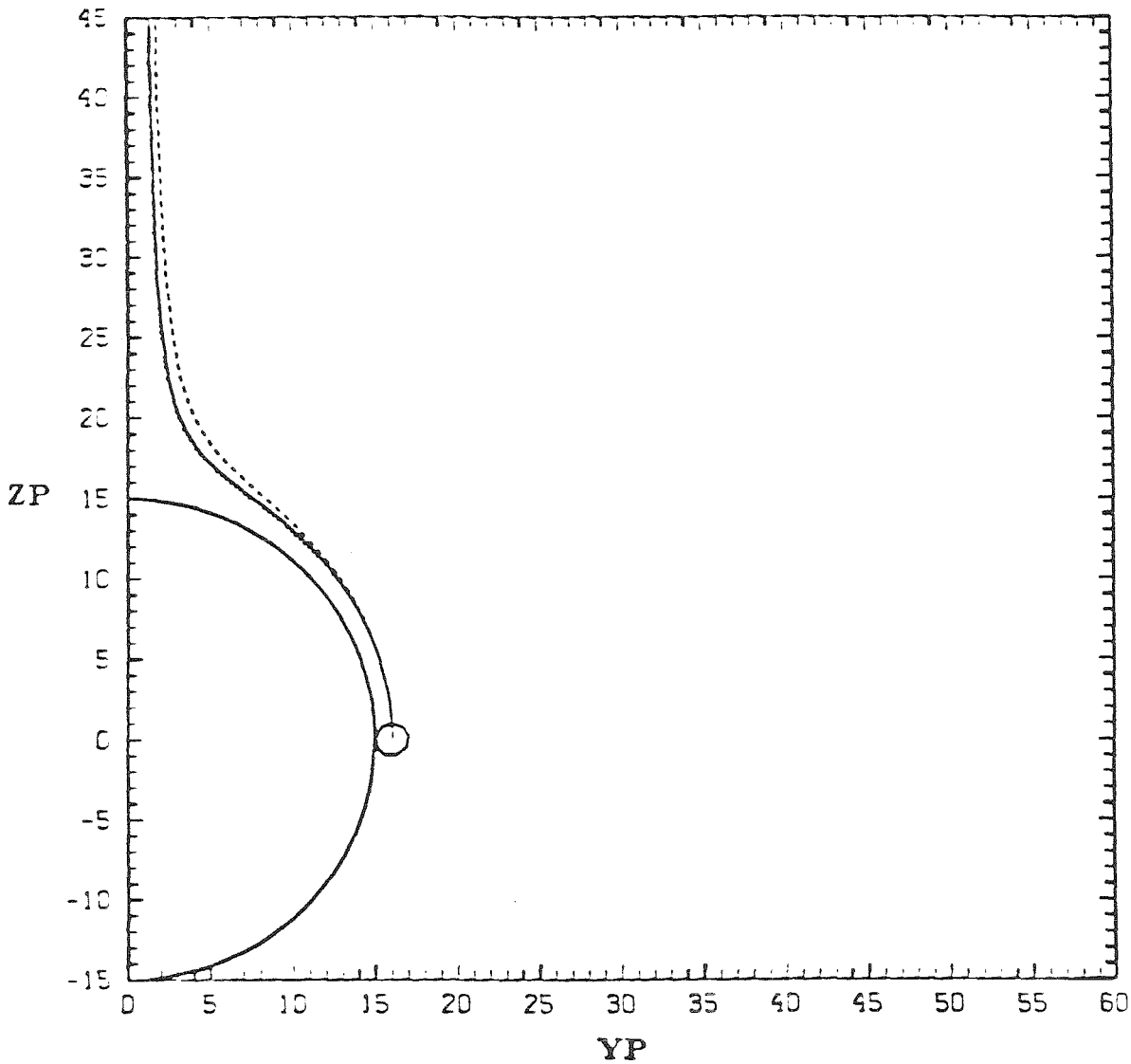

Figure 9. Effects of hydrodynamic interaction on particle trajectory for $\lambda = \infty, \frac{a}{R} = \frac{1}{15}$, critical gap = 0.05 a: ———, particle trajectory using matched asymptotic solution ; - - - - - -, fluid streamlines; ·····, particle trajectory using Jeffrey and Onishi's "exact" solutions.

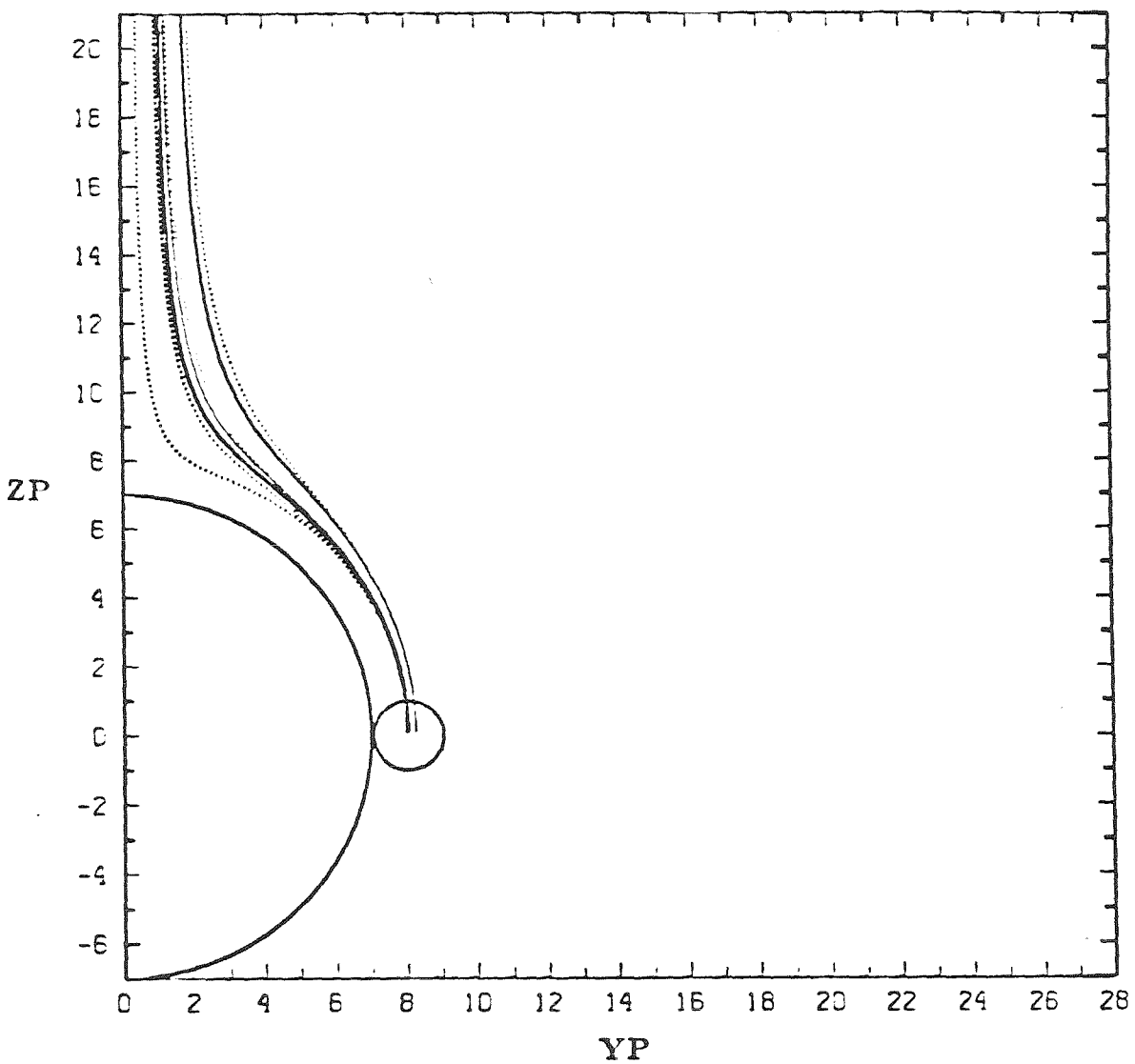

Figure 10. Effects of critical gap on hydrodynamic interaction and the particle trajectory for $\lambda = \infty, \frac{a}{R} = \frac{1}{7}$, critical gaps = 0.25 a, 0.05 a, 0.01 a, 0.0001 a: ———, particle trajectory using matched asymptotic solution ; ·····, particle trajectory using Jeffrey and Onishi's "exact" solutions.

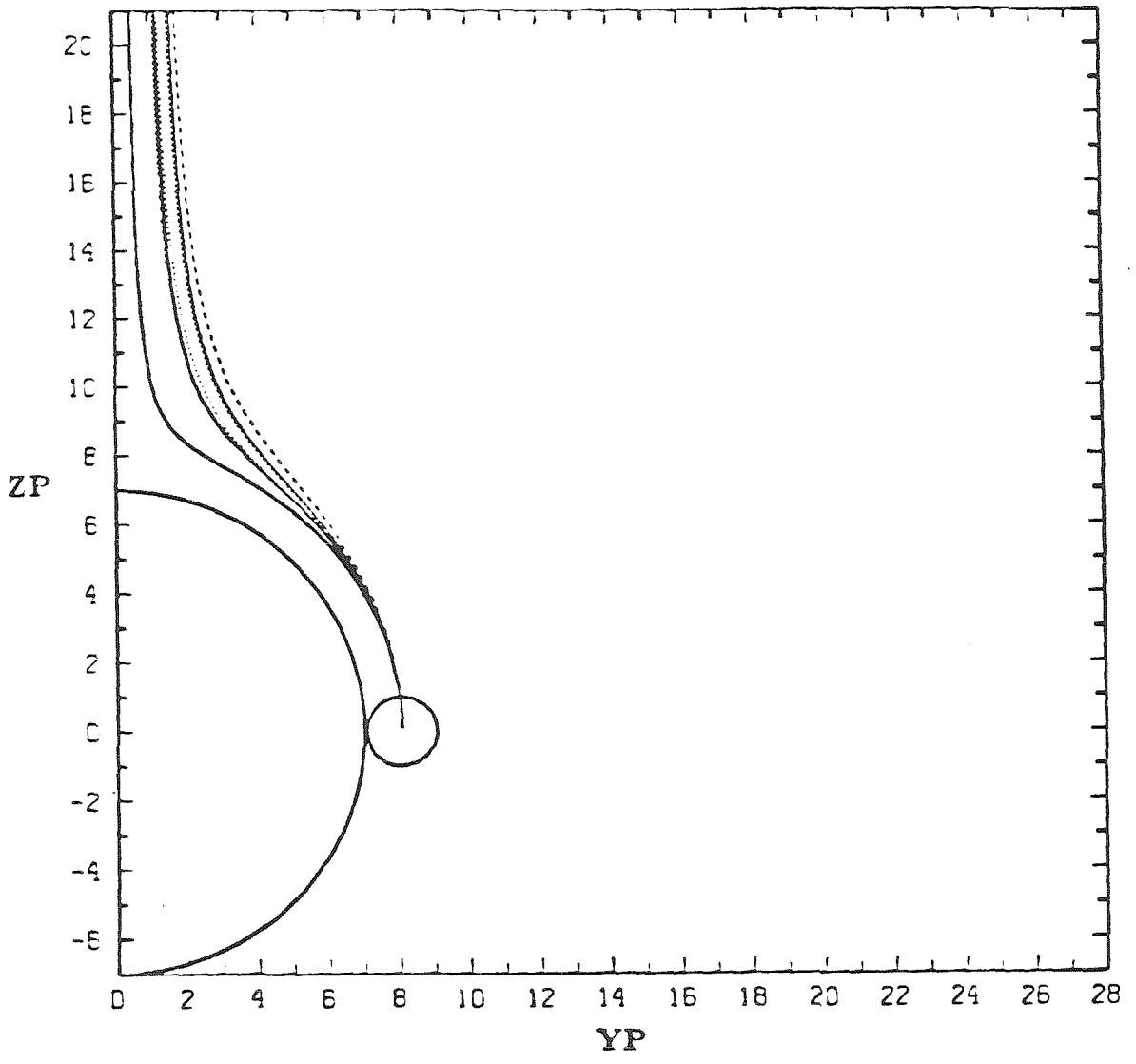

Figure 11. Effects of particle density on hydrodynamic interaction and the particle trajectory for $\lambda = \infty$, $\frac{\Delta \rho_p}{\Delta \rho_d} = -0.5,\ 0.0,\ 0.5$, $\frac{a}{R} = \frac{1}{7}$, critical gap = 0.05 a: ———, particle trajectory using matched asymptotic solution ; ·····, particle trajectory using Jeffrey and Onishi's "exact" solutions.

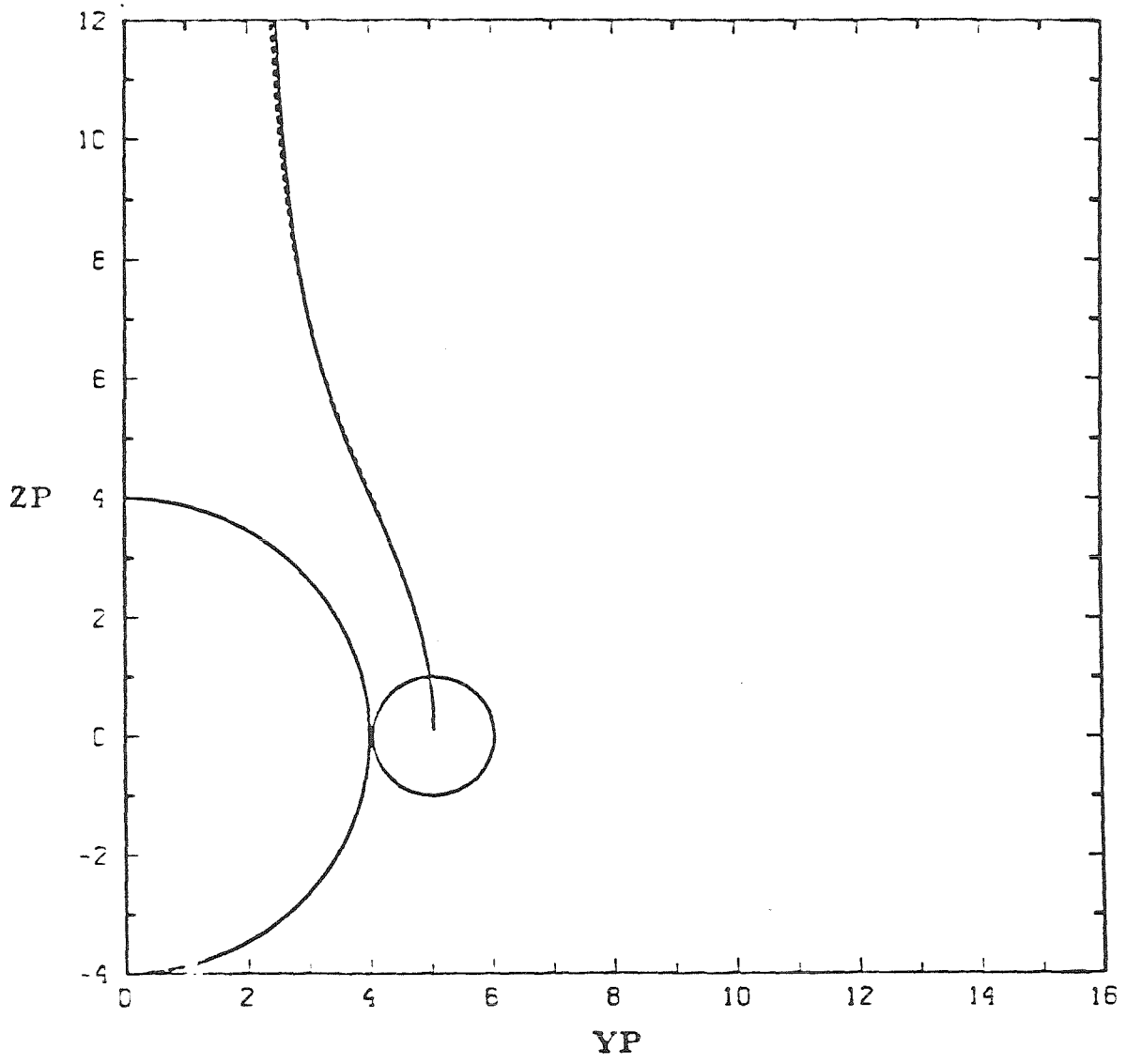

Figure 12. Effects of hydrodynamic interaction on particle trajectory for $\lambda = \infty, \frac{a}{R} = \frac{1}{4}$, critical gap = 0.05 a: ———, particle trajectory using matched asymptotic solution ; - - - - - -, fluid streamlines; ·····, particle trajectory using Jeffrey and Onishi's "exact" solutions.

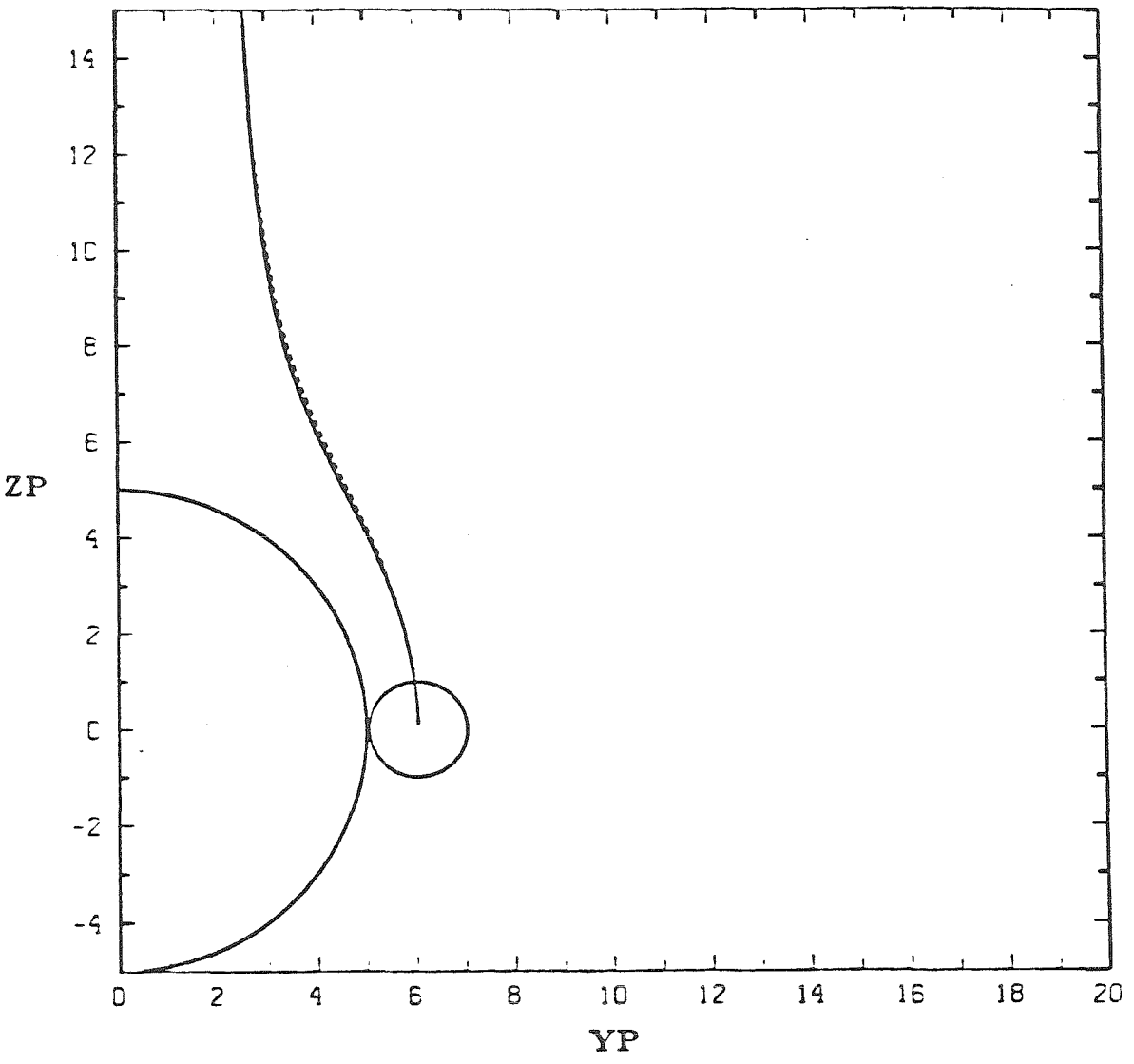

Figure 13. Effects of hydrodynamic interaction on particle trajectory for $\lambda = 1, \frac{a}{R} = \frac{1}{5}$, critical gap = 0.05 a: ———, particle trajectory using matched asymptotic solution ; - - - - - -, fluid streamlines; · · · · · · ·, particle trajectory using Jeffrey and Onishi's "exact" solutions.

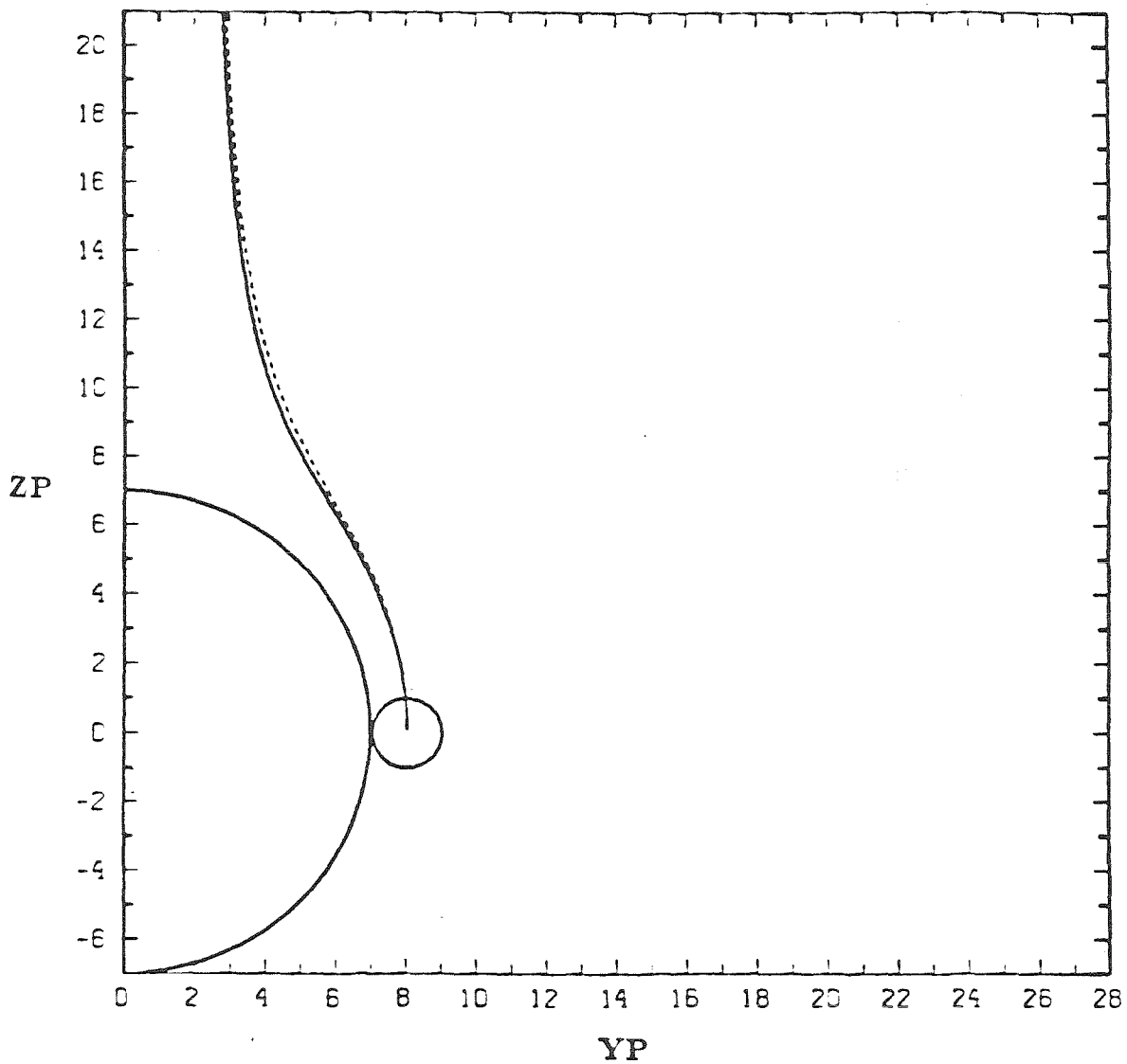

Figure 14. Effects of hydrodynamic interaction on particle trajectory for $\lambda = 1, \frac{a}{R} = \frac{1}{7}$, critical gap = 0.05 a: ———, particle trajectory using matched asymptotic solution ; - - - - - -, fluid streamlines; ·····, particle trajectory using Jeffrey and Onishi's "exact" solutions.

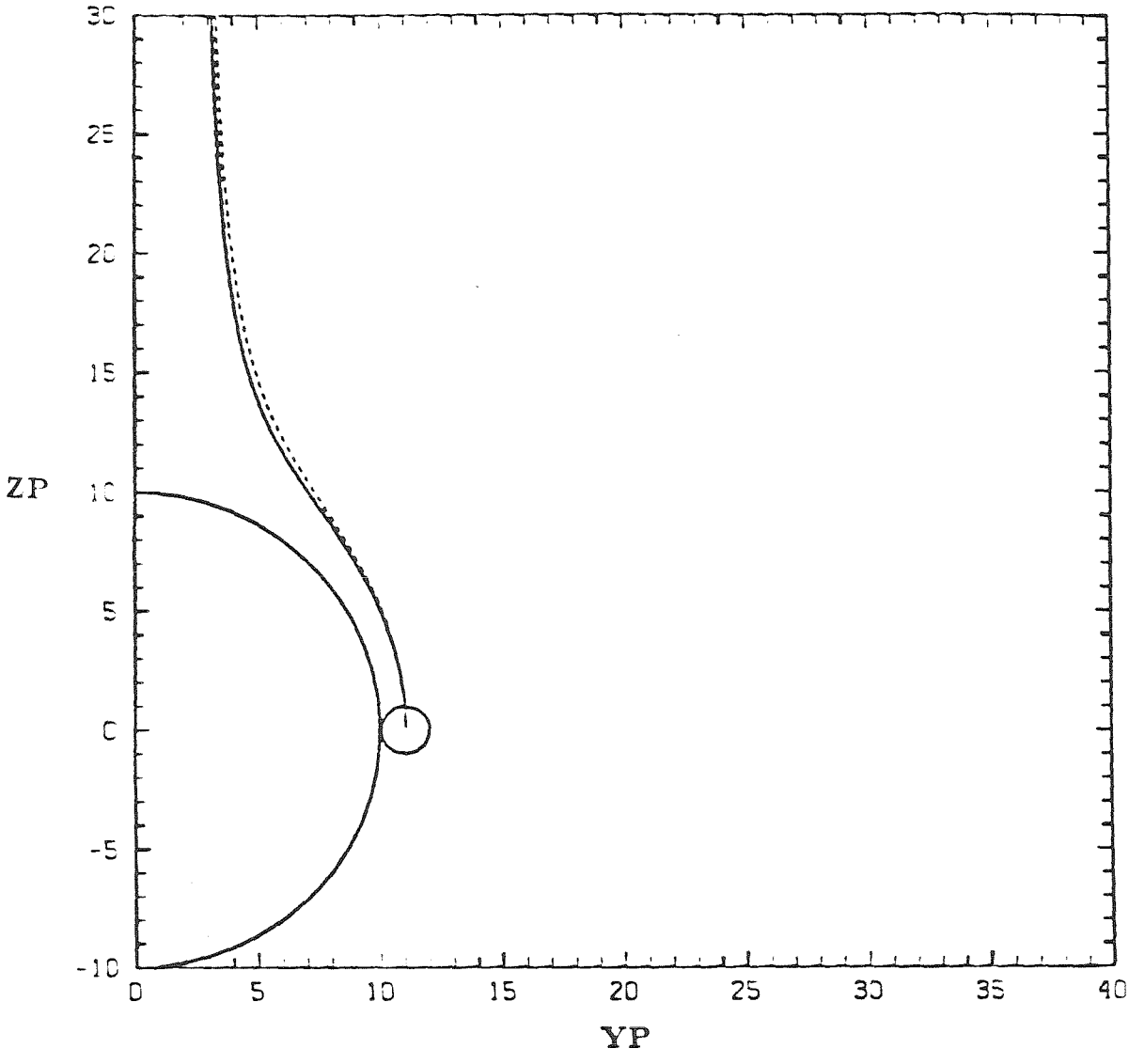

Figure 15. Effects of hydrodynamic interaction on particle trajectory for $\lambda = 1, \frac{a}{R} = \frac{1}{10}$, critical gap = 0.05 a: ———, particle trajectory using matched asymptotic solution ; - - - - - -, fluid streamlines; ·····, particle trajectory using Jeffrey and Onishi's "exact" solutions.

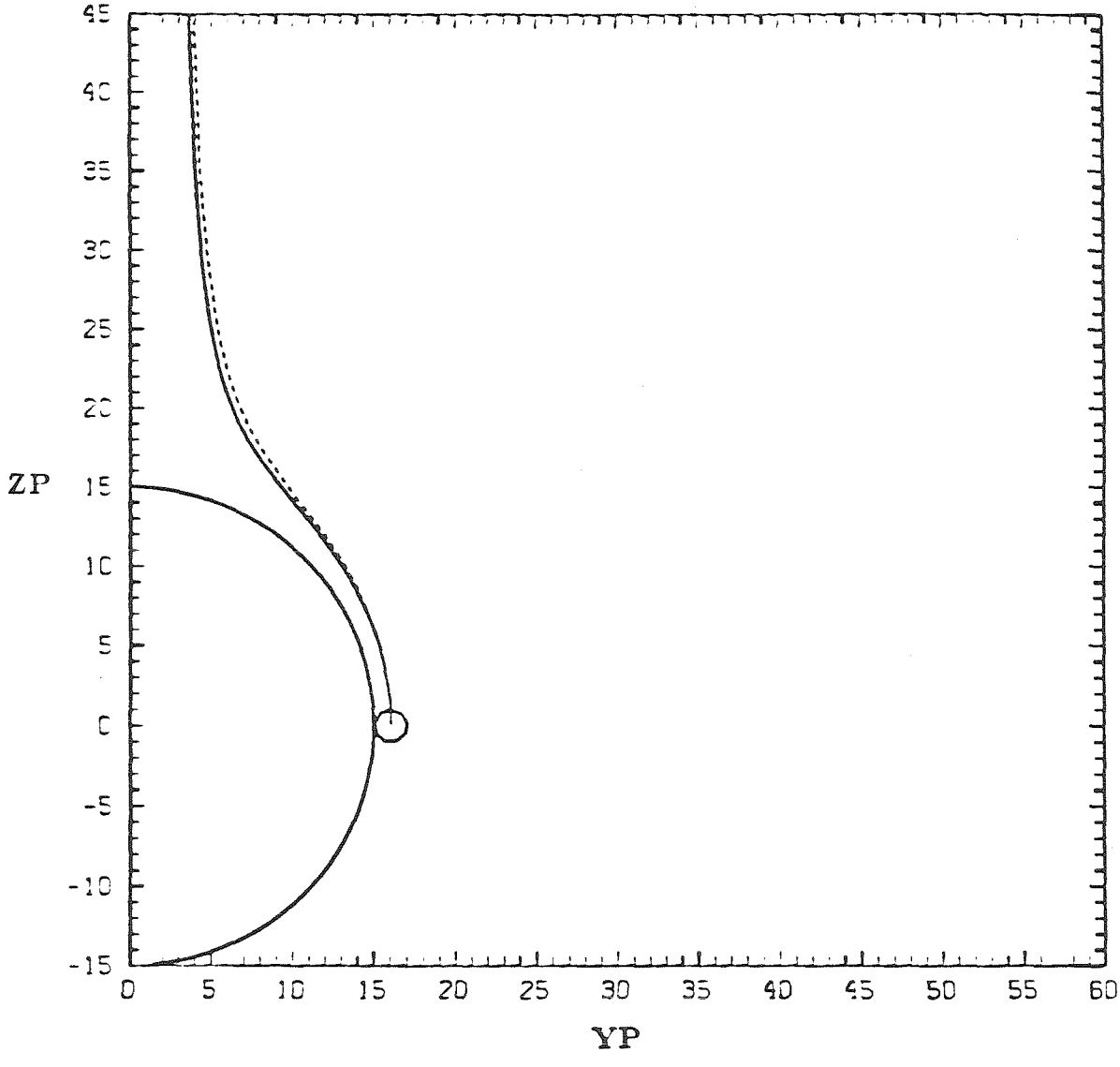

Figure 16. Effects of hydrodynamic interaction on particle trajectory for $\lambda = 1, \frac{a}{R} = \frac{1}{15}$, critical gap = 0.05 a: ———, particle trajectory using matched asymptotic solution ; - - - - - -, fluid streamlines; ·····, particle trajectory using Jeffrey and Onishi's "exact" solutions.

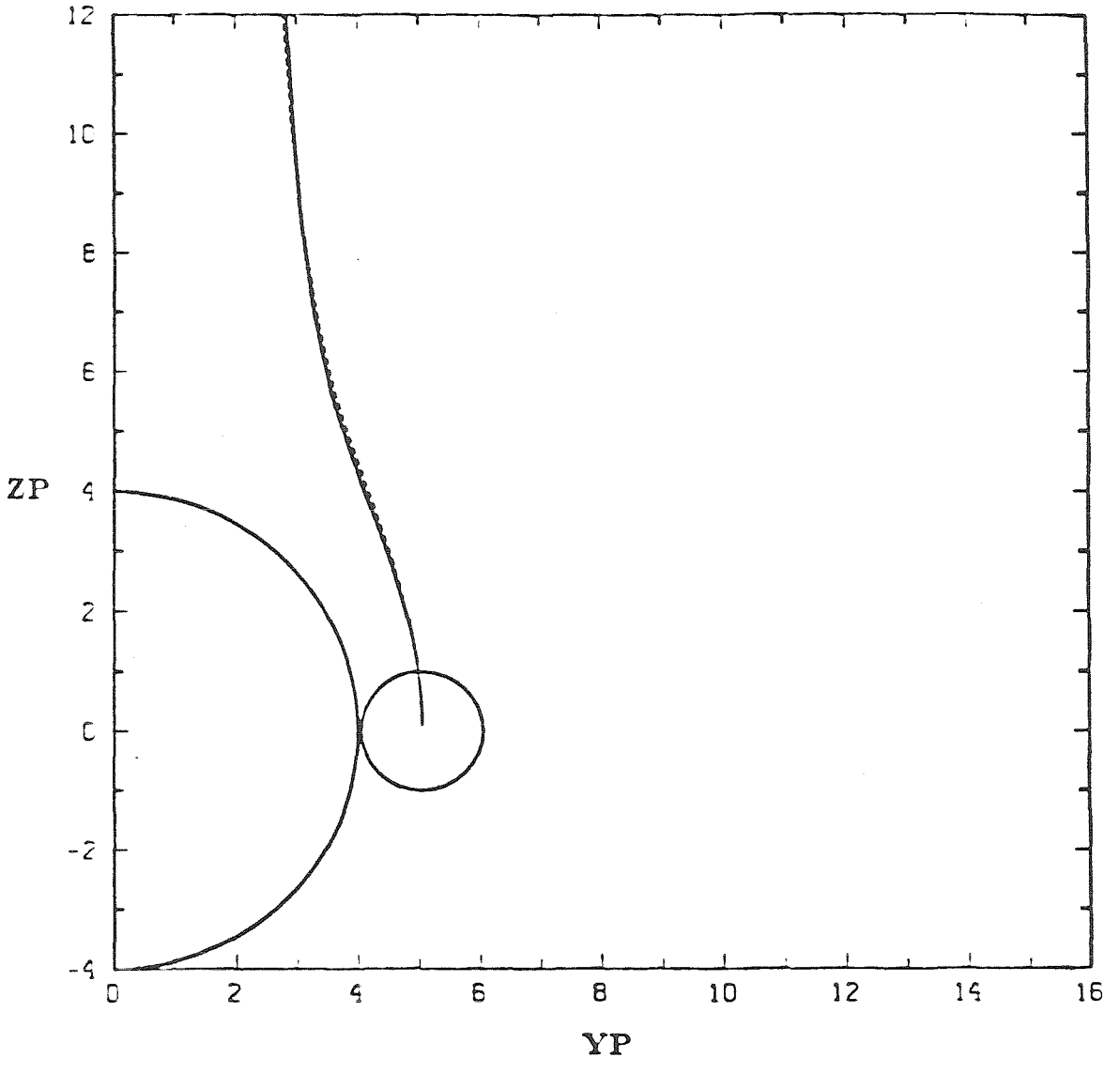

Figure 17. Effects of hydrodynamic interaction on particle trajectory for $\lambda = \infty, \frac{a}{R} = \frac{1}{4}$, critical gap = 0.05 a: ———, particle trajectory using matched asymptotic solution ; - - - - - -, fluid streamlines; ·····, particle trajectory using Jeffrey and Onishi's "exact" solutions.

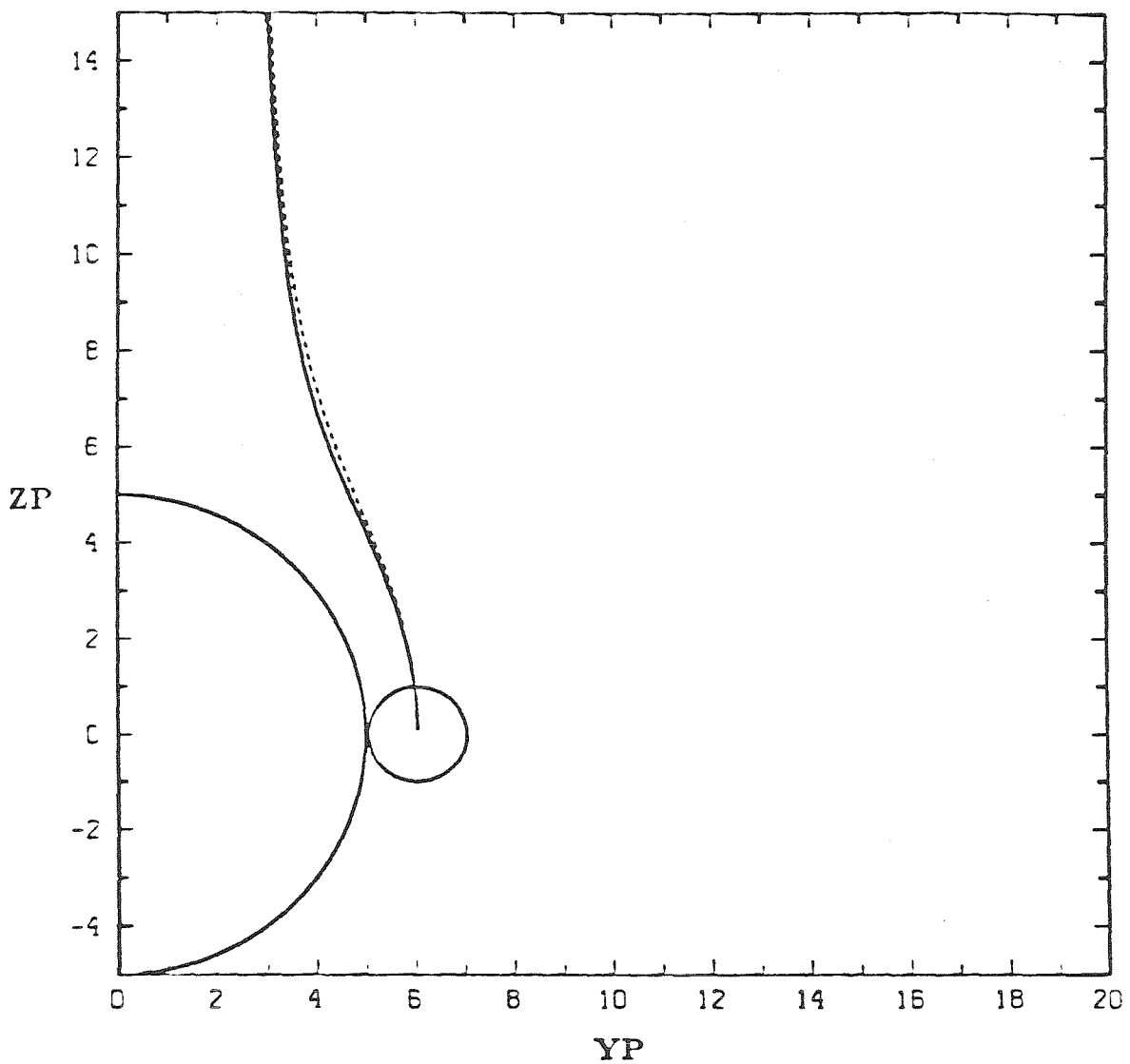

Figure 18. Effects of hydrodynamic interaction on particle trajectory for $\lambda = 1, \frac{a}{R} = \frac{1}{5}$, critical gap $= 0.05\ a$: ———, particle trajectory using matched asymptotic solution ; - - - - - -, fluid streamlines; ·····, particle trajectory using Jeffrey and Onishi's "exact" solutions.

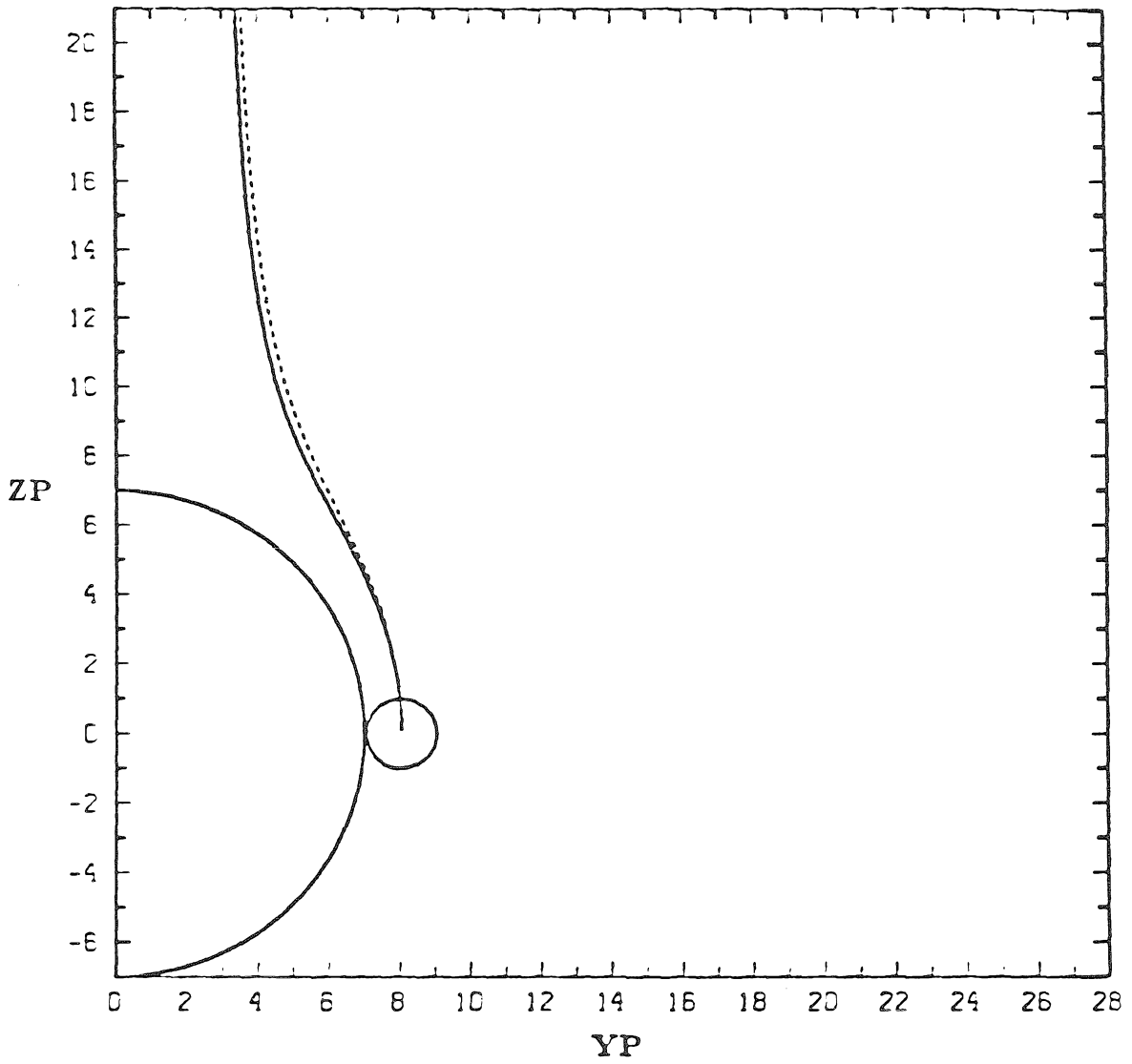

Figure 19. Effects of hydrodynamic interaction on particle trajectory for $\lambda = 1, \frac{a}{R} = \frac{1}{7}$, critical gap = 0.05 a: ———, particle trajectory using matched asymptotic solution ; - - - - - -, fluid streamlines; ·····, particle trajectory using Jeffrey and Onishi's "exact" solutions.

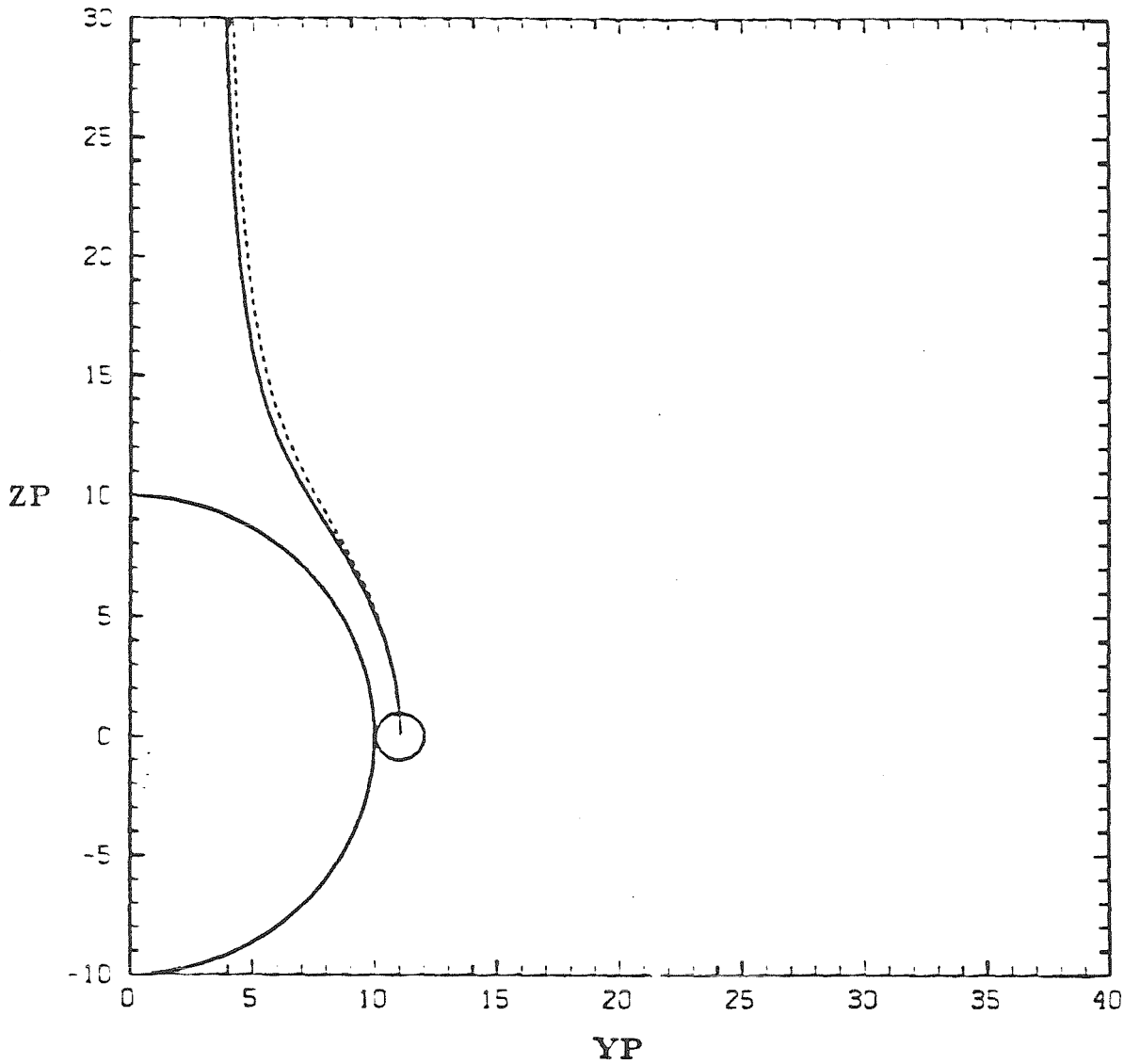

Figure 20. Effects of hydrodynamic interaction on particle trajectory for $\lambda = 1, \frac{a}{R} = \frac{1}{10}$, critical gap $= 0.05\ a$: ———, particle trajectory using matched asymptotic solution ; - - - - - -, fluid streamlines; · · · · · · ·, particle trajectory using Jeffrey and Onishi's "exact" solutions.

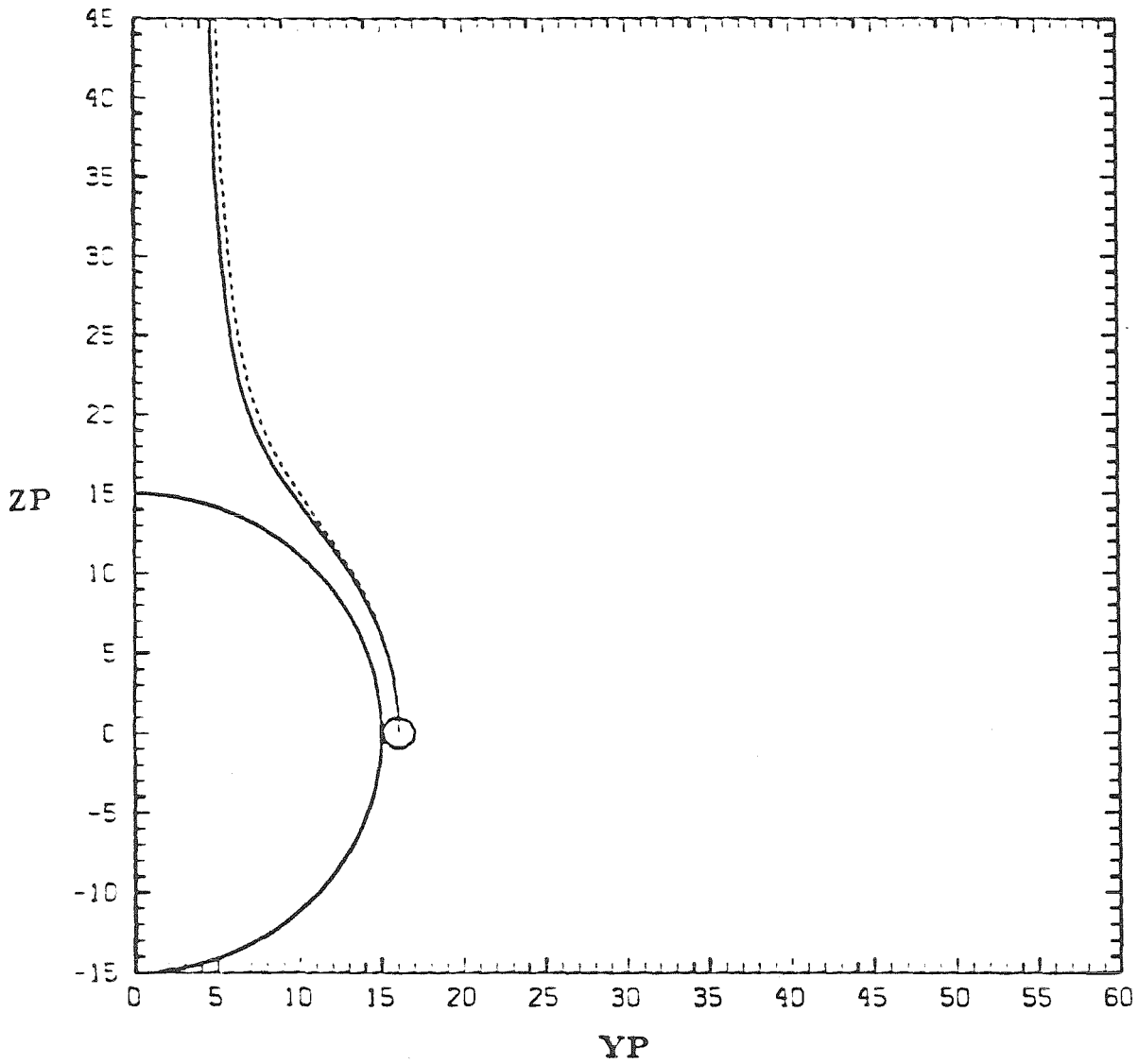

Figure 21. Effects of hydrodynamic interaction on particle trajectory for $\lambda = 1, \frac{a}{R} = \frac{1}{15}$, critical gap = 0.05 a: ———, particle trajectory using matched asymptotic solution ; - - - - - -, fluid streamlines; ·····, particle trajectory using Jeffrey and Onishi's "exact" solutions.

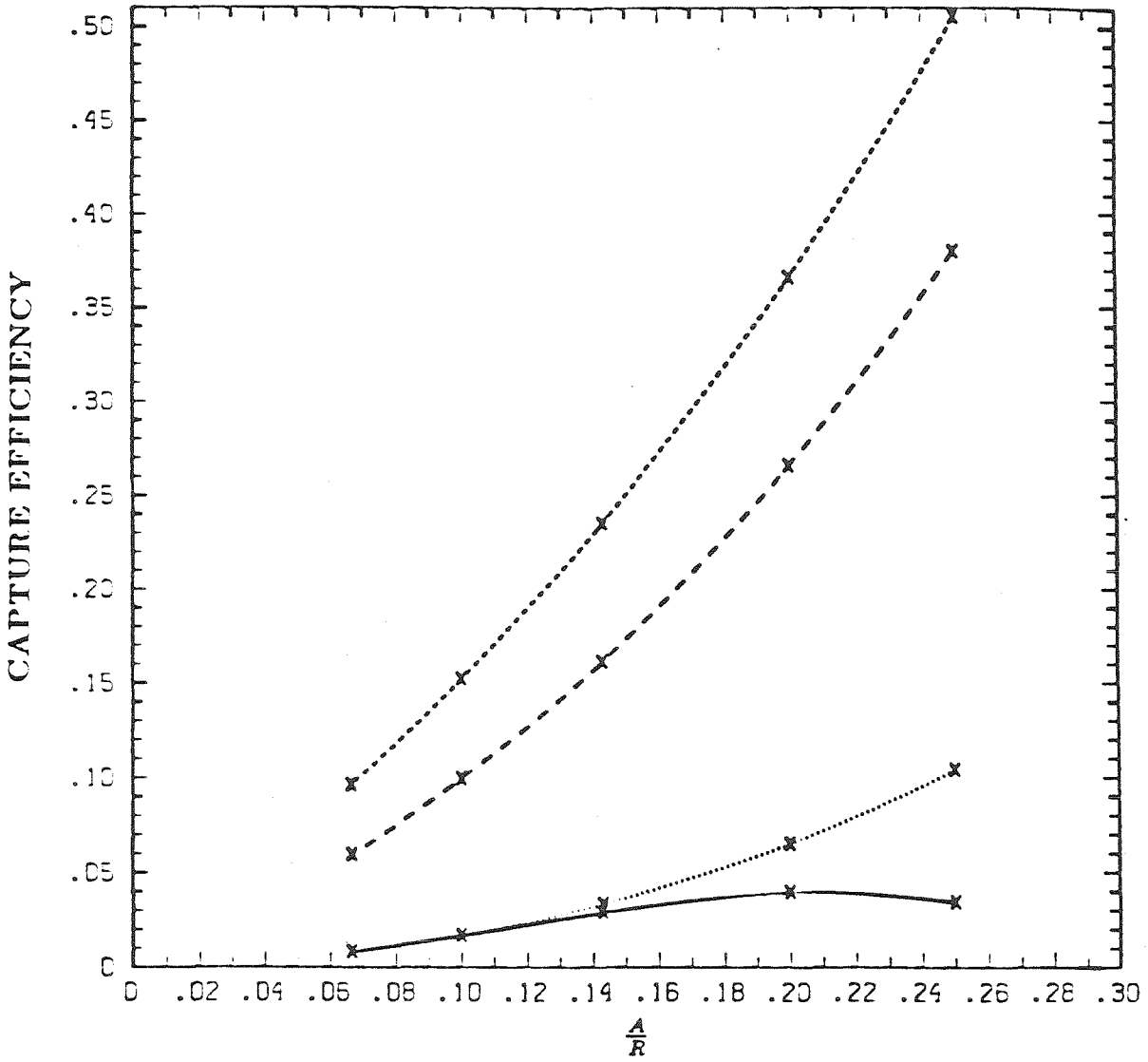

Figure 22. Capture efficiency for a critical gap of 0.05 as a function of $\frac{a}{R}$: - - - - - -, $\lambda = 0$; – – – –, $\lambda = 1$; ·····, $\lambda = \infty$, Jeffrey and Onishi's "exact" solutions; ————, $\lambda = \infty$, asymptotic solutions.

```
c           integrate the instantaneous particle velocity
c           (which is calculated from a matched asymptotic
c           expansion) to obtain the particle trajectory.
c           Note - a quadruture routine is required (this
c           routine assumes the IMSL routine "DGEAR" is
c           used, however other canned quadruture routines
c           may be used with the approprate
c           changes in notation).
c
c           a = ratio of particle to drop radius
c           e = epsilon = 1/(distance from particle center
c               to drop surface
c           mth = method of dgear used
c           mit = method of obtaining second derivatives, dgear
c           ypo = initial position of particle yp, axis pointing
c                 along equator of drop, "world coordinates"
c           zpo = initial position of particle zp, vertical axis
c           xlmda= ratio of drop to fluid viscosity, (lambda)
c           ap = particle radius (always=1.)
c           r = drop radius
c           nt = total number of iteration steps
c           dy = step size
c           dpr = ratio of density difference between particle
c                 and fluid to the density difference between
c                 the fluid and drop
c           error = allowed error per step in dgear
c           idir  = direction of integration, -1 back from
c                   near contact, +1 towards the drop.
c           zf = final value of zp
c           zprnt = value of interval over which zp is recorded
c           qdis = dispersion constant
c           qdl  = double-layer constant
c           tau = double-layer size
c
c
c           ********************************************************
c
c
      implicit real * 8 (a-h,o-z)
      implicit integer * 4 (i-n)
      external deriv,derivj
      dimension dmy327(1), wk(200)
      common xlmda,aor,dpr,ap,uz,auz,uyf,uzf,qdis
      common r,er,eg1,eg2,eg3,f,fg2,fg3,b,bg2,bg3,c,cg2
      common x11m,x12m,y11m,y12m,em,fm,swch,xr,ya,yb,yc
      common dydz,uy,auy,cg3,cg4,cg5,c4,e2,u0,rm1,r0
      common p02,p12,p21,p22,p31,p32,p41,p42,c1,c2,c3
      common r2,e3,e4,u3,s02,s12,s21,s22,s31,s32,s41
      common qdl,tau,s42,d1,d2,d3,d4
      pi = 3.141592654
```

```
      write (*,10)
   10 format (1x,'mth,mit,ypo,zpo,xlmda,r,nt,dy,dpr,err0r,
     * idir,zf,zprnt,swch,sch1,qdis,qdl,tau'/)
      read (*,*)meth,miter,ypo,zpo,xlmda,r,nt,dy,dpr,error,
     * idir,zf,zprnt,swch,sch1,qdis,qdl,tau
      write (*,*)meth,miter,ypo,zpo,xlmda,r,nt,dy,dpr,error,
     * idir,zf,zprnt,swch,sch1,qdis,qdl,tau
      ap =  1.0d+00
      d = sqrt( zpo **2 + ypo **2 ) / ap -  r / ap
      na = 1
      e = 1.0 / d
      apn = 1.5 * ap
      aor = ap / r
      a = aor
      zfin = zf
      roa = r / ap
      x = xlmda
c     compute coefficients for Fy, Fz, Tx which only
c     depend on ap/r, xlmda
      xp1 = x + 1.0
      x3m2 = (3.0 * x - 2.0)/xp1
      x2p1 = (2.0 * x + 1.0)/xp1
      x4p1 = (4.0 * x + 1.0)/xp1
      x3p2 = (3.0 * x + 2.0)/xp1
      x9p2 = (9.0 * x + 2.0)/xp1
      x5m2 = (5.0 * x - 2.0)/xp1
      x3p1 = (3.0 * x + 1.0)/xp1
      x9m5 = (9.0 * x - 5.0)/xp1
      xm1 = (x - 1.0)/xp1
      c1=(3.0*x3m2)/16.0
      c2=c1*c1
      c3=c2*c1-(x2p1/16.0)
      c4=c2*c2-9.0*x2p1*x3m2/256.-3.0*x5m2/(128.*xp1)
      c4n=c4-3.0/(64.0*xp1*xp1)
      c31=-(41.0*x+10.0)/(64.0*xp1)
      c32=(10.0-19.0*x)/(128.0*xp1)
      c33=(-2.0+11.0*x)/(32.0*xp1)
      c34=-(2.0+25.0*x)/(128.0*xp1)
      c35=(26.0-35.0*x)/(128.0*xp1)
      c41=c31*c1
      c42=c32*c1
      c43=c33*c1
      c44=c34*c1
      c45=c35*c1
      d1=(3.0*x3p2)/8.0
      d2=d1*d1
      d3=d1*d2-(x4p1/8.0)
      d31=(8.0+11.0*x)/(8.0*xp1)
      d32=-(10.0+19.0*x)/(32.0*xp1)
      d4=d2*d2-(2.+33.*x)*d1/(32.*xp1)
      d41=d31*d1
```

```
      d42=d32*d1
      d49=15.0*x2p1*x3p2/64.0
      d33=-(45.0*x+12.0)/(40.0*xp1)
      c48=3.0*x5m2/(128.0*xp1)
      c49=-(9.0*x+4.0)/(48.0*xp1)
      e2=3.0*pi/(2.0*xp1)
      e3=e2*3.0*x3m2/16.0
      e4=e2*c2-3.0*pi*x/(4.0*xp1)
      e5=e2*(c2*c1-2.0*x2p1/16.0-3.0/(8.0*xp1))
      f2=x5m2/16.0
      f3=f2*3.0*x3m2/16.0
      f4=f2*c2-((9.0*x+4.0)/(48.0*xp1))
      f5=f2*c3+c48+c49*c1
      u3=pi*(5.0*x-1.0)/(2.0*xp1)
      u0=8.0*pi
      g0=-4.0*pi
      g3=12.0*pi/(xp1*8.0)
      g4=1.5*pi*f2/xp1
      h2=d1*5.0/3.0
      h3=d2*5.0/3.0
      h4=(5./3.)*(d2*d1-(12.+45.*x)/(40.0*xp1))
      h5=5.0*(d1*(d3+d33)+d49)/3.0
      fy0=0.5
      p02=fy0*(2.0*x3p2*dpr/3.0-x3p2/6.0)
      p12=fy0*(-x3p2*c1/6.0+2.0*x3p2*f2)
      p21=-fy0*x3p2*f2
      p22=fy0*(-x3p2*c2/6.0+2.0*x3p2*f3)
      w3=x3m2*c31/3.+x3p1*c32/6.-x9p2*c33/6.
     1  -xm1*c34/2.+xm1*c35
      w4=w3*c1
      p31=-fy0*x3p2*f3
      p32=fy0*(-x3p2*c3/6.+2.*x3p2*f4+w3)
      p32=p32-(37.0+50.0*x)*x3p2/(192.0*xp1)
      p41=-fy0*x3p2*f4
      p42=fy0*(-x3p2*c4/6.+2.*x3p2*f5+w4)
      p42=p42+(100.0*x*x+189.0*x-46.0)*x3p2/(1024.0*xp1*xp1)
      p51=-fy0*x3p2*f5
      p6=6.0*pi
      q0=1.0
      q1=-c1
      q2=0.0
      q3=(2.0*c1*c2-c3-c1**3)
      q31=(2.0*c1*c2-c3-u3/u0-c1**3)
      q4=(2.0*c1*c3-3.0*c2*c1*c1-c4n+c2*c2+c1**4)
      tx0=0.5
      rm1=-2.0*x3p2*g0*tx0
      r0=tx0*x3p2*g0
      r1=0.0
      r2=tx0*(x3p2*e2/6.0-2.0*x3p2*g3)
      r2=r2+(30.0+25.0*x)*pi*x3p2/(8.0*xp1)
      r3=tx0*x3p2*g3
      fz0=0.5
      s02=fz0*(-x3p2/3.0-2.0*x3p2*dpr/3.0)
```

```
      s12=fz0*(-x3p2*d1/3.0+x3m2*h2)
      s12=s12+5.0/(4.0*xp1*xp1)
      s21=fz0*h2/xp1
      s22=fz0*(-x3p2*d2/3.0+x3m2*h3)
      s22=s22+5.0*d1/(4.0*xp1*xp1)
      s31=fz0*h3/xp1
      s32=fz0*(-x3p2*d3/3.+x3m2*h4-x3m2*d31/3.
     1 -4.*d32/(3.0*xp1))
      s32=s32+5.0*d2/(4.0*xp1*xp1)-(61.+90.*x)/
     1 (24.*xp1*xp1)
      s41=fz0*h4/xp1
      s42=fz0*(-x3p2*d4/3.+x3m2*h5-x3m2*d41/3.-4.
     1 *d42/(3.0*xp1))
      s42=s42+5.0*d3/(4.0*xp1*xp1)-(49.+60.*x)*d1
     1 /(16.*xp1*xp1)+25.*x2p1/(64.0*xp1*xp1)
      s51=fz0*h5/xp1
      t0=1.0
      t1=-d1
      t2=0.0
      t3=(2.0*d1*d2-d3-(d1**3))
      t4=(2.0*d1*d3-3.0*d2*d1*d1-d4+d2*d2+(d1**4))
   15 continue
      neqn = 1
c
c     calculate initial coordinates
c
      zp = zpo
      yp = ypo
      ho = d + roa
      hmin = ho
      ypmx = ypo
      troa = 3.0 * roa * ap
      n = 1
      k = 1
      index = 1
      dyo = dy
   25 continue
      zpend = zp + dyo * zprnt
c     call integrator, which calls subroutine deriv which
c     calculates instantaneous particle velocity
   26 call dgear (neqn,deriv,derivj,zp,dy,yp,zpend,error,
     * meth,miter,index,iwk,wk,ier)
      n = n + 1
      if( ier .gt. 128 ) then
      write (*,*) yp,zp,dypdzp,zpend,dy,index,ier
   35 format ( /,1x,'error  max eps',5e16.9,2i4)
      stop
      endif
```

```
      h = sqrt( yp**2 + zp**2 ) / ap
      s = 2.0 * h / ( r + ap )
      uyouz = uy / uz
   53 format(2e16.9)
      write (20,53)yp,zp
   40 format ( 4e11.4,e15.7,e11.4 )
      if( h .lt. hmin ) hmin = h
      if( yp .gt. ypmx ) ypmx = yp
      if( idir .eq. 1 ) go to 41
      if( zp .ge. 0.0 ) go to 50
   41 continue
      if( zp .ge. 0.0 .and. zp .ge. zfin ) go to 50
c     set limit on  number of points taken
c
      if( n .gt. nt ) go to 50
      if( yp .lt. 0.0 ) go to 50
c
c     calculate new cosine (ctp) and sine (stp) of theta-p
c
      go to 25
   50 continue
      write (*,*) ypo,zpo
   55 format (2e16.9)
      write (*,*) ypmx,zp,n
   60 format (2e16.9,i6)
      write (*,*) xlmda,ap,r
   65 format (3e16.9)
      write (*,*) hmin,yp
   70 format (2e16.9)
      stop
      end
c     deriv calculates instantaneous particle velocity
      subroutine deriv (neqn,zp,yp,dypdzp)
      implicit real * 8 (a-h,o-z)
      implicit integer * 4 (i-n)
      common xlmda,aor,dpr,ap,uz,auz,uyf,uzf,qdis
      common r,er,eg1,eg2,eg3,f,fg2,fg3,b,bg2,bg3,c,cg2
      common x11m,x12m,y11m,y12m,em,fm,swch,xr,ya,yb,yc
      common dydz,uy,auy,cg3,cg4,cg5,c4,e2,u0,rm1,r0
      common p02,p12,p21,p22,p31,p32,p41,p42,c1,c2,c3
      common r2,e3,e4,u3,s02,s12,s21,s22,s31,s32,s41
      common qd1,tau,s42,d1,d2,d3,d4
      pi = 3.141592654
      h = sqrt( yp**2 + zp**2 )
      ctp = zp / h
      stp = yp / h
      s = 2.0 * h / ( r + ap )
      a = ap / r
      d = h - 1.0 / a
      gap = d - 1.0
      gp2 = gap + 2.0
      swch1 = sch1 * swch
      swch2 = swch * 0.9999
```

```
c       far form
        h = sqrt( yp**2 + zp**2 ) / ap
        ctp =( zp / ap ) / h
        stp =( yp / ap ) / h
        d = h  - ( 1.0 / aor )
        a = aor
        e = 1.0 / d
        x = xlmda
        xp1 = x + 1.0
        x3p2 = (3.0 * x + 2.0)/xp1
c       calculate Fz, Fy, Tx. Note - Tx1 contains the
c       expansion for the coupling tensor also, i.e.,
c       it is not only the torque.
        dprc = dpr * x3p2 / 3.0
        fdis=qdis*x3p2/(gp2*gp2*gap*gap)
        th = - tau * gap
        fdl=qdl*x3p2*tau*exp(th)/(1.0-exp(th))
        fy=p02*a*a+p12*e*a*a+p21*e*e*a+p22*e*e*a*a+p31*a*e
     1  *e*e+p32*e*e*e*a*a+dprc*a*a
        fy = fy * 6.0 *pi * stp
        t12 = e2 * rm1
        t22 = e3 * rm1
        t21 = e2 * r0
        t32 = e4 * rm1
        t31 = e3 * r0
        tx1=t12*a*a*e+t22*a*a*e*e+t21*a*e*e+t32
     1  *a*a*e*e*e+t31*a*e*e*e
        tx1 = tx1 * stp / u0
        dktp=6.0*pi*(1.0+c1*e+c2*e*e+c3*e*e*e)
        fz=s02*a*a+s12*e*a*a+s21*e*e*a+s22*e*e*a*a+s31*a*e
     1  *e*e+s32*e*e*e*a*a-dprc*a*a
        fz = fz * 6.0 *pi * ctp + fdis + fdl
        aktn=6.0*pi*(1.0+d1*e+d2*e*e+d3*e*e*e)
c       uy and uz are particle velocities in local y,z
c       coordinates relative to flat interface
        uz = - fz / aktn
        uy = -( fy + tx1 ) / dktp
c
c                 to obtain the composite expansion ->
c       first, add the outer streaming flow to the
c       disturbance velocities.
c       the inner expansion of the outer flow has already been
c       left off, so that the part both solutions have in
c       common is not counted twice.
        uys = -stp*(1.0-x3p2/(4.0*h*a)-x/(4.0*xp1*(h*a)**3))
        uzs = ctp*(1.0-x3p2/(2.0*h*a)+x/(2.0*xp1*(h*a)**3))
        uy = uy + uys
        uz = uz + uzs
        uyf = uy
```

```
      uzf = uz
   90 continue
c     transform uy and uz to world coordinates, uyp and
c     uzp with respect to origin at the drop center
      uyp=(ctp*uy)+(stp*uz)
      uzp=(ctp*uz)-(stp*uy)
      dypdzp=uyp/uzp
      dydz = dypdzp
      return
      end
c     derivj - dummy subroutine used by "DGEAR", the
c     second derivatives are estimated numerically
      subroutine derivj (neqn,zp,yp,pd)
      dimension pd(1,1)
      return
      end
```

Chapter IV

Experimental investigation of the trajectory/capture of a small spherical particle by a bubble drop in low-Reynolds number flow.

Introduction

Because of the complicated nature of flotation processes, theoretical studies of flotation have necessarily considered a simplified version of the process; thus, in many cases reliable results can be obtained only through experimentation. Therefore, a very large number of experimental studies on flotation have been performed. The majority of these studies have concentrated on the "chemistry" of the process, and references to many of these studies can be found in Derjaguin and Dukhin (1979), Fuerstenau and Healy (1972), Sutherland and Wark (1955).

These studies include bubble-pickup studies and contact time measurements in addition to a large number of reaction rate constant measurements. In the latter studies, a Halimond tube device, Sutherland and Wark (1955), has been extensively used to measure separation rates by measuring the rate at which particles settle into a branch of the tube. These particles are assumed to come from bubbles that have carried them to the top of the vessel and have subsequently ruptured and allowed the particles to settle into the tube branch. The posiible sources of error associated with this type of study are numerous, although the extensive use of Halimond tubes testifies to the utility of these studies and to the complexity involved with other types of experimental studies of real flotation processes. A large number of reaction rate studies have also been performed by sampling with a hypodermic syringe the contents of a batch flotation vessel over a period of time, Reay and Ratcliff (1975), Collins and Jameson (1976), Yuu and Fukuii (1981), Flint and Howarth (1971). A coulter counter device is used to measure the particle concentrations in these samples.

As pointed out in the thesis introduction, many of the experimental studies give conflicting results for the separation rate constants. Because of this disagreement, and because of the general complexity of flotation processes, a less empirical type of experimental study is needed, so that what is actually happening in the experiments and why it is happening can be hoped to be explained. This necessarily involves investigation of the actual capture process through ob-

servation of particle trajectories and capture. A step in this direction is the experimental investigation of Anfruns and Kitchener (1977), where the number of particles attached to rising bubbles (at large bubble Reynolds number) at the top of a column was measured photographically. In this study, large differences in capture efficiency were found for different shaped particles (spherical beads versus flakes with jagged edges) although since the actual capture process was not observed, it is difficult to determine whether this increase in effeciency occurs because of more rapid film rupture near a jagged edge (as the authors conclude), or whether this increase also occurs because of effects of the particle shape on the long-range hydrodynamic interaction between the particle and the bubble. The first investigation of this type was performed by Brown (1960), who recorded particle trajectories at large bubble Reynolds number, $Re_B \approx 300$, where particle and bubble inertia are important as evidenced by the rebound phenomena that are observed. Particles and bubbles were observed from two simultaneous right-angle directions by means of a mirror system and high speed video camera. Also, Schulze and Gottschalk (1981) performed experiments measuring particle trajectories at large Reynolds numbers. This latter study has the advantage/complication of using a stoboscopic technique to measure trajectories. In this technique a "precise" plane of particles is illuminated and a strobe records the position of the particle and bubble on a single film over the course of a trajectory. The advantage of this method is the simplified measurement of the particle/bubble trajectory. However, to obtain useful results from strobe techniques in this problem the bubble must be held fixed, otherwise it is impossible to determine the correspondence of the multiple particle positions with the multiple bubble positions (if smearing of the bubble does not prevent any determination of bubble positions at all). In their study, Schulze and Gottschalk (1981) accomplish this by passing a flow through the tube to hold the bubble "stationary." They fail to realize that this flow itself may dramatically alter the particle trajectories. Other studies have accomplished this by using a solid

collector which is fixed in position by a tether. These studies, all of which considered large Reynolds numbers, found good agreement between the particle trajectories and what would be predicted by potential flow field around a free bubble. Thus, as mentioned in Chapter 3, the question of whether a bubble behaves like a solid or a gas in its interaction with a particle at low Reynolds number does not appear to have been answered. Also, the omission of investigations into this interaction is more serious in light of recent interest in effluent flotation, which is essentially a low Reynolds number process (unlike mineral flotation, which is essentially a high Reynolds number process). The creeping flow problem is also appealing, since several of the experimental difficulties encountered in the large Reynolds number problem can be cleverly solved in this problem. For instance, using the two right-angle view may lead to the loss of trajectories where the projection of the particle from the camera intersects the bubble surface, and the particle is blocked from view by the bubble. These cases are more likely to occur for small separations that are involved in trajectories that actually lead to capture. Thus, just when the hydrodynamic interaction is becoming interesting, the view of the trajectory is obscured. Also, the error and time consumption associated with interpolating positions from two views may be large with the large depth of field normally associated with lenses with large working distances. This problem can be overcome in the low Reynolds number case, since the interaction times are sufficiently large to allow allignment of the plane of interaction with the viewing plane so that only one view of the interaction is required. The method of accomplishing this will be described in a later section.

Thus, the objective of this study is the visual recording of actual particle trajectories around bubbles and particle capture by bubbles. Furthermore, stability of the captured particles can be observed along with the direct effects of additives on the particle trajectories.

In addition to the advantages of longer interaction times at low Reynolds

number, the creeping flow problem has the advantage of low bubble velocities, which allows tracking bubbles using a moving track similar to that used in a series of experiments by Goldsmith and Mason (1959). Also, the bubble remains spherical, and its trajectory does not undergo oscillations.

However, the creeping flow problem has several experimental difficulties associated with it. First, extremely small bubbles are needed to maintain the Re small and small particles are needed to maintain the importance of electroviscous and molecular forces. Thus, a microscope is required to visualize these trajectories. However, this microscope must have a very large working distance, so that the container is sufficiently large so that the effects of the container walls can be neglected. This difficulty is overcome by using a Questar^{R} long-range tele-microscope for visual observation of the particle and bubble. A second difficulty is the manufacture of the bubbles to be used in the experiments. Bubbles are generally produced experimentally, either by syringes, electrolysis or spargers. Generally, syringes are limited by the needle size; bubbles smaller than the needle diameter will not break off from the needle on their own. But both electrolysis and spargers have the disadvantages of producing swarms of bubbles and having much less control of bubble size and location. A third difficulty is the effect of vibrations on the magnified view of the particle trajectory. This is especially important in the case of tracking the bubble to look at the stability of captured particles. Lighting may also be a problem, with the required magnification and large working distance.

Experimental Apparatus and Materials

A schematic sketch (to scale) of the apparatus that was designed and built to perform these experiments is shown in Figure 1, and a photograph of the actual apparatus is shown in Figure 2. The general description of the apparatus is as follows. This apparatus consists of a platform, mounted on a track, which allows the platform to move vertically. The platform holds a rectangular optical glass tank that has a hole in the center of the bottom section of glass. Through

this hole a capillary tube/ 2 syringe device allows us to inject a small bubble into the bottom of the tank. As the bubble rises, the tank is lowered at the same rate, to maintain the bubble fixed in view of our microscope. A worm screw mounted in a linear actuator with a gearing of approximately 300:1 is used to maintain a very slow and steady translation rate. Vibrations are reduced by using a flexible coupling between the variable-speed motor drive shaft and the linear actuator drive shaft. Also, 2 adjustable, "pillow-block" ball bearing bushing assemblies are used on each of the 4 translation shafts of the track to further reduce vibrations. The apparatus is quite massive and physically large, considering the size of bubbles and particles that we are interested in viewing. The apparatus was constructed in this manner to eliminate vibrations, to take advantage of several existing components in the design, and to facilitate machining on the components that remained to be constructed. One additional key component of the design of the apparatus is the large cylindrical tube, which is mounted about a guide, which it is free to rotate around, centered about the capillary tube inside the tank.

We will now give somewhat more detailed descriptions of several of the components of the experimental apparatus, which involve special features or require unusual design. The syringes/capillary tube device is shown in photographs in Figures 3, 4 and 5. The syringe mounted vertically in Figure 3 is a Hamilton 0.5 μliter syringe with a Chaney adaptor for structural support. The needle from this syringe penetrates a septum in the bottom of the syringe housing assembly, passes into the flared end of the capillary tube and is visible inside the capillary tube inside the tank as can be seen in Figures 4 and 5, which offer a life-size view of the capillary tube inside the tank and a view of the needle inside the tank through the long-range microscope at a magnification of about X65, respectively (through the use of a higher magnification eyepiece and additional extension tubes with a CCD video camera we obtain a magnification of about X130 for the majority of the actual experiments). The seals on the inside of the

syringe housing are accomplished through the use of O-rings. A close-up view of the cylinder/tank arrangement is seen in Figure 6, and the method of attaching a shaft to the top of the cylinder for rotation is seen in Figure 7. Finally, the microscope/video camera arrangement is shown in Figure 8. A camera cradle is used to provide support and reduce vibrations in the camera. Because of the large magnifications used in this system, a cinema camera is judged to be too prone to vibrations and thus is not used. Also, the alignment and bubble formation require manipulation that is best done with the aid of a video monitor, which allows the experimenter to have his hands free. Also, because of the large magnification, lighting becomes critical to image quality. For these small particles and bubbles, diffraction rings obscure the determination of the actual physical boundaries of the particle and bubble. To shrink the diffraction rings around the objects, a collimated red light (long wavelength) is used for illumination.

The fluid used in these experiments was reagent grade glycerol, which by viscosity measurements was judged to contain between 1 and 2% (by weight) water for the several series of experiments. The viscosity at the start and end of a particular series of experiments did not differ by more than 5 %. This fluid was placed inside both the cylinder and tank to match the refractive indices and to eliminate blurring due to refraction across the boundaries of the curved glass cylinder. The cylinder was then sealed to prevent addition of water vapor to the glycerol. The particles are monodisperse, 50 micron diameter, polystyrene spheres manufactured by Particle Information Services.

Performing experiments

Careful attempts were made to keep the apparatus and materials clean, although because of the fragile nature of several of the components, it was not possible to follow standard cleaning procedures (e.g., washing and soaking in acid). As a final step in the cleaning, the part of the apparatus in contact with fluids was soaked for 24 hours in distilled/deionized water. In any case, with

these procedures it is almost certain that trace contaminents of impurities are in the system when the experiments are performed. However, these impurities are always present in any real system and their effect is mostly noticeable on the critical gap size for capture (electroviscous effects). For the system used in this study, the electroviscous effects are expected to be small anyway, because of the large particle size. Also, it has been observed that even with careful cleaning, small bubbles always tend to rise with terminal velocities of equivalent solid spheres. Thus, actual trajectories around bubbles will be measured and compared with the "slightly" contaminated system and a "highly" contaminated system obtained by the introduction of electrolyte and surfactant. In addition, the charges on the bubble and particle are measured to determine any significant effect of contaminants on the particle and bubble charges.

Experimental Techniques

In this section, we will outline briefly the experimental procedure. A volume of gas is forced to protude from the tip of the microliter syringe needle in the capillary tube and is viewed on the video monitor, as in Figure 5. From this volume a single small bubble is formed by forcing fluid through the capillary tube from the other syringe (a disposable 10 ml plastic B-D syringe with a spring-loaded plunger held whose position can be finely adjusted by a small screw assembly) and shearing off a portion of the gas. If more than one bubble is formed, the flow in the capillary is reversed, and the excess bubbles are removed by sucking them back into the microliter syringe. By rotation of the microliter syringe, the position of the bubble in the capillary can be crudely adjusted. The making of bubbles in this manner involved a lot of trial and error. For instance, it was observed on several occasions that bubbles could also be formed by rapidly rotating (spinning) the microliter syringe, again shearing off small bubbles but having the advantage that the bubbles were not swept down the tube and had to be returned by reversing the flow. Also, small bubbles could be formed by a rapid pulsing of the microliter syringe plunger. It may be noted

that the behavior of the fluid interface in forming even these small bubbles is dramatically different in the "pure" glycerol and the glycerol with surfactant added. Thus, the presence of large amounts of accidental contaminants in the "clean" system can be observed and the system can be recleaned.

Once a bubble is formed, the bubble is transported to approximately 10 radii from the capillary tube opening by the flow from the 10 ml. syringe, at which point this flow is stopped and the particle is allowed to rise through its own buoyancy into the main body of the tank. The bubble is kept in view by translating the tank downwards at the same rate that the bubble rises. Trajectory measurements are not started until the bubble has again reached a point at least 10 radii from the capillary tube. At this point, the bubble rise velocity is essentially constant and all flow not arising from the motion of the bubble has stopped (there is a some motion of the particles because of the particle buoyancy but this is very slight). These particles are also introduced into the tank by the 10 ml. syringe. This is found necessary to ensure that the particles will lie sufficiently close to the path of the bubble for a reasonable chance for an interaction to occur without obscuring all interactions by a cloud of particles. The fluid in the 10 ml. syringe is taken at the same time as the tank is filled from the same fluid source.

The microscope has a large depth of field making it difficult to tell just from looking at the stationary particles, which particles lie close to each other. However, it is obvious from the video image when the bubble is close (1-2 radii separation) to a particle, since at this point the particle begins to move relative to the background particles. When this occurs, the cylinder is rotated, and the glycerol in the cylinder undergoes a rigid body rotation, thus aligning the viewing plane with the plane of interaction of the bubble and particle. This rotation is done in small steps to maximize the separation between the particle and bubble (thus getting the viewing plane as close as possible to the plane of interaction). This alignment works best if the bubble is exactly on the axis of

the cylinder (thus we try to position the bubble in the tube so that it will be close to the axis of the cylinder), although it can also be performed for off-axis bubbles. Once the bubble and the particle are lined up, the rotation is stopped and accurate trajectories are recorded by the video camera.

Results

Several trajectories have been recorded on video tape. A relatively good (well lined up, clear picture) trajectory is reproduced in Figures 9 - 13. The photographic reproduction is noticeably poorer in quality than the video image. In Figure 9, the particle on the equator of the bubble has been lined up with the bubble and in Figures 10 - 13 the succeeding positions of the trajectories are recorded. Comparison with the theoretical calculations by digitizing these trajectories, using a summagraphics digitizing tablet, indicates that the trajectories lie somewhere between what we calculate for a solid sphere collector and a bubble collector. However, these are only preliminary results to varify the feasibility of this study, and a more exhaustive study is required to fully understand the dependence of the particle trajectory on the physical parameters. Figures 14 and 15 are before and after pictures (respectively) for a particle that is captured by the bubble. There is a noticeable jump of the particle towards the bubble upon rupture of the thin film and capture.

The effects of electrolyte (double-layer size) on the trajectories are investigated by the addition of 100 mM KCL to the glycerol. The trajectories were not noticeably different from what was observed for the "pure" fluid; however, the capture process was in many cases significantly different. As can be seen in Figures 16, 17 and 18, which are at a lower magnification, upon contact of the bubble with the particle at its right shoulder, the bubble jumps several radii in the direction of the particle. We theorize that this occurs because of the transfer of a large charge from the particle to the bubble upon contact. The ions involved in this charge transfer spread rapidly over the surface of the bubble, and the bubble swims in the opposite direction to the motion of the ions, much like a

Marongoni effect.

Appendix A. Other experimental observations

In several instances, particle transfer between two bubbles and contact of two bubbles at shared particles were observed in the expeiments. This would suggest that more rapid separations could be obtained in flotation by using a bimodal size distribution of bubbles. Small "sweeper" bubbles would ensure high efficiency through large surface areas, and large "shuttle" bubbles could pick up these small bubbles to ensure a rapid transfer rate.

Particles captured on the bubble surface were always observed to be stable, and were not pulled from the surface by the flow arising from the normal bubble motion. The stability of captured particles on the surface of a bubble held in an annular flow on the tip of the microliter syringe needle was also observed. In this case, the presence of a cap of particles led to pinching off of the particle on the axis. Once a particle was squeezed off, the flow had to be increased to pinch off the next particle. The last particle required a significantly higher flow rate to remove it.

References

Anfruns, J.F. and Kitchener, J.A., 1977 Rate of capture of small particles in flotation. *Inst. Mining Metal.* **86**, C9.

Brown, D.J., 1960 Particle trajectories, collision and attachment in froth flotation in *Aerodynamic Capture of Particles* ed. by E.G. Richardson, Pergamamon, London.

Bushell, C.H.G., 1962 Kinetics of flotation. *Trans. A.I.M.E.* **223**, 266.

Collins, G.L. and Jameson, G.J., 1976 Experiments on the flotation of fine particles. *Chem. Eng. Sci.* **31**, 985.

Collins, G.L. and Jameson, G.J., 1977 Double-layer effects in the flotation of fine particles. *Chem. Eng. Sci.* **32**, 239.

Deryagin, B.V. and Dukhin, S.S., 1979 Kinetic theory of the flotation of fine particles. *Proceedings of 13th International Mineral Processing Congress, Warsaw*, (Elsevier, Amsterdam, 1981).

Deryagin, B.V., Dukhin, S.S. and Rulev, N.N., 1976 Importance of hydrodynamic interaction in the flotation of fine farticles. *Colloid J. U.S.S.R.* **38**, 227.

Deryagin, B.V., Dukhin, S.S. and Rulev, N.N., 1977 Thin-film capillary hydrodynamic method in the theory of flotation. *Colloid J. U.S.S.R.* **39**, 926.

Dukhin, S.S. and Rulev, N.N., 1977 Hydrodynamic interaction between a solid spherical particle and a bubble in the elementary act of flotation. *Colloid J. U.S.S.R.* **39**, 231.

Ellwood, P., 1968 Electrolysis-Bred Bubbles Clarify Waters. *Chem. Eng.* **75**, 82.

Flint, L.R. and Howarth, W.J., 1971 The collision efficiency of small particles with spherical air bubbles. *Chem. Eng. Sci.* **26**, 1155.

Fuerstenau, D.W. and Healy, T.W., 1972 in *Adsorptive Bubble Separation Techniques* (R. Lemlich, ed.), Academic, New York p. 91.

Fukui, Y. and Yuu, S., 1980 Collection of submicron particles in electro-flotation. *Chem. Eng. Sci.* **35**, 1097.

Gaudin, A.M., Schuhmann, R. Jr. and Schlechter, A.W. 1942 Flotation kinetics II. The effects of the size on the behavior of galena particles. *J. Phys. Chem.* **46**, 902.

Morris, T.M., 1952 Measurement and evaluation of the rate of flotation as a function of particle size. *Trans. A.I.M.E.* **193**, 794.

Reay, D. and Ratcliff, G.A., 1973 Removal of fine particles from water by dispersed air flotation: effects of bubble size and particle size on collection efficiency. *Canad. J. Chem. Engng.* **51**, 178.

Reay, D. and Ratcliff, G.A., 1975 Experimental testing of the hydrodynamic collision model of fine particle flotation. *Canad. J. Chem. Engng.* **53**, 481.

Schulze, H.J. and Gottschalk, G. 1981 Experimental investigation of hydrodynamic interaction of particles with a gas bubble. *Colloid J. of USSR* **43**, 757.

Spielman, L.A., 1977 Particle capture from low-speed laminar flows. *Ann. Rev. Fluid Mech.* **9**, 297.

Stoos, J.A., 1987 Ph.D. dissertation. California Institute of Technology.

Sutherland, K.L. and Wark, I.W. 1955 *Principles of Flotation* Australian Institute of Mining and Metallurgy, Melbourne.

Tominson, H.S. and Fleming, M.G., 1963 in *Mineral Processing* (A. Roberts, ed.), Pergamon Press, New York.

Yuu, S. and Fukui, Y., 1981 Measurement of fluid resistance correction factor for a sphere moving through a viscous fluid toward a plane surface. *J. A.I.Ch.E.* **27**, 168.

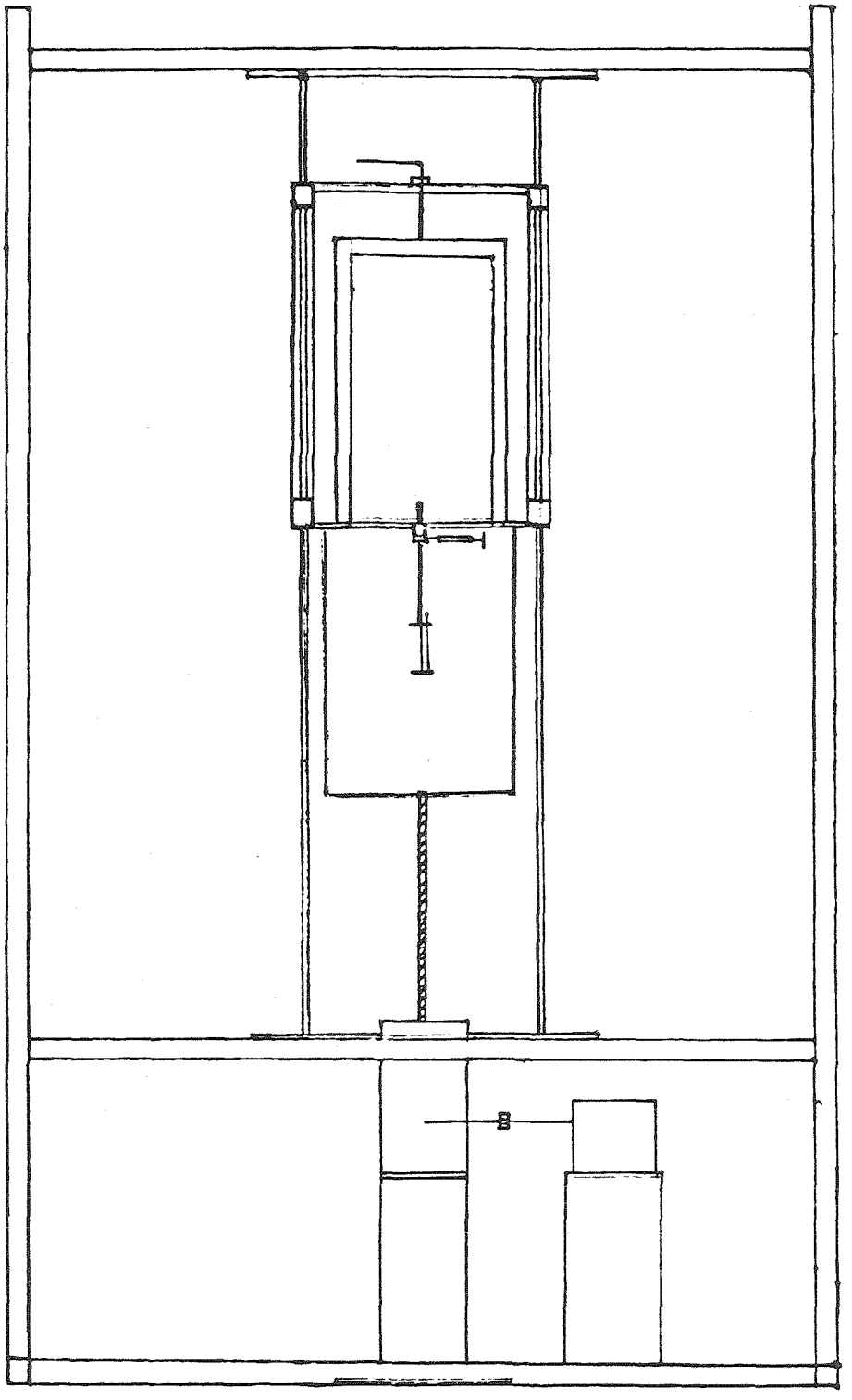

Figure 1. Schematic of the experimental apparatus.

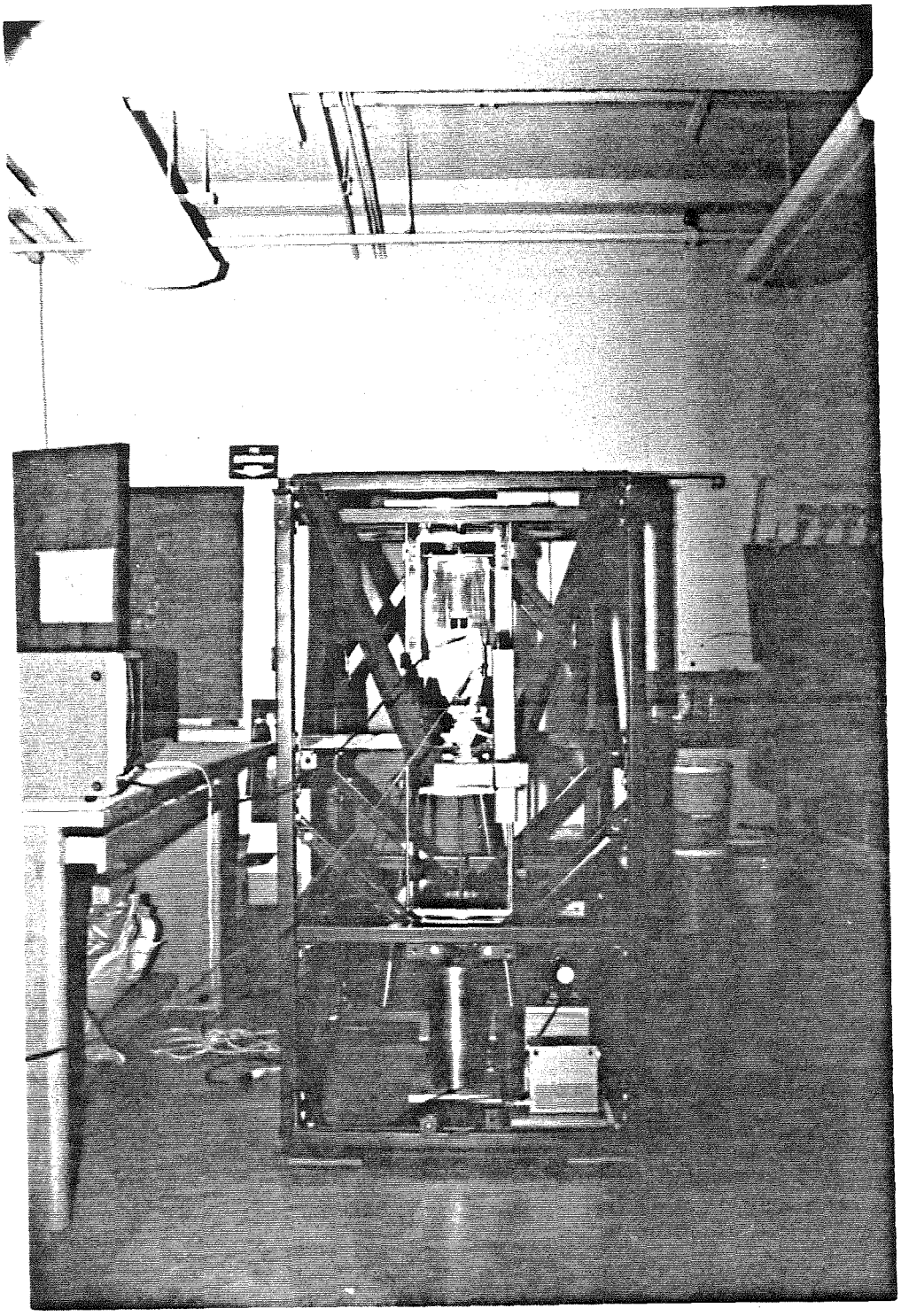

Figure 2. Photograph of the experimental apparatus.

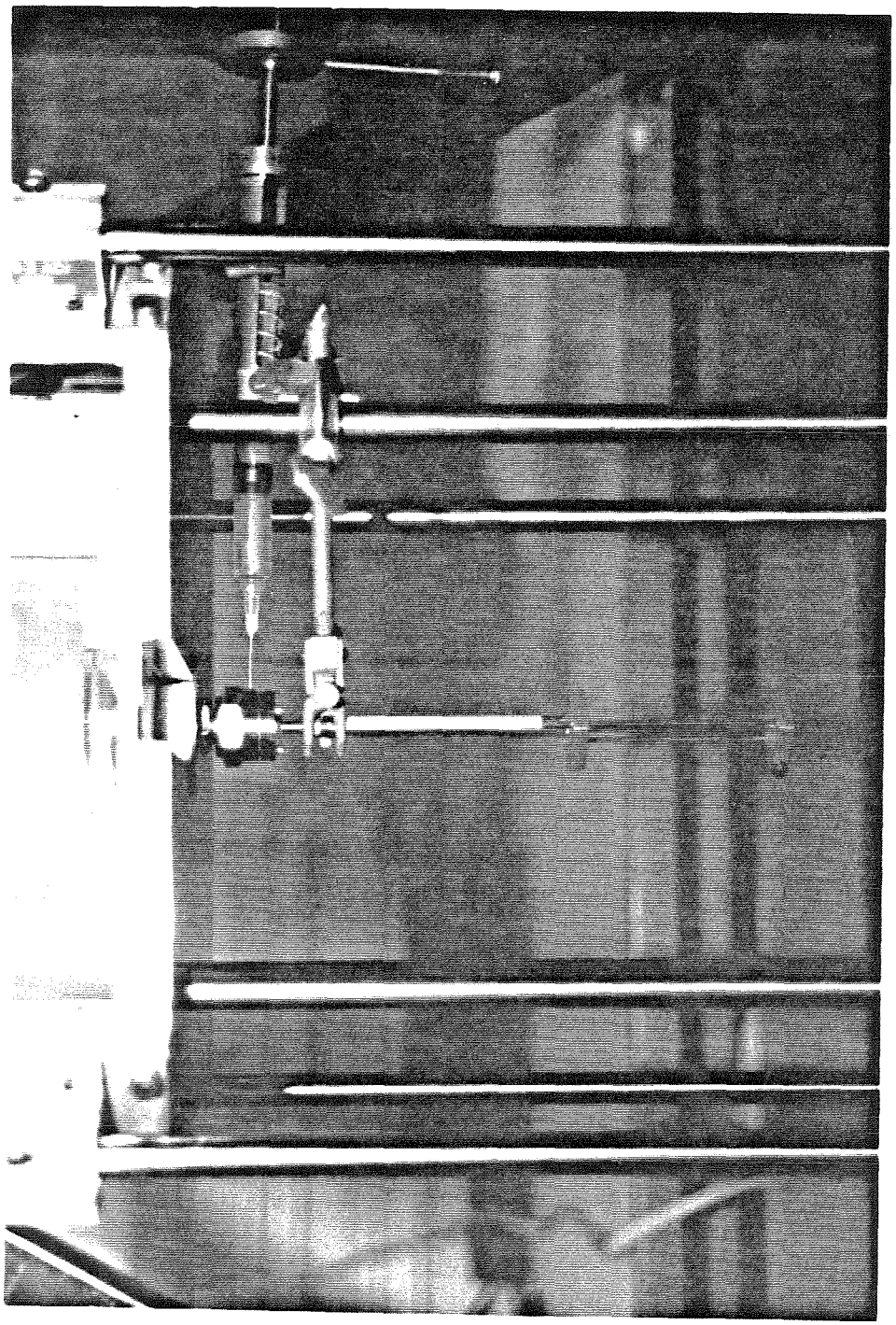

Figure 3. Syringe injection system.

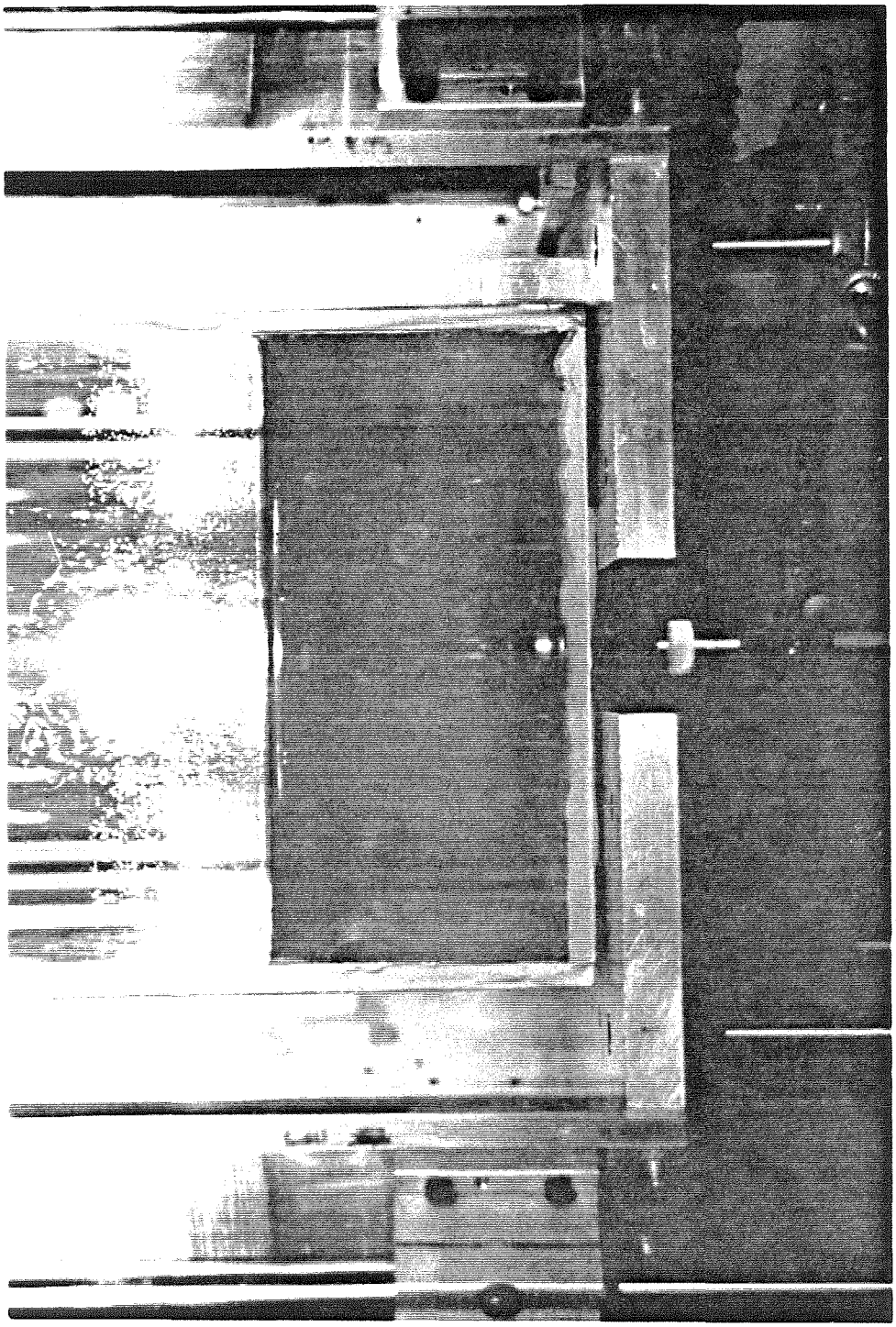

Figure 4. Capillary tube in experimental tank.

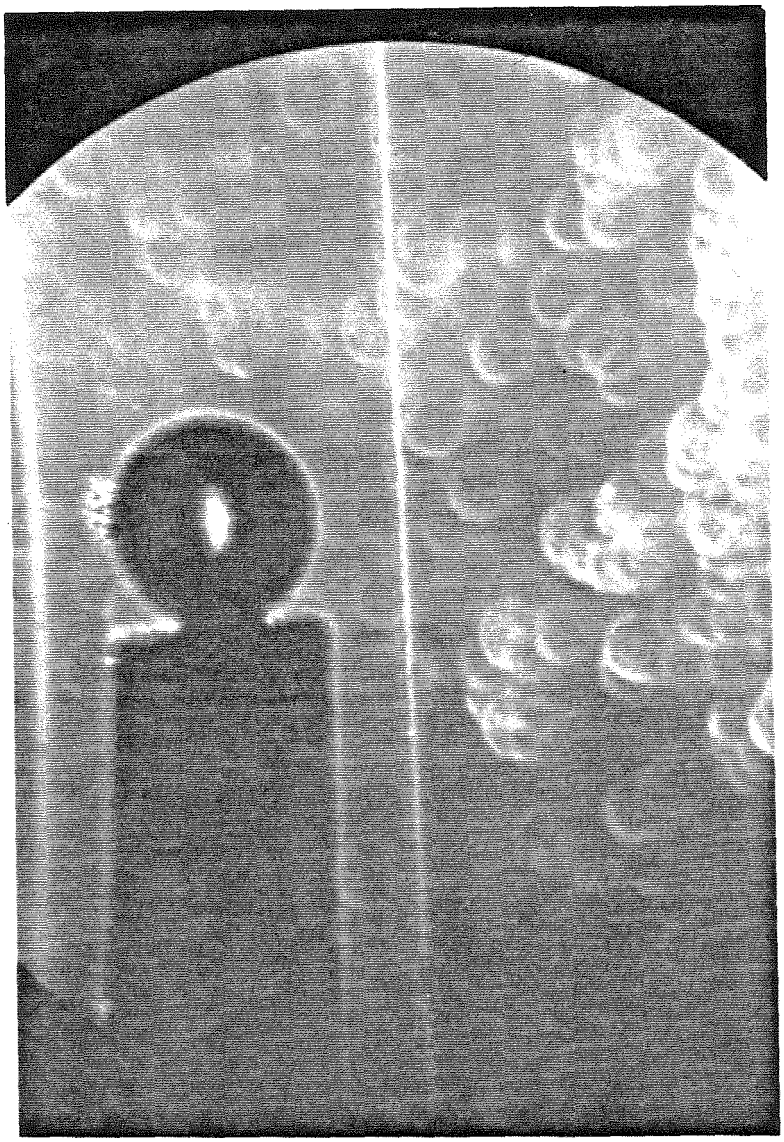

Figure 5. Magnified view of syringe in the capillary tube with an attached gas bubble.

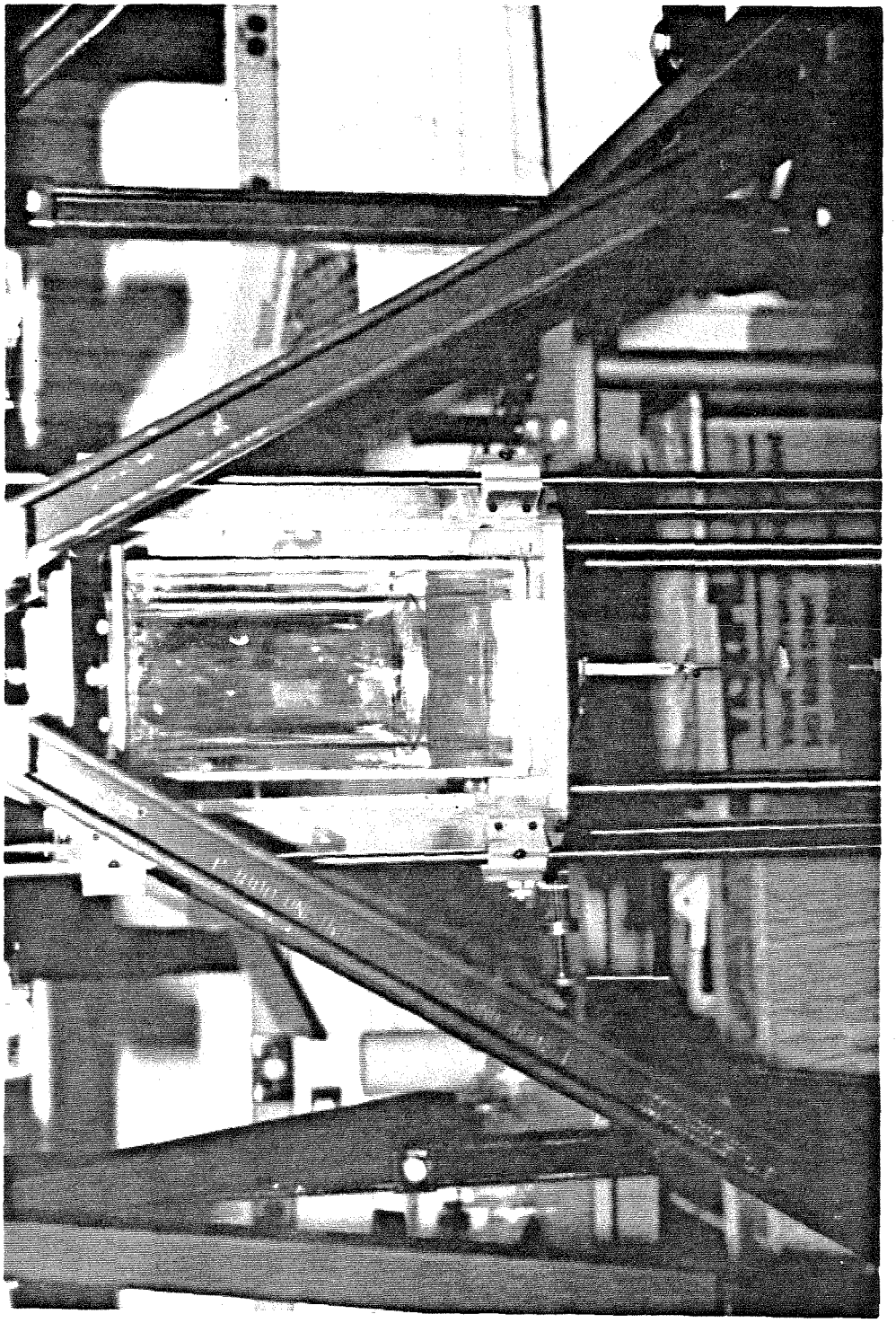

Figure 6. Translation system used in experiment.

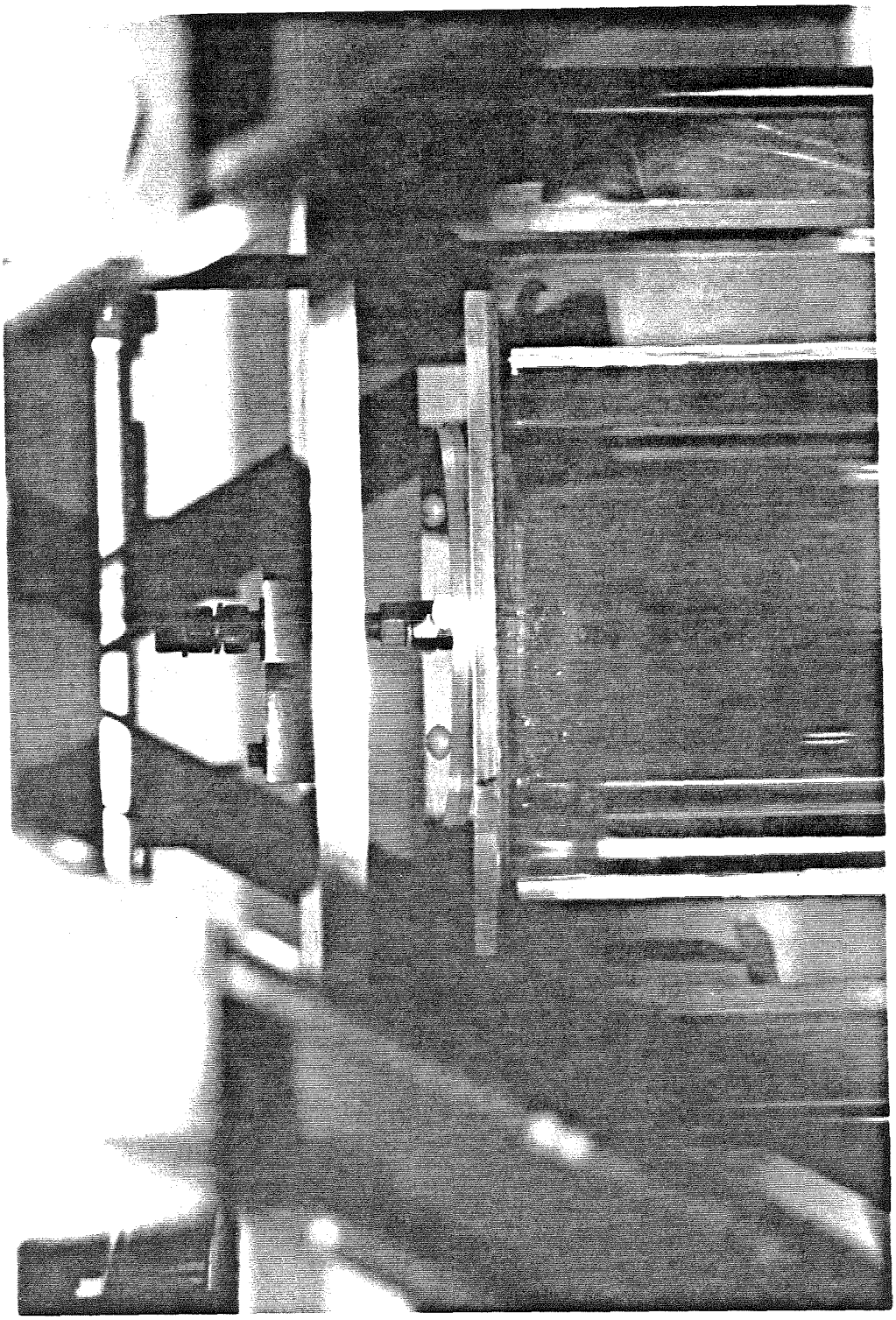

Figure 7. Cylinder rotation device.

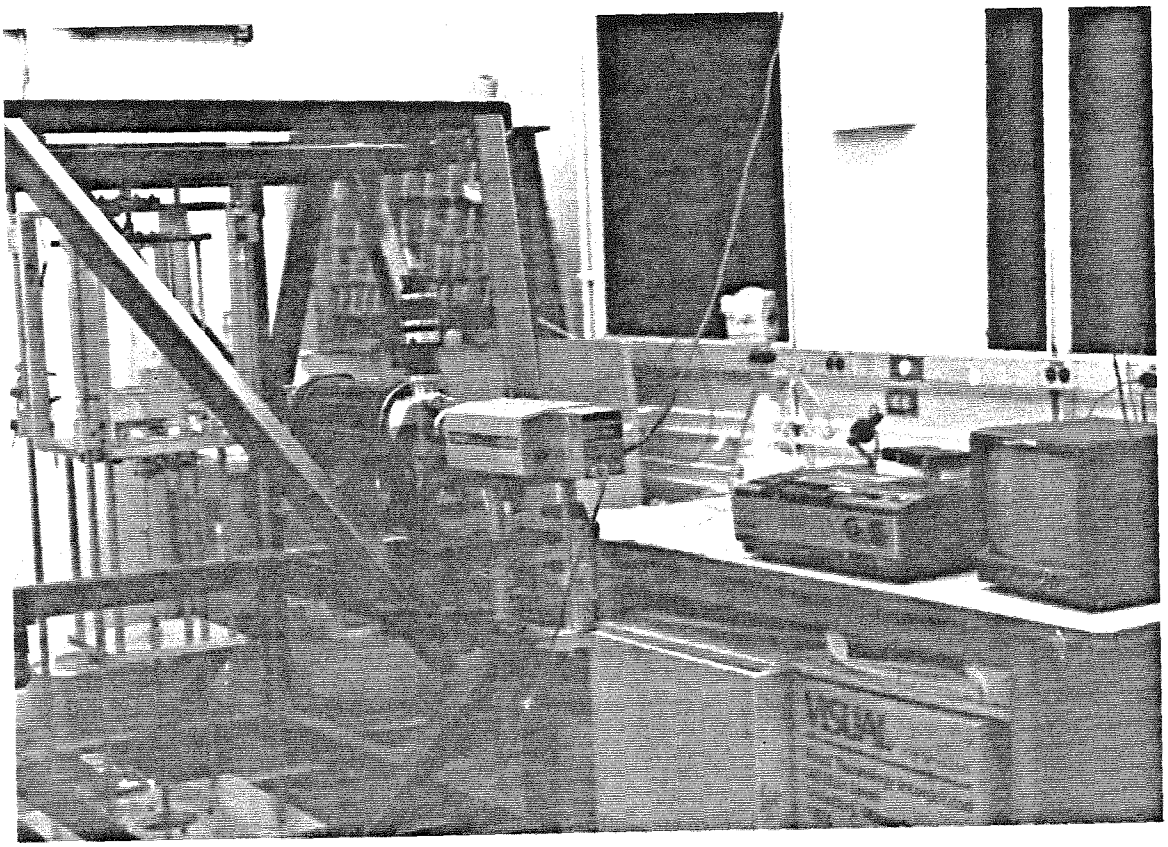

Figure 8. Microscope-video camera viewing system.

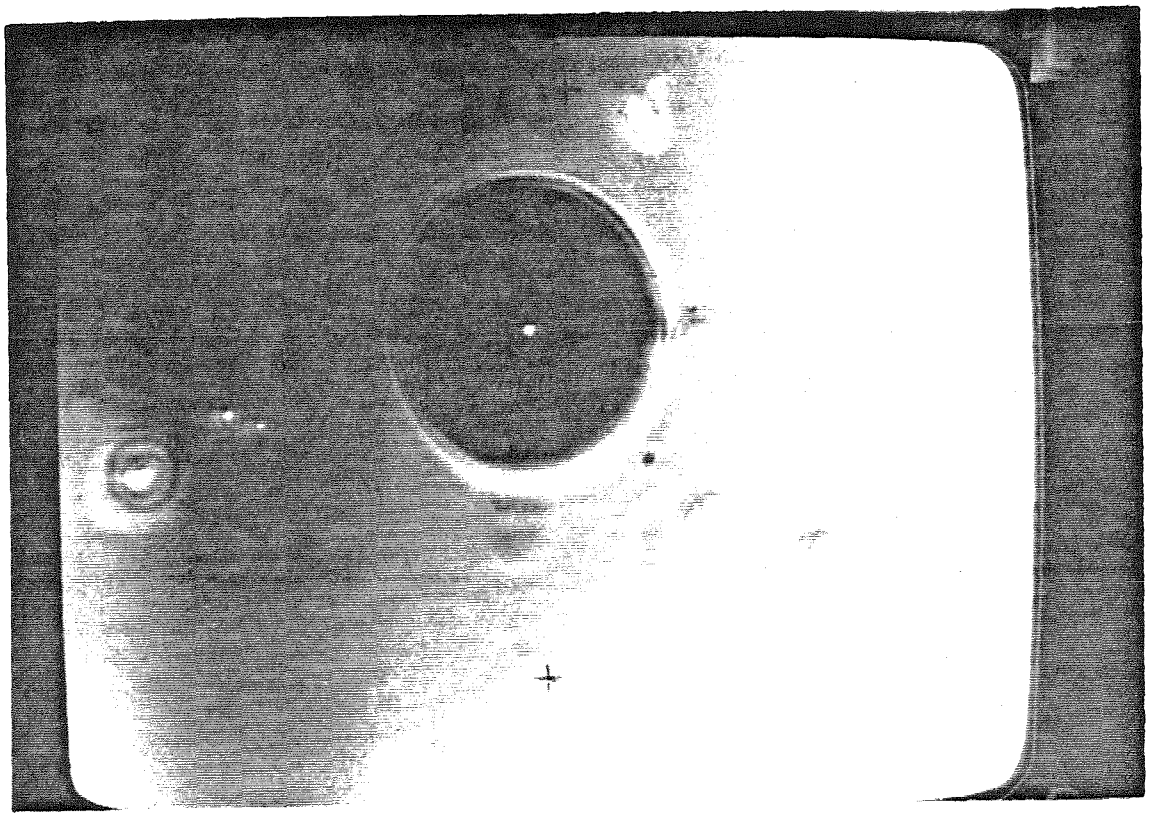

Figure 9. Photograph of particle-bubble trajectory.

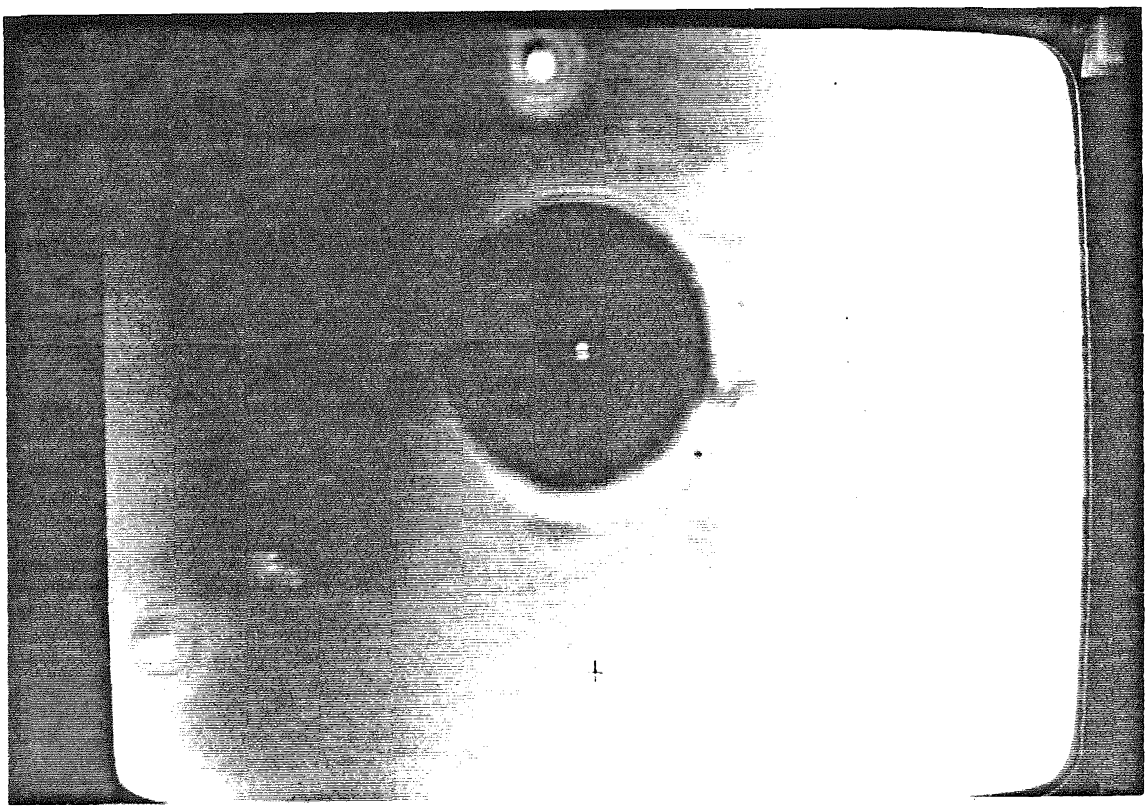

Figure 10. Photograph of particle-bubble trajectory.

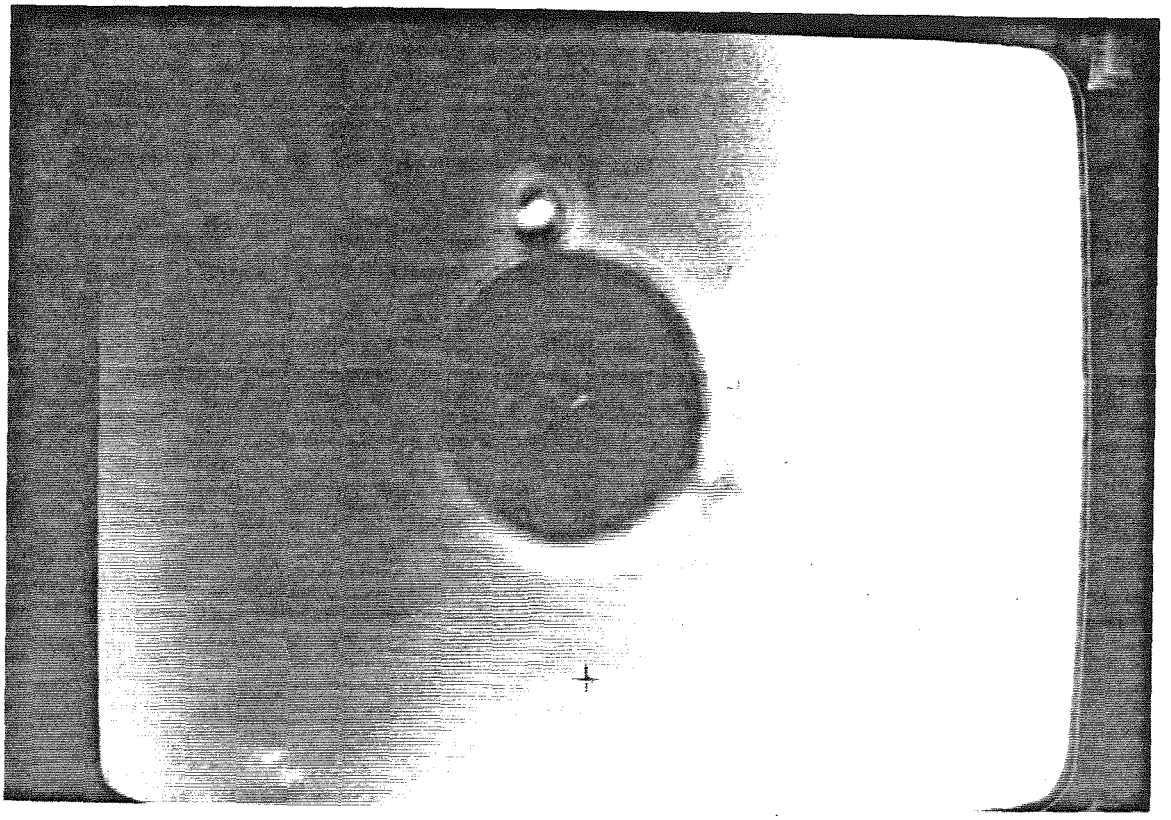

Figure 11. Photograph of particle-bubble trajectory.

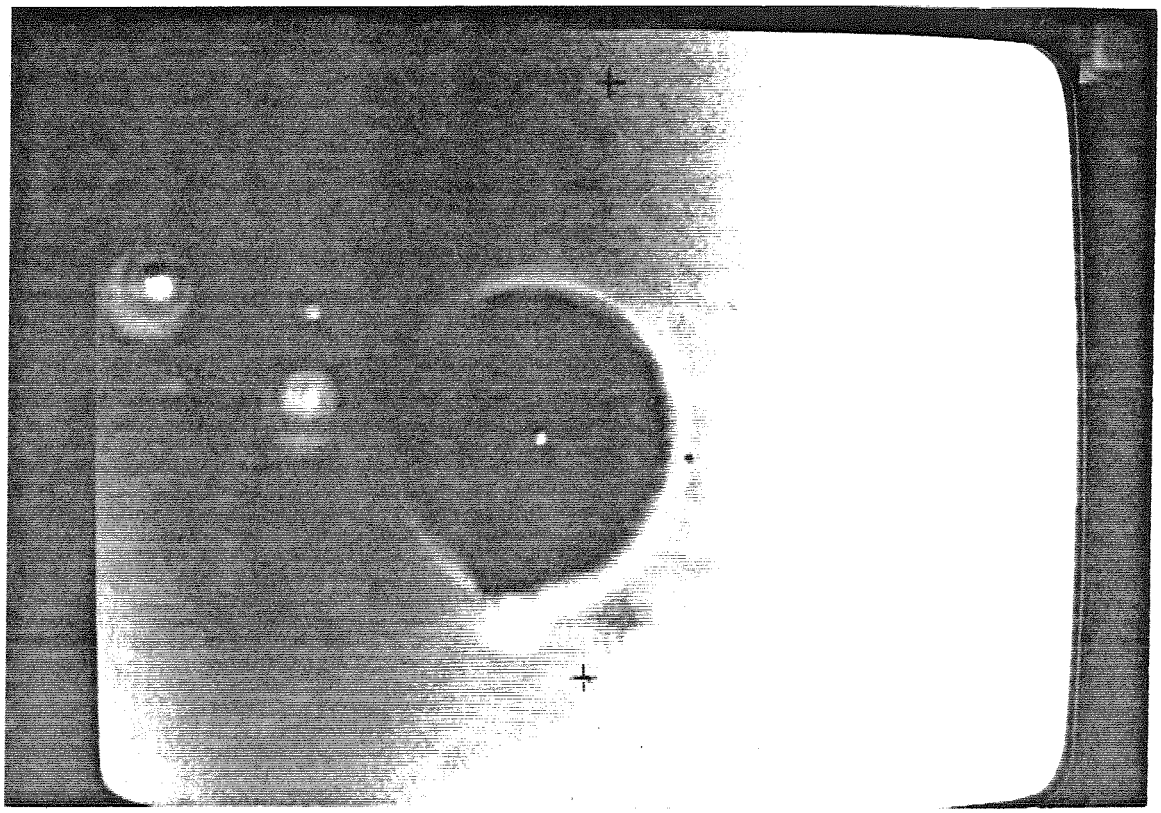

Figure 12. Photograph of particle-bubble trajectory.

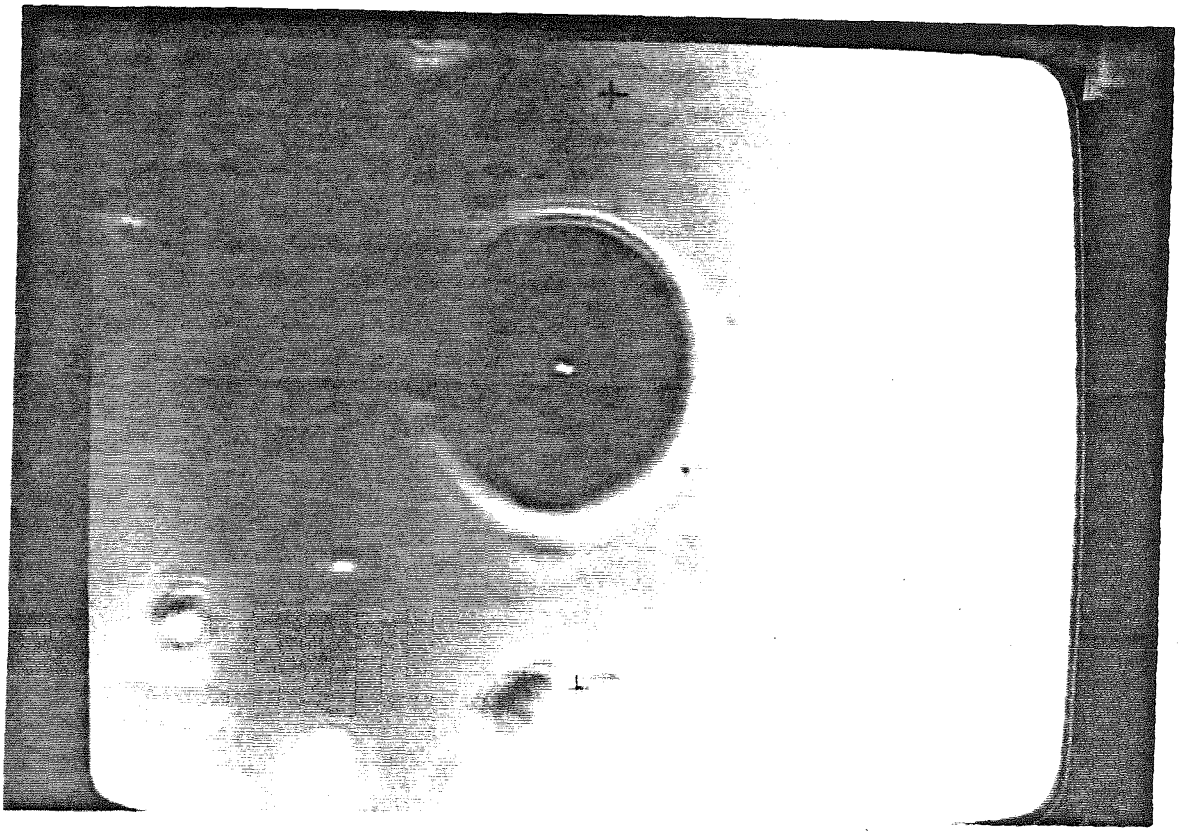

Figure 13. Photograph of particle-bubble trajectory.

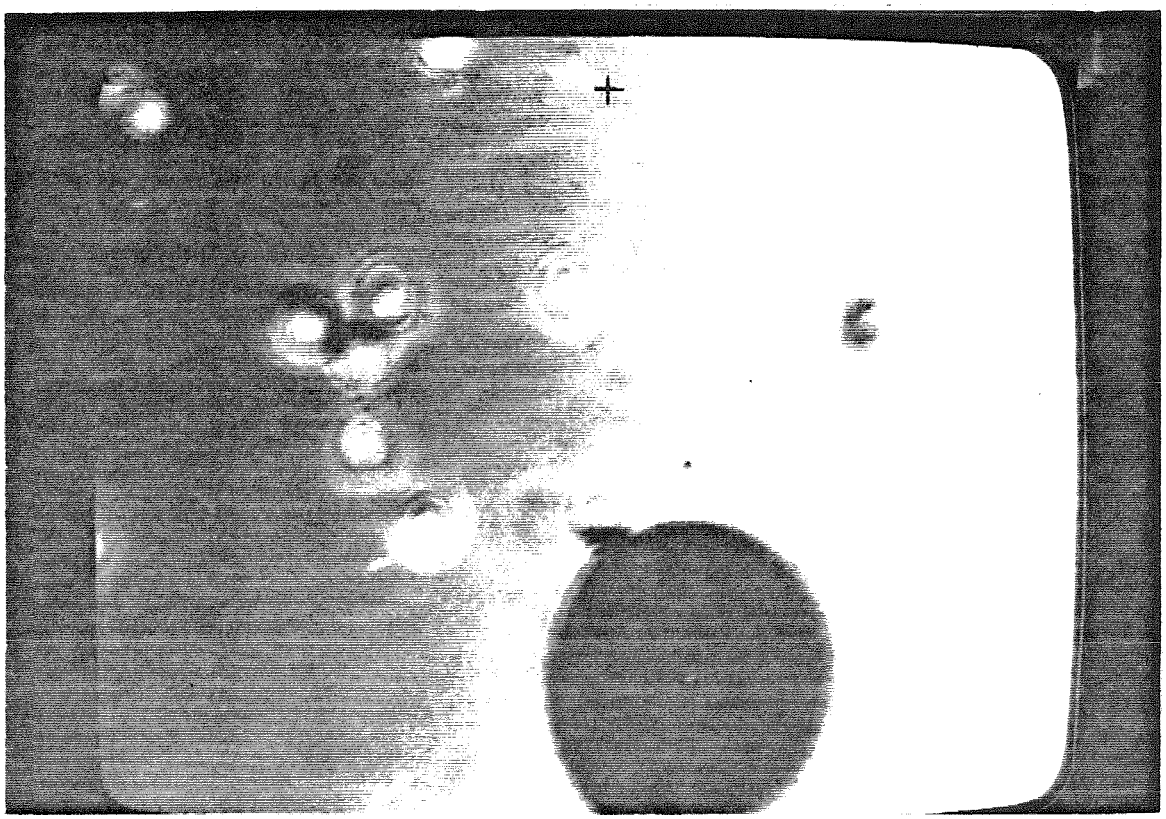

Figure 14. Immediately before capture of the particle.

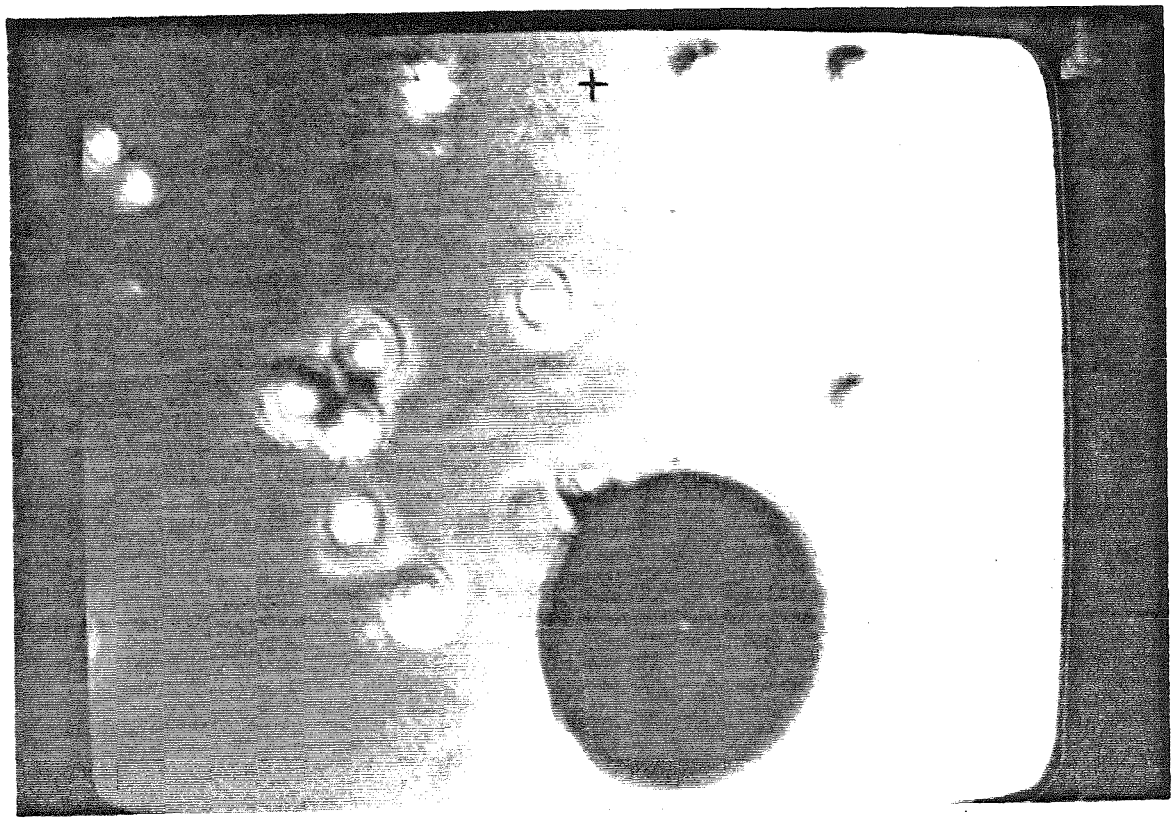

Figure 15. Immediately after capture of the particle.

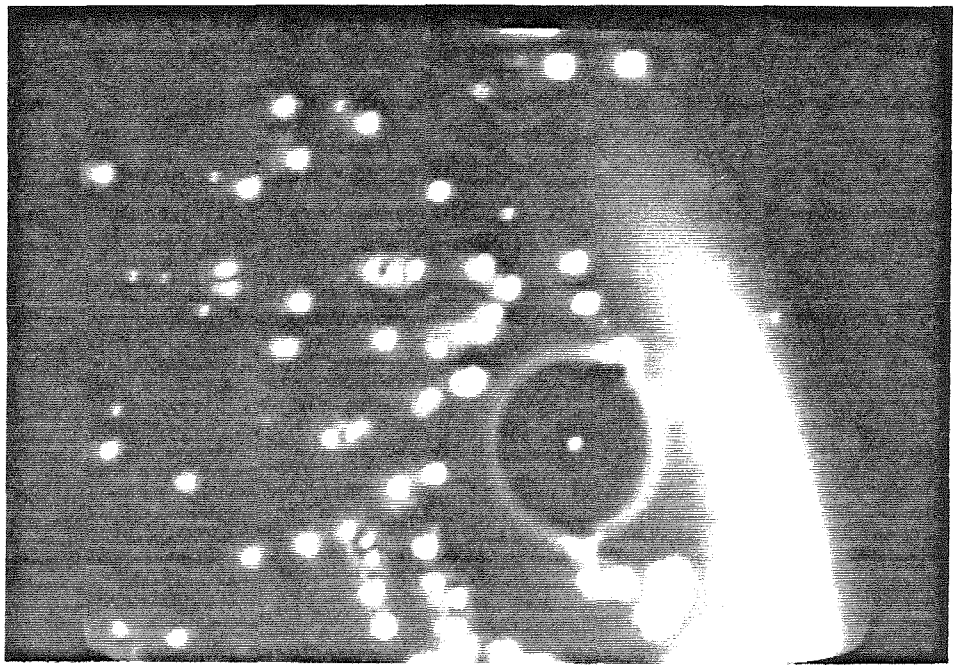

Figure 16. Immediately before capture. of the particle - large concentration of electrolyte.

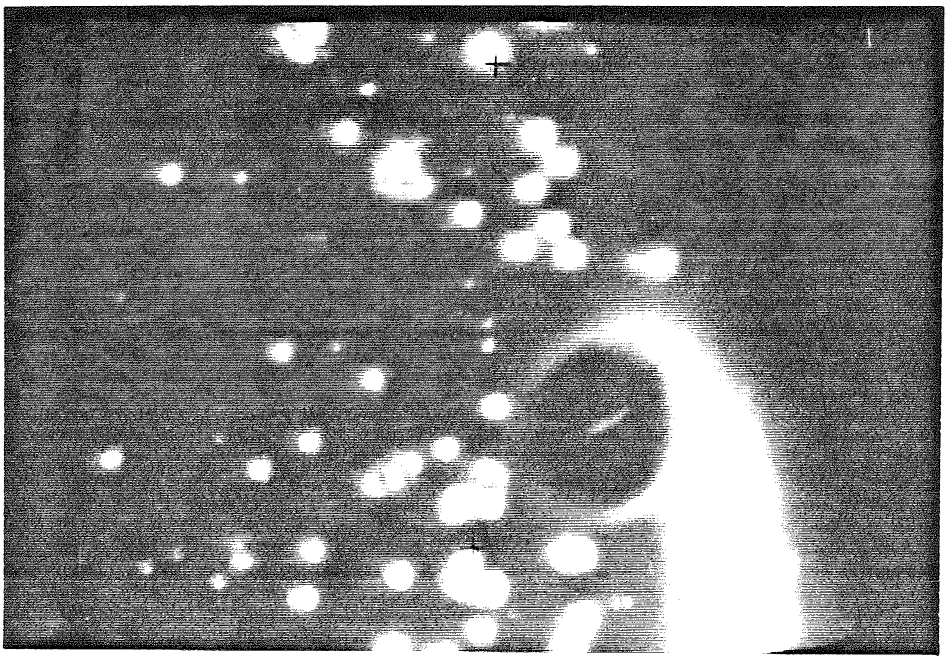

Figure 17. Jumping of bubble towards the particle upon contact - large concentration of electrolyte.

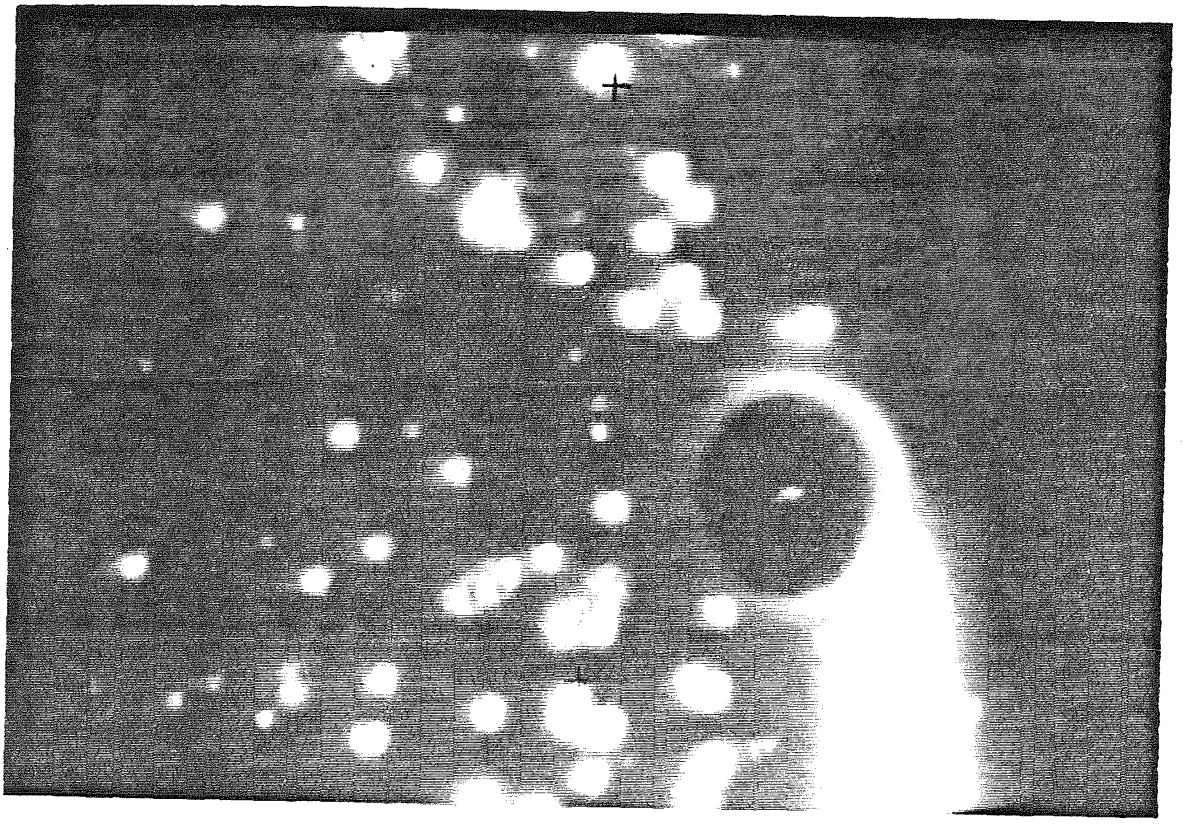

Figure 18. New bubble position after jumping.